APPLIED COMPUTATIONAL ELECTROMAGNETICS SOCIETY JOURNAL

January 2016
Vol. 31 No. 1
ISSN 1054-4887

The ACES Journal is abstracted in INSPEC, in Engineering Index, DTIC, Science Citation Index Expanded, the Research Alert, and to Current Contents/Engineering, Computing & Technology.

The illustrations on the front cover have been obtained from the research groups at the Department of Electrical Engineering, The University of Mississippi.

EMERITUS EDITORIAL ASSISTANTS

JANUARY 2016 REVIEWERS

THE APPLIED COMPUTATIONAL ELECTROMAGNETICS SOCIETY

JOURNAL

Vol. 31 No. 1 January 2016

TABLE OF CONTENTS

A Novel Compact UWB Monopole Antenna with Triple Band-Notched Characteristics with EBG Structure and Two Folded V-slot for MIMO/Diversity Applications

A. Mousazadeh and GH. Dadashzadeh

Electrical and Electronic Engineering Department
Shahed University, Tehran, 3319118651, Iran
asgar.musazadeh@yahoo.com, gdadashzadeh@shahed.ac.ir

Abstract ─ A novel compact, ultrawideband (UWB) monopole antenna with triple band-notched characteristics are presented for MIMO/diversity applications. Triple band-notched function is achieved by inserting two folded v-slot on the radiation patch and two modified mushrooms-like EBG structure above ground plane on either side of feed line. The designed MIMO antenna has a small size compared to the previous similar designs. With the purpose of mutual coupling reduction between antenna elements, two rows of modified mushroom-like EBG structures are inserted to suppress the effect of the surface wave between antenna elements. The MIMO performance of the proposed antenna is studied through mutual coupling (S12), envelope correlation coefficient (ECC) and diversity gain.

Index Terms ─ EBG, MIMO monopole antenna, triple band-notch, Ultrawideband (UWB).

I. INTRODUCTION

Recently, multiple input multiple output (MIMO) systems have been received more attraction due to having good capabilities such as robustness against multipath fading, improvement of channel capacity and spatial diversity gain required for high data rate communication links [1]. In theory, the capacity of channels can be increased linearly with the number of elements; however, in practice mutual coupling between elements reduces channel capacity [2]. Therefore, it will be a major challenge to reduce mutual coupling in MIMO systems. The more distance is between inter-elements, the lower mutual coupling will be in result, but the size of the antenna will be increased undesirably. Several methods have been proposed to reduce mutual coupling between inter-elements in compact MIMO antennas based on diminishing surface waves. Employing the lossy material is proposed in [3], A quarter-wavelength slot are used in [4], single negative magnetic (MNG) metamaterials have been proposed in [5,6], defected ground structures (DGS) are used in [7,8], radial stub loaded resonator are employed in [9] and mushroom-like EBG structures are used widely in recent researches [10-13]; however, utilizing two or more rows of these structures will increase the size of MIMO antenna, so to decrease the size of mushroom-like EBG a method of moving the via off the center proposed in [14]. This method is employed in this paper to modify mushroom-like EBG structure.

To achieve higher data transfer rate communication links, it is required that the MIMO antenna should be suitable for UWB applications. However, the frequency range of 3.1 GHz to 10.6 GHz for UWB systems will cause interference to the existing wireless communication systems, such as, the wireless local area network (WLAN) for IEEE 802.11a operating at 5.15 GHz – 5.35 GHz and 5.725 GHz – 5.825 GHz bands, WiMAX (3.3 GHz – 3.6 GHz), C-band (3.7 GHz – 4.2 GHz) and X band uplink frequency band from 7.9 to 8.4 GHz; so the UWB MIMO antenna with a single, dual and triple band-stop performance is required. There are various methods to achieve band-notched characteristic for printed monopole antennas. The most popular approach is cutting different shaped slots in radiating patch or in its ground plane, the slots using U-shaped [15], a square [16], a trapezoidal shaped [17], an H-shaped [18] have been proposed and recently mushroom-like EBG structures have been used in [19-22]. Communication systems usually require smaller antenna size in order to meet the miniaturization requirements of radio-frequency (RF) units [23]. Nevertheless, most of these antennas have the common deficiency of large size, which may lead to a challenging task in miniaturizing antenna design.

In this letter, a novel triple band-notched MIMO antenna with reduction in overall size is proposed. The size of the proposed antenna is smaller than the MIMO antennas with band-notched function reported recently in [25-30]. This paper is organized as follows: the single monopole antenna configuration is presented in Section II. Section III is followed in two parts A and B, part A discusses triple band notch characteristic of the single

Submitted On: December 20, 2014
Accepted On: September 20, 2015

monopole antenna and part B discusses MIMO application of the proposed antenna through simulated and measured results. Finally, this letter is concluded with a brief summary in Section IV.

II. ANTENNA DESIGN

The geometry and configuration of the proposed microstrip-fed monopole antenna is illustrated in Figs. 1 (a) and (b). This antenna is fabricated on the commercially cheap FR4-epoxy substrate with εr = 4.4, tan (δ) = 0.024 and dimensions of 12×20×1.6 (=h) mm^3. The width of the microstrip feed line is fixed at 2 mm and is connected to a 50 Ω SMA connector. The optimized values of proposed antenna design parameters are given in Table 1.

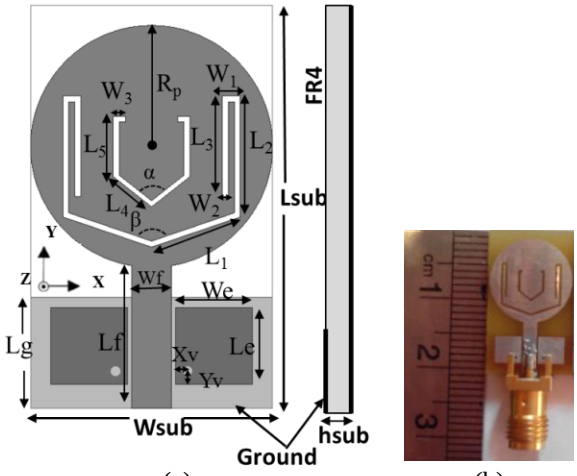

(a) (b)

Fig. 1. Triple band notched monopole antenna: (a) geometry and (b) configuration.

Table 1: Parametric values of proposed antenna

Param.	mm	Param.	mm	Param.	mm
Wsub	12	Xv	0.7	L3	5
Lsub	20	Yv	0.7	L4	2.42
hsub	1.6	g	0.2	L5	3
Wf	2	W1	0.9	Rp	3.3
Lf	7.1	W2	0.3	α	103
Lg	5	W3	0.9	β	142
We	3.8	L1	4.65		
Le	3.8	L2	6		

The basic antenna structure is a circular patch with a radius of R is printed on the top side of the dielectric substrate. To obtain the triple band-notched function two folded v-slots are embedded in the radiation circular patch and two modified mushroom-like EBG structures implemented symmetrically on both sides of the microstrip feed line above the ground plane. On the other side of the substrate, the conducting ground plane with a length of 5 mm covers only the section of the microstrip feed line.

III. RESULTS AND DISCUSSIONS

A. Triple band notch monopole antenna

The performance of the proposed antenna in parametric studies has been investigated to find optimized parameters using the Ansoft High Frequency Structure Simulator Software (HFSS, ver. 15) based on the finite element method (FEM). In the simulation setup perfect electric conductor (PEC) and an ideal excitation port are assumed.

To describe the design process, four prototypes of the proposed antenna are defined as follows (Fig. 2): AntI is a typical monopole antenna with a circular patch fed by microstrip line; in AntII, two modified off center mushroom-like EBG structures are used symmetrically on both sides of the microstrip feed line above the ground plane; AntIII includes a folded v-slot embedded in the circular patch and AntIV contains second folded v-slot inserted in the circular patch.

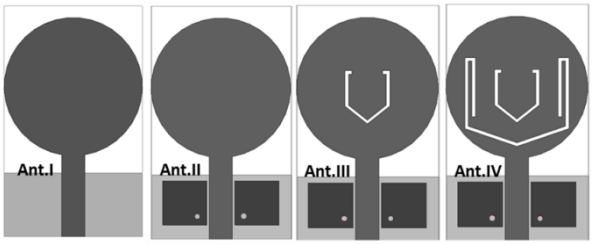

Fig. 2. Four improved prototypes of the proposed antenna.

Figure 3 presents simulated VSWR characteristic for four designed prototypes of the proposed antennas. As shown in Fig. 3, UWB impedance bandwidth can be simply achieved for Ant.I by adjusting length of ground plane (Lg = 5).

To provide band rejection around 5.1-6 GHz (WLAN band), two modified mushroom-like EBG structures employed on either side of the feed line symmetrically shown in Fig. 4 (a). Normally EBG unit cell is composed of a rectangular conductive patch and one shorting via placed at the center that connects the patch and the ground plane together. An equivalent-circuit model [24] of the EBG structure is shown in Fig. 4 (b).

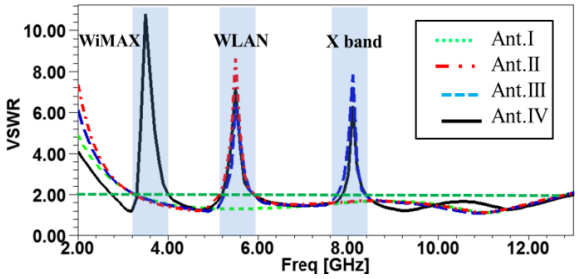

Fig. 3. Simulated VSWR of four designed prototypes of the proposed antenna.

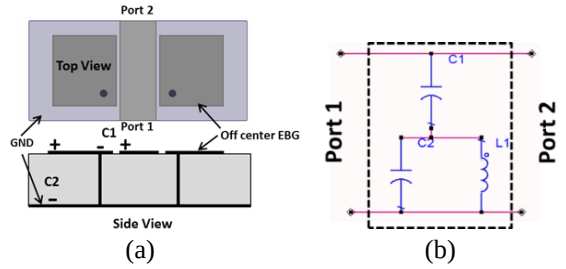

Fig. 4. (a) Two modified mushroom-look EBG structure on the either side of microstrip feed line; and (b) equivalent circuit.

The resonant frequency of the EBG cell can be obtained by:

$$fn = 1/2\,\pi\sqrt{L\,(C1 + C2)}, \quad (1)$$

$$C_1 = \frac{W\varepsilon_0(1+\varepsilon_1)}{\pi}.\cosh^{-1}\left(\frac{w+g}{g}\right), \quad (2)$$

$$L = \mu h, \quad (3)$$

where C_1 owes to the voltage gradients between the patch and the ground plane at normal mushroom EBG structure, C_2 is the coupling capacitance between the rectangular EBG structure and the feed line, and the inductance L is due to the current flowing through the via. The band gap region of EBG structure can be shown by dispersion Brillouin diagram where no mode is propagated and it can be simulated with HFSS eigenmode solver. A unit cell of EBG structure with master slave boundary is shown in Fig. 5. By adjusting parameters' value of typical mushroom-like EBG structure, desired band notch can be obtained around 5.5 GHz for w_e = le = 6.5 mm; but the width of mushroom is larger than the width of antenna ground (lg = 5), so with the aim of miniaturizing EBG structure, the position of via is moved off the center of the patch [14] and subsequently the resonant frequency is reduced to 3.3 GHz, therefore by fixing notch frequency on 5.5 GHz the value of w_e will be reduced to 3.8 mm and the structure of mushroom-like EBG will be modified. The band gap region of modified mushroom-like EBG structure is shown in Fig. 6. It can be seen that band gap is from 5.1 GHz to 6 GHz.

To realize dual band-notch characteristic, a folded v-slot is embedded in the radiation patch of Ant.II where the length of slot can be obtained approximately from the following formula:

$$L = \frac{C}{4\times f\times\sqrt{\frac{\varepsilon r+1}{2}}}, \quad (4)$$

where f is the center frequency of the band-notch.

To realize triple band-notch characteristic, third band rejection around 3.3-4 GHz (WIMAX band) can be achieved by inserting the second folded v-slot on the radiation path indicated in Ant.IV. At the notch frequencies, current is dominant around slots and is directed oppositely. Accordingly, the radiation fields generated by the oppositely directed currents cancel each other at the notch frequencies, thus notch bands will be achieved.

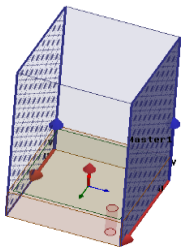

Fig. 5. A unit cell of EBG.

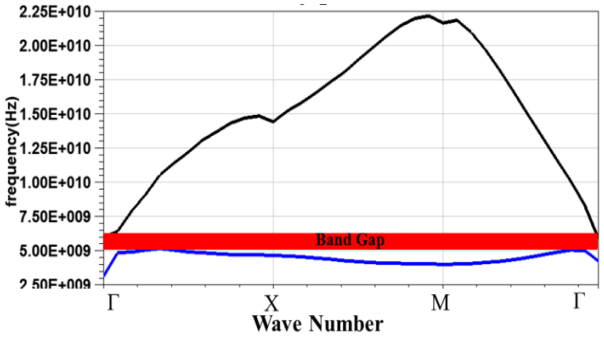

Fig. 6. Dispersion Brillouin diagram of the modified mushroom-like EBG structure.

To further explain the relation between antenna geometry and its triple band-notch characteristic, parametric study was carried out through different values of L3, Le, L5 correspond to first, second and third rejection bands respectively and the results are presented in Fig. 7 (a) to Fig. 7 (c). Figure 7 (a) shows the effect of change in L3 for 5 mm, 3.5 mm, 2.5 mm. By decreasing the value of L3, only the first band-notch shifts to high frequencies and two other band notches stand almost still. As shown in Fig. 7 (b), by decreasing the value of Le from 3.8 mm to 1.8 mm, only second band-notch shifts to up frequencies and the others do not change; and as shown in Fig. 7 (c), by decreasing the value of L5 from 3 mm to 1 mm, only third band-notch shifts up and the others do not change. As a result, we can control the notched frequencies independently by changing the values of L3, Le and L5.

Figure 8 shows the co-polarized and cross-polarized normalized radiation patterns of the proposed antenna measured and simulated at two sample frequencies of 4.5 and 9.5 GHz of E-plane (YZ-plane) and H-plane (XZ-plane). It can be seen that the dipole-like radiation patterns in XZ-plane are nearly omnidirectional for the two frequencies.

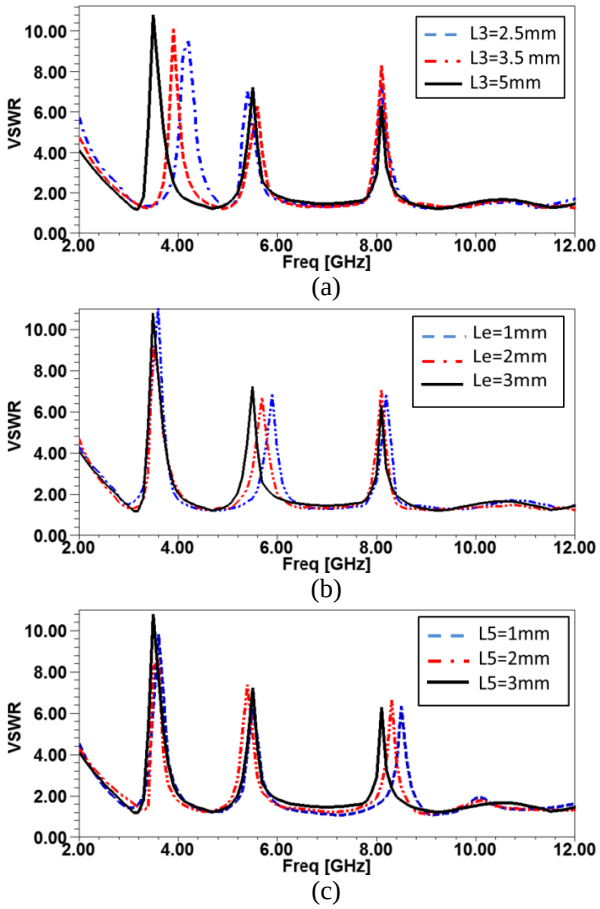

Fig. 7. Simulated VSWR of the proposed antenna with different values of: (a) L3, (b) Le, and (c) L5.

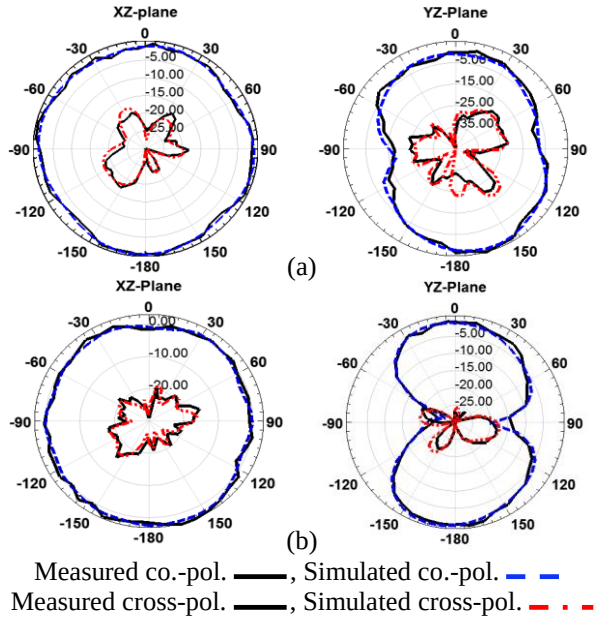

Fig. 8. Measured and simulated radiation patterns of the proposed antenna: (a) 4.5 GHz and (b) 9.5 GHz.

Figure 9 presents the effects of the inserted slots in radiation patch and EBG structures on the measured peak gain of proposed antenna in comparison with the simple monopole antenna without any slot (Ant.I). As illustrated in Fig. 9, the gain of proposed antenna decreases drastically at the notched frequencies band of 3.6, 5.5, 8.1 GHz, for other frequencies outside the notched frequencies band, the measured gain of the proposed antenna is similar to the basic antenna (Ant.I). Figure 9 shows that the inserted slots and EBG do not impose much negative effect on the antenna's radiation.

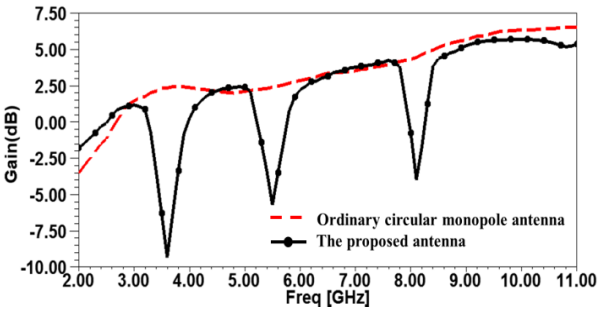

Fig. 9. Measured peak gain of proposed antenna with comparison to simulated gain of ordinary circular patch monopole antenna (Ant.I).

In Table 2, the size of proposed antenna has been compared with similar antennas proposed recently in [25-30]. As illustrated in Table 2, the proposed antenna has advantage of small size compared to others.

Table 2: Comparison of dimension of recently proposed antennas and this proposed antenna

Ref.	Width	Length	Relative Permittivity
[25]	35	35	4.4
[26]	19	24	4.4
[27]	33	28	4.4
[28]	18	20	4.4
[29]	26	36.6	4.4
[30]	24	30	4.4
Proposed antenna	12	20	4.4

B. Realization of diversity/MIMO antenna with mutual coupling reduction

The configuration of the proposed MIMO antenna is shown in Fig. 10. To achieve antenna diversity feature, two elements of proposed triple band notched monopole antenna are combined in optimized distance of about quarter wavelength ($\lambda g/4$) of 2.24 GHz [31]. For MIMO applications, we need low value of mutual coupling between two antennas, so it can be reduced significantly by employing EBG structures between antennas. As shown in Fig. 10, to reduce mutual coupling two rows of modified mushroom like EBG structures embedded

between two antennas with the same dimensions of notch EBG structure mentioned above. Simulated and measured results of mutual coupling (S12) between two antennas with and without EBG structure is presented in Fig. 11. As shown in Fig. 11, without using EBG structure mutual coupling between antennas is high, and even at some frequency ranges it exceeds -15 dB, while by using EBG the mutual coupling between antenna elements will be reduced to below -20 dB, therefore a reduction of about 5~10 dB achieved. It also can be seen that there is close correspondence between measured and simulated results.

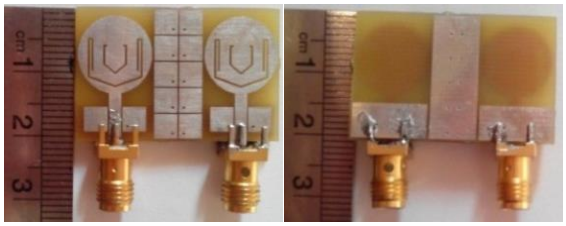

Fig. 10. MIMO antenna configuration with two rows of EBG structures.

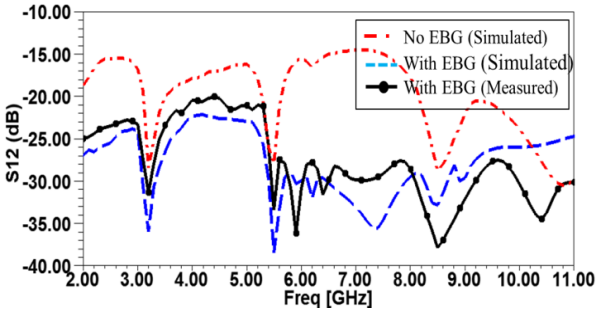

Fig. 11. Mutual coupling between antenna elements with and without EBG structure.

To verify the capability of multi antenna systems for MIMO and diversity application, envelope correlation coefficient (ECC) is an important figure of merit. The ECC, by measuring correlation factor between antenna elements shows the multipath propagation's effect of RF signals received by multi antenna systems. The ECC value can be calculated by fundamental Equation (5) based on consideration of the radiation pattern of each element [32]:

$$\rho_e = \frac{\left| \iint_{4\pi} \left[\overline{F_1}(\theta,\varphi) . \overline{F_2}(\theta,\varphi) \right] d\Omega \right|^2}{\iint_{4\pi} \left| \overline{F_1}(\theta,\varphi) \right|^2 d\Omega \iint_{4\pi} \left| \overline{F_2}(\theta,\varphi) \right|^2 d\Omega}, \quad (5)$$

where F_1 is the radiation pattern of Ant.1 where Ant.2 is terminated to 50 ohm, and F_2 will be the radiation pattern of Ant.2 where Ant.1 is terminated to 50 ohm.

Another approach to compute ECC is a simple closed form Equation (6) based on S-parameter given in [33]. The measured value of ECC is shown in Fig. 12. The maximum value of ECC is 0.003 which is as expected, due to high isolation between two antennas, which is less than the recommended value of 0.5 in [34]; then it can be deduced that the proposed antenna is more suitable for MIMO application:

$$\rho = \frac{\left| S_{11}^* S_{21} - S_{12}^* S_{22} \right|^2}{\left(1 - |S_{11}|^2 - |S_{21}|^2\right)\left(1 - |S_{22}|^2 - |S_{12}|^2\right)}. \quad (6)$$

The diversity gain can be computed in terms of correlation coefficient as given in [35]:

$$G_{app} = 10 * \sqrt{1 - |\rho|}. \quad (7)$$

The calculated value of diversity gain is presented in Fig. 13 which is very close to 10.

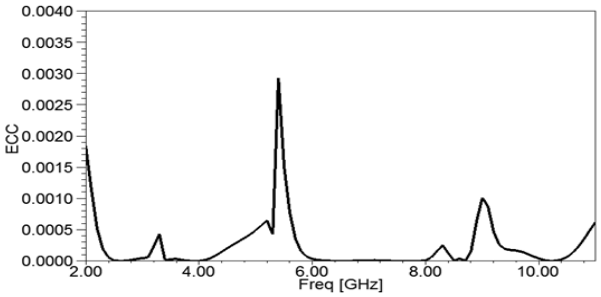

Fig. 12. Envelop correlation factor (ECC) of the proposed antenna.

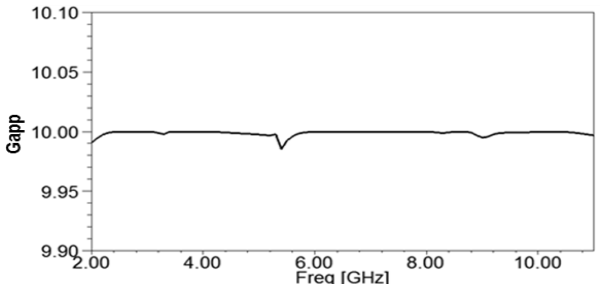

Fig. 13. Diversity gain of proposed antenna.

IV. CONCLUSION

A novel very compact printed MIMO antenna with triple band-notched characteristic has been proposed and implemented. The antenna includes two miniaturized monopole antennas, which by inserting two folded v-slot in the radiating patch and two modified mushroom-like EBG structures on either side of feed line, triple band-notched characteristic has been achieved. The proposed antenna has a good omnidirectional radiation pattern throughout the UWB frequency range and shows almost flat gain in the operating frequency band with sharp notched bands at rejected bands. To reduce mutual coupling, two rows of modified mushroom-like EBG structures implemented between two antennas. The

capability of the proposed antenna for MIMO application has been verified by studying mutual coupling (S12), envelope correlation coefficient (ECC) and diversity gain. Measured results shows that the proposed antenna has low mutual coupling (less than -20 dB) and low ECC (less than .003) which is suitable for MIMO applications. The designed antenna has a small size compared to the previous similar designs.

REFERENCES

[1] G. J. Foschini and M. J. Gans, "On limits of wireless communications in a fading environment when using multiple antennas," *Wireless Personal Communications*, vol. 6, no. 3, pp. 311-335, 1998.

[2] R. Janaswamy, "Effects of mutual coupling on the capacity of fixed length linear arrays," *IEEE Antennas and Wireless Propagation Letters*, vol. 1, pp. 157-160, 2002.

[3] S. V. Georgakopoulos, C. R. Birtcher, and C. A. Balanis, "Coupling modeling and reduction techniques of cavity-backed slot antennae: FDTD versus measurements," *IEEE Trans. Electromagn. Compat.*, vol. 43, no. 3, pp. 261-272, Aug. 2001.

[4] C. Tounou, C. Decroze, D. Carsenat, T. Mon´edi`ere, and B. J´ecko, "Diversity antennas effciencies enhancement," *Proc. IEEE Antennas Propag. Int. Symp.*, pp. 1064-1067, Honolulu, HI, June 2007.

[5] M. M. Bait-Suwailam, M. S. Boybay, and O. M. Ramahi, "Electromagnetic coupling reduction in high-profile monopole antennas using single-negative magnetic metamaterials for MIMO applications," *IEEE Trans. Antennas Propagation*, vol. 58, no. 9, pp. 2894-2902, Sep. 2010.

[6] H. R. Khaleela, H. M. Al-Rizzob, D. G. Rucker, Y. A. Rahmatallah, and S. Mohan, "Mutual coupling reduction of dual-band printed monopoles using MNG metamaterial," *IEEE International Symposium on Antennas and Propagation (APSURSI)*, pp. 2219-2222, 2011.

[7] M. Salehi, A. Motevasselian, A. Tavakoli, and T. Heidari, "Mutual coupling reduction of microstrip antennas using defected ground structure," *10th IEEE Singapore International Conference on Communication Systems*, 1-5, 2005.

[8] S. Xiao, M.-C. Tang, Y.-Y. Bai, S. Gao, and B.-Z. Wang, "Mutual coupling suppression in microstrip array using defected ground structure," *IET Microwaves, Antennas & Propagation*, vol. 5, no. 12, pp. 1488-1494, May 2011.

[9] Y. Li, W. Li, and W. Yu, "A multi-band/UWB MIMO/diversity antenna with an enhanced isolation using radial stub loaded resonator," *Applied Computational Electromagnetics Society (ACES) Journal*, vol. 28, no. 1, Jan. 2013.

[10] F. Yang and Y. Rahmat-Samii, "Microstrip antennas integrated with electromagnetic band-gap (EBG) structures: a low mutual coupling design for array applications," *IEEE Trans. Antennas Propag.*, vol. 51, pp. 2936-2946, 2003.

[11] L. Li, B. Li, H. X. Liu, and C. H. Liang, "Locally resonant cavity cell model for electromagnetic band gap structures," *IEEE Trans. Antennas Propag.*, vol. 54, pp. 90-100, 2006.

[12] Y. Q. Fu, Q. R. Zheng, Q. Gao, and G. H. Zhang, "Mutual coupling reduction between large antenna arrays using electromagnetic bandgap (EBG) structures," *Journal of Electromagnetic Waves and Applications*, vol. 20, no. 6, pp. 819-825, 2006.

[13] T. Ganatsos, K. Siakavara, and J. N. Sahalos, "Neural network based design of EBG surfaces for effective polarization diversity of wireless communications antenna systems," *PIERS Online*, vol. 3, no. 8, pp. 1165-1169, 2007.

[14] L.-J. Zhang, C.-H. Liang, L. Liang, and L. Chen, "A novel design approach for dual-band electromagnetic band-gap structure," *Progress In Electromagnetics Research M*, vol. 4, pp. 81-91, 2008.

[15] W. S. Lee, D. Z. Kim, K. J. Kim, and J. W. Yu, "Wideband planar monopole antennas with dual band-notched characteristics," *IEEE Trans. Microw. Theory Tech.*, vol. 54, no. 6, pp. 2800-2806, June 2006.

[16] S. Hu, H. Chen, C. L. Law, Z. Shen, L. Zui, W. Zhang, and W. Dou, "Backscattering cross section of ultrawideband antennas," *IEEE Antennas Wireless Propag. Lett.*, vol. 6, pp. 70-74, 2007.

[17] J. Wang, Y. Yin, X. Liu, and T. Wang, "Trapezoid UWB antenna with dual band-notched characteristics for WiMAX/WLAN bands," *Electronics Letters*, vol. 49, no. 11, pp. 685,686, May 23 2013.

[18] J.-Y. Deng, Y.-Z. Yin, Sh.-G. Zhou, and Q.-Zh. Liu, "Compact ultra-wideband antenna with tri-band notched characteristics," *Electron. Lett.*, vol. 44, pp. 2231-1233, Oct. 9, 2008.

[19] L. Peng and C. L. Ruan, "UWB band-notched monopole antenna design using electromagnetic-bandgap structure," *IEEE Trans. Microwave Theory and Technique*, vol. 59, no. 4, pp. 1074-1081, Apr. 2011.

[20] M. Yazdi and N Komjani, "Design of a band-notched UWB monopole antenna by means of an EBG structure," *IEEE Trans. Antennas Propag. Letters*, vol. 10, pp. 170-173, 2011.

[21] T. Li, H. Q. Zhai, G. H. Li, and C. H. Liang, "Design of compact UWB band-notched antenna by means of electromagnetic-bandgap structures," *Electronic Letters*, vol. 48, no. 11, May 2012.

[22] F. Xu, Z. X. Wang, X. Chen, and X. A. Wang, "Dual band-notched UWB antenna based on spiral electromagnetic-bandgap structure," *PIER B*, vol. 39, pp. 393-409, 2012.

[23] H. Schantz, *The Art and Science of Ultra Wideband*

Antennas, Artech House, 2005.

[24] G. K. Pandey, H. S. Singh, P. K. Bharti, and M. K. Meshram, "Design of WLAN band notched UWB monopole antenna with stepped geometry using modified EBG structure," *PIER B*, vol. 50, pp. 201-217, 2013.

[25] D. Sarkar, K. V. Srivastava, and K. Saurav, "A compact microstrip-fed triple band-notched UWB monopole antenna," *IEEE Antennas and Wireless Propag. Letters*, vol. 13, 2014.

[26] N. D. Trang, D. H. Lee, and H. C. Park, "Very compact printed triple band-notched UWB antenna with quarter-wavelength slots," *IEEE Antennas and Wireless Propagation Letters*, vol. 11, pp. 411-414, 2012.

[27] Z. Tang, J. Zhan, and X.-F. Wu, "Compact triple band-notched printed antenna with multi slots for UWB applications," *Microwave and Optical Technology Letters*, vol. 57, no. 9, Sep. 2015.

[28] M. Abdollahvand, G. Dadashzadeh, and D. Mostafa, "Compact dual band-notched printed monopole antenna for UWB application," *IEEE Antennas and Wireless Propagation Letters*, vol. 9, pp. 1148-1151, 2010.

[29] J. Wang, Z. Wang, Y. Yin, and X. Liu, "UWB monopole antenna with triple band-notched characteristic based on a pair of novel resonators," *Progress In Electromagnetics Research C*, vol. 49, pp. 1-10, 2014.

[30] X.-J. Liao, H.-C. Yang, N. Han, and Y. Li, "Aperture UWB antenna with triple band-notched characteristics," *Electronics Letters*, vol. 47, no. 2, Jan. 2011.

[31] G. S. Reddy, A. Chittora, S. Kharche, S. Mishra, and J. Mukherjee, "Bluetooth/UWB dual-band planar diversity antenna with WiMAX and WLAN band-notch characteristics," *PIER B*, vol. 54, pp. 303-319, 2013.

[32] R. G. Vaughan and J. B. Andersex, "Antenna diversity in mobile communications," *IEEE Trans. Veh. Techno.*, vol. 36, pp. 149-172, 1987.

[33] S. Blanch, J. Romeu, and I. Corbella, "Exact representation of antenna system diversity performance from input parameter description," *Electronics Letters*, vol. 39, no. 9, pp. 705-707, 2003.

[34] Q. Luo, J. R. Pereira, and H. M. Salgado, "Reconfigurable dualband C-shaped monopole antenna array with high isolation," *Electronics Letters*, vol. 46, no. 13, pp. 888-889, 2010.

[35] D. H. Margaret, M. R. Subasree, S. Susithra, S. S. Keerthika, and B. Manimegalai, "Mutual coupling reduction in MIMO antenna system using EBG structures," *Signal Processing and Communications (SPCOM), International Conference*, pp. 1-5, July 2012.

Asghar Mousazadeh was born in Naghadeh, Iran in 1985. He received his B.Sc. degree in Electrical Engineering (Telecommunication) from Urmia University, Urmia, Iran, in 2010 and M.Sc. degree in Electrical Engineering (Telecommunication) from Islamic Azad University, Science and Research Branch, Tehran, Iran, in 2012. He is currently pursuing the Ph.D. degree at the Electrical Engineering Department, University of Shahed, Iran. His primary research interests are in antenna design, and microwave components.

Gholamreza Dadashzadeh was born in Urmia, Iran, in 1964. He received the B.Sc. degree in Communication Engineering from Shiraz University, Shiraz, Iran in 1992 and M.Sc. and Ph.D. degree in Communication Engineering from Tarbiat Modarres University (TMU), Tehran, Iran, in 1996 and 2002, respectively. From 1998 to 2003, he has worked as Head Researcher of Smart Antenna for Mobile Communication Systems (SAMCS) and WLAN 802.11 project in Radio Communications Group of Iran Telecomm Research Center (ITRC). From 2004 to 2008, he was Dean of Communications Technology Institute (CTI) in ITRC. He is currently an Associated Professor in the Department of Electrical Engineering at Shahed University, Tehran, Iran. Dadashzadeh is a Member of IEEE, Institute of Electronics, Information and Communication Engineers (IEICE) of Japan and Iranian Association of Electrical and Electronics Engineers (IAEEE) of Iran. He honored received the First Degree of National Researcher in 2007 from Iran's Ministry of ICT. He has published more than 80 papers in referred journals and international conferences in the area of antenna design and smart antennas.

Synthesis Design of Bandpass Filter for UWB Applications with Improved Selectivity

Azzeddin Naghar [1,2], Otman Aghzout [2], Ana V. Alejos [1], and Francisco Falcone [3]

[1] Department of Teoría de la Señal y Comunicación
University of Vigo, Vigo, 36310, Spain
azz.naghar@gmail.com, analejos@uvigo.es

[2] Department of TTIM
Abdelmalek Essaadi University, Tetouan, Morocco
o.aghzout@gmail.com

[3] Department of Ingeniería Electrical y Electrónica
University of Navarra, Pamplona, Spain
francisco.falcone@unavarra.es

Abstract **—** This paper presents the design of UWB three-pole modified parallel coupled line bandpass filter with improved rejection in the out-of-band frequencies. To achieve the desired UWB requirements using the conventional bandpass filter design, a physical dimension optimization of space-gap between lines, line widths and lengths was applied. An equivalent circuit model is also presented and demonstrates reasonable agreement with simulation results. The optimized filter demonstrates an excellent UWB performance, covering the Federal Communication Commission spectrum bandwidth with low insertion loss and acceptable selectivity. However, this resulting filter structure presents very small gapping between adjacent resonators; that means the filter is unmanufactured. Then an example of an alternative filter structure is finally proposed with null gaping and short-circuited stubs that yields to a fabricated prototype with selectivity improvement. Generally speaking, reasonable agreement is achieved between measurement and simulation results.

Index Terms **—** Bandpass filter, coupling gap, parallel coupled line, rejection band, stub, UWB.

I. INTRODUCTION

The ultra-wideband (UWB) radio technology has been getting increasingly popular due to the high-speed high-data wireless connectivity demand. There is a need to design ultra-wideband bandpass filters covering the whole band permitted by the U.S. Federal Communication Commission (FCC), that extends from 3.1 to 10.6 GHz [1]. The design requirements of these circuits face new challenges among which are included an overall good performance, compact size, wide bandwidth feature and multi-band operation. Various approaches to implement UWB filters can be found through literature [2-4]. Among other microstrip line centered configurations, bandpass filters based on parallel-coupled lines have been widely used in microwave systems, due to their good performance, simple structure, low cost and ease of integration with other devices [5-6].

This paper presents the design of a three-pole parallel coupled lines microstrip bandpass filter (BPF) for UWB applications. The filter design was accomplished in three steps. Firstly, a filter is designed and optimized to cover the FCC band.

The physical parameter dimensions for this initial design are calculated by an ad-hoc tool [6] and then optimized in a second design step to achieve a better UWB performance. However, this resulting filter cannot be fabricated due to the small spacing between adjacent coupled lines.

To solve this limitation, a modified filter structure is proposed in a third design step, by null gapping the space between all the filter parallel resonators, and incorporating short circuited stubs. This final design is manufactured and offers selectivity enhancement, covering the FCC spectrum with lower insertion loss and group velocity flatness, along with elimination of the transmission at low frequency. It also presents a size reduction, and it can be implemented on low cost dielectric substrate of FR4.

II. UWB BANDPASS FILTER: DESIGN AND RESULTS

A. Edge-coupled bandpass filter for UWB applications

According to [7,8,9], the edge-coupled bandpass three-order filter is designed to cover the FCC full band, with center frequency of 6.85 GHz, and passband ripple of 0.5. The filter has been implemented on FR4 substrate with dielectric constant of 4.4 and thickness of 1.6 mm.

As a first step, we define the initial physical dimension

Submitted On: January 1, 2015
Accepted On: December 6, 2015

values of a bandpass filter – space gap (S), width (W) and length (L) of each stage – obtained using the transmission line theory approach as in [6] for a parallel coupled line microstrip (PCLM) design. These dimensions are, in mm: $S_{1,4} = 0.1$, $W_{1,4} = 0.54$, $L_{1,4} = 6.34$, $S_{2,3}$=0.14 mm, $W_{2,3}$=0.46 and $L_{2,3}$=6.36 (see Fig.1).

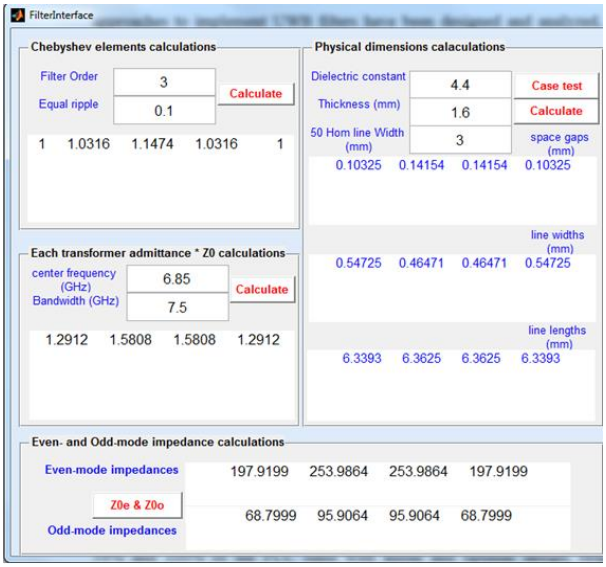

Fig. 1. Parameter calculation tool of the parallel coupled line bandpass filter at 6.85 GHz.

Figure 2 (a) shows the simulated frequency response of the proposed bandpass filter for both initial and optimized designs, using the CST MWs simulator. It can be observed that the initial filter design only covers 85% of the FCC band with low insertion loss and good rejection; however, the optimized filter case presents a UWB response working from 3.1 to 10.6 GHz with low insertion loss and relative good rejection. This improved response is due to the small coupling gap between adjacent filter resonators.

In the next step, we updated the physical dimension values of both filter designs, in mm: $S_{1-4} = 0.05$, $W_{1-4} = 0.75$, $L_{1-4} = 5.6$, $S_{2-3} = 0.075$, $W_{2-3} = 0.55$, $L_{2-3} = 5.95$. The even- and odd-mode characteristic impedances are: $Z_{0e} = 1147.33\ \Omega$, $Z_{0o} = 37.41\ \Omega$ for sections (1,4) and $Z_{0e} = 165.56\ \Omega$, $Z_{0o} = 43.57\ \Omega$ for sections (2,3).

To determine the equivalent circuit model of this filter type, the L-C components for the serial and the parallel combination respectively are calculated using the Chebyshev approximation as per (1)-(2):

$$L_s = \frac{FBW.\omega_0}{Z_0.g},\ C_s = \frac{FBW}{Z_0.g.\omega_0}, \quad (1)$$

$$L_p = \frac{FBW.Z_0}{\omega_0.g},\ C_p = \frac{g}{FBW.Z_0.\omega_0}, \quad (2)$$

where g is the Chebyshev element and FBW is the fractional bandwidth, $FBW = (\omega_1 \cdot \omega_2)/\omega_0$, with $\omega_0 = (\omega_1 \cdot \omega_2)^{0.5}$.

Figure 2 (b) shows the equivalent circuit model response for the optimized UWB PCLM bandpass filer. A good agreement between simulation and equivalent circuit results is clearly observed.

The calculated values of the L-C components for the circuit illustrated in Fig. 2 (b) are: $C_1 = C_3 = 0.625$ pF, $C_2 = 0.545$ pF, $L_1 = L_3 = 1.225$ nH, $L_2 = 1.4$ nH.

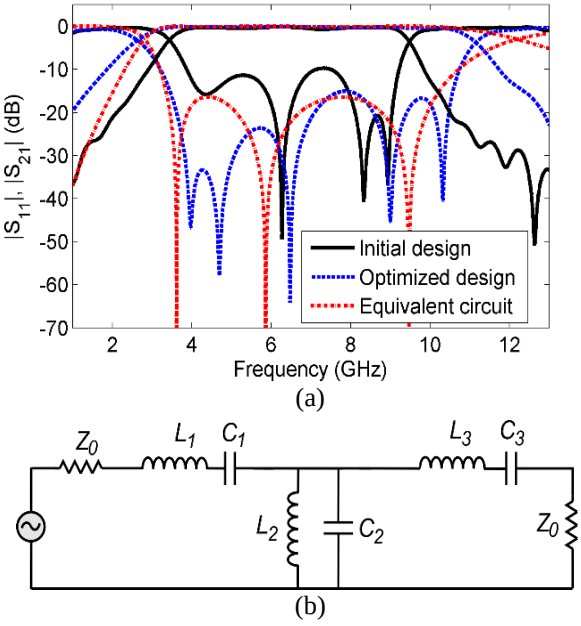

Fig. 2. UWB three-pole PCLM bandpass filter: (a) electrical response for presented cases, and (b) equivalent circuit model.

The optimized filter was unmanufactured, due to the resulting very small coupling gap between filter resonators. This geometrical parameter determines the impedance bandwidth of this filter type [6,8]. In the following section, a modified PCLM bandpass filter with null gapping and integrated short-circuited stubs is described.

B. Modified UWB bandpass filter with selectivity enhancement

The proposed filter structure consists of setting null gapping between all adjacent PCLM filter resonators and shifting the feed line position to achieve compact filter prototype.

Also, two symmetrical short-circuited stubs are incorporated for improvement of rejection in the out-of-band frequencies and elimination of the transmission at lower frequency band. In Fig. 3, we plotted the geometry of the proposed filter layout without stubs and

photograph of the fabricated prototype. The physical dimension values of this filter are, in mm: $W_1 = W_4 = 1.42$, $L_1 = L_4 = 5.8$, $W_2 = W_3 = 0.7$ and $L_2 = L_3 = 6$.

This prototype was measured using a N5222A Agilent Network Analyser. The simulated and measured return loss and insertion of this filter design is plotted in Fig. 4. We note that the fabricated UWB bandpass filter demonstrates a low insertion loss within the FFC band. However, a poor out-of-band rejection performances is seen, due to the small gaps applied between PCLM resonators. Then an enhancement of filter selectivity is necessary.

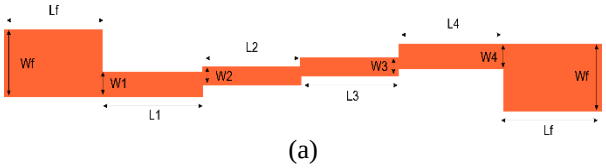

(a)

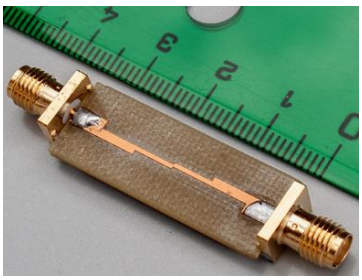

(b)

Fig. 3. Modified UWB bandpass filter without stubs: (a) filter layout, and (b) photograph of fabricated prototype.

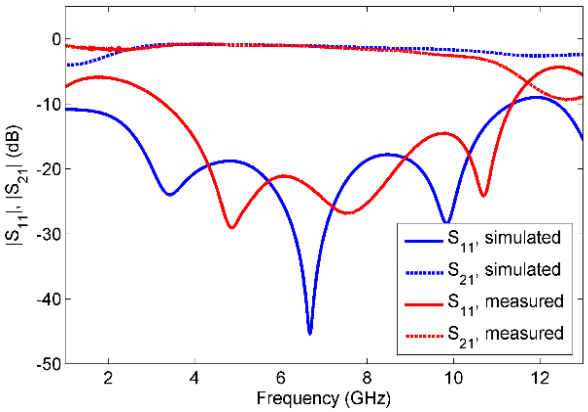

Fig. 4. Electrical response of the modified UWB bandpass filter without stubs.

To solve the limitation of poor selectivity, we added two symmetrical short-circuited as shown in Fig. 5 (a), in order to create the desired rejection and eliminate the transmission at low frequency.

The photograph of the fabricated final filter prototype is shown in Fig. 5 (b). For this design, the length and width of the stubs determine the center frequency and bandwidth of the rejected band. Whereas, the rejection level is controlled by the stub positioning parameter, D.

Figure 6 (a) shows the insertion loss of the final modified filter design, with respect to the previous proposed filter cases. The comparison indicates that the modified bandpass filter presents a wider impedance bandwidth, lower insertion loss and improved selectivity. The integrated symmetrical stubs offer a rejection peak at 12.5 GHz (-40 dB). A good agreement is achieved between measurements and simulation.

By comparing to the conventional optimized filter previously presented, the modified filter offers an enhancement in the UWB impedance bandwidth (5%) with improved selectivity. However, it presents a small increase of the insertion loss (about 1.5 dB), due to the integration of the stubs.

Finally, we plotted in Fig. 7, the simulated group delay for the initial, the optimized and the modified filter designs. Within the UWB passband, both of conventional and modified bandpass filters demonstrate flat values (<0.2 ns) of group delay, that meet the requirements established by the FCC regulations for the UWB devices.

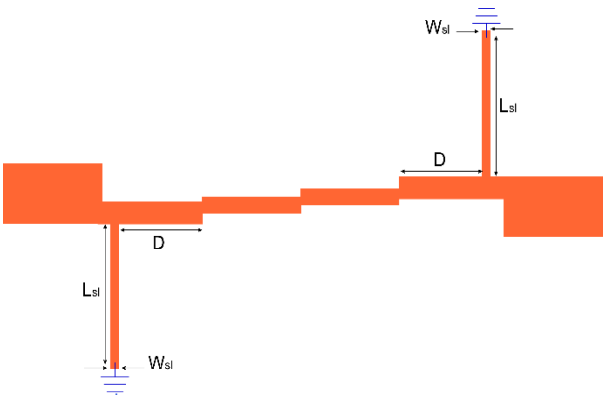

(a)

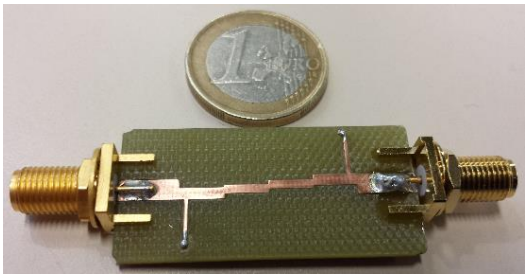

(b)

Fig. 5. Modified UWB bandpass filter with stubs: (a) filter layout, and (b) photograph of fabricated prototype.

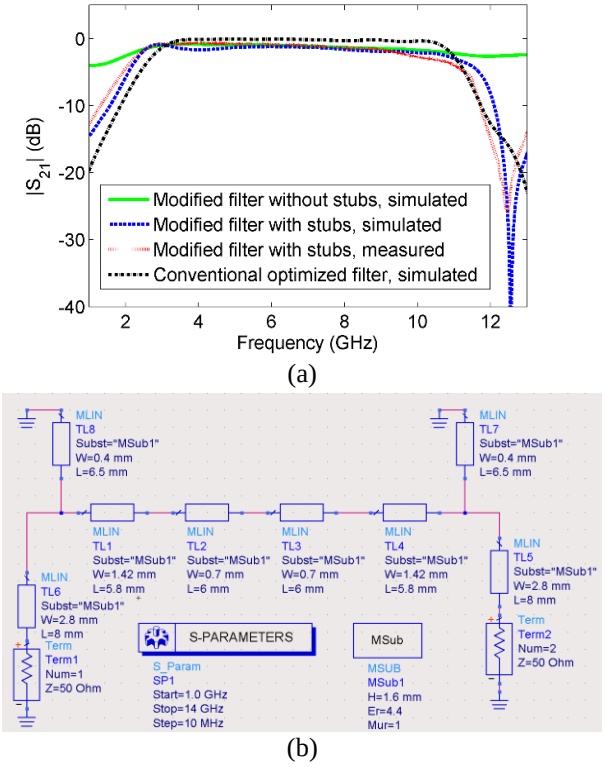

Fig. 6. (a) Insertion loss of the UWB bandpass filter for all proposed cases. (b) Schematic of distributed elements corresponding to the filter design with stubs.

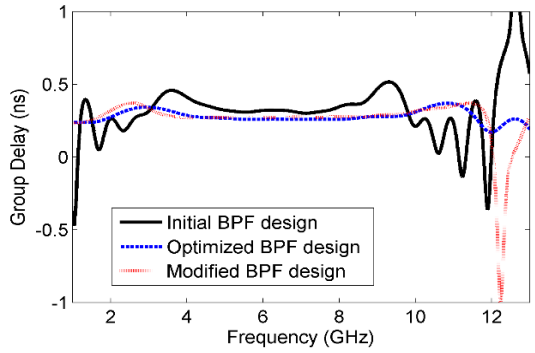

Fig. 7. Parameter calculation tool of the parallel coupled line bandpass filter at 6.85 GHz.

C. Results discussion

Based on the conformal mapping method reported in [10], the even- and odd-mode characteristic impedances of the coupled line depend on the width W and coupling gap S of one stage parallel coupled line. When the dielectric constant ε_r and thickness h of the substrate are known, the impedances Z_{0e} and Z_{0o} can be calculated as a function of the strip line width and coupling gap for each stage of parallel coupled lines of the filter. Then by decreasing the coupling gap S values, the Z_{0e} values increase, Z_{0o} decrease and consequently the bandwidth of the parallel coupled line bandpass filter increases. Detailed analysis and corresponding graphs of the even- and odd-mode impedances are depicted in [12].

Using the closed formulas developed by Hammerstad, Kirschning and Jansen for modelling the frequency-dependency of the even- and odd-mode characteristics of a parallel coupled microstrip line [10,11]. The variation of the static characteristic impedances for even- and odd-modes is calculated easily, as well as the fractional bandwidth (*FBW*) variation of the PCLM filter type. Calculated *FBW*s in (%), for different values of the coupling gaps $S_{1\text{-}4}$ and $S_{2\text{-}3}$ are presented in Table 1. This *FBW* is obtained by determining the ABCD matrix and S-parameters as indicated in [13], based on the design specification presented previously. The three-pole parallel coupled line microstrip bandpass filter implements the FR4 substrate with center frequency of 6.85 GHz and passband ripple of 0.5.

However, this filter configuration with very small coupling gap kept unmanufactured. Then we modified our design by setting null spacing between filter resonators. This resulting structure offers a relative poor selectivity which can be improved using several techniques, such as the short-circuited stubs here described. This latter allows eliminating the lower band frequency transmission.

The resonance frequency of the stub is given by (3):

$$f_{stub} = \frac{c}{2.L.(\varepsilon_{re})^{0.5}}, \tag{3}$$

where L is the total length of the slot, ε_{re} is the effective dielectric constant and c is the speed of light. The dimensions of the short-circuited stubs here used are: L_{sl} = 6.5 mm, W_{sl} = 0.4 mm and D = 4.6 mm.

Table 1: Variation of the calculated *FBW* in percentage with the small coupling gap values

Gapping ($S_{1\text{-}4}$, $S_{2\text{-}3}$)	Z_{0e} *(1-4, 2-3)*	Z_{0o} *(1-4, 2-3)*	*FBW %*
0.084, 0.709	75.45, 58.52	29.96, 37.74	17.52%
0.03, 0.292	85.61, 66.86	27.47, 33.44	28.32%
0.014, 0.04	100.82, 82.61	26.29, 28.04	43.8%
0.013, 0.015	113.27, 134.1	27.06, 26.29	58.39 %

III. CONCLUSION

In this paper a modified parallel coupled line microstrip bandpass filter for UWB application is presented. Based on a classical design of the parallel coupled line microstrip filters, an UWB bandpass filter is firstly introduced and discussed. Later an optimized design is obtained demonstrating an improved performance with respect to the FCC requirements for UWB devices. A low insertion loss with relative good rejection was obtained within the FCC passband. The equivalent circuit model was also calculated and good agreement is seen with simulation. However, the filter presents very

small gap values so demanding a high accuracy in the manufacturing process not achievable for our capabilities.

A limit case is proposed with null gapping to yield a fabricated prototype. The short-circuited stubs are integrated to improve the filter selectivity and eliminate the transmission at low frequency. Measurements results demonstrate the validity of the design method proposed in this paper, achieving an improved performance in terms of UWB bandwidth, low insertion loss and good rejection band without increasing the complexity of the filter structure.

The proposed technique is a good candidate for UWB bandpass filter design, and it can be generally applied to obtain UWB bandpass filters for any specifications.

This work can be extended to achieve a wider rejection in the out-of-band frequencies regardless the used selectivity enhancement technique. As an example, an array of stubs with multiple close resonances.

As set-off, the filter width dimension has grown, and as possible solution to this disadvantage we propose the design of the stub in meander shape. A solution as replacing stubs by stub-slots in the input feedline would affect the S_{21} parameter introducing a larger insertion loss. Despite the disadvantage of the increasing width dimension, the short-circuited stub is a solution valid to jointly achieve an improved selectivity and the elimination of the low-frequency transmission.

ACKNOWLEDGMENT

Research supported by the Xunta de Galicia (Grant EMR2012/238) and Erasmus Mundus Green IT (Grant 2012-2625/001-001-EMA2).

REFERENCES

[1] Federal Communications Commission, "First report and order in the matter of revision of Part 15 of the commission's rules regarding ultrawideband transmission systems," *Tech Report*, ET-Docket 98-153, FCC02-48, Apr. 2002.

[2] X. Li and X. Ji, "Novel compact UWB bandpass filters design with cross-coupling between λ/4 short-circuited stubs," *IEEE Microw. Wireless Compon. Lett.*, vol. 24, no. 1, pp. 23-25, Jan. 2014.

[3] H. Shaman and J. S. Hong, "A novel ultra-wideband (UWB) bandpass filter (BPF) with pairs of transmission zeroes," *IEEE Microw. Wireless Compon. Lett.*, vol. 17, no. 2, pp. 121-123, Feb. 2007.

[4] Z.-X. Zhang and F. Xiao, "An UWB bandpass filter based on a novel type of multi-mode resonator," *IEEE Microw. Wireless Compon. Lett.*, vol. 22, no. 10, pp. 506-508, Oct. 2012.

[5] P. Cai, Z. Ma, X. Guan, Y. Kobayashi, T. Anada, and G. Hagiwara, "Synthesis and realization of novel ultra-wideband bandpass filters using 3/4 wavelength parallel-coupled line resonators," *Asia-Pacific Microwave Conference*, Yokohama, Japan, pp. 159-162, Dec. 2006.

[6] A. Naghar, O. Aghzout, A. Vazquez Alejos, M. Garcıa Sanchez, and M. Essaaidi, "Design of compact wideband multi-band and ultrawideband band pass filters based on coupled half wave resonators with reduced coupling gap," *IET Microwave, Antennas and Propagation*, pp. 1-7, 2015.

[7] A. Naghar, O. Aghzout, A. Vazquez Alejos, M. Garcıa Sanchez, and M. Essaaidi, "Development of a calculator for edge and parallel coupled microstrip band pass filters," *IEEE International Symposium on Antennas and Propagation*, Memphis, USA, pp. 2018-2019, Jul. 2014.

[8] A. Naghar, O. Aghzout, A. Vazquez Alejos, M. Garcıa Sanchez, and M. Essaaidi, "Design of compact multi-band bandpass filter with suppression of second harmonic spurious by coupling gap reduction," *Journal of Electromagnetic Waves and Applications*, vol. 29, no. 14, pp. 1813-1828, Aug. 2015.

[9] S. Akhtarzad, T. R. Rowbotham, and P. B. Johns, "The design of coupled microstrip lines," *IEEE Transactions on Microwave Theory and Techniques*, vol. MTT-23, no. 6, pp. 486-492, Jun. 1975.

[10] E. Hammerstad and O. Jensen, "Accurate models for microstrip computer-aided design," *Symposium on Microwave Theory and Techniques*, pp. 407-409, Jun. 1980.

[11] M. Kirschning and R. H. Jansen, "Accurate wide-range design equations for the frequency dependent characteristic of parallel coupled microstrip lines," *IEEE Trans. Microwave Theory Tech*., vol. MTT-32, no. 1, pp. 83-90, Jan. 1984.

[12] C. S. Ye, Y. K. Su, M. H. Weng, C. Y. Hung, and R. Y. Yang, "Design of the compact parallel-coupled lines wideband bandpass filters using image parameter method," *Progress In Electromagnetics Research*, vol. 100, pp. 153-173, 2010.

[13] K.-S. Chin, Y.-C. Chiou, and J.-T. Kuo, "New synthesis of parallel-coupled line bandpass filters with Chebyshev responses," *IEEE Trans. Microwave Theory Tech.*, vol. 56, no. 7, pp. 1516-1523, Jul. 2008.

Azzedin Naghar was born in Tetouan, Morroco. He received the Engineer degree in Telecommunication Engineering at the National School of Applied Sciences from Abdelmalek Essaadi University, Tetouan, Morocco in 2011. He is currently working toward the Ph.D. degree in Electrical

Engineering with the Department of Teoría de la Señal y comunicación, University of Vigo, Pontevedra, Vigo, Spain. His research interests include UWB antenna design and RF filters.

Otman Aghzout was born in Tétouan, Morocco. He received the Electronics degree from Abdelmalek Essaadi University, Tétouan, Morocco, in 1995, the M. and the Ph.D. degrees in Telecommunications Engineering at the High School of Telecommunications Engineering (ETSITGC) of Canary University, Spain in 2000 and January 2002, respectively. He has also been a Researcher Student at the Microwave Group of the Dept. of Electronics and Electromagnetism, University of Seville (Seville, Spain) from 1996 till 1999. In January 2002, he joined the Medical Technology Center (CTM) of the University Hospital of GC, where he worked in Medical Engineering applications for two years. From 2002-2004 he has been a Teacher Assistant on Telecommunications Engineering and Postdoctoral Researcher at the Department of the Signal Processing Engineering, High School of TE (ETSITGC). Since 2009 he joined the Dept. of Engineering Technologies: Telecommunications and Mecatronics (TITM) as an Associate Professor of Telecommunications Engineering, National School of Applied Sciences, UAE, Tétouan, Morocco. Currently he is interested on printed microwave passive and active circuits, filters and antenna designs.

Ana Vazquez Alejos has been working with the Department of Signal Theory and Communications, University of Vigo, as Research and Teaching Staff. She completed her Ph.D. thesis on the radio channel characterization for the millimeter wave frequencies. In 2009 she was granted with the Marie Curie International Outgoing Fellowship, carrying out the outgoing phase in the New Mexico State University (NM, USA), with a research focused on propagation through dispersive media, and radar waveform generation. In 2002, her M.S. thesis received the Ericcson Award by the Spanish Association of Electrical Engineers, as the best Multimedia Wireless Project. Her research work includes radio propagation, communication electronics, wideband radio channel modeling, multimedia wireless systems, waveform and noise code design, and radar.

Alejos is a Reviewer for several IEEE and IET Journals, and works for the IEEE TMC Spain Chapter.

Francisco Falcone received the Telecommunication Engineering degree and Ph.D. degrees from the Universidad Publica de Navarra (UPNA), Pamplona, Spain, in 1999 and 2005, respectively.

From 1999 to 2000, he was a Microwave Commissioning Engineer with Siemens–Italtel. From 2000 to 2008, he was a Radio Network Engineer with Telefonica Moviles. In 2009, he cofounded the spinoff Tafco Metawireless. From 2003 to 2009, he was an Assistant Lecturer with UPNA, and since June 2009, has been an Associate Professor with the same university. From 2005 to 2008, he was Internal Instructor with Telefonica Moviles.

His research areas cover complex and artificial electromagnetic media, EBG, metamaterials, enhanced transmission and plasmonic guiding, as well mobile system design and analysis.

Falcone works for the IEEE MTT-11 committee, IEEE ES Spain Chapter, and IEEE TMC Spain Chapter. He was recipient of the CST Best Paper award in 2003 and 2005, a Ph.D. award in 2006 from the Colegio Oficial de Ingenieros de Telecomunicacion, and a Ph.D. award at UPNA, in 2010.

A Compact UWB Slot Antenna with Reconfigurable Band-Notched Function for Multimode Applications

Ali Musavand [1], Yashar Zehforoosh [1], Hamed Ojaroudi [2], and Nasser Ojaroudi [3]

[1] Department of Electrical Engineering
Urmia Branch, Islamic Azad University, Urmia, Iran
a.musavand@iaurmia.ac.ir

[2] Young Researchers and Elite Club
Germi Branch, Islamic Azad University, Germi, Iran

[3] Young Researchers and Elite Club
Ardabil Branch, Islamic Azad University, Ardabil, Iran

***Abstract*—** A novel design of printed slot antenna with multi-resonance and switchable band-notched performances is presented whose frequency characteristics can be reconfigured electronically to have both a single- or dual-band notch function. The presented antenna is reconfigurable to suppress unwanted interfering signals by using PIN diodes integrated within the antenna configuration. The presented antenna consists of square radiating stub with a pair of rotated Ω-shaped slits, feed-line with an inverted U-shaped slot, and a slotted ground plane. By cutting an inverted U-shaped slot at the feed-line we can gave a new resonance at the higher frequencies that with this structure, an UWB frequency range can be achieved. In the presented antenna, we use two PIN diodes across the Ω-shaped structures that by changing the ON/OFF conditions of the PIN diodes, the antenna can be used for multimode applications. In the proposed structure, when D_1&D_2=OFF, the UWB antenna with a single band-notched characteristic can be achieved. By changing the condition of integrated diodes to D_1&D_2=ON, the pair of rotated Ω-shaped slits at radiating stub have been converted to four L-shaped slits that with this design the antenna can be used to generate a dual band-notched function to isolate and block any interference in the UWB frequency range.

***Index Terms* —** Band-notched function, multimode wireless communications, reconfigurable slot antenna, UWB systems.

I. INTRODUCTION

In UWB communication systems, one of key issues is the design of a compact antenna while providing wideband characteristic over the whole operating band. Consequently, a number of microstrip antennas with different geometries have been experimentally characterized. Moreover, other strategies to improve the impedance bandwidth which do not involve a modification of the geometry of the planar antenna have been investigated [1-3].

The frequency range for UWB systems between 3.1-10.6 GHz will cause interference to the existing wireless communication systems; for example 7.25-7.75 GHz for downlink of X-band satellite communication, so the UWB antenna with a band-notched function is required. Lately, to generate the frequency band-notched function, several modified planar antennas with band-notched characteristic have been reported [4-5].

In this paper, a compact reconfigurable antenna with single and/or dual band-stop and multi resonance performances is presented. In the proposed structure, multimode operation is provided by changing the ON/OFF conditions of the PIN diodes that the antenna can be used to generate either a single or dual notch band to isolate and block any interference in UWB frequency range. [6-8]. Good VSWR and radiation pattern characteristics are obtained in the frequency band of interest. Simulated and measured results are presented to validate the usefulness of the proposed antenna structure for UWB applications.

II. ANTENNA DESIGN

The presented small slot antenna fed by a microstrip line is shown in Fig. 1, which is printed on FR4 substrate of thickness 0.8 mm, permittivity 4.4, and loss tangent 0.018. The basic slot antenna structure consists of a square radiating stub, a feed line, and a slotted ground plane. The square radiating stub has a width of W. The radiating stub is connected to a feed line with width of W_f and length L_f. The width of the microstrip feed line is fixed at 1.5 mm, as shown in Fig. 1. On the other side of the substrate, a conducting ground plane is placed.

Submitted On: October 22, 2013
Accepted On: October 22, 2015

The proposed antenna is connected to a 50-SMA connector for signal transmission.

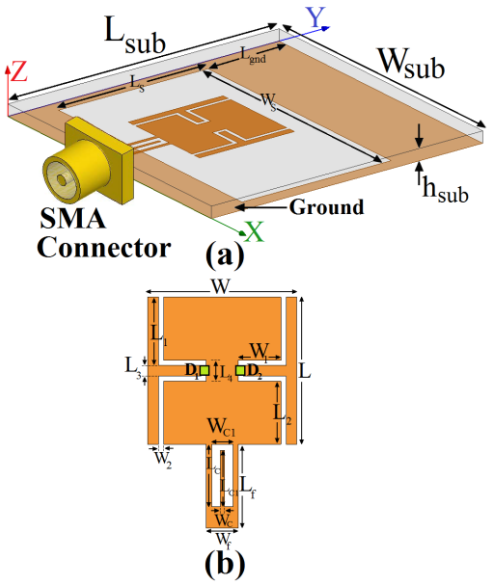

Fig. 1. (a) Side view of the proposed slot antenna, and (b) top view of modified square radiating stub.

The optimized values of proposed antenna design parameters are as follows: W_{sub} = 20 mm, L_{sub} = 20 mm, h_{sub} = 0.8 mm, W_f = 1.5 mm, L_f = 4 mm, W = 7 mm, L = 7 mm, W_s = 18 mm, L_s = 11 mm, W_1 = 2 mm, L_1 = 3.25 mm, W_2 = 0.25 mm, L_2 = 3 mm, L_3 = 0.5 mm, W_C = 0.2 mm, L_C = 3.3 mm, W_{C1} = 1 mm, L_{C1} = 2.8 mm, W_D = 0.5 mm, L_D = 0.5 mm, and L_{gnd} = 3.5 mm.

III. RESULTS AND DISCUSSIONS

Configuration of the presented reconfigurable slot antenna was shown in Fig. 1. The proposed microstrip antenna with various design parameters was constructed and the numerical and experimental results of the input impedance and radiation characteristics are presented and discussed. The proposed microstrip-fed antenna was fabricated and tested. The parameters of this proposed antenna are studied by changing one parameter at a time and fixing the others. Ansoft HFSS simulations are used to optimize the design and agreement between the simulation and measurement is obtained [9].

A. UWB antenna with single band-notched function (D_1&D_2=OFF)

Geometry for the ordinary slot antenna (Fig. 2 (a)), with an inverted U-shaped slot at feed-line (Fig. 2 (b)), and with a pair of rotated Ω-shaped slits (Fig. 2 (c)) are compared in Fig. 2.

Simulated VSWR characteristics for the structures that were shown in Fig. 2 are compared in Fig. 3. As shown in Fig. 3, it is observed that the upper frequency bandwidth is affected by using the inverted U-shaped slot and we can gave additional resonance at higher bands that provides an UWB frequency range. To generate a band-notched function, we use a pair of Ω-shaped slits in the square radiating stub.

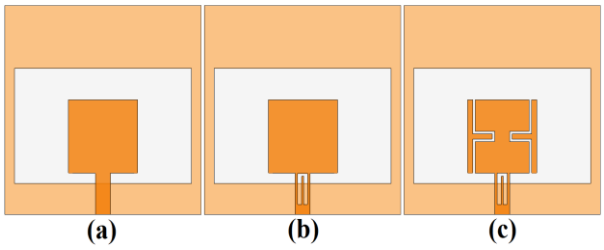

Fig. 2. (a) Basic structure (ordinary slot antenna), (b) the ordinary antenna with an inverted U-shaped slot at feed-line, and (c) the proposed slot antenna structure (D_1&D_2=OFF).

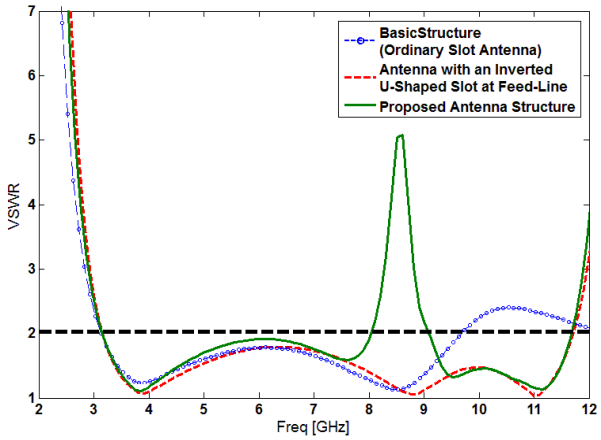

Fig. 3. Simulated VSWR characteristics for the various antenna structures shown in Fig. 2.

In order to know the phenomenon behind this multi-resonance and band-stop performance, the simulated current distributions for the proposed antenna at 11 GHz and 8.5 GHz are shown in Fig. 4. It can be observed in Fig. 4 (a) that, the current concentrated on the edges of the interior and exterior of the inverted U-shaped slot. Therefore, the antenna impedance changes at this frequency (11 GHz) due to the resonant properties of this structure [2].

Other important design parameter of this structure is the pair of rotated Ω-shaped slits used in the square radiating stub. Figure 4 (b) presents the simulated current distributions at the notched frequency (8.5 GHz). As shown in Fig. 4 (b), in the notched frequency the current flows are more dominant around of the rotated Ω-shaped slits. As a result, the desired high attenuation near the notched frequency can be produced [5-6]. It

can be observed that the directions of surface currents on the radiation stub of the antenna are reversed in compared with each other, which cause the antenna impedance changes at these frequencies to generate resonance and notch band characteristics.

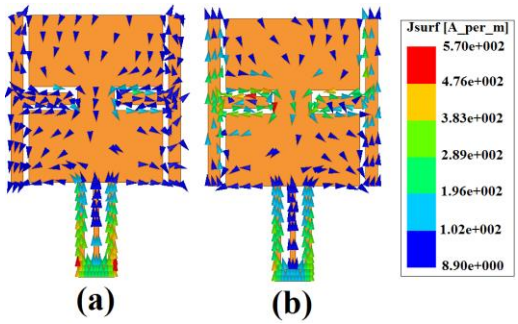

Fig. 4. Simulated surface current distributions on the radiating stub: (a) at 11 GHz, and (b) at 8.5 GHz.

B. UWB antenna with reconfigurable band-notched function (D_1&D_2=ON)

In the proposed antenna configuration, by changing the conditions of PIN diodes the desired double band notching characteristics can be achieved. Geometry for the presented antenna with single band-notched function (D_1&D_2=OFF) (Fig. 5 (a)), and with dual band-notched function (D_1D_2=ON) (Fig. 5 (b)) are compared in Fig. 5.

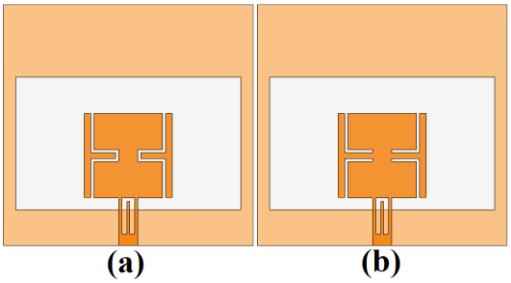

Fig. 5. Various structures for the proposed reconfigurable slot antenna: (a) D_1&D_2=OFF, and (b) D_1&D_2=ON.

To know the phenomenon behind this single or dual band-notched performance, the simulated current distributions for the proposed antenna on the radiating stub at 7.5 and 9.5 GHz (notched frequencies) are presented in Fig. 6. As shown in Figs. 6 (a) and 6 (b), the current flows are more dominant around of four L-shaped slits. Therefore, the antenna impedance changes at this frequency due to the resonant properties of the L-shaped structure. By changing the condition of integrated diodes to D_1&D_2=ON, the pair of rotated Ω-shaped slits at radiating stub have been converted to four L-shaped slits, that with this design the antenna can be used to generate a dual band-notched function to isolate and block any interference in the UWB frequency range. The first and second notches are affected from corners inserted L-shaped slits. Figure 6 (b) clearly shows at the second notched frequency, the inserted L-shaped slits act as half-wave resonant structures [8].

As seen in these figures, the current direction on the radiation stub is opposite to each other, so the far fields produced by the currents on the reject structures cancel out each other in the reject band.

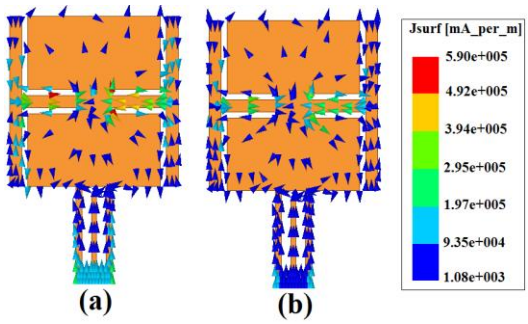

Fig. 6. Simulated surface current distributions for the proposed slot antenna at the notched frequencies: (a) at 7.5 GHz, and (b) at 9.5 GHz.

After checking all dimensions and final adjustments, the proposed antenna with final design was fabricated. Measured and simulated VSWR characteristics for the structures that were shown in Fig. 5 are compared in Fig. 7. As shown in Fig. 7, it is observed that the single frequency band-notched function around of 8-9 GHz is affected by using a pair of Ω-shaped slits on the radiating stub and by changing the condition of integrated diodes to D_1&D_2=ON, the pair of rotated Ω-shaped slits at radiating stub have converted to four L-shaped slits and a dual band-notched performance in 7-8 GHz and 9-10 GHz can be generated. The presented antenna has the frequency band of 3.02 to over 12.43 GHz with a variable single or/and dual band-stop performance.

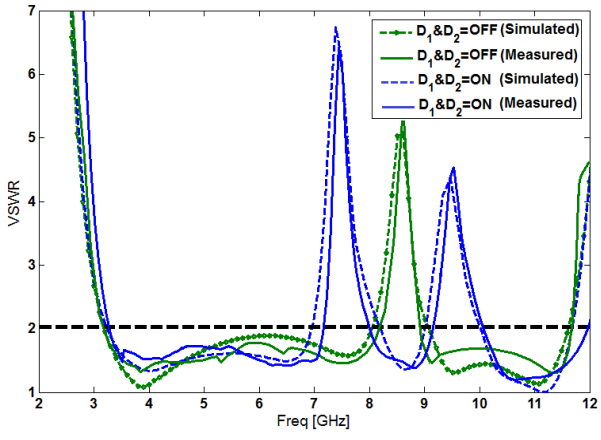

Fig. 7. Measured and simulated VSWR characteristics for the various structures shown in Fig. 5.

In a physical network analyzer measurement, the feeding mechanism of the proposed antenna is composed of a SMA connector and a microstrip line (the microstrip feed-line is excited by a SMA connector), whereas the simulated results are obtained using the Ansoft simulation software (HFSS), that in HFSS by default, the antenna is excited by a wave port that it is renormalized to a 50-Ohm full port impedance at all frequencies. In order to confirm the accurate return loss characteristics for the designed antenna, it is recommended that the manufacturing and measurement processes need to be performed carefully.

The VSWR characteristic of the antenna was measured using the HP 8720ES network analyzer in an anechoic chamber. The radiation patterns have been measured inside an anechoic chamber using a double-ridged horn antenna as a reference antenna placed at a distance of 2 m. Also, two-antenna technique using an Agilent E4440A spectrum analyzer and a double-ridged horn antenna as a reference antenna placed at a distance of 2 m is used to measure the radiation gain in the z axis direction (x-z plane). Measurement set-up of the proposed antenna for the VSWR, antenna gain and radiation pattern characteristics are shown in Fig. 8.

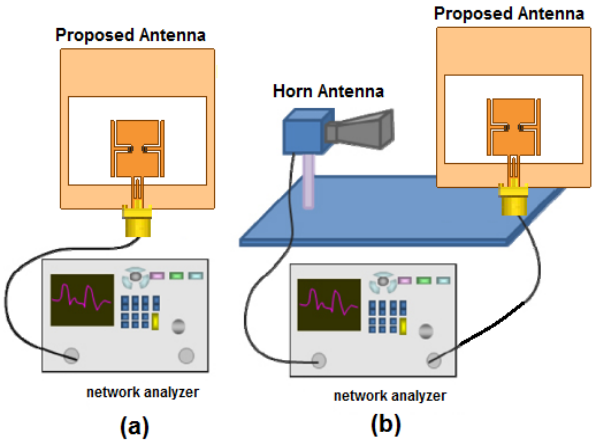

Fig. 8. Measurement set-up of the proposed antenna: (a) VSWR, and (b) antenna gain and radiation patterns.

Figure 9 depicts the measured and simulated radiation patterns of the antenna including the co-polarization and cross-polarization in the H-plane (x-z plane) and E-plane (y-z plane). It can be seen that nearly omnidirectional radiation pattern can be observed on x-z plane over the whole UWB frequency range. The radiation patterns on the y-z plane are like a small electric dipole leading to bidirectional patterns in a very wide frequency band. The main purpose of the radiation patterns is to demonstrate that the antenna actually radiates over a wide frequency band. With the increase of frequency, the radiation patterns become worse because of the increasing effects of the cross-polarization [10].

The radiation intensity corresponding to the isotropic ally radiated power is equal to the power accepted by the antenna divided by 4π. This can be expressed as:

$$G = \frac{4\pi U(\varphi,\theta)}{P_{in}}. \quad (1)$$

It is assumed that the antenna is receiving a signal in the direction of maximum gain. It is also common for the gain to be expressed in decibels and referenced to an isotropic source (G = 1), as shown:

$$G(dBi) = 10\,Log\,(G/1). \quad (2)$$

Measured maximum gains of the proposed antenna for different conditions of active elements are shown in Fig. 10. As illustrated, sharp decreases of the maximum gain in the notched frequencies (7.5, 8.6 and 9.5 GHz) are shown. For other frequencies outside the notched frequency band, the antenna gains are almost constant. As seen, the proposed antenna has sufficient and acceptable gain level in the operation bands [11].

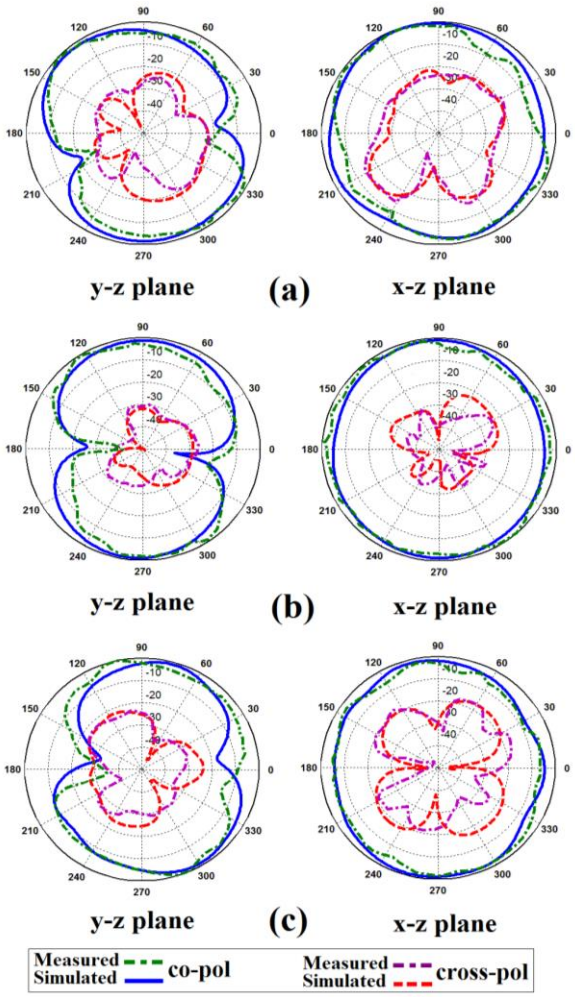

Fig. 9. Simulated and measured radiation patterns of the proposed antenna for D_1&D_2=ON: (a) 5 GHz, (b) 8.5 GHz, and (c) 11 GHz.

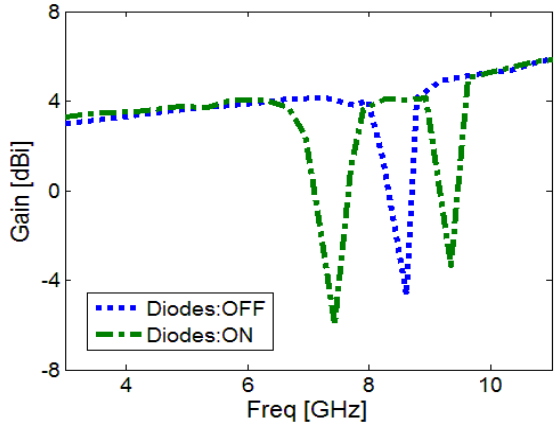

Fig. 10. Measured gain characteristics of the antenna for different conditions of active elements.

IV. CONCLUSION

A new reconfigurable slot antenna with multi-resonance and electrically switchable notch band functions for UWB applications is presented. The antenna is reconfigurable to suppress unwanted interfering signals by using PIN diodes integrated within the antenna configuration. By changing the ON/OFF conditions of the PIN diodes the antenna can be used to generate single or dual notch band in order to block any interference in the UWB frequency band. The designed antenna has a small size. Simulated and experimental results show that the proposed antenna could be a good candidate for UWB applications.

REFERENCES

[1] H. Schantz, *The Art and Science of Ultra Wideband Antennas*, Artech House, 2005.

[2] M. Ojaroudi, Sh. Yzdanifard, N. Ojaroudi, and M. Nasser-Moghaddasi, "Small square monopole antenna with enhanced bandwidth by using inverted T-shaped slot and conductor-backed plane," *IEEE Transactions on Antenna and Propagation*, vol. 59, pp. 670-674, 2011.

[3] A. Ghazi, M. N. Azarmanesh, and M. Ojaroudi, "Multi-resonance square monopole antenna for ultra-wideband applications," *Progress In Electromagnetics Research C*, vol. 14, pp. 103-113, 2010.

[4] M. Ojaroudi, Sh. Yzdanifard, N. Ojaroudi, and R. A. Sadeghzadeh, "Band-notched small square-ring antenna with a pair of T-shaped strips protruded inside the square ring for UWB applications," *IEEE Antennas and Wireless Propagation Letters*, vol. 10, pp. 227-230, 2011.

[5] M. Ojaroudi, Gh. Ghanbari, N. Ojaroudi, and Ch. Ghobadi, "Small square monopole antenna for UWB applications with variable frequency band-notch function," *IEEE Antennas and Wireless Propagation Letters*, vol. 8, pp. 1061-1064, 2009.

[6] D. Piazza, P. Mookiah, M. D'Amico, and K. R. Dandekar, "Experimental analysis of pattern and polarization reconfigurable circular patch antennas for MIMO systems," *IEEE Trans. Veh. Technol*., vol. 59, pp. 2352-2362, 2010.

[7] S.-L. S. Yang, A. A. Kishk, and K.-F. Lee, "Frequency reconfigurable U-slot microstrip patch antenna," *IEEE Antennas Wirel. Propag. Lett*., vol. 7, pp. 127-129, 2008

[8] S. Nikolaou, N. D. Kingsley, G. E. Ponchak, J. Papapolymerou, and M. M Tentzeris, "UWB elliptical monopoles with a reconfigurable band notch using MEMS switches actuated without bias lines," *IEEE Trans. Antennas Propag*., vol. 57, pp. 2242-2251, 2009.

[9] Ansoft High Frequency Structure Simulation (HFSS), ver. 13, Ansoft Corporation, 2010.

[10] Y. S. Li, X. D. Yang, C. Y. Liu, and T. Jiang, "Analysis and investigation of a cantor set fractal UWB antenna with a notch-band characteristic," *Progress In Electromagnetics Research B*, vol. 33, pp. 99-114, 2011.

[11] Y. Zhang, W. Hong, C. Yu, Z. Q. Kuai, Y. D. Don, and J. Y. Zhou, "Planar ultrawideband antennas with multiple notched bands based on etched slots on the patch and/or split ring resonators on the feed line," *IEEE Transactions on Antennas and Propagation*, vol. 56, no. 9, pp. 3063-3068, 2008.

Switchable Multiband Monopole CRLH Antenna

Abdullah K. Alqallaf [1], Rabie K. Dib [2], and Muhammad F. Karim [3]

[1] Electrical Engineering Department, College of Engineering and Petroleum
Kuwait University, P. O. Box 5969, Safat 13060 Kuwait
al.qallaf@ku.edu.kw

[2] Electronics Engineering Department, College of Technological Studies
Public Authority of Applied Education and Training, Kuwait
rk.dib@paaet.edu.kw

[3] Electrical and Computer Engineering
National University of Singapore, Singapore
elemfk@nus.edu.sg

Abstract ─ In this paper, a switchable multiband monopole composite right/left-handed (CRLH) antenna is designed, fabricated and measured. The structure consists of a monopole loaded with three CRLH unit cells. By incorporating the three unit cells it aids in generating multiband frequencies. The switchable antenna is developed by placing the pin diodes which enables the simultaneous operation of unit cells. A detailed parametric study is done to investigate the influence and the effect of CRLH cells dimensions. The simulation and measured results are in good agreement. The results show multiple bands from 1-4 GHz. The measured maximum gain of antenna is 3.13 dBi.

Index Terms ─ CRLH, metamaterials, monopole antenna, multiband, switchable.

I. INTRODUCTION

Reconfigurability of an antenna is a characteristic that can enhance the capability and versatility of antenna in certain applications. The switchable is applicable to the frequency of operation or the variation in the direction of the main beam beamwidth. In frequency-switchable antennas, the frequency of operation can be electronically tuned with the aid of microelectromechanical system (MEMS), or solid-state devices like varactor diodes and switching p-i-n diodes [1]-[5].

Switchable antennas enables a narrowband alternative to wideband antennas in communication systems where a single antenna has to be used for radio communication in different frequency bands. The other feature of these antennas is that, as the bandwidth is inversely related to the size of the antenna by fundamental limits, a smaller resonant antenna can cover a broad frequency range. In addition, the underlying band selectiveness can relax the filtering requirements for the radio system connected to the antenna. Patch antenna, planar inverted-F antennas (PIFAs), and slot antennas have shown great capability for switchable frequency antennas [1]-[7]. Recently, antennas have been loaded with metamaterial cells which can provide simultaneous negative electric permittivity and negative magnetic permeability. Such unit cells can be used to reduce the operating frequency significantly and to provide multifrequency operation [8]-[15].

A conventional resonant-type antennas are loaded with composite right/left-handed (CRLH) unit cells, this allows it to operate at the zeroth-order mode or negative-order modes. These types of techniques were demonstrated for the dipole antenna [9], patch antenna [10]-[12], and slot antenna [13]. In another type, conventional antennas are either electrically or magnetically coupled to metamaterial cells [14], [15]. CRLH cells help to reduce the operating frequency.

In this paper, a new microstrip-fed multiband monopole switchable antenna loaded with three CRLH unit cells. The antenna is designed to work at multiple bands of operation. The three CRLH cells are connected through p-i-n diodes. Each CRLH cells has its own characteristics of operation. A parametric study is done to investigate the influence and the effect of CRLH cells dimensions. The measurements of the S-parameters were performed using PNA series network analyzer, Agilent E8364B. The numerical simulations are carried out using CST (Computer Simulation Technology) Microwave Studio 2012 and MATLAB 2012.

II. DESIGN OF THE SWITCHABLE MULTIBAND MONOPOLE CRLH ANTENNA

The switchable monopole CRLH antenna is shown

Submitted On: September 9, 2015
Accepted On: December 5, 2015

in Fig. 1. The dimension of the ground plane is pertinent to determine the radiation pattern and also the operating bandwidth of the antenna. In our case, the monopole length was designed to operate around 2.4 GHz on Rogers 4003 with substrate thickness of 0.8 mm and dielectric constant equal to 3.38. The dimensions are given in Table 1. A diode is placed between every consecutive CRLH cells. The diodes are controlled by the bias-circuit to vary the number of the connected cells. Switching OFF the diodes will lead to a single CRLH cell, whereas switching ON the diodes will connect the other cells to the proposed antenna as shown in Fig. 1.

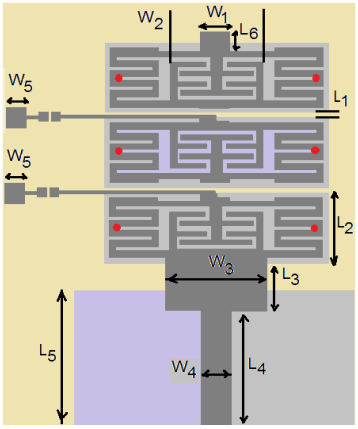

Fig. 1. Structure of switchable CRLH monopole antenna (not to scale).

Table 1: Dimensions of the CRLH antenna

Symbol	Length in (mm)
L_1	0.4
L_2	7
L_3	15.5
L_4	55
L_5	55
L_6	1.5
W_1	3
W_2	20
W_3	12
W_4	4.5
W_5	2
t_1	0.3
t_2	7
t_3	5.5
t_4	1.5
t_5	1
d	1
W_c	0.4
W_s	0.7
S_c	0.6
S_s	0.3

A. Design of a unit cell CRLH

The conventional CRLH unit cell is presented in [16]. It relies on the interdigital capacitor to provide the series capacitance and on the shunt short-circuited stub for the parallel inductance. There are three modifications made to the conventional unit cell as shown in Fig. 2. The major modification is that the unit cell is made symmetric so that even if the unit cell radiates, the radiation from the right side will cancel the radiation from the left side and the radiation-pattern will be controlled mainly by the monopole. The other change is that the capacitor is rotated to reduce its length in the lateral direction so that the unit cell occupies a small portion of the monopole. Moreover, short-circuited stubs are added before the interdigital capacitor to enhance the inductance of the unit cell. The upper and lower stubs are connected by one via to the ground to reduce the number of the required vias. It should be noted that the ground of the CRLH unit cell is not connected to the main ground of the microstrip-fed monopole. As presented in Table 1, the dimensions of the interdigital capacitor and the stub inductor are adjusted so that the CRLH unit cell is nearly balanced around 2.4 GHz on Rogers 4003. Figures 3 (a)-(b) demonstrates the simulation results of S_{11}, for the single CRLH cell and the three connected CRLH cells, respectively.

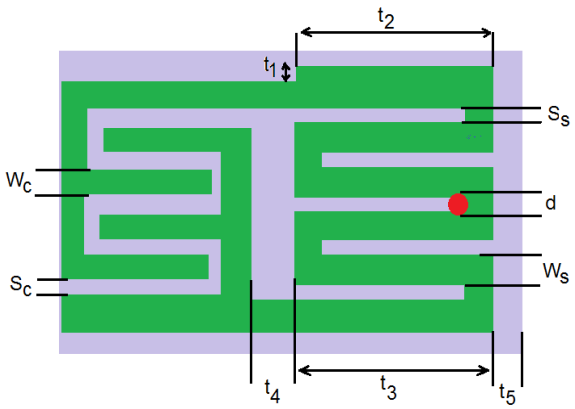

Fig. 2. Structure of a unit cell (not to scale).

B. Parametric variation of the slot width

In this subsection, the interdigital slot width, Ws, is varied to investigate the influence on the performance of antenna. As depicted in the Fig. 4, the slot width varies from 0.5 mm to 0.7 mm. Due to the fabrication tolerance limits, the slot width cannot be furtherly reduced. The operating frequency is slightly shifted to lower frequency with the increase in the slot width. The gain with frequency plot depicts that the 0.6 gives the maximum and stable gain over the frequency range from 0.5 GHz to 4 GHz as shown in Fig. 5.

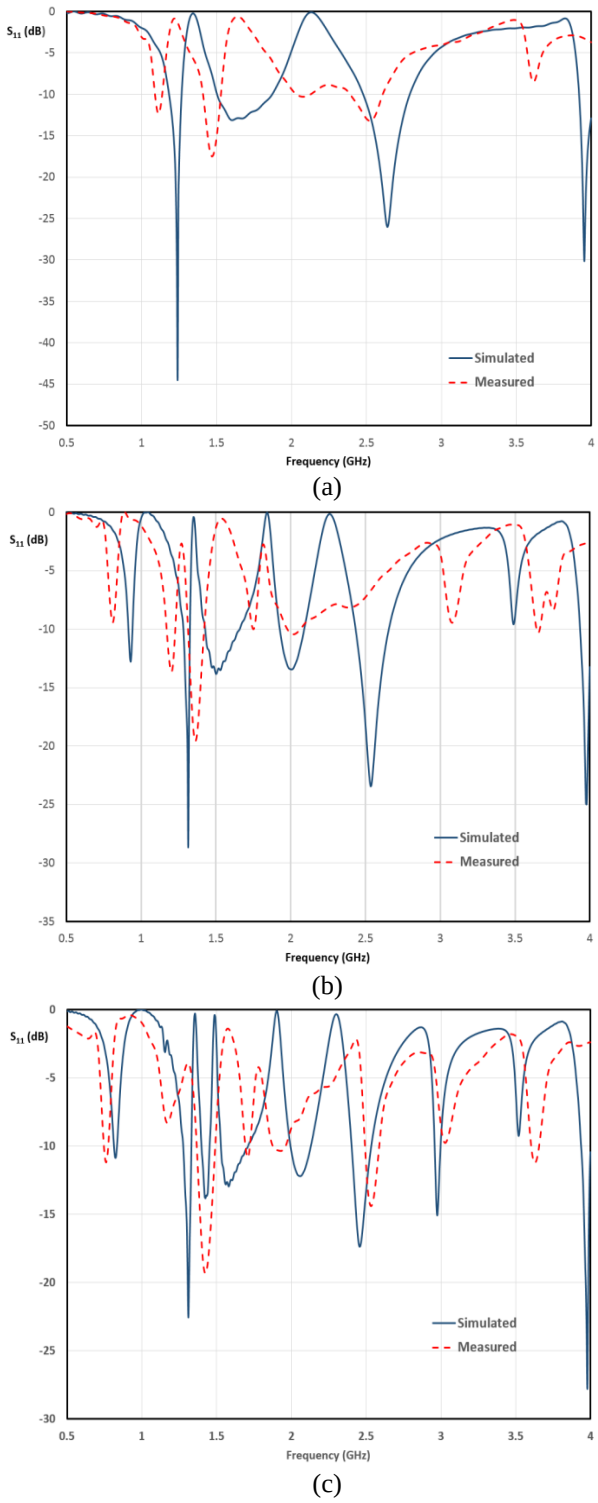

Fig. 3. Measured and simulation results of S_{11}: (a) single CRLH cell, (b) two CRLH cells, and (c) three CRLH cells.

C. Varying the number of CRLH cells

The number of CRLH cells has a significant influence on the performance of the antenna. A unit cell configuration was studied in the previous section. The increase in the number of CRLH cells generates the multiband configuration. The frequency shifts to lower frequency as the number of CRLH cells increase. The shift in the frequency for the first resonance is 0.7 GHz when compared to a unit cell CRLH. Moreover, there are seven operating bands within1-3 GHz as shown in Fig. 6. In Fig. 7, the result for the gain plot signifies a constant gain of over 1.5 dBi. The maximum gain of 4.5 dBi is centered at 2.6 GHz.

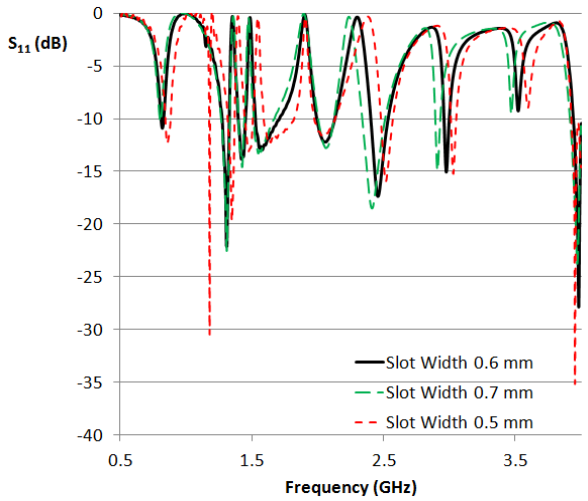

Fig. 4. Simulated plot for S_{11} at different slot widths.

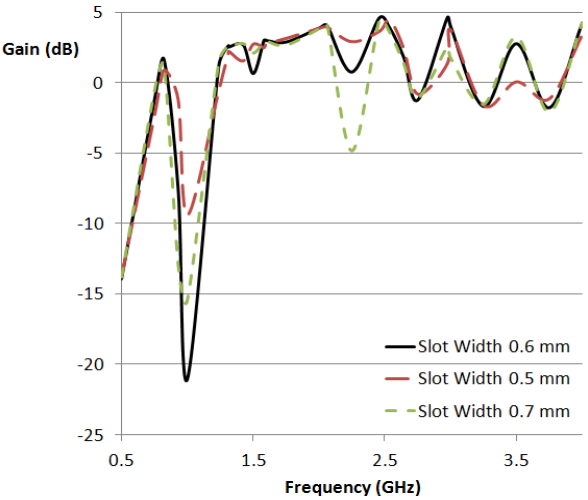

Fig. 5. Simulated plot for gain variation at different slot widths.

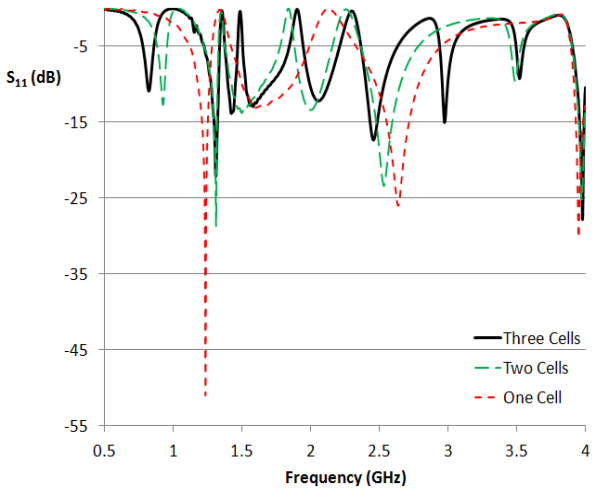

Fig. 6. Simulated plot of S_{11} for single, two, and three CRLH cells antenna.

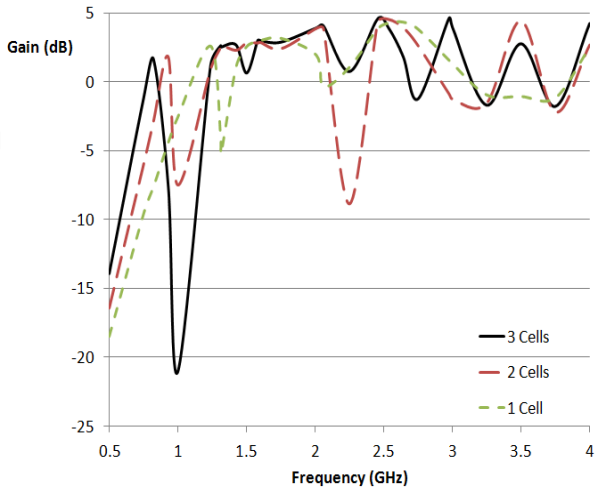

Fig. 7. Simulated plot of gain variation for single, two, and three CRLH cells antenna.

III. MEASURED RESULTS AND DISCUSSION

The CRLH switchable antenna is fabricated on Rogers 4003 substrate with 0.8 mm thickness. Table 1 shows the optimized dimensions. The fabricated switchable three CRLH cells antenna structure is shown in Fig. 8. The pin diodes are used to switch between the cells. A separate DC bias line is drawn to provide voltage for the operation of the diodes. The measured S_{11} for the switchable monopole CRLH antenna is shown in Fig. 9. When the pin diodes D1 and D2 are switched OFF, only single unit cell CRLH is connected to the monopole antenna. By connecting the second CRLH cell to the monopole antenna when the first diode, D1 is switched ON, resulting into two CRLH cells antenna configuration. Consequently, by switching ON the second diode D2, the third CRLH cell is connected to the monopole antenna. Results show the multiband characteristics of the antenna when all the three cells are radiating. Table 2 depicts the gains and the efficiencies of the three CRLH cells antenna at the seven corresponding resonant frequency bands.

Table 2: Simulation results of the three CRLH cells antenna at the resonant frequencies

Frequency (GHz)	Gain (dB)	Efficiency (%)
0.822	1.635	92.3
1.312	2.617	97.6
1.424	2.673	96.0
1.5815	2.987	95.9
2.061	4.044	93.9
2.4565	4.572	98.2
2.9745	4.594	96.7

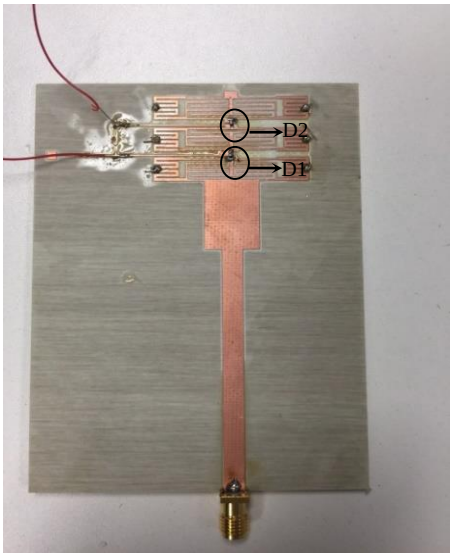

Fig. 8. Fabricated switchable monopole CRLH antenna.

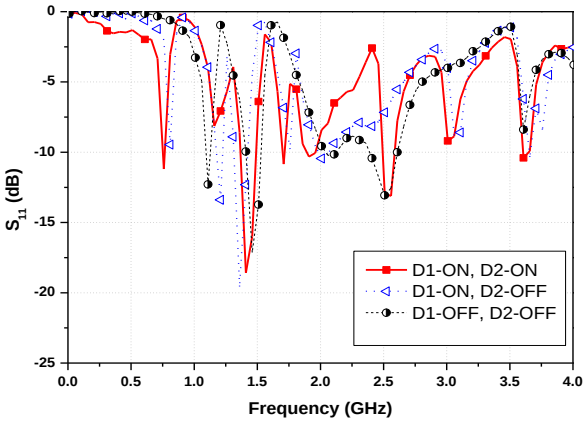

Fig. 9. Measured results for the switchable monopole CRLH antenna.

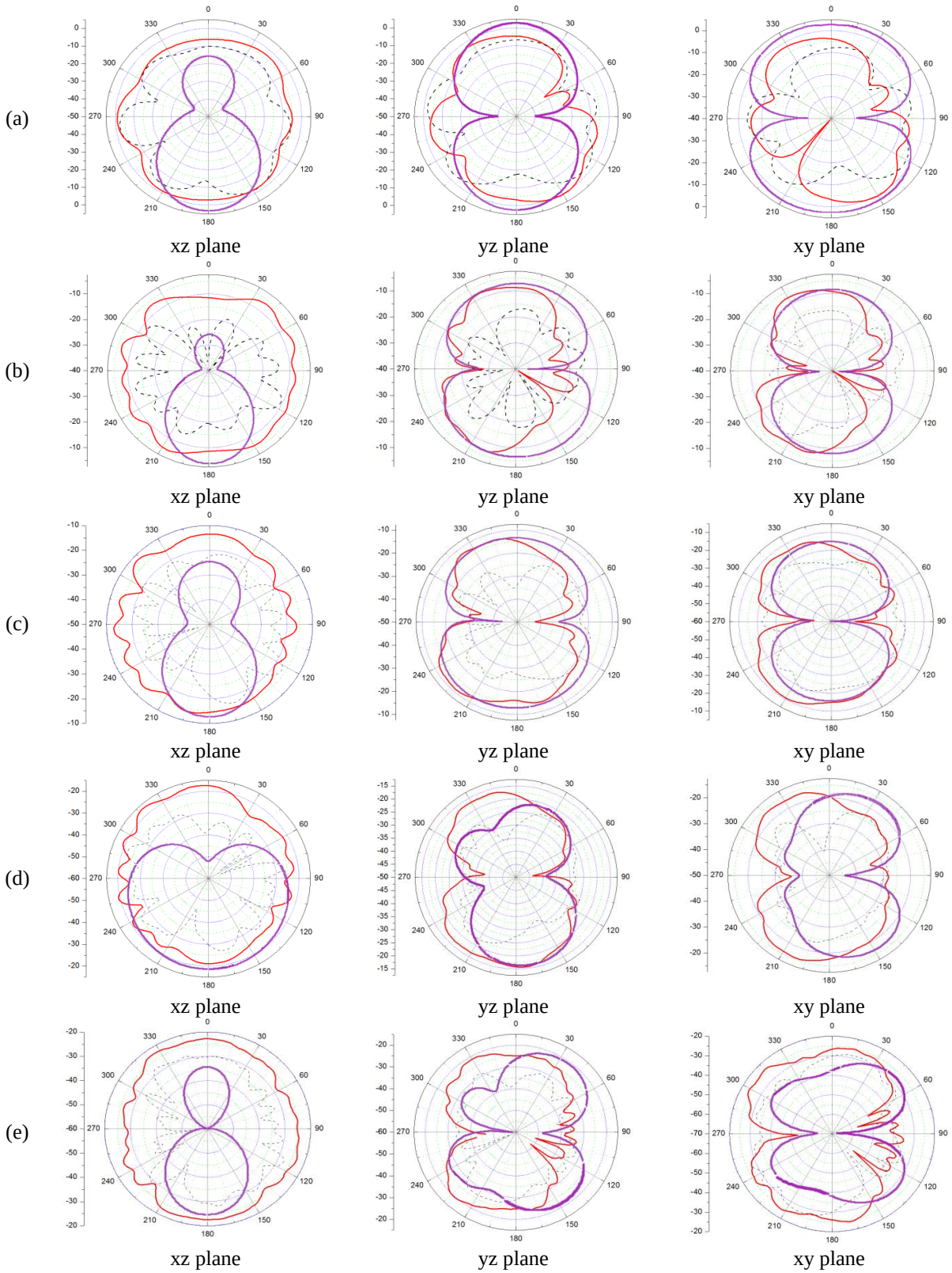

Fig. 10. Comparison between simulated (purple-line) and measured (red-line) radiation pattern for the three planes of the three CRLH antenna cells operated at the five resonance-frequencies: (a) f = 0.76 GHz, (b) f = 1.41 GHz, (c) f = 1.71 GHz, (d) f = 1.91 GHz, and (e) f = 2.55 GHz.

The simulated radiation patterns which are quasi-omni-directional at the seven operating frequency bands are illustrated in Fig. 10 (purple-line). Note that the radiation patterns of the three CRLH cells are consistent with the conventional microstrip-fed monopole antenna presented in [17], except the last two at the resonance frequency of 2.9745 GHz. The measured radiation patterns for the switchable monopole CRLH antenna are shown in Fig. 10 (red-line). It operates at 5 different frequency bands and depicts a monopole pattern. The measured maximum gain of antenna is 3.13 dBi.

The comparison study of the radiation pattern for the three planes of the three CRLH antenna cells operated at the five resonance-frequencies presented in Fig. 10 shows that the simulated and measured results are in good agreement.

IV. CONCLUSION

A switchable multiband monopole composite right/left-handed (CRLH) antenna was proposed. The antenna principle of operation was explained, and a prototype was designed and measured. The structure consists of a monopole loaded with three CRLH unit cells. The switchable antenna was developed by placing the pin diodes which enables the simultaneous operation of unit cells. The simulation and measured results are in good agreement. The results show multiple bands from 1-4 GHz. The measured maximum gain of antenna is 3.13 dBi.

REFERENCES

[1] S. V. Hum and H. Y. Xiong, "Analysis and design of a differentially-fed frequency agile microstrip patch antenna," *IEEE Trans. Antennas Propag.*, vol. 58, no. 10, pp. 3122-3130, Oct. 2010.

[2] V.-A. Nguyen, R.-A. Bhatti, and S.-O. Park, "A simple PIFA-based tunable internal antenna for personal communication handsets," *IEEE Antennas Wireless Propag. Lett.*, vol. 7, pp. 130-133, 2008.

[3] N. Behdad and K. Sarabandi, "Dual-band reconfigurable antenna with a very wide tunability range," *IEEE Trans. Antennas Propag.*, vol. 54, no. 2, pp. 409-416, Feb. 2006.

[4] C. R. White and G. M. Rebeiz, "Single-and dual-polarized tunable slot-ring antennas," *IEEE Trans. Antennas Propag.*, vol. 57, no. 1, pp. 19-26, Jan. 2009.

[5] H. Li, J. Xiong, Y. Yu, and S. He, "A simple compact reconfigurable slot antenna with a very wide tuning range," *IEEE Trans. Antennas Propag.*, vol. 58, no. 11, pp. 3725-3728, Nov. 2010.

[6] J. L. A. Quijano and G. Vecchi, "Optimization of an innovative type of compact frequency-reconfigurable antenna," *IEEE Trans. Antennas Propag.*, vol. 57, no. 1, pp. 9-18, Jan. 2009.

[7] M. Komulainen, M. Berg, H. Jantunen, E. T. Salonen, and C. Free, "A frequency tuning method for a planar inverted-F antenna," *IEEE Trans. Antennas Propag*., vol. 56, no. 4, pp. 944-950, Apr. 2008.

[8] M. Palandoken, A. Grede, and H. Henke, "Broadband microstrip antenna with left-handed metamaterials," *IEEE Trans. Antennas Propag*., vol. 57, no. 2, pp. 331-338, Feb. 2009.

[9] H. Iizuk and P. S. Hall, "Left-handed dipole antennas and their implementations," *IEEE Trans. Antennas Propag*., vol. 55, no. 5, pp. 1246-1253, May 2007.

[10] C.-J. Lee, K. M. K. H. Leong, and T. Itoh, "Composite right/left-handed transmission line based compact resonant antennas for RF module integration," *IEEE Trans. Antennas Propag*., vol. 54, no. 8, pp. 2283-2291, Aug. 2006.

[11] F. J. Herraiz-Martínez, V. González-Posadas, L. García-Muñoz, and D. Segovia-Vargas, "Multi-frequency and dual-mode antennas partially filled with left-handed structures," *IEEE Trans. Antennas Propag*., vol. 56, no. 8, pp. 2527-2539, Aug. 2008.

[12] M. Schüßler, J. Freese, and R. Jakoby, "Design of compact planar antennas using LH transmission lines," in Proc. *IEEEMTT-S Int. Microw. Symp*., vol. 1, pp. 209-212, Jun. 2004.

[13] P. B. Nesbitt and G. Mumcu, "A small slot dipole loaded with CRLH TL unit cells," *IEEE AP-S Int. Symp. Dig*., pp. 1032-1035, Jul. 2011.

[14] A. Erentok and R. W. Ziolkowski, "Metamaterial-inspired efficient electrically-small antennas," *IEEE Trans. Antennas Propag*., vol. 56, no. 3, pp. 691-707, Mar. 2008.

[15] J. Zhu, M. A. Antoniades, and G. V. Eleftheriades, "A compact tri-band monopole antenna with single-cell metamaterial loading," *IEEE Trans. Antennas Propag.*, vol. 58, no. 4, pp. 1031-1038, Apr. 2010.

[16] C. Caloz and T. Itoh, *Electromagnetic Metamaterials*: *Transmission Line Theory and Microwave Applications*, Hoboken, NJ: Wiley Interscience, 2006.

[17] M. J. Ammann and M. John, "Optimum design of the printed strip monopole," *IEEE Antennas Propag. Mag.*, vol. 47, no. 6, pp. 59-61, Dec. 2005.

Abdullah K. Alqallaf received the B.S. and M.S. degrees in Electrical Engineering from Kuwait University in 1996 and 1999, respectively, and the Ph.D. degree in Electrical Engineering from the Universityof Minnesota – Twin Cities, St. Paul, MN, in 2009. He is an Assistant

Professor with the Department of Electrical Engineering at the Kuwait University. Alqallaf's research interests are Microwave Imaging Techniques, Multimedia Signal Processing, Communication, Bioinformatics and Medical Image Analysis. Alqallaf is an IEEE Board Member - Professional Activities - Kuwait Section.

Rabie K. Dib received the B.S. and M.S. degrees in Electrical Engineering from Kuwait University in 1999 and 2002, respectively. He is an Instructor with the Electronics Engineering Dept., College of Technological Studies at Public Authority of Applied Education and Training, Kuwait. Dib's research interests are Electromagnetics, Communication, Antenna Design, Microwave Imaging Techniques and analysis.

Muhammad Faeyz Karim received his Ph.D. and M.Sc. degrees in 2008 and 2003 from Nanyang Technological University (NTU), Singapore and B.Eng. from NUST, Pakistan in 2000. Karim has published more than 50 scientific papers in reputable international journals and conferences. He has co-authored a book on "RF MEMS Switches and Integrated Switching Circuits", Springer, USA, 2010. He received the best paper award in Asia-Pacific Conference of Transducers and Micro-Nano Technology in 2003. He was involved in organizing the Microwave Photonics Conference (MWP), 2011 and IEEE IMWS Conference 2013 in Singapore, served as TPC Member for IEEE RFIT2009 & RFIT 2011, Session chairs for number of conferences and Reviewers for IEEE Transactions on MTT/AP, IEEE MWCL and IET MAP. His current research interests are in the area of RF & millimeter wave for RF MEMS devices, active/passive millimeter wave sensing and imaging systems, RF & hybrid energy harvesting, RF Nanoelectronics, tunable & reconfigurable filters, antenna miniaturization techniques, passives modules & circuits, and radio-over-fiber technologies.

A New Dual-Band, Dual-Polarized and Single Feed Reconfigurable Antenna

A. Sedghara and Z. Atlasbaf

Faculty of Electrical and Computer Engineering
Tarbiat Modares University (TMU), Tehran, Iran
ailar.sedghara@gmail.com, atlasbaf@modares.ac.ir

Abstract ─ In this paper, a new single feed reconfigurable annular-ring slot antenna for polarization and frequency diversity for WLAN and WiMAX applications is proposed. This antenna has a simple structure; it contains two concentric circular slots, and four tuning stubs on one side of the substrate, and a 50 Ω microstrip feed line and two stubs on the other side. The proposed antenna can be switched between two resonant frequencies, 2.4 GHz (WLAN) and 3.5 GHz (WiMAX). Furthermore, it can be switched between left-hand circular polarization (LHCP) and right-hand circular polarization (RHCP) at both resonant frequencies. Using seven switches (PIN diode), on both sides of the substrate. Details of the antenna design are shown and the results are also exhibited and discussed. Simulation and experimental results indicate that the proposed antenna demonstrates a good impedance bandwidth at the two resonant frequencies, and satisfactory axial ratios in the circularly polarized states.

Index Terms ─ Annular-ring slot antenna, dual-band, dual-polarized, reconfigurable antenna.

I. INTRODUCTION

Multifunction antennas, with different radiation characteristics in a single antenna element, have become an important research area in antenna engineering field. Reconfigurable antennas with the ability of radiating more than one pattern at different frequencies and various polarizations offer several degrees of freedom to antenna designers. Therefore, these antennas are good candidate in the future wireless communication systems. Application areas that drive the development of reconfigurable antennas include multifunction wireless devices, multiple-input multiple-output (MIMO) systems, and ultra-wideband systems, anti-jamming secure communication to accommodate the ever demanding requirements of such systems [1]. Reconfigurable antennas are divided into 4 main categories, consisting antennas that exhibit reconfigurable return loss, radiation pattern, polarization, and different combinations of the previous categories.

The reconfigurable antenna with polarization agility offers an impressive enrichment in receiving the communication signal which includes an exceptional ability of multipath fading reduction. Moreover, multi-band reconfigurable antennas are desirable in modern communication systems. Hence, designing a new microstrip antenna with reconfigurable polarization and frequency is the main motivation in this paper.

The microstrip antennas with polarization diversity have been studied and their characteristics reported in [2-4]. The antenna studied in [5] uses dual-feeding for reconfigurability, while an antenna with the simple feeding network is one of the main factors in wireless communication systems.

In order to achieve polarization switching in single-fed microstrip patch antennas, one simple method is changing the electrical characteristics of the perturbation segments through PIN diodes. Several polarization reconfigurable antennas based on this method have been proposed [6]-[7].

Some reconfigurable antennas that have been introduced, present combinations of polarization and frequency diversities. Patch antennas with switchable slot (PASS) with both frequency and polarization diversities which are discussed in [5,8,9] utilize dual-fed structures. Reference [4] proposes a reconfigurable single-feed microstrip patch antenna with frequency and polarization diversities using some PIN diodes and a U-slot, incorporated into a square patch. This antenna does not provide polarization diversity in any of the resonant frequencies.

In this paper, we present a single-feed antenna that exhibits dual-band and dual-polarized reconfigurablity for different antenna configurations, suitable for WLAN and WiMAX applications. In our work, for polarization diversity at the first resonant frequency of the proposed antenna, tuning stubs on the ground plane are used. Moreover, for polarization diversity at the second resonant frequency, two open stubs perpendicular to feed line are used, too. Another advantage of the proposed antenna in this paper, is its single layer structure. The antenna is simulated, fabricated and tested. The measurement results show

Submitted On: February 15, 2014
Accepted On: May 25, 2015

good agreement with those obtained by simulations.

II. ANTENNA DESIGN

The geometry of the antenna is shown in Fig. 1. It has two concentric circular slots printed on a 1.6 mm thick FR4_epoxy substrate of relative permittivity 4.4. The microstrip feed line is placed on the opposite side of the substrate and the annular slot is placed on the other side. For the annular slots, the inner radius is R2 with slot width of S2, and the outer radius is R1 with slot width of S1. A pair of stubs is loaded with four PIN diodes in the annular-ring slot with length (Ls) and width (Ws) to have polarization diversity at the first resonant frequency.

The microstrip feed line is broken into two segments, with PIN diode inserted between two paths with transformer in antenna feed line and two matching stubs with the length (Lsf) and width (Wsf), leads to have an appropriate impedance matching for all states. Two open stubs which are connected by two PIN diodes allow polarization diversity at the second resonant frequency.

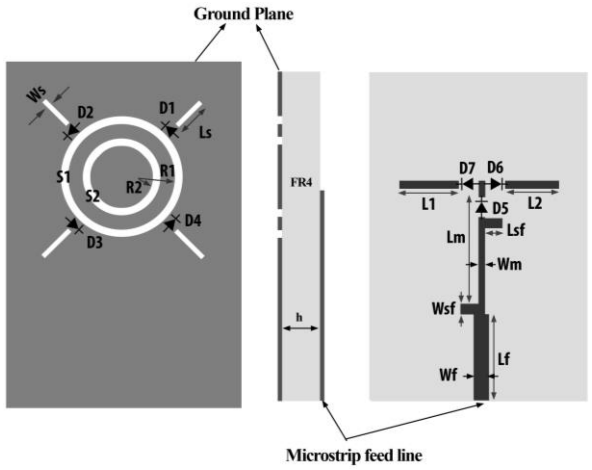

Fig. 1. Geometry of the proposed antenna.

A. Frequency diversity

By changing the circumference of the annular-ring slots, the proper operating frequency can be obtained. Hence, in order to allow one resonant frequency to operate, either inner or outer slot should be excited. To have frequency diversity, the PIN diode (D5) is inserted in the feed line. When the PIN diode is biased (on-state), inner ring slot is excited for generating the second resonant frequency.

On the other hand, when the PIN diode is in "off-state", the outer ring slot is excited and generates the first resonant frequency. The outer radius (R1) is selected proportional to 2.4 GHz for the WLAN application, and the inner radius (R2) is selected proportional to 3.5 GHz for the WiMAX application. Hence, the proposed antenna can operate with frequency diversity using only one PIN diode.

Figure 2 illustrates the surface current distribution on the proposed antenna structure at frequencies 2.4 GHz and 3.5 GHz. The surface current distributions are obtained, through HFSS. It is obvious that either inner or outer slot is excited. It shows they operate independently.

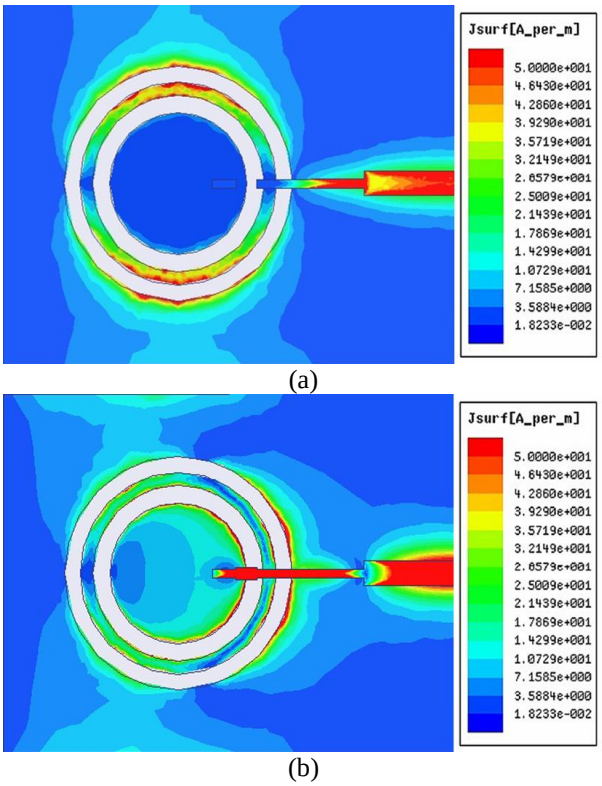

Fig. 2. Surface current distribution on the proposed antenna structure at: (a) 2.4 GHz, and (b) 3.5 GHz.

B. Polarization diversity

Generally, the annular-ring slot antenna operates in the fundamental TM11 mode. Circular polarization operation is excited by loading a pair of stubs in the annular-ring slot. The fundamental TM_{11} mode can be splitted into two near degenerate resonant modes. Therefore, circular polarization (CP) operation can be obtained and optimized by varying the tuning stub dimensions. The two near resonant modes have almost equal amplitudes and 90° phase difference in CP operation. When a pair of tuning stubs is located at 135° and -45°, the LHCP operation can be obtained. On the other hand, when a pair of tuning stubs is placed at -135° and 45°, the RHCP operation can be obtained. Based on this structure, the proposed antenna can switch by four PIN diodes (D1, D2, D3, and D4) between LHCP and RHCP states at 2.4 GHz for WLAN application.

As it was explained, to radiate circular polarization, two orthogonal modes should be excited with the same amplitude and a 90° phase difference. Generally, two orthogonal modes of the circular microstrip antenna can be excited in series with the microstrip feed line through the coupling of the ring slots. The magnitudes of the two orthogonal modes are related to the amplitudes of the vertical and horizontal directed currents under the ring slot. It means that by altering the current distributions in the microstrip feed line, the CP radiation of the ring slot coupled microstrip antenna can be achieved. Hence, polarization diversity can be attained by adjusting the stub length.

In order to have polarization diversity between LHCP and RHCP states at the second resonant frequency, two stubs perpendicular to feed line are used. When either of them is excited, LHCP or RHCP mode is achieved. Inserting two PIN diodes (D6 and D7) to excite one stub every time are utilized. Therefore, the antenna can also switch between LHCP and RHCP states at 3.5 GHz for the WiMAX application, too. Different diodes combinations and their associated operation status are summarized in Table 1.

Table 1: Different diodes combinations and their associated operation status

	D5	D1 and D3	D2 and D4	D6	D7	Freq.	Polarization
Ant. 1	Off	Off	On	Off	Off	F_L	LHCP
Ant. 2	Off	On	Off	Off	Off	F_L	RHCP
Ant. 3	On	On	On	On	Off	F_H	LHCP
Ant. 4	On	On	On	Off	On	F_H	RHCP

C. Matching approach

The proposed feed line consists of double-stub shunt tuning circuits to achieve input impedance matching for LHCP and RHCP polarizations at both resonant frequencies. Generally, stub spacing near 0 or λ/2 lead to very frequency sensitive matching networks. In practice, stub spacing are usually chosen λ/8 or 3λ/8 [10]. The spacing used in this paper is about 14 mm that is, on average, λ/8 for both frequencies. Symmetrical stubs are used to achieve the best responses.

III. RESULTS

The S-parameters, axial ratio and pattern shape of the proposed antenna have been simulated and tested. It is worth mentioning that the size of the gaps for all states is proportional to the PIN diode models MA4P274-1141T [11].

For the on-state diode, the equivalent circuit that can be extracted from its data sheet is represented by a resistor (R = 3 Ω), while for the off state diode, the equivalent circuit is represented by a capacitor (C = 0.35 PF). The ground plane should be separated into four parts by using thin slits to supply the DC voltage. The DC voltage is supplied directly through the divided ground plane. The details of the design parameters are summarized in Table 2.

Table 2: Details of design parameters (mm)

R_1	R_2	S_1	S_2	Ls_f
12.45	7.7	2	2.8	3.45
Ws_f	W_s	L_s	L_m	W_m
2	0.5	10	23	1.1
L_f	L_1	L_2	W_f	h
17.11	13.45	13.45	3.059	1.6

The S-parameters of the proposed antenna for all states described in Table 1, has been measured. Figure 2 shows the S-parameters of the antenna for the first resonant frequency mode. In this figure the simulation and measurement results of the two states Ant.1 (Fig. 3 (a)) and Ant. 2 (Fig. 3 (b)), are shown.

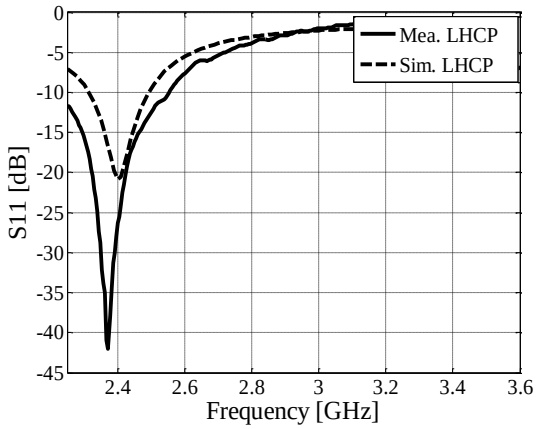

(a) Ant.1

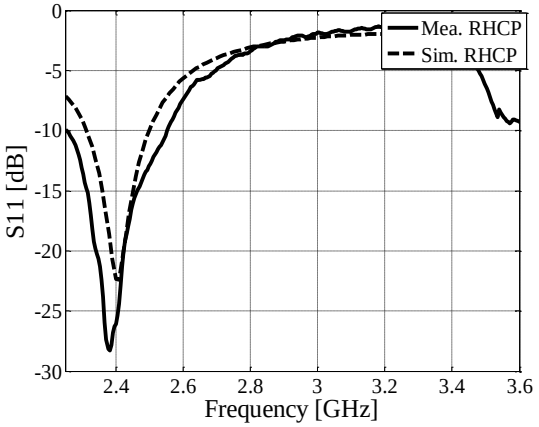

(b) Ant.2

Fig. 3. Simulated and measured S11 of the proposed antenna at 2.4 GHz (WLAN application): (a) LHCP mode (Ant.1), and (b) RHCP mode (Ant.2).

Figure 4 shows the S-parameters of the antenna for the second resonant frequency mode. The results of this figure are on the case when two diodes on the microstrip feed line is “on-state”.

When the antenna works in Ant.3 state, the results are shown in Fig. 4 (a), and when it works in Ant.4 state, they are shown in Fig. 4 (b).

The measured impedance matching bandwidths are 12.7% and 14.28% of the first resonant frequency for RHCP and LHCP modes, and they are 21.31% and 19.32% of the second resonant frequency for RHCP and LHCP modes, respectively.

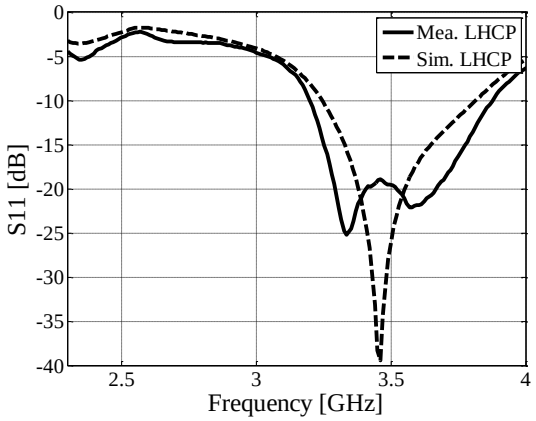

(a) Ant.3

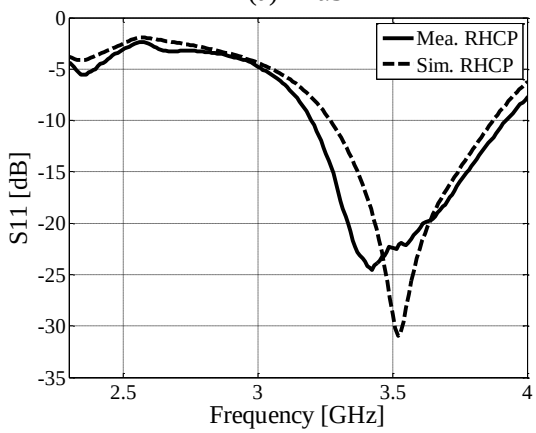

(b) Ant.4

Fig. 4. Simulated and measured S11 of the proposed antenna at 3.5 GHz (WiMAX application): (a) LHCP mode (Ant.3), and (b) RHCP mode (Ant.4).

Figure 5 shows the simulated and measured axial ratio of the proposed antenna in all states. The simulated 3 dB axial ratio bandwidth is 4.7% for the first resonant frequency and 18.37% for the second one.

The simulated radiation patterns for both resonant frequencies are depicted in Fig. 6 and Fig. 7. Evidently, the antenna yields satisfactory results for the co-polarization and cross-polarization main beams.

The radiation patterns in the CP states were simulated at frequencies where the minimum axial ratio occurs. Results show that broadside radiation patterns with good LHCP and RHCP characteristics are obtained at the resonant frequency.

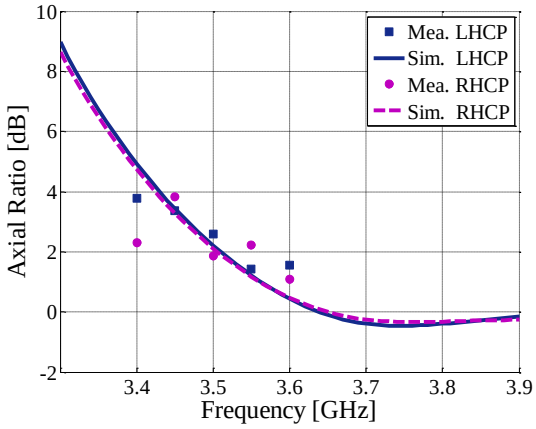

(a) Ant.1 and Ant.2

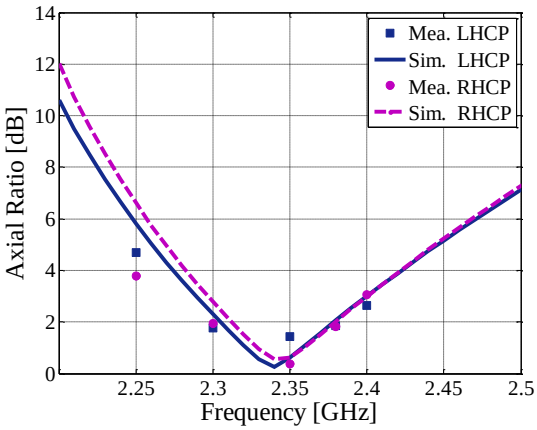

(b) Ant.3 and Ant.4

Fig. 5. Simulated and measured axial ratio of the proposed antenna for circular polarization for: (a) WLAN application (Ant.1 and Ant.2), and (b) WiMAX application (Ant.3 and Ant.4).

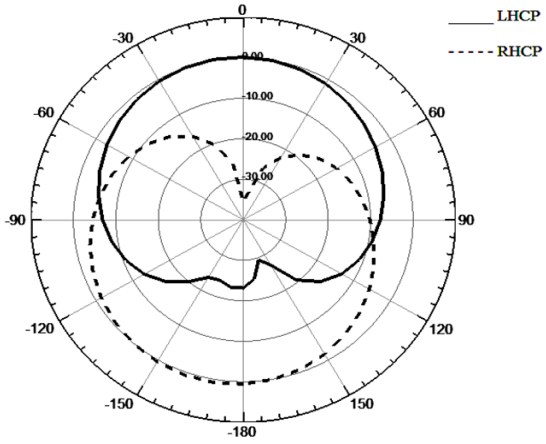

(a) Ant.1

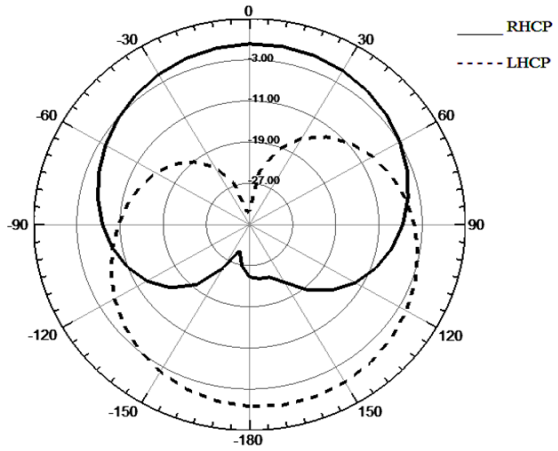

(b) Ant.2

Fig. 6. Simulated radiation patterns of the proposed antenna for circular polarization at 2.4 GHz: (a) LHCP mode (Ant.1), and (b) RHCP mode (Ant.2).

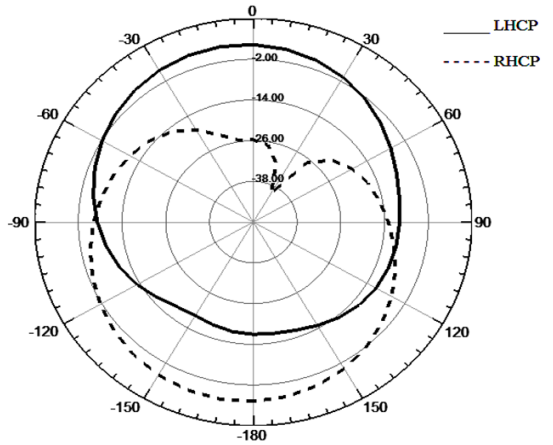

(a) Ant.3

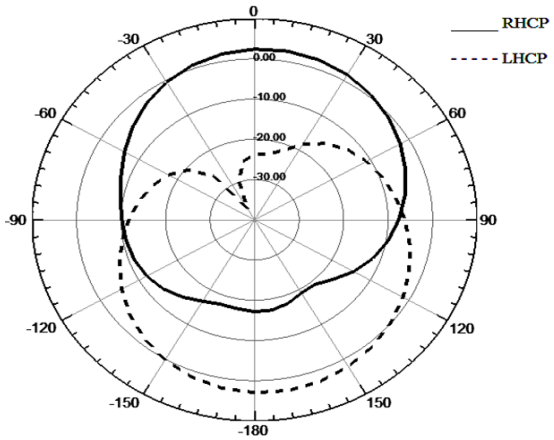

(b) Ant.4

Fig. 7. Simulated radiation patterns of the proposed antenna for circular polarization at 3.5 GHz: (a) LHCP mode (Ant.3), and (b) RHCP mode (Ant.4).

IV. CONCLUSION

Design of a new dual-band dual-polarized and single feed reconfigurable annular-ring slot antenna for WLAN and WiMAX applications has been presented in this paper. The proposed antenna can be switched between two resonant frequencies 2.4 GHz (WLAN) and 3.5 GHz (WiMAX). Also, it can be switched between left-hand circular polarization (LHCP) and right-hand circular polarization (RHCP) at both resonant frequencies with a single feed. The antenna polarization is switched by four stubs at the ground plane for the first resonant frequency, and two open stubs at the feed line for the second one. The frequency diversity of the proposed antenna can be switched by only one PIN diode. Good impedance matching performance for all states is observed using two open stubs. A prototype has been fabricated and tested. The simulated and measured results agree very well as confirming the validity of our used models.

ACKNOWLEDGMENT

The authors wish to thank ITRC (Iran Telecommunication Research Center) for supporting this work under the contract number 15706.

REFERENCES

[1] C. A. Balanis, *Antenna Theory Analysis and Design*, 3rd ed., Wiley, 2005.

[2] Y. B. Chen, T. B. Chen, Y. C. Jiao, and F. S. Zhang, "A reconfigurable microstrip antenna with switchable polarization," *Journal of Electromagnetic Waves and Applications*, vol. 20, no. 10, pp. 1391-1398, 2006.

[3] M. T. Zhang, Y. B. Chen, Y. C. Jiao, and F. S. Zhang, "Dual circularly polarized antenna of compact structure for RFID application," *Journal of Electromagnetic Waves and Applications*, vol. 20, no. 14, pp. 1895-1900, 2006.

[4] K. Chung, Y. Nam, T. Yan, and J. Chio, "Reconfigurable microstrip patch antenna with switchable polarization, *ETRI Journal*, no. 3, pp. 379-382, June 28, 2006.

[5] N. Jin, F. Yang, and Y. Rahmat Samii, "A novel patch antenna with switchable slot (PASS): dual-frequency operation with reversed circular polarizations," *IEEE Trans. Antennas Propag*., vol. 54, no. 3, pp. 1031-1034, Mar. 2006.

[6] Y. J. Sung, "Reconfigurable patch antenna for polarization diversity," *IEEE Trans. Antennas Propag*., vol. 56, no. 9, pp. 3053-3054, Sep. 2008.

[7] D. H. Hyun, J. W. Baik, S. H. Lee, and Y. S. Kim, "Reconfigurable microstrip antenna with polarization diversity," *Electronics Letters*, vol. 44, no. 8, pp. 509-510, Apr. 10, 2008.

[8] S. Rezvani, Z. Atlasbaf, and K. A. Forooraghi,

"New compact reconfigurable patch antenna for polarization and frequency diversity," *Electromagnetics*, pp. 287-293, 2012.

[9] S. Rezvani, Z. Atlasbaf, and K. Forooraghi, "A novel miniaturized reconfigurable slotted microstrip patch antenna with DGS," *Electromagnetics*, pp. 349-354, 2011.

[10] D. M. Pozar, *Microwave Engineering*, 2nd ed., New York: Wiley, 1998.

[11] Data Sheet MA4P274-1141T PIN Diodes, MA-Com. Application Note.

Ailar Sedghara was born in 1987. She received the B.S. degree in Electrical Engineering from the Shahed University, and the M.S. degree in Communication Engineering from the Tarbiat Modares University, Tehran, Iran, in 2010, 2013 respectively.

Her research activity was focused on some types of antennas, it includes multi-band, dual polarized, slot arrays, and MIMO antennas.

In 2013, she joined the Department of Electrical Engineering, University of Payame Noor, as a Lecturer.

Her current research interests include antenna theory and design, RF circuits, and some types of filters like microstrip, strip.

Zahra Atlasbaf (M'08) received the B.S. degree in Electrical Engineering from the University of Tehran, Tehran, Iran, in 1993, and the M.S. and Ph.D. degrees in Electrical Engineering from the University of Tarbiat Modares, Tehran, Iran, in 1996 and 2002, respectively.

She is currently an Associate Professor with the Faculty of Electrical and Computer Engineering, Tarbiat Modares University. Her research interests include numerical methods in electromagnetics, theory and applications of metamaterials, and microwave and antenna design.

Additional Losses in Ultra-Wide Band Reflector Systems

Hazel Kara and Nurhan Turker Tokan

Department of Electronics and Communications Engineering
Yıldız Technical University, Esenler, Istanbul, 34220, Turkey
hazelkara.ieee@gmail.com, nturker@yildiz.edu.tr

Abstract ─ The increasing demand of ultra-wide band (UWB) antennas in reflector systems, especially for radioastronomy, necessitates the analysis of reflector losses for directive UWB feeds. UWB technology has significant advantages; however its usage in reflector systems brings some extra losses to be considered. Ideally, all areas of the reflector should be illuminated with equal energy from the feed antenna at all frequencies of the band. However, this is not possible for a wide band system. Different phase center locations and 10 dB beamwidth values at different frequencies within the band result in spillover, amplitude taper and phase losses in a reflector system. These losses should be analyzed in detail for the effectively working of the system. The purpose of this work is to discuss the additional losses that occur in a UWB reflector system and demonstrate these losses with a given example. A directive Vivaldi antenna is used as the feed antenna of the UWB reflector and the effect of the losses on the directivity is shown.

Index Terms ─ Amplitude taper loss, cross-polarization loss, phase error loss, reflector, spillover loss, Vivaldi, UWB.

I. INTRODUCTION

Reflectors are widely used high-gain antennas for high-resolution radars and radioastronomy. Maximum gain for a reflector system is possible when there is uniform amplitude and phase distribution, no spill over and no ohmic losses. This case is not possible in practice. However, if the losses in a reflector system are known, it is possible to compensate them. The efficiency of a reflector system is investigated and the losses due to nonuniform amplitude and phase distribution, spillover, cross-polarization and feed blockage are investigated in [1-5]. Even the losses due to struts that support the feed of a primary-fed paraboloid are worked out [4]. In these works, it is shown that the losses and resulted efficiency of the system can be determined directly from the feed antenna pattern. Also, the gain of the system can be evaluated from the feed pattern that defines the aperture efficiency.

Today, there is an increasing interest in extremely large bandwidth high-performance applications. Such applications range from deep space investigation to commercial telecommunication links and radars with high spatial resolutions [6-8]. Some applications, such as radioastronomy, often necessitate directive antennas as feeds of large reflector. When a wide band antenna is to be used as a reflector feed, the phase center variation with frequency introduces an error on the phase of the primary field impinging on the reflector surface. This is because the antenna phase center will be coincident with the focus only at one particular frequency and when displaced at other frequencies, phase error losses (PEL) due to axial defocusing increase [9]. High phase losses due to unstable phase center for an UWB system can be reduced by optimizing the positioning of the feed antenna [10]. This is even more critical for directive planar UWB feeds such as linear and exponentially tapered slot antenna.

Optimum illumination of the reflector is achieved when the power radiated by the feed antenna is 10 dB less at the edges than its maximum at the center. Thus, 10 dB beamwidth is mostly used to determine focus to diameter ratio (f/D) of the system. If the reflector is fed with an UWB antenna, 10 dB beamwidth would change within the operation band. At high frequencies of the band it gets smaller. Fixed f/D chosen at a specific frequency in the band will result as the spillover and amplitude taper losses at the other frequencies of the band. The choice of f/D for the UWB reflector will result as high spillover loss at low frequencies if f/D is chosen using the 10 dB beamwidth of the higher frequencies. Similarly, high amplitude taper loss is resulted with the usage of f/D determined at low frequencies for the dish. For a wide band reflector system, the losses due to varying phase, amplitude and spillover can disrupt the efficiency of the system. These losses should be accounted for different frequencies within the band and a compromise should be made for the placement of the feed antenna to reduce the total loss as much as possible.

In this work, additional losses that occur in UWB

Submitted On: June 12, 2015
Accepted On: November 8, 2015

reflector systems are discussed and demonstrated with a directive UWB antenna fed reflector. UWB feed antenna is measured and simulated by a commercial software based on the finite-integration (FIT) method. A code using the measured pattern of the feed antenna is written. The constant phase surfaces on the feed antenna are determined and phase center variation with frequency is obtained. By numeric integration of the measured feed pattern additional losses are calculated. The effect of these losses on directivity is demonstrated. In the next section, the well-known reflector loss definitions are considered for UWB reflector systems.

II. LOSSES OF A REFLECTOR IN UWB APPLICATIONS

A feed antenna at the focus of the parabolic reflector radiates energy towards the reflector, which reflects it into a narrow beam of energy. In order to have optimum performance from a reflector antenna, the feed antenna has to be matched to the parabolic reflector. The maximum gain is achieved when the reflector surface is uniformly illuminated by a feed antenna with a constant field and feed pattern should drop to zero at the edges. However, practical feed antennas have radiation patterns that drop gradually at the edges. Thus, for the feed antenna, a compromise between spillover and adequate illumination has to be made [5]. Some of the power radiated by the source cannot be intercepted by the reflector. The power that spills over the edge results as spillover loss. Spillover loss of the system can be found by using the feed pattern [1]:

$$SPL = \frac{\int_0^{2\pi}\int_{\psi_b}^{\psi_o} |E(\psi,\phi)|^2 \sin\psi \, d\psi \, d\phi}{\int_0^{2\pi}\int_0^{\pi} |E(\psi,\phi)|^2 \sin\psi \, d\psi \, d\phi}, \qquad (1)$$

$E(\psi,\phi)$ is the feed pattern and $\psi_b = 2\tan^{-1}[b/(2f)]$ where b is the central blockage radius of the feed antenna. ψ_o is the half subtended angle of the reflector and relates to f/D by $\psi_o = 2\tan^{-1}[1/(4f/D)]$. Traditionally, the reflectors are designed in a way that the power radiated by the feed antenna is 10 dB less at the edges compared to its maximum at the center of the reflector. The difference between the desired feed pattern and the actual feed radiation pattern results in illumination loss. The illumination loss consists of phase losses and amplitude taper losses. An additional requirement for optimum performance is that all the feed energy be in phase, so that it appears to be radiated from a single point at the focus. A unique phase center at the focus of the reflector would eliminate phase error losses. These losses can be evaluated from the feed pattern. The phase error loss (PEL) can be estimated with the integral of the feed pattern [1]:

$$PEL = \frac{\left|\int_0^{2\pi}\int_{\psi_b}^{\psi_o} E(\psi,\phi)\tan(\psi/2)\, d\psi \, d\phi\right|^2}{\left[\int_0^{2\pi}\int_{\psi_b}^{\psi_o} |E(\psi,\phi)|\tan(\psi/2)\, d\psi \, d\phi\right]^2}. \qquad (2)$$

Unequal phase center locations in different planes introduce phase error losses due to astigmatism. It is detected by the depth of the nulls in the E- and H-planes. Phase error loss due to astigmatism is not as severe as the losses due to axial defocusing [1].

All rays from the focus of the reflector travel the same physical distance to the aperture plane. The aperture distribution has uniform phase if the phase center is coincident with the focus. However, there is going to be a non-uniform amplitude distribution on the aperture plane. This is because the power density of the rays departing from the focus propagates spherically until it reaches to the reflector surface. The spherical wave spreads from the feed as $1/\rho$. At the surface of the reflector, the wave curvature changes to a plane wave and propagates to the aperture plane at a constant amplitude. The amplitude taper losses can be evaluated from the feed pattern by [1]:

$$ATL = \frac{\left[\int_0^{2\pi}\int_{\psi_b}^{\psi_o} |E(\psi,\phi)|\tan(\psi/2)\, d\psi \, d\phi\right]^2}{\pi\left[\tan^2(\psi_o/2) - \tan^2(\psi_b/2)\right]\int_0^{2\pi}\int_{\psi_b}^{\psi_o} |E(\psi,\phi)|^2 \sin\psi \, d\psi \, d\phi}. \qquad (3)$$

Some part of the feed energy is reflected back from the reflector surface into the feed antenna and doesn't become part of the main beam. This loss is referred to as feed blockage loss. In the expressions given by (1)-(3), losses due to the blockage of the feed antenna are also accounted in the integration of the feed pattern.

The illumination loss together with spillover loss and blockage losses determines the aperture efficiency of the reflector system. In the above expressions, the cross-polarized power radiated by the source is ignored. The cross-polarization efficiency (XOL) is given as:

$$XOL = \frac{\int_0^{2\pi}\int_0^{\pi} |E_c(\psi,\phi)|^2 \sin\psi \, d\psi \, d\phi}{\int_0^{2\pi}\int_0^{\pi} (|E_c(\psi,\phi)|^2 + |E_X(\psi,\phi)|^2)\sin\psi \, d\psi \, d\phi}, \qquad (4)$$

where E_c is the co-polarized field and E_x is the cross-

polarized field [1]. These polarizations corresponds to Ludwig's [11] third definition of cross-polarization.

If the efficiency definitions given above are used to express the directivity of the reflector system, the directivity can be given as:

$$Dir = 10\log\left[(\pi/\lambda)^2(D_r^2 - D_b^2)\right] + SPL\,(dB) + ATL\,(dB) + PEL\,(dB) + XOL\,(dB), \quad (5)$$

where D_r is the reflector diameter and D_b is the diameter of the central blockage [1].

In UWB reflector applications, the feed antenna covers a wide frequency range. Both the radiated pattern and phase center on the feed will change with frequency. Thus, the loss definitions should be considered within the operation band, and a compromise should be made to have the lowest performance degradation for the reflector system. Hereafter, the above loss definitions are considered for the wide band case.[2]

10 dB beamwidth of the feed antenna used to define f/D ratio of the reflector system for optimum illumination will decrease as the frequency increases within the band. If f/D ratio is chosen according to the beamwidth of the lowest frequency as demonstrated in Fig. 1 (a), the reflector illumination will be compatible with low frequencies. As a result, the system will have low spillover at low frequencies and high amplitude taper loss at high frequencies. Similarly, if f/D ratio is chosen with 10 dB beamwidth of the highest frequency, the reflector illumination will be compatible with high frequencies and the system will have high spillover at lower frequencies. (Fig. 1 (b)).

To determine the phase center location of a radiating element, spherical measurements of the antenna are mostly used [12]. Phase center location, which is the point on the feed where the radiation spreads spherically outward, with the phase of the signal being equal at any point on the sphere, moves with changes in the frequency. The evaluation of the feed center from the feed radiation pattern is described in [9]. In any wide band application, phase error losses are unavoidable.

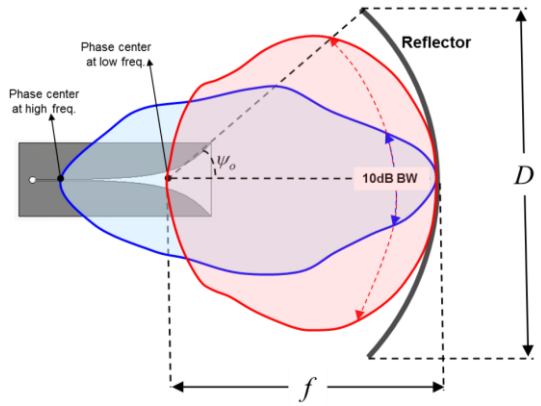

(a)

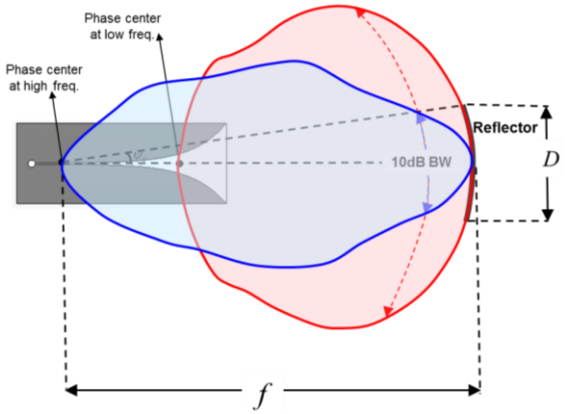

(b)

Fig. 1. Spillover and amplitude taper losses at: (a) low frequency and (b) high frequency.

Phase center variation of a directive antenna is demonstrated in Fig. 2. The blue point is the focus point of the paraboloidal reflector. With its current positioning, it would be possible to illuminate the reflector perfectly at low frequencies of the band. However, at high frequencies there will be distance between the phase center location and the focus point of the reflector. This will result in phase error losses in the system. The variation in phase center location with frequency results as axial defocusing.

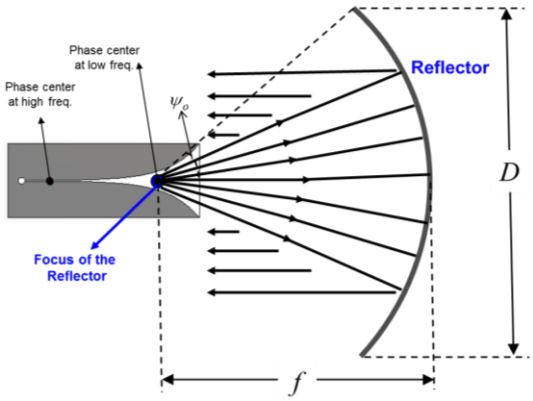

Fig. 2. Phase center variation of a directive UWB antenna at high and low frequencies of its band.

In UWB reflectors, the feed blockage loss will have different levels at different frequencies. The losses at each frequency should be considered separately. If the feed antenna is a 3-D antenna, like widely used horn feed, the blockage error is even more critical [13]. If the feed antenna is a planar one, like the Vivaldi antenna, which is a well-known reflector feed, the blockage error will be seen in one plane only since the thickness of the antenna is very small on the other plane. In Fig. 3, the blockage effect of a planar antenna is demonstrated at

high and low frequencies. In Fig. 3 (a), the reflector is fed from the phase center of a lower frequency within the band. The blockage angle is shown with blue area. In this case, blockage in E-plane is less due to wider pattern compared to the blockage of the feed antenna fed from the high frequency phase center given in Fig. 3 (b). In these two figures, the E-plane blockage is demonstrated. In Fig. 3 (c), almost zero blockage due to planar feed antenna can be observed in H-plane.

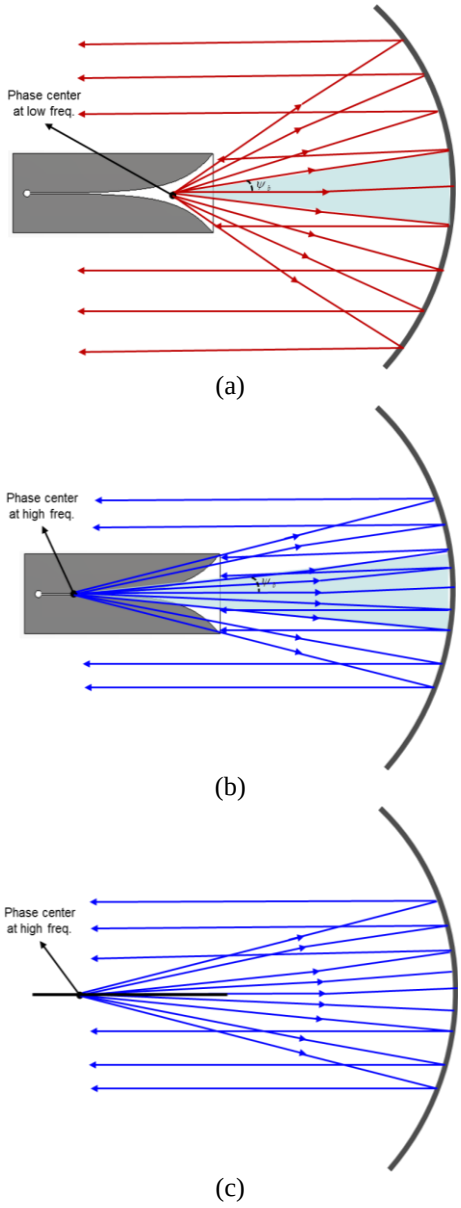

Fig. 3. Blockage demonstration for (a): E-plane fed from low frequency phase center, (b) E-plane fed from high frequency phase center, and (c) H-plane fed from high frequency phase center.

III. ADDITIONAL LOSSES OF A VIVALDI FED REFLECTOR ANTENNA

Vivaldi which is known as exponentially tapered antenna, is an end fire radiator usually supported on a thin, low ε_r substrate. Despite the completely planar geometry of Vivaldi, it can produce almost symmetric radiation patterns in the E- and H-planes. As the length of the antenna increases, its beam width narrows and the directivity increases. They are the most utilized antennas in UWB high-performance applications. They are travelling wave type antenna with a directional radiation along its aperture [14-15]. Its time domain characteristics are investigated and proved to be weakly-dispersive in [16-18].

To demonstrate the additional losses of a high-gain UWB reflector antenna, a long Vivaldi shown in Fig. 4 is used. Its dimensions are demonstrated in Fig. 4 (b). The antenna operates in the band of 2 GHz – 12 GHz (6:1 bandwidth). The length of the exponential tapering is 2.13 wavelengths at the lowest frequency and its exponential flaring is given by $S(z) = (W_{slot} / 2)\, e^{az}$, where $a = 0.018$ and $W_{slot} = 0.43mm$. A quarter wavelength open circuit stub is used for UWB matching. The dielectric constant of the dielectric material of the antenna is chosen $\varepsilon_r = 2.33$, and the thickness of the substrate is $t = 0.635mm$.

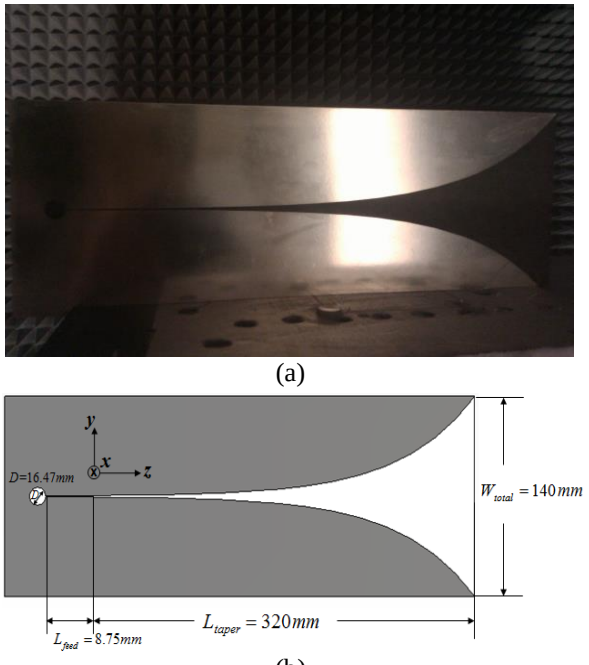

Fig. 4. (a) Vivaldi antenna in measurement setup, and (b) its dimensions.

Scattering parameters of Vivaldi antenna have been measured using an Agilent vector network analyzer, which is able to perform measurements up to 70 GHz. The matching behavior of Vivaldi has been investigated in terms of S_{11}. The transmit–receive antenna link has been characterized in terms of S_{12}. The absolute gain has been measured as a function of the frequency by comparison with reference standard gain horn. Vivaldi antenna presented in this paper is analyzed by means of the commercial code CST based on the finite-integration (FIT) method. The measured and simulated directivities of the Vivaldi antenna are given in Fig. 5.

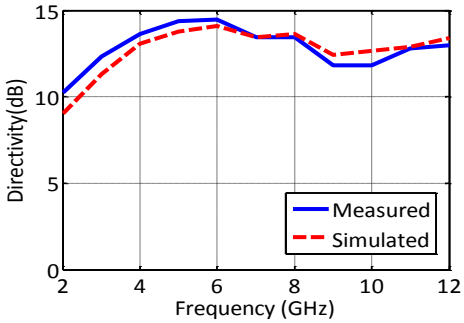

Fig. 5. Measured and simulated directivities of the Vivaldi antenna.

The Vivaldi antenna used to demonstrate UWB losses of a reflector antenna has a directive pattern over a very wide band. This is a demand for an UWB reflector feed. However, high directivity necessitates the usage of a long Vivaldi. This will result as high phase center variations on the antenna. The Vivaldi antenna given in Fig. 4 has a slot length 8.75 mm. *z*-axis starts from the end of the slot and goes along the flaring, which is 32 cm long. In Fig. 6, the phase center variation of this antenna is given. Phase centers are obtained from measurement results by detecting the locations where almost constant phase within 10 dB beamwidth is obtained on the antenna for the frequency of interest.

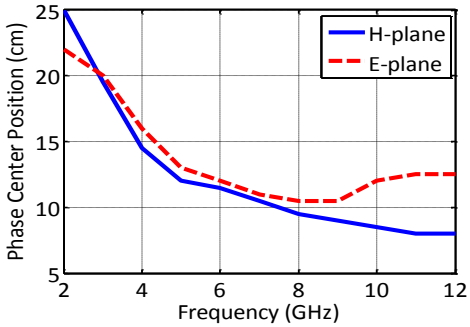

Fig. 6. Phase center positions of the Vivaldi antenna at E- and H-plane.

The phase center locations demonstrate the positions on the antenna where the antenna spreads spherically to free space with a constant phase at that specific frequency. The vertical axis of the figure demonstrates the z-axis and variations of the phase center along the flaring of the Vivaldi with frequency. At 12 GHz, where the H-plane pattern has 37° as the 10 dB beamwidth, the phase center is close to the end of the slot both for E- and H-planes. At lower frequencies, the phase center is close to the end of the antenna flaring in both planes. At 2 GHz, it is further than 22 cm from the slot. The 10 dB beamwidth at this frequency is 85°. As expected, at high frequencies, the wave departs from a location close to the slot; whereas at lower frequencies, the departure point moves towards the flaring of the antenna. The phase centers are investigated both in E- and H-planes. Similar characteristics are observed. The variation between the lowest and highest frequencies in H-plane is 17 cm, which is 6.8 wavelengths at the highest frequency. It is 9.5 cm in E-plane, which is equal to 3.8 wavelengths at 12 GHz. This distance between phase center locations at lowest and highest frequencies will cause the phase error loss due to axial defocusing. The 10 dB beamwidth in H-plane varies from 85° to 37° between 2 GHz and 12 GHz. Similarly, the beamwidth in E-plane varies with frequency between 90° and 60°. Thus, the reflector is designed with the feed subtended angle of 70°. This results in the focal length to reflector diameter ratio (f/D) of approximately 0.8. This f/D is determined using the beamwidth at 4 GHz. This point is chosen as the point on the feed antenna that coincides with the focus of the reflector. As defined in the second section, f/D ratio results as the spillover and amplitude taper losses. Since, the observed system works, ultra-wide band lower losses are expected at the frequency where the f/D is chosen and the location where the feed antenna is mounted. In Fig. 7, the losses for this case are demonstrated. By human based optimization, this location is determined as the location which gives the lowest total loss. The losses are obtained from the integration of the feed pattern. Since the focus is at the phase center of 4 GHz, lower PEL is seen at that frequency. Also, the reflector is designed according to the 10 dB beamwidth of that frequency. Thus, lower spillover can be observed in both H- and E-planes. In Fig. 8, the directivity of an ideal reflector is given with the black solid line. The reduction effect of the losses in directivity is demonstrated. The curves of this figure are obtained by using Eq. (5), which shows the effects of losses on directivity. The blue line shows the directivity in H-plane fed by Vivaldi from the focus at the phase center at 4 GHz. Due to lower blockage error in this plane, lower loss is observed; especially at frequencies close to 4 GHz. Since blockage is less in H-plane (see Fig. 3 (c)), it is expected to see higher directivity at H-plane around 4 GHz.

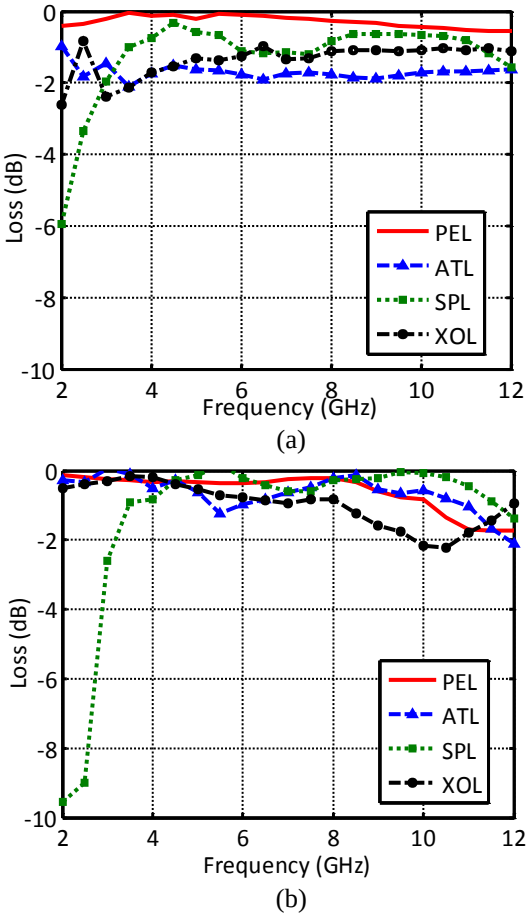

Fig. 7. Losses of the Vivaldi fed reflector antenna: (a) E-plane and (b) H-plane.

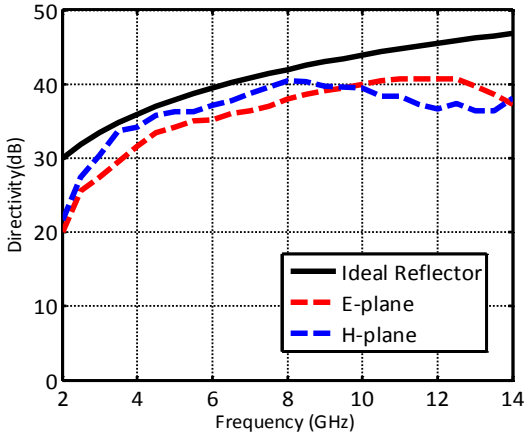

Fig. 8. Directivity of the reflector system.

IV. CONCLUSION

In reflector applications, it is desirable to have a single feed that covers the entire frequency band of operation with a symmetric, directive pattern, dual-linear polarization, and frequency invariant phase center and radiation pattern [13]. However, when an UWB reflector is discussed, phase center and radiation pattern variation with frequency is guaranteed. These variations with frequency result as phase error loss, spillover loss, amplitude taper loss and blockage error in the reflector system. Since these losses are unavoidable, the effects of them on the reflector system should be analyzed to have knowledge on the performance of the system. In this work, additional losses that occur in UWB reflector systems are discussed and demonstrated with a Vivaldi fed reflector. By using the measured pattern of the feed antenna, the constant phase surfaces on the feed antenna are determined and phase center variation with frequency is obtained. By numeric integration of the measured feed pattern, additional losses are calculated. The effect of these losses on directivity is demonstrated.

REFERENCES

[1] T. A. Milligan, *Modern Antenna Design*, Wiley-IEEE Press, 2005.

[2] W. V. Capellen, "Efficiency and sensitivity definitions for reflector antennas in radio-astronomy," *SKADS MCCT Technical Workshop*, Dwingeloo, The Netherlands, Nov. 26-30, 2007.

[3] C. A. Balanis, *Antenna Theory Analysis and Design*, 3rd edition, Wiley-Interscience, 2005.

[4] P. S. Kildal, E. Olsen, and J. A. Aas, "Losses, sidelobes, and cross polarization caused by feed-support struts in reflector antennas: design curves," *IEEE Trans. Antennas Propagat.*, vol. 36, no. 2, pp. 182-190, Feb. 1988.

[5] P. Wade, *Parabolic Dish Antennas*, in the W1GHz Online Microwave Antennas Book, Ch. 11, 1998. [Online Available: http://www.qsl.net/n1bwt/chap11.pdf].

[6] U. Schwarz, F. Thiel, F. Seifert, R. Stephan, and M. A. Hein, "Ultra-wide band antennas for magnetic resonance imaging navigator techniques," *IEEE Trans. Antennas Propagat.*, vol. 58, no. 6, pp. 2107-2112, June 2010.

[7] N. Chahat, M. Zhadobov, R. Sauleau, and K. Ito, "A compact UWB antenna for on-body applications," *IEEE Trans. Antennas Propagat.*, vol. 59, no. 4, pp. 1123-1131, Apr. 2011.

[8] A. Ardenne, B. Smolders, and G. Hampson, "Active adaptive antennas for radio astronomy; results of the initial R&D program toward the Square Kilometer Array," *Proceedings SPIE Conference 4015 Radio Telescope*, Munich, Germany, 2000.

[9] N. Turker Tokan, "Performance of Vivaldi antennas in reflector feed applications," *Applied Computational Electromagnetics Society Journal*, vol. 28, pp. 802-808, Sep. 2013.

[10] N. Turker Tokan, "Optimization of the UWB feed antenna position in reflector applications," *International Journal of Antennas and Propagation*, DOI: http://dx.doi.org/10.1155/2014/961818, 2014.

[11] A. C. Ludwig, "The definition of cross polarization," *IEEE Trans. Antennas Propagat*., vol. AP-21, pp. 116-119, Jan. 1973.
[12] P. Li and L. Jiang, "The far field transformation for the antenna modeling based on spherical electric field measurements," *Progress In Electromagnetics Research*, vol. 123, pp. 243-261, 2012.
[13] K. Lee, C. Chen, and R. Lee, "UWB dual-linear polarization dielectric horn antennas as reflector feeds," *IEEE Trans. Antennas Propagat.*, vol. 55, pp. 798-804, 2007.
[14] P. J. Gibson, "The Vivaldi aerial," *Proc. of 9th European Microwave Conference*, pp. 101-105, 1979.
[15] T. Namas and M. Hasanovic, "Ultra-wide band antipodal Vivaldi antenna for road surface scanner based on inverse scattering," *28th Annual Review of Progress in Applied Computational Electromagnetics (ACES)*, pp. 882-887, Columbus, Ohio, Apr. 2012.
[16] E. Pancera, *Strategies for Time Domain Characterization of UWB Components and Systems*, Dissertation in Universität Karlsruhe (TH) Fakultät für Elektrotechnik und Informationstechnik, Germany, 2009.
[17] A. Mehdipour, K. Mohammadpour-Aghdam, and R. Faraji-Dana, "Complete dispersion analysis of Vivaldi antenna for ultra-wide band applications," *Progress In Electromagnetics Research*, vol. 77, pp. 85-96, 2007.
[18] E. Pancera, T. Zwick, and W. Wiesbeck, "Spherical fidelity patterns of UWB antennas," *IEEE Trans. Antennas Propag.*, vol. 59, pp. 2111-2119, 2011.

Hazel Kara was born in Zonguldak, Turkey. She received her B.Sc. degree in Electronics and Communication Engineering from Yıldız Technical University, in 2015. She is currently working on a Master's of Science in Communication Engineering at Yıldız Technical University. Her research interests include wideband antennas, microwave devices and reflector systems.

Nurhan Turker Tokan received her B.Sc. degree in Electronics and Communications Engineering from Kocaeli University in 2002 and her M.Sc. and Ph.D. degrees in Communication Engineering from Yıldız Technical University (YTU), Istanbul, Turkey, in 2004 and 2009, respectively. From May 2003 to May 2009, she worked as a Research Assistant in the Electromagnetic Fields and Microwave Technique Section of the Electronics and Communications Engineering Department of YTU, Istanbul, Turkey. Between May 2009 and April 2015, she worked as an Assistant Professor in the Electronics and Communications Engineering Department of YTU. Since April 2015, she has been working as an Associate Professor at the same department. From October 2011 to October 2012, she was Postdoctoral Researcher in the EEMCS Department of Delft University of Technology, Delft, Netherlands. From October 2012 to May 2013, she was a Postdoctoral Fellow supported by European Science Foundation at the Institute of Electronics and Telecommunications (IETR), University of Rennes 1, Rennes, France. She is the author or co-author of more than 30 papers published in peer-reviewed international journals and conference proceedings. Her current research interests are analysis and design of antennas with emphasis on dielectric lens antennas and wideband antennas, microwave circuits and intelligent systems.

Dual-Band 4-Way Wilkinson Power Divider Based on Improved Simplified Composite Right and Left Handed Transmission Lines

Hemn Younesiraad and Mohammad Bemani

Electrical and Computer Department
University of Tabriz, Tabriz, Iran
hemn64@gmail.com, bemani@tabrizu.ac.ir

Abstract ─ In this paper, by using improved simplified composite right and left handed transmission lines (I-S-CRLH-TL), a novel 4-way parallel Wilkinson power divider (WPD) is presented. The proposed WPD exhibits the benefits of excellent isolation and equal power split between output ports in the dual frequency band. Also, the dual-band nature of this divider, low cost and easy integration with printed circuits and printed antennas in a compact size makes this device a very good candidate for feeding dual-band antennas and microwave devices. The proposed divider is designed and fabricated on a low cost substrate with permittivity of 4.4 and thickness of 0.79 mm to work at two arbitrary frequency bands of 0.95 GHz and 2.43 GHz. There is a good agreement between simulated and measured results in all cases. The design concept of this paper can be easily extended to another type of dual-band microwave components.

Index Terms ─ Dual-band, metamaterial, Wilkinson power divider.

I. INTRODUCTION

Wilkinson power dividers (WPDs) are important and indispensable part of microwave circuits including filters, phase shifters and antenna arrays [1]-[4]. It is known that, traditional WPDs are implemented with quarter wave transmission lines (TLs). But it is clear that these WPDs exhibit degrees of limitation such as relatively narrow band and cannot satisfy the flexible multiband applications. Nowadays, due to the requirement of dual-band microwave or wireless communication systems, various techniques have been used to design multiband components which can provide a device to simultaneously use different frequency band [1]-[10]. One of these components is Wilkinson power divider (WPD). Recently, many efforts have been used to design dual-band and multiband WPDs [1], [4]-[8]. On the other hand, in the last decades, while a lot of works have been reported about designing of dual-band and multiband WPDs with two output ports, not much work have been reported on dual-band WPDs with more output ports. The 4-way dividers in [11,12] are based on conventional transmission lines and work only around a single frequency band. In [13], a 4-way divider was presented based on negative reflective index transmission lines (NRI-TL structures), but this divider is a single band series divider. Also, in [14] by using CRLH-TLs structures, a dual-band 4-way series power divider was presented with low isolation characteristics and poor equal power split.

On the other hand, recently a novel type of metamaterial transmission line has been introduced called simplified composite right and left handed (S-CRLH) transmission line [15,16]. In [16], S-CRLH-TL has been introduced for realizing dual-band applications. It should be emphasized that, the idea of S-CRLH-TL is superior since the structures can be easily designed and engineered to realize the required phase shifters without using the series capacitors. Also, as we know, the implementation of series capacitors (such as integrated capacitors) is difficult, because these capacitors have inherent high frequency parasitic resonance and also cannot achieve larger capacitors. On the other hand, the lumped capacitors may cause great insertion loss along the main transmission line and produce extra and unwanted parasitic effects.

In this paper, based on I-S-CRLH-TL structures, a novel dual-band 4-way parallel power divider is designed and fabricated at two arbitrary frequency bands of $f_1 = 0.95$ GHz (UHF) and $f_2 = 2.4$ GHz (ISM). These two frequency bands are used in radio frequency identification (RFID) technology. However, it should be emphasized that the design procedure and design concept of this paper can be applied to any type of microwave devices. The proposed divider presents excellent isolation and equal power split between output ports in the pass-band. The organization of this paper is as follows: Section II describes theoretical analysis and design methodology leading to dual-band S-CRLH transmission lines. Section III introduces a dual-band 4-way parallel WPD. The simulated and experimental results are discussed in Section III. Finally conclusions

Submitted On: June 14, 2015
Accepted On: November 8, 2015

are made in Section IV.

II. DESIGN THEORY

Figure 1 depicts the unit cell of S-CRLH-TL structure. In Fig. 1, L_R, L_L, C_R and d are series inductance, parallel inductance, parallel capacitance and electrical length of the S-CRLH-TL unit cell, respectively.

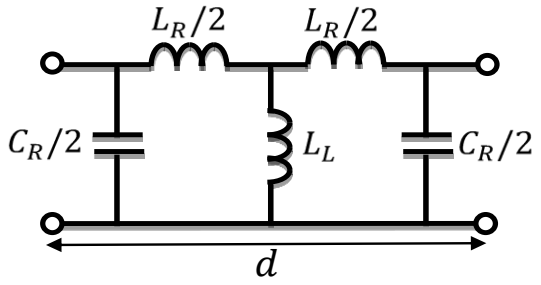

Fig. 1. Circuit model of S-CRLH-TL unit cell.

As can be seen in Fig. 1, unlike the conventional CRLH-TLs, in the S-CRLH-TL structures the series capacitance is removed. Based on Bloch theory, the characteristic impedance and dispersion relation are given by [17]:

$$\gamma(\omega) = \frac{1}{d} cosh^{-1}(A), \quad (1a)$$

$$Z_B(\omega) = \frac{BZ_0}{\sqrt{A^2-1}}, \quad (1b)$$

where ω and $Z_B(\omega)$ are angular frequency and Bloch impedance, respectively. Also, A and B are the elements of the T matrix of the unit cell and can be written as:

$$A = \frac{4L_R+8L_L-4\omega^2 L_R C_R L_L-\omega^2 L_R^2 C_R}{8L_L}, \quad (2a)$$

$$B = \frac{j\omega L_R(4L_L+L_R)}{4L_L}. \quad (2b)$$

Furthermore, in Equation (1), $\gamma = \alpha_s + j\beta_s$, where α_s and β_s are attenuation constant and phase shift constant, respectively. In addition, as we know in the propagation pass-band $\alpha_s = 0$, therefore, Equation (1) can be rewritten as:

$$\beta_s d = \cos^{-1}(A). \quad (3)$$

The above equation shows the characteristic nonlinear phase response of S-CRLH-TLs; therefore, the phase response of these structures can be engineered to produce the desired phase shifts. In this paper, in order to design dual band TLs, a topology of S-CRLH-TLs is considered as shown in Fig. 2, which is known as I-S-CRLH-TLs. This transmission line is composed of two conventional S-CRLH-TL unit cells with input and output conventional TLs at the lateral terminals. It is clear that the total phase shift characteristic of this structure is the superposition of the conventional transmission lines and conventional S-CRLH-TLs. Therefore, for given two frequencies of f_1 and f_2 and two phase shifts of φ_1 and φ_2, the following equations should be satisfied:

$$\varphi_t(f_1) = 2\big(\varphi_s(f_1) + \varphi_{C-TL}(f_1)\big) = \varphi_1, \quad (4a)$$

$$\varphi_t(f_2) = 2\big(\varphi_s(f_2) + \varphi_{C-TL}(f_2)\big) = \varphi_2, \quad (4b)$$

where φ_t is the total phase shift of the proposed structure. Also, φ_s and φ_{C-TL} are the phase shifts of the conventional S-CRLH-TLs and conventional transmission lines, respectively. It should be noted that, based on Equation (3), we can write $\varphi_s = \beta_s d \cos^{-1}(A)$. Moreover, the phase shift of the conventional transmission lines are given by $\varphi_{C-TL} = \beta_{C-TL} l_{C-TL}$. If $\beta_s d = \varphi_{is}$ (i=1,2), then $A = \cos\varphi_{is}$ and therefore, Equation (3) leads to the following equations:

$$\cos\varphi_{1s} = \frac{4L_R+8L_L-4\omega_1^2 L_R C_R L_L-\omega_1^2 L_R^2 C_R}{8L_L}, \quad (5a)$$

$$\cos\varphi_{2s} = \frac{4L_R+8L_L-4\omega_2^2 L_R C_R L_L-\omega_2^2 L_R^2 C_R}{8L_L}. \quad (5b)$$

Solving the above equations for ω_1 and ω_2, it reveals that:

$$\omega_1 = \sqrt{\frac{L_R+\frac{2L_L}{L_R}(1-\cos\varphi_{1s})}{C_R\left(1+\frac{L_R}{4}\right)}}, \quad (6a)$$

$$\omega_2 = \sqrt{\frac{L_R+\frac{2L_L}{L_R}(1-\cos\varphi_{2s})}{C_R\left(1+\frac{L_R}{4}\right)}}. \quad (6b)$$

Now, if $Z_B(\omega) = mZ_0$ (m is an arbitrary constant), by using the Equations (1b) and (2) we can write:

$$\frac{j\omega_1 L_R(4L_L+8L_R)}{4L_L} = m\sqrt{cos^2\varphi_{1s}-1}, \quad (7a)$$

$$\frac{j\omega_2 L_R(4L_L+8L_R)}{4L_L} = m\sqrt{cos^2\varphi_{2s}-1}. \quad (7b)$$

Therefore, solving the Equations (5a)-(7b) for given parameter of ω_1, ω_2, φ_{1s} and φ_{2s}, the elements of the proposed structure can be realized. As an example of application, a dual-band stub with $Z_{stub} = 70\,\Omega$ was designed in order to produce phase shifts of $\varphi_1 = +90^0$ and $\varphi_2 = -90^0$ at $f_1 = 0.9\,GHz$ and $f_2 = 2.4\,GHz$, and $m = \sqrt{2}$, respectively. This stub is designed on FR4 substrate with thickness (h) of 0.79 mm, relative permittivity of $\varepsilon_r = 4.4$ and loss tangent of 0.019. Therefore, from Equation (4)-(7), it reveals that $L_L = 11.99\,nH$, $L_R = 2.24\,nH$, $C_R = 2.55\,pF$ and $l_{C-TL} = 14.73\,mm$. The proposed TL were designed in the Agilent Design Systems (ADS) circuit simulator with source termination of $Z_{source} = 50\,\Omega$ and load termination of $Z_{load} = 100\,\Omega$.

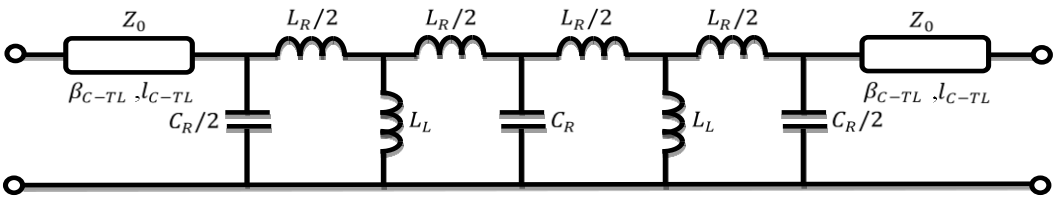

Fig. 2. Circuit model of I-S-CRLH-TLs structure.

Figure 3 displays the S-parameter characteristics of this line. Therefore, these results are distinct proof of the dual-band operation of the designed I-S-CRLH-TL stub.

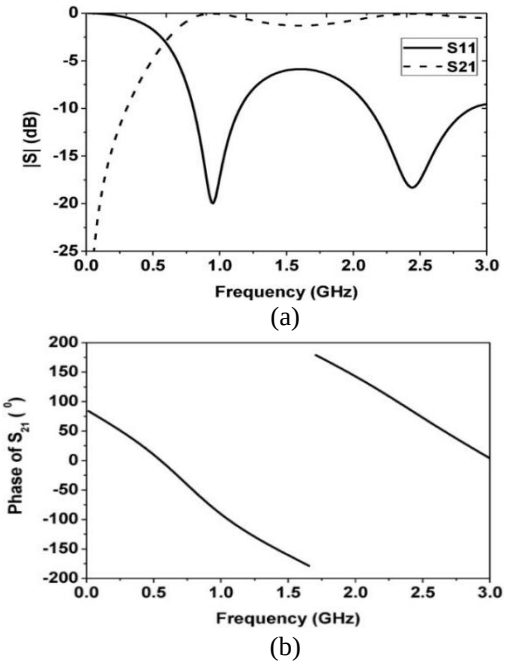

Fig. 3. S-parameter characteristics of the designed I-S-CRLH TLs: (a) return loss and insertion loss, and (b) phase of the insertion loss.

III. DESIGN OF DUAL-BAND WILKINSON POWER DIVIDER

As we know, the classical 2-way WPD consist of two quarter wavelength branch lines with characteristic impedance of $\sqrt{2}Z_o$ and isolation resistor of $2Z_0$, where Z_0 is characteristic impedance of conventional TLs. In order to design 4-way WPD, a 2-way WPD is cascaded with two similar structures at the output ports. Therefore, in order to design a 4-way WPD, six I-S-CRLH transmission lines are required. These lines are designed to produce phase shifts of $\varphi_1 = +90^0$ and $\varphi_2 = -90^0$ at $f_1 = 0.9\,GHz$, and $f_2 = 2.4\,GHz$, respectively. In addition, as we know, the synthesis method for implementation of I-S-CRLH-TLs using microstrip technology has been introduced in [9] and [10], where L_L is implemented by microstrip short circuited stubs and L_R and C_R are realized using microstrip high and low impedance short line elements, respectively. In this proposed structure, two unit cells are shared using a via at top of the structure. This structure is shown in Fig. 4. The proposed 4-way WPD is made up of six dual-band stubs in a square shape configuration. The impedance of these stubs are set to be 70.7 Ω at the design frequencies of $f_1 = 0.915\,GHz$ and $f_2 = 2.440\,GHz$.

The dimensions of these stubs are summarized in Table 1. Finally, the novel 4-way WPD is designed and fabricated. Figure 5 exhibits the fabricated prototype of the proposed divider. Figure 6 exhibits the measured and simulated magnitude of S_{11} for the designed 4-way parallel WPD. As can be seen in this figure, the designed divider can fully cover the desired frequency bands. Moreover, the transmission characteristics to each of the output ports are displayed in Fig. 7. These results demonstrate that the proposed dual-band 4-way WPD splits the input power between output ports equally. The small difference between measured and simulated results can be attributed to small tolerance in substrate permittivity (FR4, $\varepsilon_r = 4.4 \pm 0.2$). Also, the difference between measured and simulated results at high frequency is caused by the extra parasitic capacitance from the input and output ports which were not fully considered during the simulations.

Table 2 compares the physical characteristics and electrical performances of the proposed 4-way WPD with another 4 way power divider presented in [14]. It can be concluded from this table that the designed power divider in this paper provides better input and output return losses, better equal power split and isolation between outputs in both the frequency bands in comparison to [14]. On the other hand, the proposed divider in this paper is fully planar, while the divider presented in [14] is based on the lumped elements.

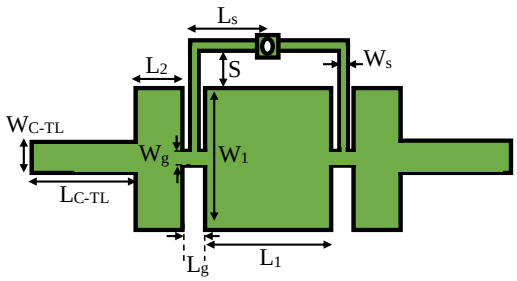

Fig. 4. Symmetrical structure of I-S-CRLH transmission line structure.

Table 1: Dimensions of the dual-band I-S-CRLH-TL structure (Unit: Millimeters)

W_1	L_1	L_1	W_g	L_g
12.41	8.72	4.36	0.85	1.30
L_s	W_s	S	W_{C-TL}	W_{C-TL}
0.45	5.24	0.71	1.38	8.1

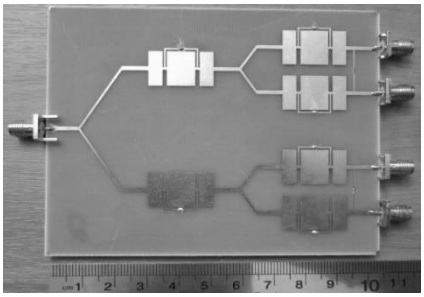

Fig. 5. Fabricated prototype of the proposed dual-band parallel 4-way WPD.

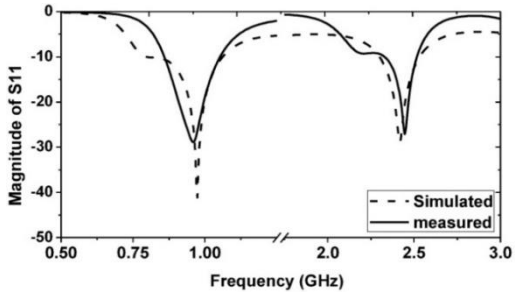

Fig. 6. Magnitude of S_{11} for the proposed dual-band 4-way WPD.

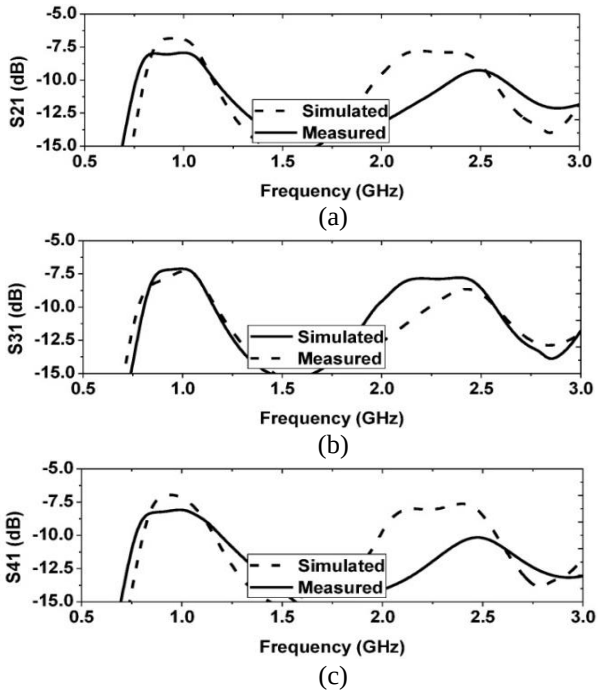

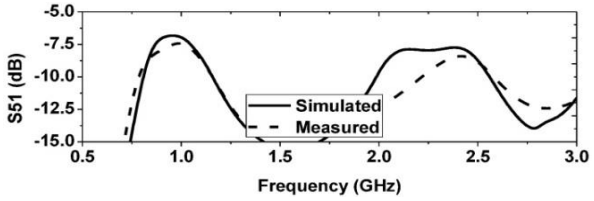

Fig. 7. Transmission characteristics to each of the output ports: (a) S_{21}, (b) S_{31}, (c) S_{41}, and (d) S_{51}.

Table 2: The comparison of the physical parameters and measured performances between proposed 4-way WPD and designed 4-way divider of [14]

			This Work	[14]
Resonance Frequency (GHz)		f_1	0.91	0.91
		f_2	2.44	2.44
Substrate		ε_r	4.4	4.4
		h	0.79	0.79
Circuit Size (λ)		f_1	0.26×0.29	0.23×0.20
		f_2	0.69×0.77	0.62×0.57
Return Loss S_{11} (dB)		f_1	28.8	17.1
		f_2	27.7	22.3
Return Loss S_{22} (dB)		f_1	25.1	15.1
		f_2	23.4	20.4
Return Loss S_{33} (dB)		f_1	24.5	16.5
		f_2	22.7	21.4
Return Loss S_{44} (dB)		f_1	30.4	29.4
		f_2	27.6	23.5
Return Loss S_{55} (dB)		f_1	25.5	23.9
		f_2	24.1	19.9
Insertion Loss (dB)	S_{21}	f_1	7.4	6.8
		f_2	7.7	7.9
	S_{31}	f_1	7.5	6.6
		f_2	8.0	7.7
	S_{41}	f_1	7.4	7.1
		f_2	10.1	7.6
	S_{51}	f_1	7.5	7.2
		f_2	7.9	8.3
Isolation (dB)	S_{32}	f_1	27.3	22.9
		f_2	31.5	35.3
	S_{42}	f_1	34.7	22.4
		f_2	37.4	34.1
	S_{52}	f_1	33.5	21.2
		f_2	35.3	44.7
	S_{43}	f_1	31.5	19.1
		f_2	29.4	26.1
	S_{53}	f_1	32.7	21.2
		f_2	33.5	30.5
	S_{54}	f_1	29.5	22.7
		f_2	28.2	27.8

IV. CONCLUSIONS

In this paper, we presented a novel methodology for designing dual-band 4-way parallel Wilkinson divider. The proposed divider is designed and fabricated on an inexpensive FR4 substrate. The results of the measurements verified the operation of the designed dual-band divider. The dual-band nature of this 4-way divider, close space between output ports and easy integration with planar devices make it a very good candidate for feeding many analog circuits, such as antenna arrays.

REFRENCES

[1] M. Bemani, S. Nikmehr, and S. Hosseinzadeh, "Arbitrary dual-band unequal Wilkinson power divider based on negative refractive index transmission lines," *Int. J. Electron. Commun. (AEÜ)*, vol. 67, pp. 382-386, 2012.

[2] L. Xi, L. Yang, S.-X. Gong, and Y.-J. Yang, "A dual-band Wilkinson power divider with bandwidth enhancement," *Microw. Opt. Technol. Lett*., vol. 51, no. 9, pp. 2043-2046, 2009.

[3] M. Bemani and S. Nikmehr, "Dual-band N-Way series power divider using CRLH-TL metamaterials with application in feeding dual-band linear broadside array antenna with reduced beam squinting," *IEEE Trans. Circuits Syst. I*, Reg. Papers, vol. 60, no. 12, pp. 3239-3246, Dec. 2013.

[4] M. Bemani, S. Nikmehr, and H.-R. Takfallah, "Dual-band N-Way series power divider using CRLH-TL metamaterials with application in feeding dual-band linear broadside array antenna with reduced beam squinting," *IET Microwaves, Antennas & Propagation*, vol. 61, no. 3, pp. 1223-1233, 2014.

[5] H. L. Zhang, B.-J. Hu, and X.-Y. Zhang, "Compact equal and unequal dual-frequency power divider based on composite right/left-handed transmission lines," *IEEE Trans. Ind. Electron*., vol. 59, no. 9, pp. 3464-3472, Sept. 2012.

[6] Y. Wu, Y. Liu, and Q. Xue, "An analytical approach for a novel coupled-line dual-band Wilkinson power divider," *IEEE Trans. Microwave Theory Tech.*, vol. 59, no. 2, pp. 286-294, Feb. 2011.

[7] J.-C. Li, J.-C. Nan, X.-Y. Shan, and Q.-F. Yan, "A novel modified dual-frequency Wilkinson power divider with open stubs and optional/isolation," *J. Electromagnetic Waves Appl*., vol. 24, no. 16, pp. 2223-35, 2010.

[8] B. Li, X. Wu, and N. Yang, "Dual-band equal/unequal Wilkinson power divider based on coupled-line section with short-circuited stub," *Progress in Electromagnetics Research*, vol. 111, pp. 163-178, 2011.

[9] S. Y. Yang, C. S. Cho, L. W. Lee, and J. Kim, "A novel dual-band balun using branch-line with open stubs," *Microw. Opt. Thecnol. Lett*., vol. 52, no. 3, pp. 642-644, Mar. 2010.

[10] H. Younesiraad, M. Bemani, and S. Nikmehr, "Small multi-band rectangular dielectric resonator antennas for personal communication devices," *International Journal of Electrical and Computer Engineering (IJECE)*, vol. 4, no. 1, pp. 1-6, 2014.

[11] K.-A.-A. Shamaileh, A. Qaroot, and N. Dib, "Design of N-way power divider similar to bagley polygon divider with an even number of output ports," *Progress In Electromagnetics Research Letter C*, vol. 20, pp. 83-93, 2011.

[12] S. Kim, S. Jeon, and J. Jeong, "Compact two-way and four-way power dividers using multi-conductor coupled lines," *Microw. Wireless Compon. Lett*., vol. 21, no. 3, pp. 130-132, Mar. 2011.

[13] M.-A. Antoniades and G.-V. Eleftheriades, "A broadband series power divider using zero-degree metamaterial phase-shifting lines," *Microw. Wireless Compon. Lett*., vol. 15, no. 11, pp. 808-810, Nov. 2005.

[14] M. Bemani and S. Nikmehr, "Non-radiating arbitrary dual-band equal and unequal 1:4 series power dividers based on CRLH-TL structures," *IEEE Trans. Ind. Electron*., vol. 61, no. 3, pp. 1223-1233, 2014.

[15] T. Jang, S.-H. Hwang, Y.-S. Bang, J.-M. Kim, Y.-K. Kim, C.-W. Baek, and S. Lim, "Switchable composite right/left-handed (SCRLH) transmission line using MEMS switches," *Microw. Wireless Compon. Lett*., vol. 19, no. 12, pp. 804-806, Dec. 2009.

[16] F. Wei, Q.-Y. Wu, X.-W. Shi, and L. Chen, "Compact UWB bandpass filter with dual notched bands based on SCRLH resonator," *Microw. Wireless Compon. Lett*., vol. 21, no. 1, pp. 28-30, Jan. 2011.

[17] M. D. Pozar, *Microwave Engineering*, Third Edition, John Wiley & Sons, 2004.

Hemn Younesiraad was born in Iran in 1985. He received the B.S. and M.S. degrees in Electrical Engineering from the University of Tabriz, Tabriz, Iran, in 2010 and 2012, respectively. His research interests include antenna and radio wave propagation, metamaterial structures, dielectric resonator antennas, composite right and left-handed structures and negative refractive-index transmission lines, medical antennas.

Mohammad Bemani received the B.S. degree in Electrical Engineering from the University of KN Toosi University of Technology, Tehran, Iran, in 2007, the M.S. and the Ph.D. degrees from the University of Tabriz, Tabriz, Iran, in 2009 and 2013 in Electrical Engineering. From 2010 to 2013, he was a Teaching Assistant at the University of Tabriz, where he contributed to the design and teaching of undergraduate courses relating to electromagnetics. During the same period, he was a Research Assistant at the University of Tabriz, where he was involved in the development of microwave devices and antennas based on negative-refractive-index transmission-line (NRI-TL) metamaterials and CRLH structures. His research interests include multi-band and UWB components, reconfigurable antenna, dielectric resonator antennas, fractal antennas, composite right- and left-handed structures and negative-refractive-index transmission lines. He is currently an Assistant Professor in the Department of Electrical and Computer Engineering at the University of Tabriz, Tabriz, Iran.

Using Folded Open-Loop Ring Resonator to Design a Common-Mode Suppression and Frequency Adjustable Balun-Bandpass Filter

Chia-Mao Chen [1], Shoou-Jinn Chang [2], Jia-Chun Zheng [3], Jian-Chiun Liou [4], and Cheng-Fu Yang*[5]

[1] Department of Electrical Engineering
National Cheng Kung University, Tainan 701, Taiwan
jmchen0813@gmail.com

[2] Institute of Microelectronics and the Department of Electrical Engineering
Advanced Optoelectronic Technology Center, Center for Micro/Nano Science and Technology
National Cheng Kung University, Tainan 701, Taiwan
changsj@mail.ncku.edu.tw

[3] School of Information Engineering, Jimei University, Xiamen 361021, China.
jchzheng@jmu.edu.cn

[4] Department of Electronic Engineering
National Kaohsiung University of Applied Sciences, Kaohsiung 807, Taiwan
jcliou@kuas.edu.tw

[5]*Department of Chemical and Materials Engineering
National University of Kaohsiung, Kaohsiung 811, Taiwan
cfyang@nuk.edu.tw

Abstract ─ A compact and simple balun-bandpass filter was investigated by using a pair of half-wavelength open-loop ring resonators (OLRRs) and two microstrip lines. The balun-bandpass filter could be designed easily with a different center frequency by changing the path length of OLLRRs. The design methodology was adopted based on EM simulation to obtain these optimally designed parameters of the OLRRs, and microstrip lines and the filters were fabricated on FR4 substrate. The filters with the frequencies of 2.6 GHz and 5.2 GHz were designed to prove the characteristic of frequency adjustable and they were fabricated with the properties of wide bandwidth and low insertion loss. The balun-bandpass filters presented an excellent in-band balanced performance with common-mode rejection ratio over than 40 dB and 34 dB in the passbands of 2.6 GHz and 5.2 GHz, respectively. Good correlation was seen between simulation and measurement, and the result showed that first run pass had been achieved in the majority of our design.

Index Terms ─ Balanced impedance, balun-bandpass filter, frequency adjustable, open-loop ring resonators (OLRRs).

I. INTRODUCTION

As compared with conventional single-ended circuits balanced circuit has higher immunity to the environmental noise. Therefore, many devices have been designed in balanced topologies, such as low-noise amplifiers, mixers, oscillators, power amplifiers, filters, and antennas. Baluns, which are used as an interface device, are necessary for the conversion between balanced devices and unbalanced ones. A modern communication system needs a compact and low-cost RF module; thus, a device with multifunction is desired. The balun diplexer or filter are such devices that they are not only with a filtering function, but they are also a balun converting between balanced singles and unbalanced ones. Recently, several methods have been developed to design the balun filters [1-6]. For multi-service and multi-band communication systems, the diplexer is an essential component that is built by two bandpass filters (BPFs) with different passband frequencies [7-9].

In the present study, a generalized methodology for designing a novel and simple single passband balun BPF was investigated. The low-loss balun BPF was designed by using a folded open-loop ring resonators

Submitted On: June 24, 2015
Accepted On: December 6, 2015

(OLRRs) with equal physical dimensions to couple two microstrip lines, as Fig. 1 shows. The OLRRs were placed between two microstrip lines and had a perimeter of about a half wavelength of the designed resonant frequency. The OLRRs had its maximum electric field density near the open ends of the line and had its maximum magnetic field density around the center valley of the microstrip line. The resonant frequency was adjustable via the length of the OLRRs to provide a high-performance passband response. We would show that a compact microstrip balun filter was designed with high isolation and CM suppression. Based on the proposed idea, two filters with the central frequencies of 2.6 GHz and 5.2 GHz for WLAN and WiMAX applications were implemented by changing the different lengths of OLRRs. Finally, we fabricated two high-performance balun BPFs on FR4 substrates, and the predicted results were well confirmed by the measured results. We would show that the proposed balun BPFs had low insertion loss, a wide bandwidth, transmission zeros, and simple structure, and no extra circuit was needed to suppress the harmonic, respectively.

II. DESIGN METHODOLOGY

The balun BPF with central frequency of 2.6 GHz for LTE band system was first designed to prove the proposed idea accomplished by using OLRRs and the discriminating coupling technique [10-13]. When the discriminating coupling technology is used, the second harmonics of coupled-line BPFs are rejected without requiring any extra circuit and degrading in-band performance and the effect of common-mode suppression will be achieved [9]. The coupled structures resulted from different orientations of a pair of open-loop ring resonators (OLRRs) and from the microstrip lines, which were separated by a spacing S_{OLRR}, as Fig. 1 shows. Each of the OLRRs essentially acted as a folded half-wavelength resonator. Any coupling in those structures was the proximity coupling; basically, the coupling was formed through fringe fields. The nature and the extent of the fringe fields determined the nature and the strength of the coupling effect. At the resonance of fundamental mode, each of the OLRRs had the maximum electric field density at the side with an open gap (g_{OLRR}) and the maximum magnetic field density at the opposite side. Therefore, the electric coupling could be obtained if the open sides of two coupled resonators were proximately placed.

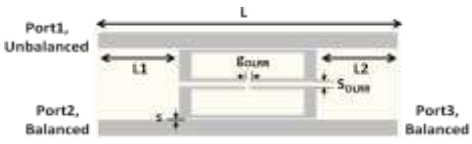

Fig. 1. Proposed balun-bandpass filter (BPF) based on OLRRs.

To obtain the maximum magnetic coupling, the center valley of the OLRRs should be positioned in the proper location along the microstrip lines at which the maximum magnetic field intensity existed. For the transverse electromagnetic (TEM) field structure, both the electric and magnetic field vectors lied in the transverse plane, which was perpendicular to the uniform propagation axis. Under the assumptions of the TEM mode of propagation and a lossless line, the fields $\vec{E}$ and $\vec{H}$ were uniquely related to voltage and current, respectively. Based on transmission line theory, the magnitudes of voltage and current on the microstrip lines could be expressed in terms of the incident wave and the reflection coefficient for an open-circuited line as:

$$|V(z)| = \left|V_0^+\right|\left|1+e^{j(\theta-2\beta l)}\right|, \quad (1)$$

$$|I(z)| = \frac{\left|V_0^+\right|}{Z_0}\left|1-e^{j(\theta-2\beta l)}\right|, \quad (2)$$

where $l = -z$ is measured away from the load at $z = 0$, and θ is the phase of the reflection coefficient. When θ-2 βd has a magnitude of zero or any multiple of 2π radian, voltage in (1) is at its maximum magnitude and current in (2) is at its minimum magnitude, respectively. Figure 2 depicts the normalized voltage/current distributions of the open-ended transmission lines. At a distance of a quarter wavelength from the receiving end, the voltage becomes zero while the current is at its maximum. If the line has a value of half wavelength, the current distribution near the center of the transmission line is at its maximum, and high magnetic coupling results from a high conduction current. Once the point of I_{max} is found, the point of H_{max} can be easily determined. When odd-mode excitation is applied to balanced port, there is a voltage null at the center of the microstrip line, the voltage/current distributions are shown in Fig. 3.

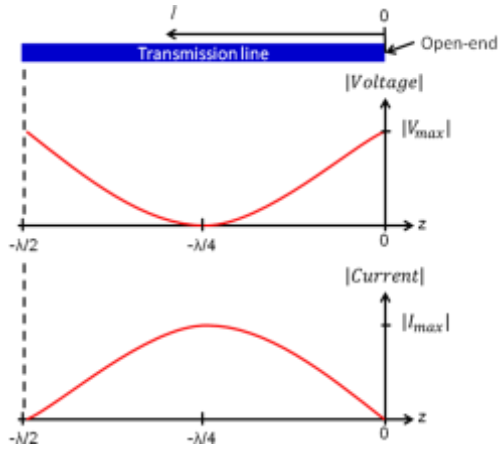

Fig. 2. Voltage and current distribution in microstrip line terminated at open end.

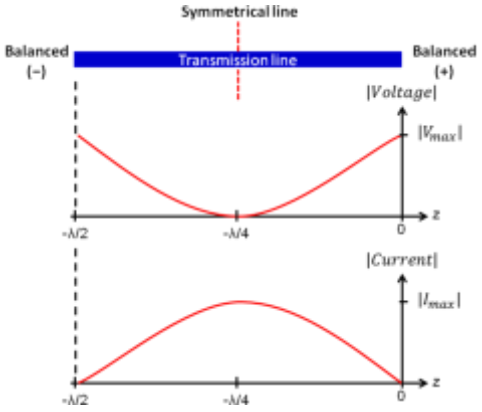

Fig. 3. Voltage and current distributions of the odd-mode.

To demonstrate the proposed structure was available, balun BPF was designed using OLRRs to couple the microstrip transmission lines. After the designed balun BPFs were simulated using the HFSS simulator with loss factors (conductor loss and dielectric loss) included in the simulated response to find the optimal parameters. In order to characterize the balance characteristic of the balun BPFs, the mode conversion between the unbalanced three-port network and the unbalanced-to-balanced two-port network was applied to obtain the single-ended to differential-mode and common-mode -parameters [7,14]:

$$S_{ss11} = S_{11}, \quad (3)$$

$$S_{ds21} = (S_{21} - S_{31})/(2)^{1/2}, \quad (4)$$

$$S_{cs21} = (S_{21} + S_{31})/(2)^{1/2}, \quad (5)$$

where S_{ss11} is the return loss at the unbalanced port 1, S_{ds21} is the two-port S-parameters from the unbalanced port 1 to differential-mode balanced port 2, and S_{cs21} is the two-port S-parameters from the unbalanced port 1 to common-mode balanced port 2, respectively.

III. DESIGN OF BALUN-BANDPASS FILTERS

The balun BPFs were designed on a pair of half-wavelength OLRRs with the center frequencies of 2.6 GHz and 5.2 GHz by changing the length of OLRRs. The simulated results shown in Fig. 4, Fig. 5 and Fig. 6 for balun BPF with center frequency of 2.6 GHz was used to prove that the proposed idea could be used to design the balun BPFs with common-mode suppression. Electric coupling was obtained if the open sides of the coupled resonators were placed near each other, and magnetic coupling was obtained if the sides with the maximum magnetic field of the coupled resonators were placed near each other. The coupling spacing *s* between the main microstrip line and OLRRs was 0.2 mm and the spacing S_{OLRR} between two resonators was 0.61 mm. Figure 4 and Fig. 5 illustrate the effect of different S_{OLRR} and *s* on the frequency response of the balun filter by full-wave simulated.

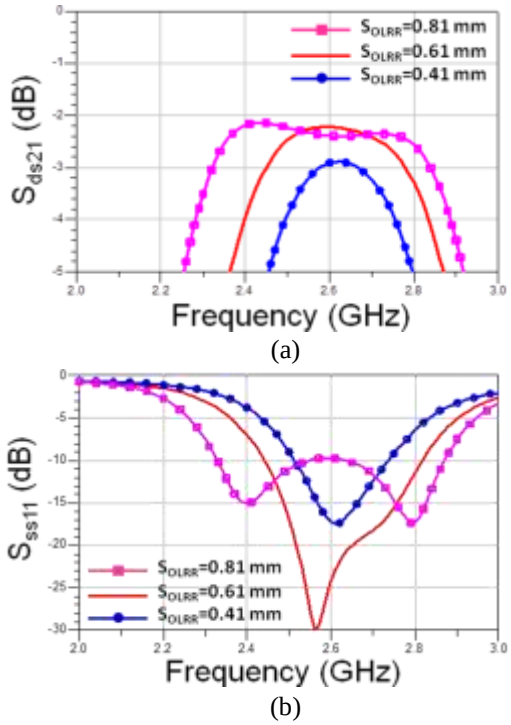

Fig. 4. Simulation results of various gap S_{OLRR} for designed balun BPF at 2.6 GHz. (a) Differential-mode response, S_{ds21}. (b) Differential-mode response, S_{ss11}.

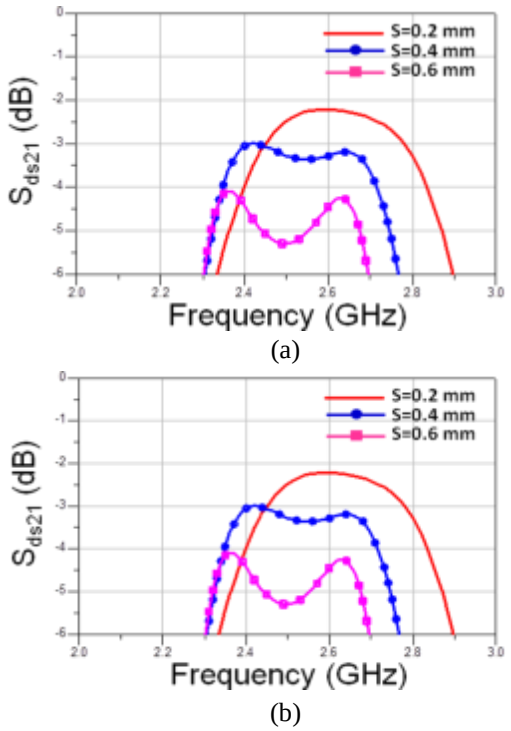

Fig. 5. Simulation results of various gap *s* for designed balun BPF at 2.6 GHz. (a) Differential-mode response, S_{ds21}. (b) Differential-mode response, S_{ss11}.

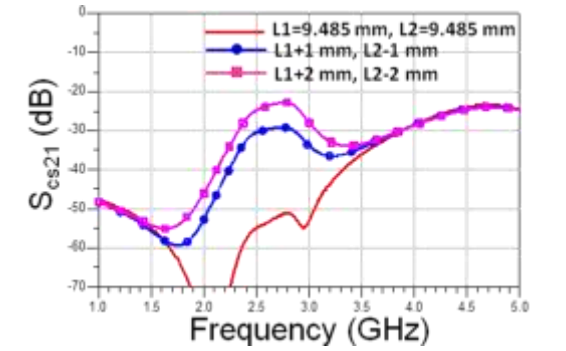

(a)

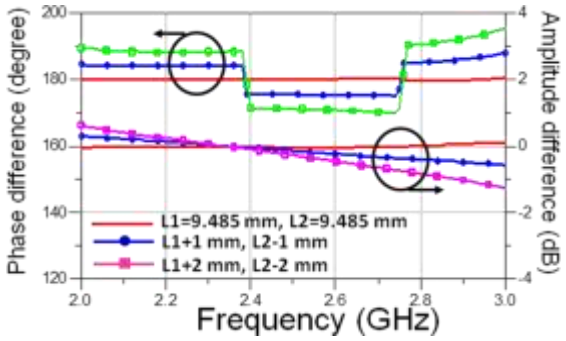

(b)

Fig. 6 Simulation results of different orientations for OLRRs for 2.6 GHz designed. (a) Common-mode response, S_{ds21}. (b) Phase/amplitude difference.

The results in Fig. 4 show that as the coupling spacing *s* decreased the two resonant peaks moved outwards and the trough in the middle deepens, which implies an increase in the coupling. The coupling of the coupled line stricture in Fig. 5 could be found from the coupling gap *s*. A smaller gap resulted in a stronger I/O coupling or a smaller external quality factor of the resonator. To further demonstrate the importance of optimal locations for balun characteristic, Fig. 6 shows a comparison of passband responses of different orientations for OLRRs. The simulation result of the designed balun BPF shows good match in input impedance, good amplitude, and phase balance between two output ports, and a wide passband, respectively.

The balun BPF using OLRRs was fabricated on an FR4 substrate with a relative permittivity of 4.4 and a thickness between the two electrodes was 1.0 mm. The dimension for the proposed 2.6 GHz balun BPF was 35 mm × 13.23 mm, as shown in Fig. 7 (a), and the photograph of the fabricated balun BPF is shown in Fig. 7 (b). The dimension for the proposed 5.2 GHz balun BPF was 17 mm × 13.43 mm, as shown in Fig. 8 (a), and the photograph of the fabricated balun BPF is shown in Fig. 8 (b). Measurements were carried out using an Agilent N5071C network analyzer.

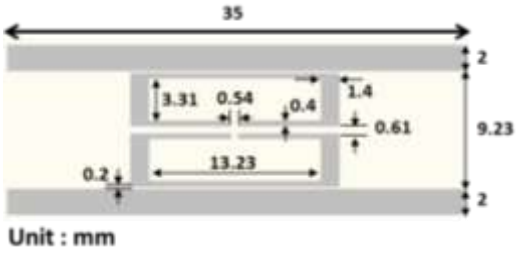

(a)

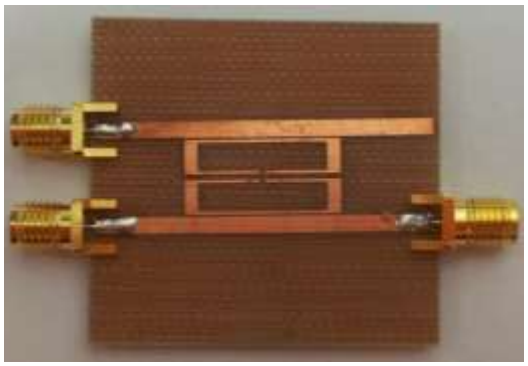

(b)

Fig. 7. (a) Layout pattern and (b) photograph of the designed balun BPF with central frequency of 2.6 GHz.

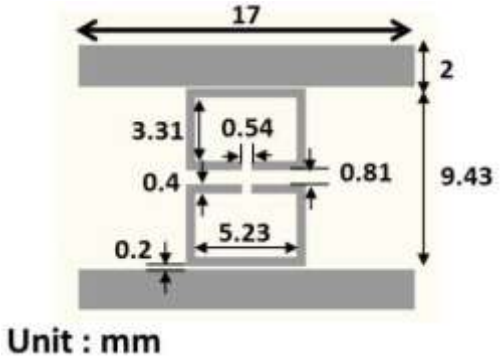

(a)

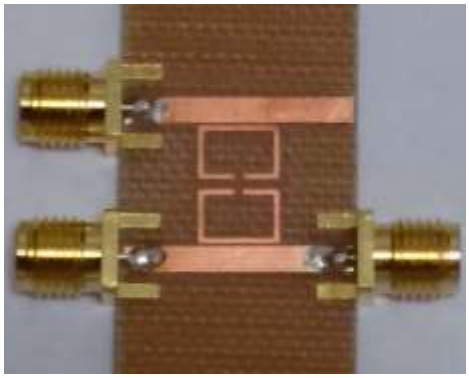

(b)

Fig. 8. (a) Layout pattern and (b) photograph of the designed balun BPF with central frequency of 5.2 GHz.

Figures 9 (a) and 9 (b) show the full-wave simulated and measured results of the S-parameters and phase/ amplitude differences for the circuit at low band. For differential-mode operation, the passband in Fig. 9 was centered at 2.6 GHz with 1 dB bandwidth of 240 MHz, or 9.23% and the minimum insertion loss including SMA connectors was measured to be 2.46 dB. Figure 9 (b) shows that the amplitude difference between S_{21} and S_{31} was below 0.2 dB and the phase difference between S_{21} and S_{31} was within 180 $\pm$ 2º for low band. Both the simulated and measured S_{cs21} values were smaller than 40 dB within operating band of the designed 2.6 GHz balun BPF, which demonstrates the effect of good common-mode suppression at the differential output port. Figures 10 (a) and 10 (b) show those for the circuit at high band, respectively. The passband in Fig. 10 was centered at 5.44 GHz with 1 dB bandwidth of 280 MHz, or 5.15% with minimum insertion loss including SMA connectors at 3.13 dB. The simulated and measured S_{cs21} values were smaller than 34 dB with in operating bands of the designed 5.2 GHz balun BPF. Figure 10 (b) show that the amplitude difference between S_{21} and S_{31} was below 0.3 dB and the phase difference between S_{21} and S_{31} was within 180 $\pm$ 3º for high band. The little differences between the simulated and measured results are mainly caused by the fabrication error (circuit etching), the SMA connector, and numerical error.

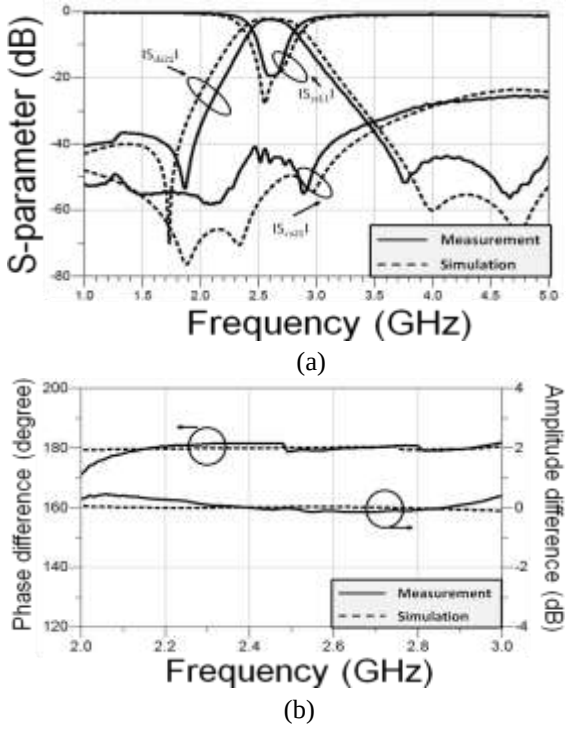

Fig. 9. Measured: (a) S-parameters and (b) phase/ amplitude difference of the designed balun BPF with central frequency of 2.6 GHz.

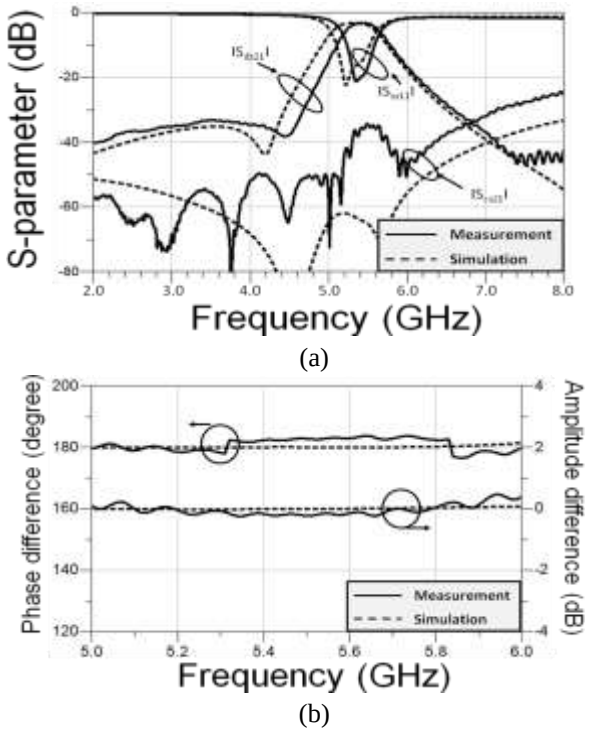

Fig. 10. Measured: (a) S-parameters and (b) phase/ amplitude difference of the designed balun BPF with central frequency of 5.2 GHz.

VI. CONCLUSION

We proposed a simple and effective method to design the microstrip balun BPFs with the properties of common-mode suppression and central frequency adjustable. The dimension for the proposed 2.6 GHz balun BPF was 35 mm × 13.23 mm and for the proposed 5.2 GHz balun BPF was 17 mm × 13.43 mm, respectively. Both the simulated and measured S_{cs21} values were smaller than 40 dB within operating band of designed 2.6 GHz balun BPF and smaller than smaller than 34 dB within operating band of designed 5.2 GHz balun BPF, which demonstrates good common-mode suppression at the differential output port. The fabricated 2.6 (5.44) GHz BPF had the properties of with 1 dB (1 dB) bandwidth of 230 MHz or 8.85% (280 MHz or 5.15%), minimum insertion loss including SMA connectors of 2.6 dB (3.13 dB), and the S_{ds21} value values were smaller than 40 dB (34 dB) within operating band. The amplitude difference between S_{21} and S_{31} was below 0.2 dB (0.3 dB) and the phase difference between S_{21} and S_{31} was within 180 $\pm$ 2º (180 $\pm$ 3º) at operating band. In this study, the designed and fabricated balun BPFs not only possessed good bandpass characteristics but they also provided great balun performance.

ACKNOWLEDGMENT

The authors acknowledge financial supports of NSC

101-2221-E-005-065, NSC 102-2622-E-390-002-CC3, and NSC 102-2221-E-390-027. This work was also supported by Fujian Nature Science Foundation under Grant No. 2013J01203 and Key Project of Science and Technology Project of Fujian Province in China under Grant No. 2014H0036.

REFERENCES

[1] M. Tamura, T. Ishizaki, and M. Hoft, "Design and analysis of vertical split ring resonator and its application to unbalanced-balanced filter," *IEEE Trans. Microw. Theory Tech*., vol. 58, no. 1, pp. 157-164, 2010.

[2] L. K. Yeng and K. L. Wu, "An LTCC balanced-to-unbalanced extracted-pole bandpass filter with complex load," *IEEE Trans. Microw. Theory Tech*., vol. 54, no. 4, pp. 1512-1518, 2006.

[3] E. Y. Jung and H. Y. Hwang, "A balun-BPF using a dual mode ring resonator," *IEEE Microw. Wireless Compon. Lett*., vol. 17, no. 9, pp. 652-654, 2007.

[4] S. J. Kang and H. Y. Hwang, "Ring-balun-bandpass filter with harmonic suppression," *IET Microw. Antennas Propag*., vol. 4, no. 11, pp. 1847-1854, 2010.

[5] L. H. Zhou, H. Tang, J. X. Chen, and Z.-H. Bao, "Tunable filtering balun with enhanced stopband rejection," *Electron. Lett*., vol. 48, no. 14, 2012.

[6] G. S. Huang and C. H. Chen, "Dual-band balun bandpass filter with hybrid structure," *IEEE Microw. Wireless Compon. Lett*., vol. 21, no. 7, pp. 356-358, 2011.

[7] Q. Xue, J. Shi, and J. X. Chen, "Unbalanced-to-balanced and balanced-to-unbalanced diplexer with high selectivity and common-mode suppression," *IEEE Trans. Microw. Theory Tech*., vol. 59, no. 11, pp. 2848-2855, 2011.

[8] Z. H. Bao, J. X. Chen, E. H. Lim, and Q. Xue, "Compact microstrip diplexer with differential outputs," *Electron. Lett*., vol. 46, no. 11, pp. 766-768, 2010.

[9] Y. X. Ji and J. Xu, "Compact BPF and diplexer using capacitively loaded λ/4 shorted meander line resonator," *J. Electromagnet. Waves Appl*., vol. 28, no. 1, pp. 112-118, 2014.

[10] C. Y. Chen and C. Y. Hsu, "A simple and effective method for microstrip dual-band filters design," *IEEE Microw. Wireless Compon. Lett*., vol. 16, no. 5, pp. 246-248, May 2006.

[11] J. S. Hong, *Microstrip Filters for RF/Microwave Applications*, 2nd edition, Wiley, New York, 2011.

[12] X. Y. Zhang and Q. Xue, "Harmonic-suppressed bandpass filter based on discriminating coupling," *IEEE Microw. Wireless Compon. Lett*., vol. 19, no. 11, pp. 695-697, 2009.

[13] Y. C. Li, X. Y. Zhang, and Q. Xue, "Bandpass filter using discriminating coupling for extended out-of-band suppression," *IEEE Microw. Wireless Compon. Lett*. vol. 20, no. 7, pp. 369-371, 2010.

[14] W. R. Eisenstadt, R. Stengel, and B. M. Thompson, *Microwave Differential Circuit Design Using Mixed-Mode S-Parameters*, Boston, MA, USA, 2006.

Chia-Mao Chen was born in Kaohsiung, Taiwan, on August 13, 1979. He received the B.S. from Kao Yuan University, Luzhu, Taiwan, in 2002, the M.S. degree from National Kaohsiung University of Applied Science (KUAS), Kaohsiung, Taiwan, in 2004, and is currently working toward the Ph.D. degree at National Cheng Kung University (NCKU), Tainan, Taiwan. His current research interests include design of antennas and microwave circuits.

Shoou-Jinn Chang (M'06–SM'10) was born in Taipei, Taiwan, on January 17, 1961. He received the B.S. degree from National Cheng Kung University (NCKU), Tainan, Taiwan, in 1983, the M.S. degree from the State University of New York, Stony Brook, NY, USA, in 1985, and the Ph.D. degree from the University of California, Los Angeles, USA, in 1989, all in Electrical Engineering. From 1989 to 1992, he was a Research Scientist with Nippon Telegraph and Telephone Basic Research Laboratories, Musashino, Tokyo, Japan. He joined the Department of Electrical Engineering, NCKU, in 1992 as an Associate Professor, where he was promoted to Full Professor in 1998. He is currently the Deputy Director of the Advanced Optoelectronic Technology Center, NCKU. From August to September 2001, he was a Visiting Scholar with the Institute of Microstructural Science, National Research Council, Canada; from August to September 2002, he was a Visiting Scholar with the Institute of Physics, Stuttgart University, Stuttgart, Germany; and from July to September 2005, he was a Visiting Scholar with the Faculty of Engineering, Waseda University, Tokyo. He is also an Honorary Professor with the Changchun University of Science and Technology, China. His current research interests include semiconductor physics, optoelectronic devices, and nanotechnology. Chang received the Outstanding Research Award from

the National Science Council, Taiwan, in 2004. He is a Fellow of the Optical Society of America and the International Society for Optical Engineers.

Jia-Chun Zheng was born on June 9, 1965. Since 2000, Zheng was an Associate Professor and was a Vice President from 2011 at the School of Information Engineering, Jimei University, and he was also a Postgraduate Tutor from 2008. His current research interests are focused on sea transportation information system, signal processing, underwater acoustic communication, wireless sensor network. So far, his achievements have been awarded as the third prize of Scientific and Technological Progress in Xiamen, two utility model patents, and two software copyrights. He has published more than 20 papers and edited a textbook.

Jian-Chiun Liou was born in Taiwan on Oct. 18, 1974. He received a Ph.D. degree from the Institute of Nanoengineering and Microsystems, National Tsing Hua University, Hsinchu, Taiwan, in 2009. He joined the Printing Technology Development and Manufacturing Section of the Optoelectronics and Systems Laboratories at the Industrial Technology Research Institute (ITRI), Hsinchu, in 1999. In August 2014, he has joined the faculty of the National Kaohsiung University of Applied Sciences (KUAS). Currently, he is a Professor of Electronic Engineering department at the KUAS. He is a holder of 71 patents, and has written more than 28 SCI Journal papers and 38 conference technical papers on MEMS, optical-N/MEMS, and display-related and micro-/nanofluidics related fields. Liou was the recipient of the following honors: ITRI/OES Research Achievement Award (2004), ITRI Research Paper Publication Award (2004), ITRI/EOL Research Achievement Award (Individual person Award, 2005), ITRI Paper Awards (2012), ITRI/EOL Outstanding Advanced Research Silver Award (2013), International Inventor Prize (2014), Nation Academic Award (2014). He has also been a consultant to three Taiwanese companies.

Cheng-Fu Yang was born in Taiwan on July 12, 1964. After graduating in the "Department of Electrical Engineering" from Cheng Kung University in 1986, Yang also gained his Master and Ph.D. in 1988 and 1993 from the "Department of Electrical Engineering" of Cheng Kung University. After obtaining the Ph.D. degree, Yang entered academic life in 1993, first at the "Department of Electronic Engineering, Chinese Air Force Academy", and since February 2000 as a Professor at the Chinese Air Force Academy, Taiwan. In February 2004, had joined the faculty of the National University of Kaohsiung (NUK) and he is a Professor in the Department of Chemical and Materials Engineering. He was the first one to get the Distinguished Professor in NUK. He was the Fellow of "Taiwanese Institute of Knowledge Innovation" (TIKI) on Oct, 2014 and he was the Fellow of "The Institution of Engineering and Technology" (IET) on May, 2015. His current research interests are focused on fine ceramics, microwave ceramics, dielectric thin films, optical materials, transparent conducting oxides, solar cell materials, microwave antennas, and microstrip filters. So far, he has published more than 175 SCI journal papers and more than 130 EI journal papers, and he also has published more than 260 domestic and international conference papers.

Design of High Performance Miniaturized Lowpass Filter Using New Approach of Modeling

Sohrab Majidifar

Department of Electrical Engineering
Kermanshah University of Technology, Kermanshah, Iran
s.majidi@kut.ac.ir

Abstract ─ In this paper a compact microstrip lowpass filter (LPF) is presented using the taper-loaded resonator. Based on a new approach, the resonator response as a function of its model component is obtained. The proposed equation between the insertion loss and LC parameters of the resonator, enable designers to calculate the proper amount of these parameters for a considered response, through the mathematical equations. The response of the final filter is improved using H-shape and spiral-shape defected ground structure. This filter is designed, fabricated and measured and as it is shown in the simulation results, the cutoff frequency is 1.53 GHz, the roll-off rate is better than 29.3 dB/GHz and the insertion loss is less than 0.1 dB from DC to 1.1 GHz.

Index Terms ─ Circuit model, defected ground structure, taper loaded resonator.

I. INTRODUCTION

Suppression of high frequency unwanted signals is one of the microstrip LPF's applications in microwave system [1-3]. These filters design in various shapes using different resonators but, in new structures, the main attempt is the improvement of the response parameters such as stopband bandwidth, selectivity and compactness. Researchers have used different methods to achieve these goals. Some articles have focused on sharpness improvement [4-6]. In [4], by combining three shunt open stubs, a compact LPF with very high selectivity is obtained. In this filter, sharp response with a roll off rate of 49 dB/GHz is achieved. A compact structure with high selectivity and wide stopband is designed in [5]. This filter is composed of two folded stepped impedance open stubs and a semi-circle ended suppressing cell. In [6], a novel Hilbert curve ring fractal DGS and its equivalent model are investigated, and by cascading three improved Hilbert curve ring DGS cells, a sharp response microstrip LPF is designed. The insertion loss of the passband is below 0.5 dB in this filter.

In [7-11], researchers have designed lowpass filters with wide stopband. A compact lowpass filter with wide stopband using novel windmill resonators is presented in [7]. At the 3 dB cutoff frequency of 1.76 GHz, the designed LPF achieves a wide stopband with overall 20 dB attenuation up to seven times the cutoff frequency. In order to design a lowpass filter with wide stopband, a novel meandered-slot resonator is presented in [8]. The 3 dB cutoff frequency of this filter is 2.2 GHz and this LPF achieves an ultra-wide stopband of 12.8 times the cutoff frequency with more than 20 dB attenuation. Novel compact and wide stopband elliptic-function resonator is proposed in [9]. Two broad stopband LPFs using one and two of the proposed resonators are designed. This resonator introduces four transmission zeros in the stopband and the positions of them can be tuned easily to get different stopband characteristics. A bandstop structure is embedded into classical stepped impedance lowpass filter in [10] to make the stopband wider. This filter has a small size. A novel complementary triangular split ring resonator (CTSRR) using DGS is introduced in [11]. In order to design a high-performance lowpass filter with a cutoff frequency of 1.80 GHz, CTSRR units are cascaded together. A LPF with wide stopband is developed in [12]. This filter is composed of two radial stub resonators that are asymmetrically connected to each other by a stepped impedance structure. This structure results in high rejection and wide stopband. A compact elliptic-function microstrip LPF using stepped impedance resonators loaded (SIRs-loaded) hairpin resonators are presented in [13]. Two LPFs using one-cell and two-cell is designed in this work. The two-cell filter has a 3 dB cutoff frequency at 2 GHz and a size of only 0.081 $\lambda g \times 0.096 \lambda g$. A novel complementary split-ring resonators (CSRRs) DGS are proposed to design LPFs with excellent performance in terms of low ripple in the pass band, sharp selectivity and wide stop band [14].

The authors in [15-17] have focused on compactness in LPF design. Using an improved split ring resonator, a new compact miniaturized stepped impedance LPF is proposed in [15]. In [16], both symmetrically loaded resonant patches and meander transmission line are adopted to achieve wide stopband and compact size. A novel microstrip lowpass filter based on a T-shaped

Submitted On: May 21, 2015
Accepted On: November 8, 2015

resonator is proposed in [17] that presents a compact size. The physical size of this filter excluding the feeding lines, is 13.1 mm * 8.2 mm.

In this article, a taper loaded resonator is proposed to design a LPF with wide stopband and compact size. The proposed resonator is presented and studied with an LC model and then it is used to implement a high performance LPF.

II. PROPOSED RESONATOR

Figure 1 shows the layout, circuit model and EM simulation results of the proposed taper-loaded resonator. Resonator dimensions are as follows: L = 22 mm, L1 = 6 mm, L2 = 4 mm, L3 = 9.66 mm, W1 = 0.1 mm and W2 = 1.2 mm.

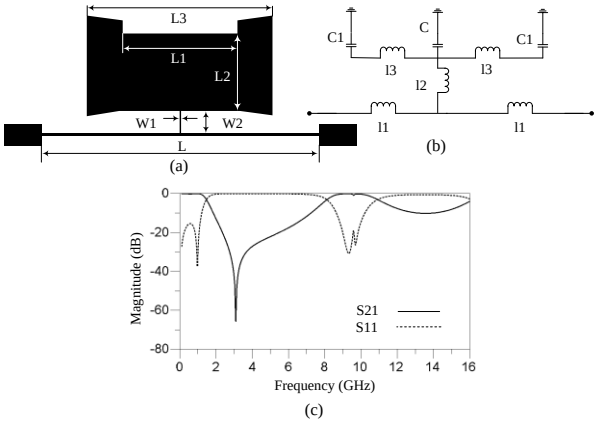

Fig. 1. Pproposed resonator: (a) layout, (b) circuit model, and (c) EM simulation results in a wide span.

As it is depicted in Fig. 1 (b), l1 introduce the inductance of the transmission line, the inductance of the high impedance stub with the length of W2 is l2, l3 shows the internal inductance of the low impedance part of the resonator and the body capacitance of the middle part and loaded tapers are presented as C and C1 respectively.

Using Equations (1-4), the LC parameters of the proposed model are calculated as follows [5], [18,19]: l1 = 7.5 nH, l2 = 1 nH, l3 = 0.3 nH, C1 = 0.55 pF and C = 1.5 pF. The calculation of the tapered parts is done using the average length of the tapers:

$$C = [8.85\ (10)^{-12}\{[\frac{\varepsilon r\ w}{h}]^{1.08} + [2\pi(\frac{\varepsilon r+1}{2})(\frac{1}{\ln(\frac{8h}{w}+1)} - \frac{w}{8h})]^{1.08}\}^{0.926}]\ l. \quad (1)$$

In the following equations, the calculated characteristic impedance (Zc) and effective permittivity (ε_{re}) are: Zc = 154 Ω and ε_{re} = 1.695 for W = 0.1 mm, Zc = 13.9 Ω and ε_{re} = 2.08 for W = 6 mm and for W = 1.83 ε_{re} = 1.94 and Zc = 36.5 Ω:

$$L = \frac{l\ z_c}{v_p}, \qquad v_p = \frac{c}{\sqrt{\varepsilon_{re}}}. \quad (2)$$

For w/h ≤ 1:

$$\varepsilon_{re} = \frac{\varepsilon_r+1}{2} + \frac{\varepsilon_r-1}{2}\{[1+12\frac{h}{w}]^{-0.5} + 0.04\ [1-\frac{w}{h}]^2\},$$
$$z_c = \frac{\eta}{2\pi\sqrt{\varepsilon_{re}}}\ln[8\frac{h}{w} + 0.25\frac{w}{h}]. \quad (3)$$

For w/h ≥ 1:

$$\varepsilon_{re} = \frac{\varepsilon_r+1}{2} + \frac{\varepsilon_r-1}{2}[1+12\frac{h}{w}]^{-0.5},$$
$$z_c = \frac{\eta}{\sqrt{\varepsilon_{re}}}\{\frac{w}{h} + 1.393 + 0.677\ln[\frac{w}{h} + 1.444]\}^{-1}, \quad (4)$$

where, C and L are capacitance and inductance of the resonator parts, v_p represents the phase velocity, w, l and h are line widths, line lengths and substrate thickness respectively, η is a constant equal to 120π Ω and c represents the light speed. The circuit and EM simulated results of the resonator are shown in Fig. 2.

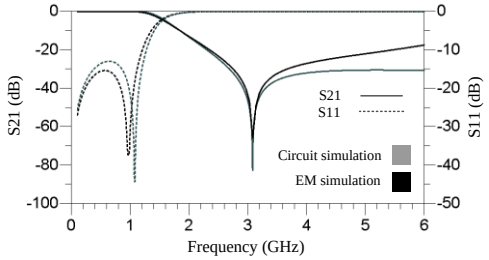

Fig. 2. EM and circuit simulation results in a narrow span.

Matching between circuit simulation and EM simulation results shows the detailed description of the proposed circuit model. Resonator response extraction as a function of the LC parameters causes that dependence of this response to each element be calculated, and using Equations (1-4) dependence of this response as a function of the resonator dimension can be calculated.

The equations where calculating the insertion loss of the resonator based on the LC parameters, are as (5-9):

$$Z_{11} = Z_{22} = 0.5\ I(+1-8\pi^2 f^2 C1\ l2 + 16\ l2\ \pi^4 f^4 C\ l3\ C1 - 4\ l2\ \pi^2 f^2 C - 4\ l3\ \pi^2 f^2 C1)\ /\ \pi\ f(-2\ C1 + 4\ l3\ C1\ \pi^2 f^2 C - C), \quad (5)$$

$$Z_{21} = Z_{12} = 0.5\ I(+1-8\pi^2 f^2 C1\ l2 + 16\ l2\ \pi^4 f^4 C\ l3\ C1 - 4\ l2\ \pi^2 f^2 C - 4\ l3\ \pi^2 f^2 C1 - 8\ l1\ \pi^2 f^2 C1 + 16\ l1\ \pi^4 f^4 C1\ l3\ C - 4\ l1\ \pi^2 f^2 C)\ /\ \pi\ f(-2\ C1 + 4\ l3\ C1\ \pi^2 f^2 C - C), \quad (6)$$

$$S_{21} = \frac{2\ Z_{21}\ Z_0}{(Z_{11}+Z_0)\ (Z_{22}+Z_0) - Z_{12}\ Z_{21}}, \quad (7)$$

$$S_{21} = (50\ \mathrm{I}(-8\ \mathrm{l2}\ \pi^2\mathrm{f}^2\mathrm{c1}+16\ \mathrm{l2}\ \pi^4\mathrm{f}^4\mathrm{C}\ \mathrm{l3}\ \mathrm{C1}-4\ \mathrm{l2}\ \pi^2\mathrm{f}^2\mathrm{C}-4\ \mathrm{l3}\ \pi^2\mathrm{f}^2\mathrm{C1}+1))\ /\ (\pi\ \mathrm{f}(-2\ \mathrm{C1}+4\ \mathrm{c}\ \mathrm{l3}\ \pi^2\mathrm{f}^2\mathrm{C1}-\mathrm{C})\ ((0.5\ I(-8\ \mathrm{l2}\ \pi^2\mathrm{f}^2\mathrm{C1}+16\ \mathrm{l2}\ \pi^4\mathrm{f}^4\mathrm{C}\ \mathrm{l3}\ \mathrm{C1}-4\ \mathrm{l2}\pi^2\mathrm{f}^2-4\ \mathrm{l3}\ \pi^2 f^2\mathrm{C1}+1-8\ \mathrm{l1}\ \pi^2\mathrm{f}^2\mathrm{C1}+16\ \mathrm{l1}\ \pi^4\mathrm{f}^4\mathrm{C}\ \mathrm{l3}\ \mathrm{C1}-4\ \mathrm{l1}\ \pi^2\mathrm{f}^2\mathrm{C})\ /\ \pi\ \mathrm{f}(-2\mathrm{C1}+4\ \mathrm{Cl3}\ \pi^2\mathrm{f}^2\mathrm{C1}-\mathrm{C})+50)^2+0.25\ (-8\ \mathrm{l2}\ \pi^2\mathrm{f}^2\mathrm{C1}+16\ \mathrm{l2}\ \pi^4\mathrm{f}^4\mathrm{C}\ \mathrm{l3}\ \mathrm{C1}-4\ \mathrm{l2}\ \pi^2\mathrm{f}^2\mathrm{C}-4\ \mathrm{l3}\ \pi^2\mathrm{f}^2\mathrm{C1}+1)^2\ /\ \pi^2\mathrm{f}^2(-2\ \mathrm{C1}+4\ \mathrm{C}\ \mathrm{l3}\ \pi^2\mathrm{f}^2\mathrm{C1}-\mathrm{C})^2)), \quad (8)$$

where "f" represents the frequency in Hz and "Z_0" is the terminal impedance. If in Equation (8), we set l1 = 7.5 nH, l2 = 1 nH, l3 = 0.3 nH, C = 1.5 pF and C1 = 0.55 pF, then S_{21} turns to a function of "f" as (9):

$$S_{21} = 50\ \mathrm{I}\ (-1.106\ 10^{-20}\pi^2 f^2+3.96\ 10^{-42}\pi^4 f^4+1)/(\pi\ \mathrm{f}\ (-2.6\ 10^{-12}+9.9\ 10^{-34}\pi^2 f^2)((0.5\ I(-8.9\ 10^{-20}\pi^2 f^2+3.366\ 10^{-41}\pi^4 f^4+1)/\pi\ f(9.9\ 10^{-34}\pi^2 f^2-2.6\ 10^{-12})+50)^2+0.25(1.1`\ 10^{-20}\pi^2 f^2+3.96\ 10^{-42}\pi^4 f^4+1)^2\ /\ \pi^2 f^2(-2.6\ 10^{-12}+9.9\ 10^{-34}\pi^2 f^2)^2)). \quad (9)$$

Figure 3 shows the magnitude of S_{21} as a function of "f" (according to the Equation (9)).

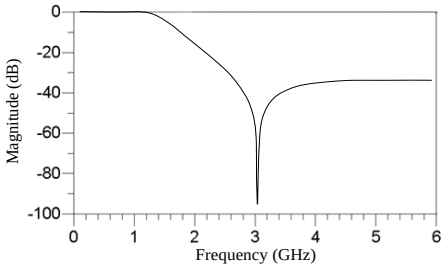

Fig. 3. Magnitude of S_{21} as a function of "f" (according to the Equation (9)).

The sharpness of the resonator is introduced by (10):

$$\Delta f = f_s - f_c, \quad (10)$$

where "f_s" is the first -20 dB point and "f_c" is the 3 dB cutoff frequency of the resonator. Let f_1 to be the smallest positive root of (11) and f_2 denotes the positive root of (12), then $\Delta f = f2 - f1$ defines the sharpness of LC resonator response:

$$A = 20\ \log|S_{21}(f)| + 3 = 0, \quad (11)$$

$$B = 20\ \log|S_{21}(f)| + 20 = 0. \quad (12)$$

Figure 4 depicts Δf in terms of l1, l2, C and C1.

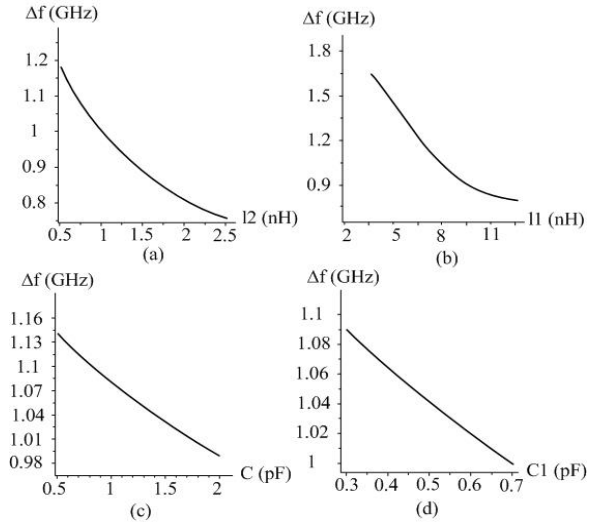

Fig. 4. Sharpness of LC resonator response as a function of l1, l2, C and C1.

III. FILTER DESIGN

As it is seen in Fig. 1 (c), the transition poles at 9.3 GHz and 9.68 GHz limit the stopband of the proposed resonator. Creating transition zeros near the pole frequencies improves the stopband bandwidth of the resonator. So, low impedance tapered stubs add to the sides of the resonator and form the basic structure of the LPF. Figures 5 (a) and 5 (b) show the layout and simulation results of the proposed resonator with added low impedance stubs.

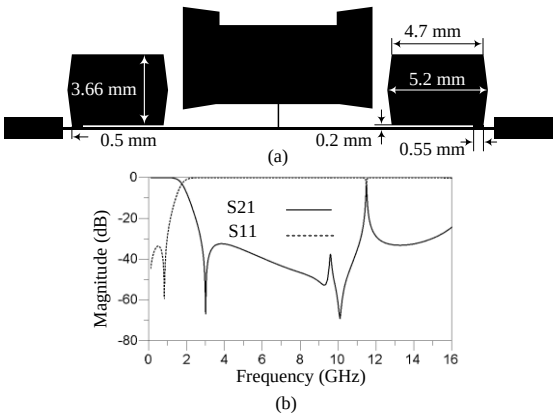

Fig. 5. Basic structure of LPF3: (a) layout and (b) simulation results.

According to Fig. 5 (b), the transition pole that is created at 11.46 GHz limits the stopband of the proposed structure. To deactivate this pole effect without size variation, the defected ground structure (DGS) is used in the final design of the LPF. The layout of the DGS spiral and H-shaped resonators are shown in Fig. 6 (a). The simulation results of the transition line with/without DGS are shown in Fig. 6 (b). As seen in this figure, a transition zero appears at 11.45 GHz when DGS is used.

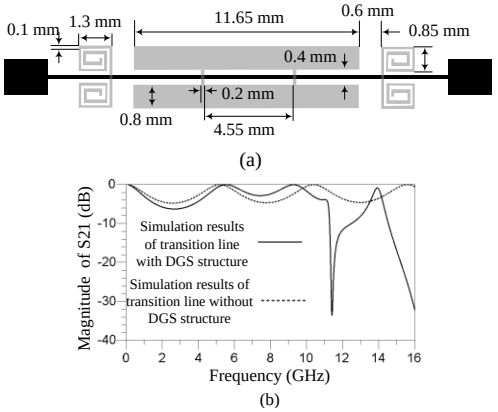

Fig. 6. Spiral and H-shaped DGS: (a) layout and (b) simulation results.

As it is shown in Fig. 6 (b), the transition zero that is created by DGS deactivates the transition pole of the basic structure (at 11.46 GHz) and expand the stopband of the filter response. Layout, fabrication picture and simulation/measurement results of the proposed LPF are presented in Fig. 7.

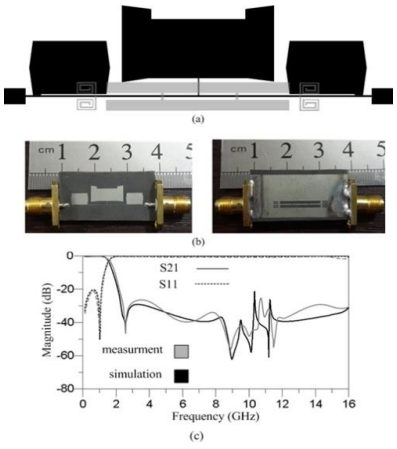

Fig. 7. Proposed LPF: (a) layout, (b) fabrication picture, and (c) simulation and measurement results.

IV. RESULTS DISCUSSION

The LPF has a sharpness of 0.58 GHz with the rate of 29.3 dB/GHz and a cutoff frequency at 1.53 GHz. According to the measurement results, the stopband of this filter is expanded from 2.11 GHz to 16 GHz with more than 24 dB attenuation level. Table 1 compares the performance of the proposed filters with the referenced works. This comparison is based on the equations that are shown in Table 2. These equations describe the sharpness, stopband rejection level, stopband bandwidth, physical size and architecture of the proposed filter and referenced work. The α_{max}, α_{min}, f_s, f_c and λ_g are introduced in the Table 3.

Table 1: Performance comparison among proposed filters and referenced works

Ref.	fc	RSB	SF	ς	NCS	AF	FOM
This work	1.53	9.1	2.4	29.3	0.0075	2	42660
[4]	2.49	1.69	2	54.8	0.0323	1	5734
[5]	2.28	5.47	2	121.4	0.0338	1	39293
[6]	2.3	1.56	2.7	188.9	0.207	2	796
[7]	1.76	7	2	51.5	0.048	1	15021
[8]	2.2	12.8	2	58.6	0.055	1	27276
[9]	2	5.15	2	24.29	0.0094	1	26627
[10]	1.8	2.8	1.6	34	0.031	1	4914
[11]	1.8	16.5	2	250	0.251	2	16434
[12]	2.07	8.62	2.4	36.17	0.0621	1	12050
[13]	2	11.2	1	21.25	0.0078	1	30649
[14]	5.3	0.85	3.5	160	0.391	2	609
[15]	2.2	2.4	2.3	85	0.051	2	4600
[16]	1.3	9.4	1.7	21	0.0088	1	38134
[17]	3.09	4.91	2	45.95	0.031	1	14555

Table 2: Filter specifications and its equations

Equation	Specifications
$\zeta = \frac{a\max - a\min}{fs - fc}$	Sharpness in dB/GHz
$SF = \frac{\text{max attenuation level in stopband}}{10}$	Suppression factor
$RSB = \frac{\text{stopband bandwidth}}{fc}$	Relative stopband bandwidth
$NCS = \frac{\text{physical size}}{\lambda g^2}$	Normalized circuit size
AF	Architecture factor, which is signed as 1 when the design is 2D and as 2 when the design is 3D
$FOM = \frac{\xi \times \text{RSB} \times \text{SF}}{NCS \times AF}$	Figure-of-merit (FOM) is the overall index of the filter

Table 3: Description of the αmax, αmin, fs, fc and λg

Phrase	Description
α_{max}	3 dB attenuation point
α_{min}	20 dB attenuation point
fs	20 dB stopband frequency
fc	3 dB cutoff frequency
λ_g	Guided wavelength at cutoff frequency

As it is shown in Table 1 the FOM of the proposed filter is greater than those of [4-17].

V. CONCLUSION

A high performance lowpass filter, based on the taper loaded resonator is designed, fabricated and measured. The physical size of this filter is 0.15 λg × 0.05 λg and as indicated in the results, the cut off frequency is 1.53 GHz, the roll-off rate is better than 29.3 dB/GHz, the insertion loss is less than 0.1 dB from DC to 1.1 GHz and the rejection is greater than 24 dB from 2.11 to 16 GHz.

ACKNOWLEDGMENT

Author would like to thank Dr. Behzad Ghanbari for his technical support.

REFERENCES

[1] A. S. Al-Zayed, M. B. Asad Allah, and S. F. Mahmoud, "Lowpass filter design based on microstrip meander line with HDGS," *The Applied Computational Electromagnetics Society*, vol. 29, no. 6, 2014.

[2] G. Zhang, J. Wang, Y. Dou, and H. Cui, "Compact microstrip lowpass filter with ultra-wide stopband using stepped-impedance tyrapezoid resonators," *The Applied Computational Electromagnetics Society*, vol. 29, no. 4, 2014.

[3] Y. Dou, J. Wang, H. Cui, and J. L. Li, "Miniaturized microstrip lowpass filter with ultra-wide stopband," *The Applied Computational Electromagnetics Society*, vol. 28, no. 7, 2013.

[4] R.-Y. Yang, Y.-L. Lin, C.-Y. Hung, and C.-C. Lin, "Design of a compact and sharp rejection low-pass filter with a wide stopband," *Journal of Electromagnetic Waves and Applications*, vol. 26 pp. 2284-2290, 2012.

[5] S-V. Makki, A. Ahmadi, S. Majidifar, H. Sariri, and Z. Rahmani, "Sharp response microstrip LPF using folded stepped impedance open stubs," *Radioengineering Journal*, vol. 22, pp. 328-332, 2013.

[6] J. Chen, Z.-B. Weng, Y.-C. Jiao, and F.-S. Zhang, "Lowpass filter design of Hilbert curve ring defected ground structure," *Progress In Electromagnetics Research PIER*, vol. 70, pp. 269-280, 2007.

[7] H. Cao, W. Ying, H. Li, and S. Yang, "Compact lowpass filter with wide stopband using novel windmill resonator," *Journal of Electromagnetic Waves and Applications*, vol. 26, pp. 2234-2241, 2012.

[8] H. L. Cao, W. B. Ying, H. Li, and S. Z. Yang, "Compact lowpass filter with ultra-wide stopband rejection using meandered-slot dumbbell resonator," *Journal of Electromagnetic Waves and Applications*, vol. 26, pp. 2203-2210, 2012.

[9] M. H. Yang, J. Xu, Q. Zhao, L. Peng, and G. P. Li, "Compact, broad-stopband lowpass filters using SIRs-loaded circular hairpin resonator," *Progress In Electromagnetics Research PIER*, vol. 102, pp. 95-106, 2010.

[10] Q. He and C. Liu, "A novel low-pass filter with an embedded band-stop structure for improved stop-band characteristics," *IEEE Microwave and Wireless Components Letters*, vol. 19, pp. 629-631, 2009.

[11] H. Taher, "Ultrawide stopband low-pass filter using triangular resonators defected ground," *Journal of Electromagnetic Waves and Applications*, vol. 28, pp. 542-550, 2014.

[12] M. Hayati, S. Majidifar, and O. S. Fathabadi, "Compact microstrip lowpass filter with wide stopband and high attenuation," *Microwave Journal*, vol. 4, Apr. 2012.

[13] M. H. Yang, J. Xu, Q. Zhao, and X. Sun, "Wide-stopband and miniarurized lowpass filters using SIRs-loaded hairpin resonators," *Electromagnetic Waves and Applications*, vol. 28, pp. 542-550, 2014.

[14] L. H. Weng, S. J. Shi, X. Q. Chen, Y. C. Guo, and X. W. Shi, "A novel CSRRs DGS as lowpass filter," *Journal of Electromagnetic Waves and Applications*, vol. 22, pp. 1899-1906, 2008.

[15] S-H. Fu, C-M. Tong, X-M. Li, W. Zhang, and K. Shen, "Compact miniaturized stepped impedance low-pass filter with sharp cut off characteristic," *Microwave and Optical Technology Letters*, vol. 51, pp. 2257-2258, 2009.

[16] L. Ge, J. P. Wang, and Y.-X. Gue, "Compact microstrip low-pass filter with ultra-wide stopband," *Electronics Letters*, vol. 46, pp. 689-691, 2009.

[17] H. Sariri, Z. Rahmani, A. Lalbakhsh, and S. Majidifar, "Compact LPF using T-shaped resonator," *Frequenz Journal*, vol. 67, pp. 17-20, 2013

[18] W. Che, Y. F Tang, J. Zhang, and Y. L. Chow, "Formulas of dielectric and total attenuations of a microstrip line," *Radio Science*, vol. 45, 2010.

[19] J. S Hong and M. J. Lancaster, *Microstrip Filters for RF/Microwave Applications*, John Wiley & Sons, 2001.

Sohrab Majidifar received his B.Sc. and M.Sc. in Electrical Engineering from Razi University of Kermanshah in 2009 and 2011 respectively. He joined Kermanshah University of Technology in 2011 as a Lecturer. He has published more than 18 papers in international journals and conferences. His research interests include microwave passive circuits, microwave sensors, chipless RFID and RFIC.

Electromagnetic Modeling of Electronic Device by Electrical Circuit Parameters

Diego De Moura and Adroaldo Raizer

Department of Electrical Engineering
Federal University of Santa Catarina, Florianópolis, 88040-970, Brazil
diegodemouraa@gmail.com, adroaldo.raizer@ufsc.br

Abstract ─ This article proposes an electric model to determine the values of the electric fields of an electronic device. When applying the method, the integrated circuit device will be modeled on the resistance, inductance and capacitance values (R, L, C parameters) provided by the IBIS (*Input/Output Buffer Information Specification*), also considering the internal activity of the integrated circuit. The electric parameters of the printed circuit board tracks will be extracted by software based on the moments method and fast multipole method. Simulations of the electric model are performed in the time and frequency domain by the Fourier transform, and from the obtained harmonics, the values of the electric fields are calculated with software based on the finite elements method. Measurements were performed in order to validate the simulations.

Index Terms─Electrical circuit parameters, electromagnetic modeling, electronic device, IBIS model, internal activity.

I. INTRODUCTION

Problems related to electromagnetic compatibility (EMC) have increased significantly in recent decades, due to the increase of commutation speed and level of integration of electronic devices.

From this perspective, studies concerning the electromagnetic compatibility of electronic devices through numerical modeling have intensified.

The first significant contribution towards noise modeling of electronic components was with the IBIS model in the 90s, which proposed a standardized description of the electric performance of the input/output structures in integrated circuits [1].

Since then, the IBIS model has been improved and used in research aiming to diminish the problems with noise in electronic devices [2], [3], [4].

Despite the constant improvement of the IBIS models, the information provided for the internal activity of integrated circuits has limitations regarding their application in the EMC area.

This way, other models based on circuit parameters have been proposed to predict the electromagnetic emission of electronic components. In Japan, the IMIC model *(Interface Model for Integrated Circuits)* was proposed with the aim of standardizing the terminals and operation signals of integrated circuits [5]. Japanese researchers also propose the LECCS model (*Linear Equivalent Circuit and Current Source*), in which circuit parameters are used in order to model the core of integrated circuits, also considering the internal activity model by sources of current [6], [7].

At the same time in France, the standardization of components is proposed through the ICEM model (*Integrated Circuit Emission Model*). Being that the structure of this model also uses sources of current to model the internal activity (IA) of the integrated circuit, and in addition, PDN (*The Passive Distribution Network*) models are used to model the power source and decoupling capacitors of the IC's [8].

Based on the proposal of the LECCS and ICEM models, a range of studies are proposed in the setting of electromagnetic modeling of integrated circuits. Thus, in [9], [10], [11] the LECCS model is used to analyze conducted emission of microcontrollers, power sources and FPGA, respectively.

From the same conception in [12], the ICEM model is used to analyze the emission of microcontroller circuits. Whereas in [13], the characterization and modeling of CMOS circuit emissions is performed. Also, in [14], a model for determining conducted emission of the integrated circuit is proposed up to the frequency of 3 GHz. Being that comparisons are made with the ICEM model.

Although the LECCS, ICEM and other cited models, provide the constant advance of the EMC area applied to integrated circuits, their application are usually related to chip-level modeling.

Also in [15], [16], [17], [18], studies on electromagnetic modeling are performed through the partial element equivalent circuit (PEEC method). Through this method, the problem is transferred from the electromagnetic domain to the circuit domain, where conventional circuit simulator can be utilized to analyze the equivalent circuit. Usually the extracted circuit is not used to determine the

Submitted On: June 1, 2015
Accepted On: November 8, 2015

electric fields.

In this work, the modeling by electrical circuit parameters is used to determine the electromagnetic emission of the printed circuit board of the electronic device, with the integrated circuit device being modeled after the R, L, C parameters provided by the IBIS model. In addition, in order to model the internal activity of the IC, a voltage source is used. The R, L, C models of the tracks will be extracted by software based on the moments method and fast multipole method.

The signal circuit simulations are performed from the patterned electrical circuit in the time and frequency domain by Fourier transformation. Through the harmonics obtained, the electric fields (E) along the distance variation are calculated by software based on the finite elements method.

Aiming to validate the simulations, measurements of the signals are also performed in the time and frequency domain by the digital oscilloscope. The electric fields (E) are measured at distances close to the electronic device through a near-field probe. Whereas, in order to obtain the far-field values, measurements will be made in a gigahertz transverse electromagnetic (GTEM) cell.

II. ELECTRONIC DEVICE SELECTION

To demonstrate the effectiveness of the proposed methodology, an electronic device with emission source characteristics is selected. Such device, seen in Fig. 1 and Fig. 2, consists of a printed circuit board 13 cm long by 3 cm wide, of FR4 dielectric material with $\varepsilon = 4.4$ (relative electric permittivity). The circuit tracks are of microstrip topology made of copper (conductivity 58.10^6 S/m).

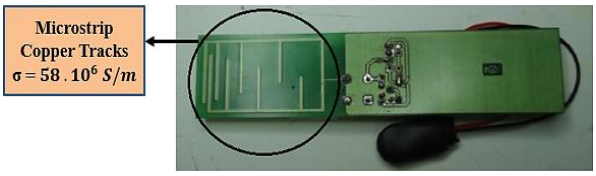

Fig. 1. Bottom view of the electronic device.

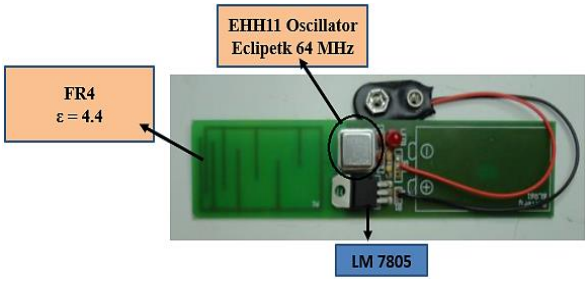

Fig. 2. Top view of the electronic device

Besides that, the circuit consists of a trapezoidal signal oscillator (EHH11-Eclipetk) responsible for generating the excitation signal of the tracks in the 64 MHz frequency [19]. The supply of the circuit (5V) is performed by a 9V battery connected to the circuit through an LM7805 voltage regulator.

The choice of device was motivated by the fact that printed circuit board tracks excited by trapezoidal signals are responsible for generating a multiplicity of harmonic components. These components are usually mechanisms which cause EMC problems [20].

III. MODELING AND NUMERICAL SIMULATIONS OF ELECTRONIC DEVICE

The modeling of EHH11 oscillator circuit was performed using the IBIS model supplied by the manufacturer (Eclipetk) [21]. Among the features that this model provides are the die (semiconductor) capacitance values information referenced as (Ccomp), and also the R, L, C parameters of the integrated circuit pins.

The IBIS model of clock pin for the EHH11 oscillator signal in circuit format can be seen in Fig. 3. The values provided by the model for the pin are: inductance (LCLKOUT = 2.90 *nH*), capacitance (CCLKOUT = 0.85 *pF*) and resistance (RCLKOUT = 75 *m* Ω). It is also possible to view the value provided for the capacitance of the (die) semiconductor (Ccomp_CLKOUT = 1.70 *pF*).

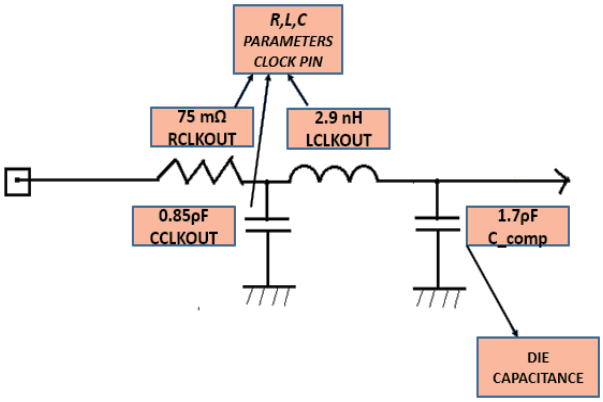

Fig. 3. Clock pin representation by the IBIS model.

The extraction of the R, L, C parameters of the device tracks was performed using the software based on the boundary element method (moments method) and fast multipole method [22]. Multipole acceleration can reduce required computation time extracting parameters R, L, C of printed circuit boards [30], [31], [32].

As it is possible to see in Fig. 4, the values obtained for the frequency of 64 *MHz* are, L = 62.336 *nH*, C = 1.9917 *pF* and R = 0.18235 Ω. For the circuit representation the equivalent π model was used, in which $C_1 = C_2 = \frac{C}{2}$.

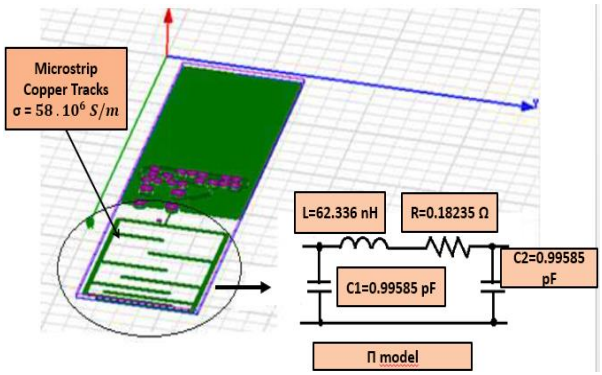

Fig. 4. R, L, C tracks circuit.

It is possible to observe that firstly the modeling of the output pin of the signal through the R, L, C parameters provided by the IBIS model of the EHH11 component was performed. Subsequently, the R, L, C parameters of the tracks were extracted. And in order for the circuit to be capable of simulation, the IBIS model of the IC was connected to the model of the tracks. In addition, a voltage source (clock) was connected in the internal capacitance of the semiconductor (die) of the integrated circuit (Ccomp_CLK) = 1.70 *pF*) which represents the model of the internal activity of the IC. Also, through simulations, the circuit load was determined *RL* = 100 Ω. The electric circuit in its final modeling can be seen in Fig. 5 [23].

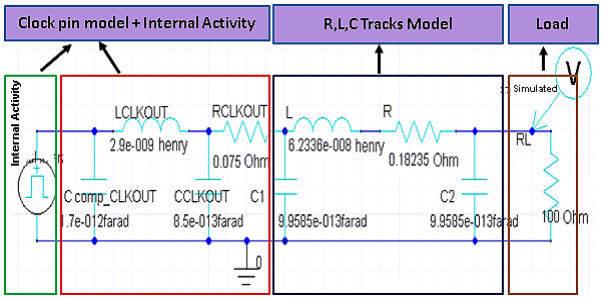

Fig. 5. Model of the electronic device by circuit parameters.

The signal circuit simulations are performed from the patterned electrical circuit in the time and frequency domain by Fourier transformation. As seen in Fig. 6, the signal obtained in the time domain in the 100 Ω load has the following specifications: amplitude $V = 5\ V$, rise time t_r = 2.391 *ns*, fall time t_f = 1.762 *ns*, pulse width *PW* = 3.6595 *ns* and period *PER* = 15.625 *ns*.

The simulation performed in the frequency domain can be seen in Fig. 7. The analysis was directed toward a few odd harmonics 1st (64 MHz), 3rd (192 MHz), 5th (320 MHz), 7th (448 MHz), 9th (576 MHz) and 11th (704 MHz), usually resulting from trapezoidal signals.

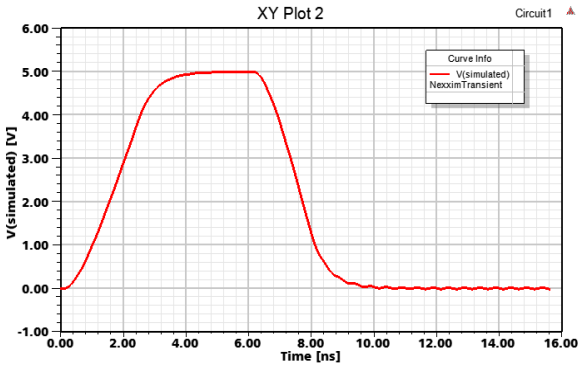

Fig. 6. Simulated signal in the time domain.

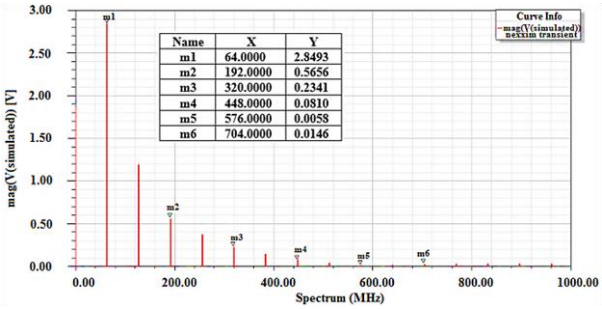

Fig. 7. Simulation in the frequency domain.

The calculations of electric fields as from the amplitudes of harmonics resulting from Fourier analysis were performed using the software based on the finite elements method (FEM) [24]. FEM is based on the differential formulation of Maxwell's equations [25], [26]. For the differential based techniques, the discretization of the complete computational domain is performed, this technique delivers predominantly the solution in field variables, i.e., $\vec{E}$ and $\vec{H}$. This is suitable for far and near field analysis [29].

As it can be seen in Fig. 8, the physical characteristics of the electronic device were modeled, such as dielectric constant of FR4 (ε = 4.4) and conductivity of the copper tracks (σ = 58.10^6 S/m). The boundary condition was also inserted around the device, i.e., an air box with permittivity and relative permeability equal to 1.0006 and 1, respectively.

Moreover, for solution dominion is used finite element boundary integral (FEBI) [28]. This condition allows the absorption of the incident field and not dependent on the incident angle.

The calculations of electric fields along the distance variations were performed using a test plan inserted in 8 different distances (1 cm, 2 cm, 4 cm, 10 cm, 20 cm, 30 cm and 300 cm) of the electronic device. Thus, the harmonics (1st, 3rd, 5th, 7th, 9th, and 11th) and their respective amplitudes were selected as excitation of the device tracks.

The simulations were performed in the basic frequency (64 MHz), third harmonic (192 MHz), fifth harmonic (320 MHz), seventh harmonic (448 MHz), ninth harmonic (576 MHz) and the eleventh harmonic (704 MHz).

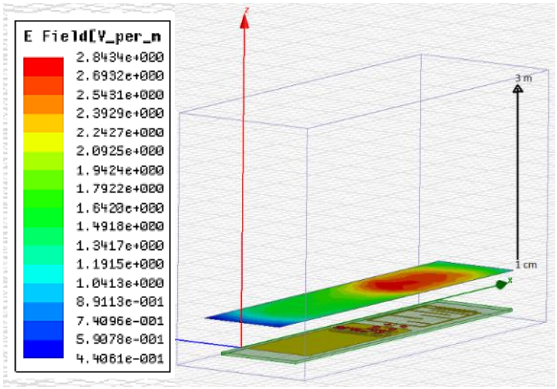

Fig. 8. Modeling and simulation of the electric fields.

IV. MEASUREMENTS OF THE ELECTRONIC DEVICE

In order to validate the results obtained from the simulations, signals measurements were performed in the time and frequency domain using a digital oscilloscope.

Figure 9 illustrates the specifics of the signal in the time domain: amplitude of 5,08 *V*, frequency equal to 64,06 *MHz*, period of 15,62 *ns*, rise and fall time equal to 2.214 *ns* and 1.707 *ns* respectively.

Upon confirming the operation of the signal in the time domain, analyses of the signal were performed in the frequency domain by the Fourier transform. In Fig. 10, the measurements of some harmonics resulting from the application of the transform are shown: 1ª (64 *MHz*), 3ª (192 *MHz*), 5ª (320 *MHz*), 7ª (448 *MHz*), 9ª (576 *MHz*) and 11ª (704 *MHz*). Their respective frequency values in (MHz) and amplitude in (V) are shown in Table 1.

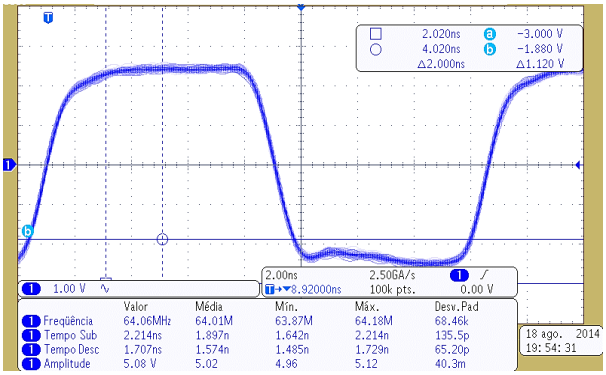

Fig. 9. Excitement signal in the time domain.

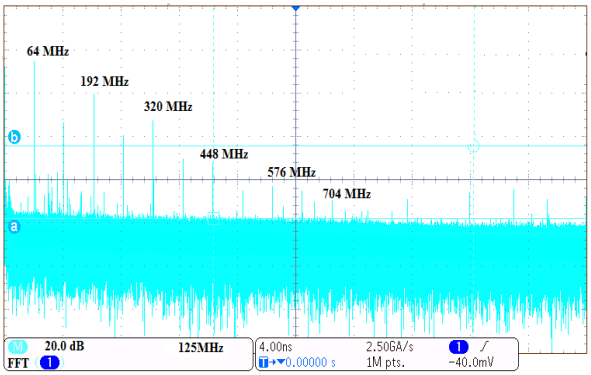

Fig. 10. Analysis of the signal in the frequency domain.

Measurements of the values of the electric fields (E_z) were also performed. For the near field region a near-field probe (HZ-14) was used, together with a field receptor (ESPC), allowing measurements of the electric field (E_z) values in the 9 kHz to 1 GHz range. It is worth noting that the probe has an antenna factor equal to 67 dBuV/m and is manufactured with an integrated amplifier which enables increase of gain [33].

In the configuration of the near field measurements illustrated in Fig. 11, it is possible to see the probe and fields receiver, both in a fixed position and the device under test moving at distances of 1 cm, 2 cm, 4 cm, 6 cm, 10 cm, 20 cm and 30 cm from the probe. Furthermore, in order to prevent electromagnetic fields from the outside environment to interfere with the measurements, a Faraday cage was used.

In the near field measurements are obtained through voltage induced values in the probe terminal and these values are added to the antenna factor, according to Equation (1):

$$|E|\,[dB\,(\mu\,V/m) = dB\,(\mu V) + AF\,]. \qquad (1)$$

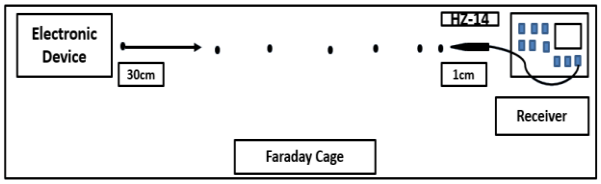

Fig. 11. Measurement setup for distances of 1 cm to 30 cm.

For measurements in the far-field region, a receiver and a GTEM cell were used. With the electronic device (EUT) properly positioned in the cell, close to the absorbers so as to center it between the conductive plate (septum) and the ground of the chamber, which are 100 cm apart. Thus, it is seen that d = 50 cm, as shown in Fig. 12.

Once the circuit is properly positioned, the peak value measurements of the of the electric far-fields (E_z) are performed in accordance with the (CISPR 22) standard, which is, Class B equipment, radiation range

of 30 MHz to 1 GHz and 3 m (300 cm) distance. Using the relationship ($\lambda/2\pi$), it is possible to conclude that for the frequency of 64 MHz, the distance of 3 m is considered far field region [34].

Measurements for the values of the near and far electric fields were performed for the previously analyzed harmonics. Fundamental frequency (64 MHz), third harmonic (192 MHz), fifth harmonic (320 MHz), seventh harmonic (448 MHz), ninth harmonic (576 MHz) and the eleventh harmonic (704 MHz).

The measurement results for the values of the electric field (E_z) in dBμV/m due to the distance variation in (cm) for each of the aforesaid frequencies, are compared to the simulations and shown below.

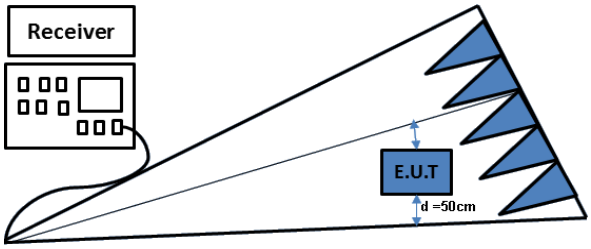

Fig. 12. Measurement GTEM for 3-meter distance.

V. COMPARISONS BETWEEN SIMULATED AND MEASURED RESULTS

The results obtained through numerical simulations were compared with the measurements made in the laboratory.

Firstly, the device excitation signals (64 MHz) in the time domain were compared, as shown in Fig. 13. It is possible to observe through the purple signal (measured signal) that it has the following characteristics: period (15,62 *ns*), amplitude 5 *V*, rise and fall time equal to 2.2 *ns* and 1.7 *ns* respectively. By making the comparison of the measured signal with the simulated signal (red signal), it is concluded that it has the same characteristics as the measured signal.

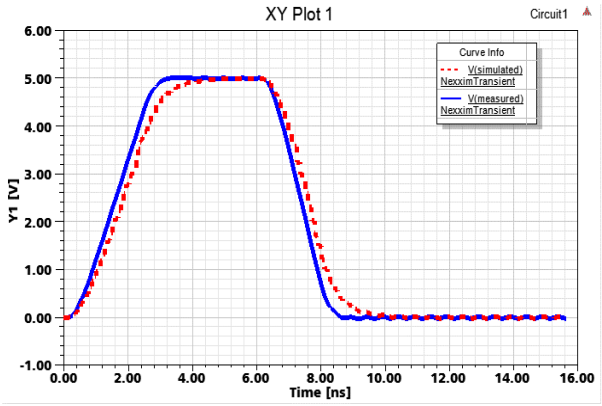

Fig. 13. Comparison of the signals in the time domain.

Afterwards, the amplitudes of the harmonics in the frequency domain were compared. As analysis of Table 1 shows, it is possible to observe that the 1st harmonic presents a difference in amplitude of (0.3493 *V*), the 3rd (0.0756 *V*), the 5th (0.0741 *V*), the 7th (0.063 *V*) the 9th (0.0092 *V*) and the 11th (0.0046 *V*).

Table 1: Comparison of the signal amplitudes in the frequency domain

Frequency (MHz)	Amplitude of the Measured Signal (V)	Amplitude of the Simulated Signal (V)	Differences of Amplitude |V|
64 (1st)	2.5	2.8493	|0.3493|
192 (3rd)	0.49	0.5656	|0.0756|
320 (5th)	0.16	0.2341	|0.0741|
448 (7th)	0.018	0.0810	|0.063|
576 (9th)	0.015	0.0058	|0.0092|
704 (11th)	0.01	0.0146	|0.0046|

Finally, the values of the measured and simulated electric fields were confronted, as shown in Figs. 14, 15, 16, 17, 18 and 19. The values of electric field were used in measurements and simulations, because these variables are usually used in the normative references of electromagnetic emission of electronic devices [27].

It is noted by the measured values (blue curve) and simulated values (red curve), that the values of the electric fields (E_z) in (dBμV/m) over the distance variation, in (cm), show great similarity. However, the most significant differences are observed in the 7th harmonic (448 MHz) or 20 cm (10.96 *dBμV/m*), 30 cm (10.73 *dBμV/m*) as shown in Fig. 16 and 9th harmonic (576 MHz), or 1 cm (9.88 *dBμV/m*) 2 cm (10.7 *dBμV/m*), 4 cm (9.72 *dBμV/m*), 6 cm (9.59 *dBμV/m*), 10 cm (9.1 *dBμV/m*) and 20 cm (6.52 *dBμV/m*) as shown in Fig. 17.

In other words, analyzing the difference between the amplitudes of the seventh and ninth harmonic in dB, were obtained |13.1| dB for seventh harmonic and |8.2| dB for the ninth harmonic, as shown in Table 2. Therefore, the most significant differences in the values of electric fields were observed for the same.

In addition, the near-field probe model of the GTEM cell and measurement uncertainties were not considered. Thus, such factors may also have caused the discrepancies between the amplitude values of the electric fields (E).

Table 2: Comparing the amplitudes of the seventh and ninth harmonic in dB

Frequency (MHz)	Amplitude of the Measured Signal V→dB	Amplitude of the Simulated Signal V→dB	Differences of Amplitude |dB|
448 (7th)	(0.018 V) = -34.9 dB	(0.0810) = -21.8 dB	|13.1|
576 (9th)	(0.015) = -36.5 dB	(0.0058) = -44 dB	|8.2|

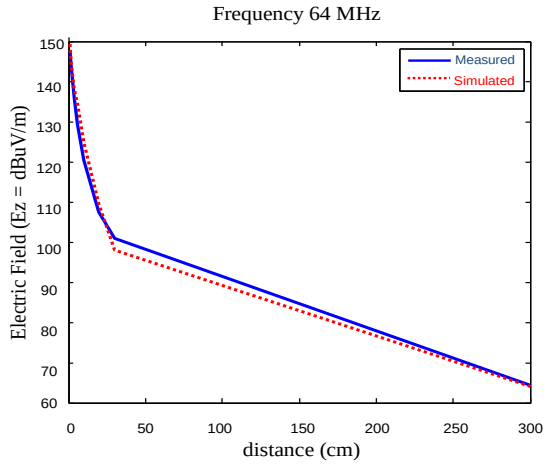

Fig. 14. Comparisons between electric fields measured and simulated for the 64 MHz frequency.

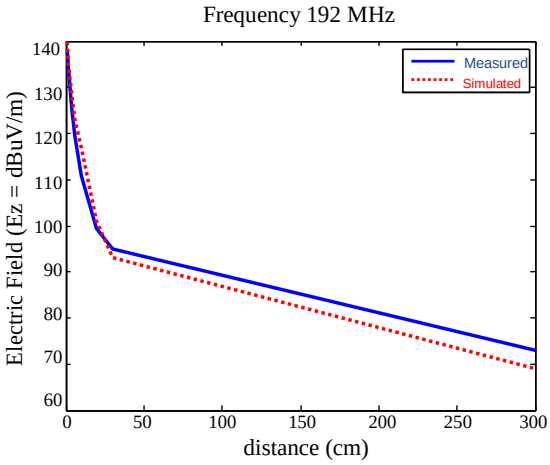

Fig. 15. Comparisons between electric fields measured and simulated for the 192 MHz frequency.

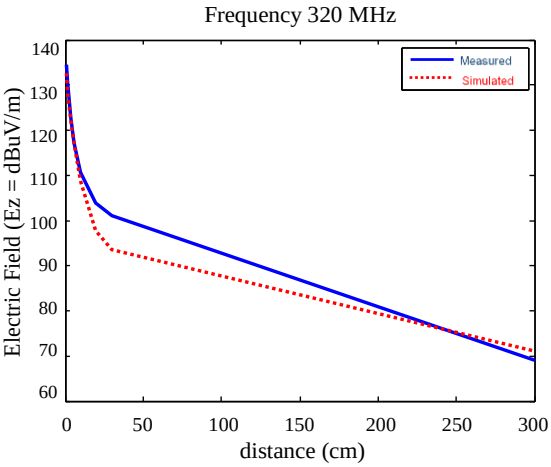

Fig. 16. Comparison between electric fields measured and simulated for the 320 MHz frequency.

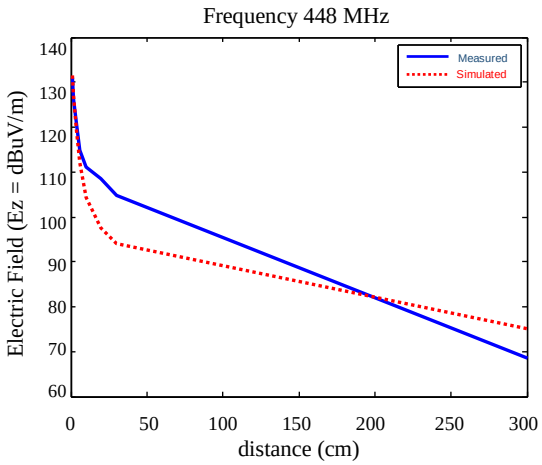

Fig. 17. Comparison between electric fields measured and simulated for the 448 MHz frequency.

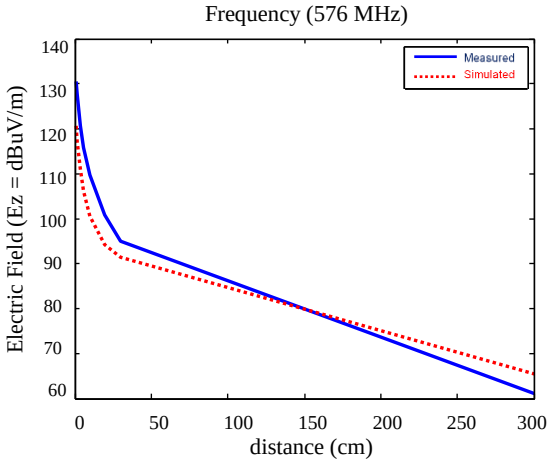

Fig. 18. Comparison between electric fields measured and simulated for the 576 MHz frequency.

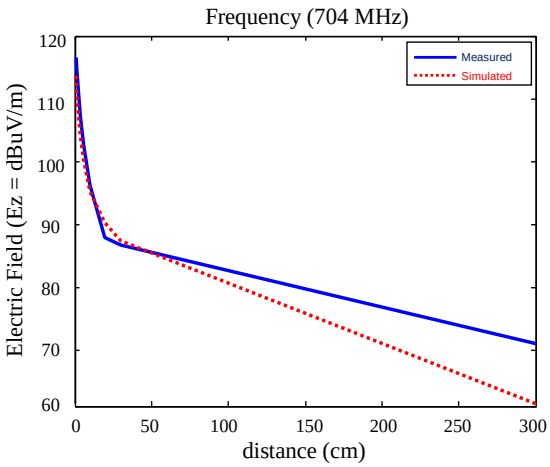

Fig. 19. Comparison between electric fields measured and simulated for the 704 MHz frequency.

VI. CONCLUSION

This article has demonstrated a new methodology for the analysis of electric fields by an electronic device. The technique applied incorporates a complete modeling of the electronic device, in which the integrated circuit is modeled after the IBIS model, also considering its internal activity model. In addition, the R, L, C parameters of the tracks are extracted.

Thus, this way it is possible to obtain an electric and simulated circuit, enabling the determination of the signals in the time and frequency domain, and consequently, the values of electric fields can be determined by simulation based on the finite elements method.

From the obtained results, it can be said that the proposed methodology, can be a starting point for standardized models of printed circuit boards in determining the electromagnetic emission of the same.

REFERENCES

[1] IBIS, Electronic Behavioral Specifications of Digital Integrated Circuits I/O Buffer Information Specification, International Electrotechnical Commission (IEC) 62014-1, 2003.

[2] P. Pulici, A. Girardi, G. P. Vanalli, R. Izzi, G. Bernardi, G. Ripamonti, A. G. M. Strollo, and G. Campardo, "A modified IBIS model aimed at signal integrity analysis of systems in package," *IEEE Transactions on Circuits and Syst*., vol. 55, no. 7, pp. 1921-1928, Aug. 2008.

[3] B. B. M'Hamed, F. Torrès, A. Reineix, and P. Hoffmann, "Complete time-domain diode modeling: application to off-chip and on-chip protection devices," *IEEE Trans. on Electromagn. Compat.*, vol. 53, no. 2, pp. 349-365, May 2011.

[4] N. Monnereau, F. Caignet, N. Nolhier, M. Bafleur, and D. Tremouilles, "Investigation of modeling system ESD failure and probability using IBIS ESD models," *IEEE Trans. on Device and Materials Reliability*, vol. 12, no. 4, pp. 599-606, Dec. 2012.

[5] I/O Interface Model for Integrated Circuits (IMIC), International Electrotechnical Commission (IEC) 62404, 2003.

[6] O. Wada, Y. Fukumoto, H. Osaka, W. Zhi Liang, O. Shibata, S. Matsunaga, T. Watanabe, E. Takahashi, and R. Koga, "High-speed simulation of PCB emission and immunity with frequency-domain IC/LSI source models," in Proc. *IEEE Int. Symp. Electromagn. Compat.*, vol. 1, pp. 4-9, 2003.

[7] K. Ichikawa, M. Inagaki, Y. Sakurai, I. Iwase, M. Nagata, and O. Wada, "Simulation of integrated circuit immunity with LECCS model," in Proc. *17th Int. Symp. Electromagn. Compat.*, Zurich, Switzerland, pp. 308-311, 2006.

[8] Integrated Circuits Emission Model (ICEM), International Electrotechnical Commission (IEC) 62014-3, 2004.

[9] K. Iokibe, R. Higashi, T. Tsuda, K. Ichikawa, K. Nakamura, Y. Toyota, and R. Koga, "Modeling of microcontroller with multiple power supply pins for conducted EMI simulations," in Proc. *2012 IEEE Int. Symp. Electrical Design of Advanced Packaging and Systems*, Seoul, Korea, pp. 135-138, 2008.

[10] T. Ibuchi and T. Funaki, "A study on EMI noise source modeling with current source for power conversion circuit," in Proc. *2012 IEEE Int. Symp. Electromagn. Compat*., EMCEUROPE, Rome, Italy, pp. 1-6, 2012.

[11] K. Iokibe and Y. Toyota, "Estimation of data-dependent power voltage variations of FPGA by equivalent circuit modeling from on-board measurements," in Proc. *2013 Int. Workshop Electromagn. Compat. Integr. Circuits*, EMCCOMPO, Nara, Japan, pp. 175-179, 2013.

[12] C. Labussière-Dorgan, S. Bendhia, E. Sicard, J. Tao, H. J. Quaresma, C. Lochot, and B. Vrignon, "Modeling the electromagnetic emission of a microcontroller using a single model," *IEEE Trans. on Electromagn. Compat*., vol. 50, no. 1, pp. 22-34, Feb. 2008.

[13] B. Vrignon, S. Delmas Bendhia, E. Lamoureux, and E. Sicard, "Characterization and modeling of parasitic emission in deep submicron CMOS," *IEEE Trans. on Electromagn. Compat.*, vol. 47, no. 2, pp. 382-387, May 2005.

[14] N. Berbel, R. F. Garcia, and I. Gil, "Characterization and modeling of the conducted emission of integrated circuits up to 3 GHz," *IEEE Trans. on Electromagn. Compat.*, vol. 56, no. 4, pp. 382-387, Aug. 2014.

[15] D. Daroui and J. Ekman, "Parallel implementation of the PEEC method," *Journal of Applied Computat. Electromag. Society*, vol. 25, no. 5, pp. 410-422, 2010.

[16] G. Antonini, "Fast multipole formulation for PEEC frequency domain modeling," *Journal of Applied Computat. Electromag. Society*, vol. 17, no. 3, Nov. 2002.

[17] D. Daroui and J. Ekman, "Efficient PEEC-based simulations using reluctance method for power electronic applications," *Journal of Applied Computat. Electromag. Society*, vol. 27, no. 10, pp. 830-841, 2012.

[18] F. Freschi and M. Repetto, "A general framework for mixed structured/unstructured PEEC modelling," *Journal of Applied Computat. Electromag. Society*, vol. 23, no. 3, pp. 200-206, 2008.

[19] (2014). [Online]. Available: http://www.ecliptek.com/oscillators/EHH11/.

[20] H. W. Ott, *Noise Reduction Techniques in Electronic Systems*, 2nd ed., New York: Wiley-Interscience, 1988.
[21] (2014). [Online]. Available: http://www.ecliptek.com/IBIS/ehh11a.ibs.
[22] Ansys Q3D Extractor, ver. 15.0, Ansys Corporation, Canonsburg, PA, Estados Unidos, 2014.
[23] Ansys Designer, ver. 8.0, Ansys Corporation, Canonsburg, PA, Estados Unidos, 2012.
[24] Ansys High Frequency Structure Simulation (HFSS), ver. 15.0, Ansys Corporation, Canonsburg, PA, Estados Unidos, 2014.
[25] Z. J. Cendes, "Vector finite elements for electromagnetic field computation," *IEEE Trans. Magnetics*, vol. 27, pp. 3958-3966, Sep. 1991.
[26] Z. J. Cendes and J. F. Lee, "The transfinite element method for modeling MMIC devices," *IEEE Trans. on MTT*, vol. 36, pp. 1639-49, Dec. 1988.
[27] *Radio Disturbance and Immunity Measuring Apparatus*, CISPR 22, ed. 6, International Electrotechnical Commission (2008).
[28] J. Liu and J.-M. Jin, "A novel hybridization of higher order finite element and boundary integral methods for electromagnetic scattering and radiation problems," *IEEE Trans. Antennas Propagat*., vol. 49, no. 12, pp. 1794-1806, Dec. 2001.
[29] J. Ekman, *Electromagnetic Modeling Using the Partial Element Equivalent Circuit Method*, Ph.D. Theses, EISLAB, LuleÂ, Sweden, 2003.
[30] X. Wang, D. Liu, W. Yu, and Z. Wang, "Improved boundary element method for fast 3-D interconnect resistance extraction," *IEICE Trans. on Electronics*, vol. E88-C, no. 2, pp. 232-240, Feb. 2005.
[31] K. Nabors and J. White, "FastCap: a multipole accelerated 3-D capacitance extraction program," *IEEE Trans. Computer-Aided Design*, vol. 10, no. 11, pp. 1447-1459, 1991.
[32] M. Kamon, M. J. Tsuk, and J. K. White, "Fasthenry: a multipole accelerated 3-D inductance extraction program," *IEEE Trans. Microwave Theory Tech*., pp. 1750-1758, Sep. 1994.
[33] (2015) [Online] https://www.rohde-schwarz.com/en/product/hz-14_3-productstartpage_63493-11717.html.
[34] A. C. Balanis, Antenna Theory Analysis and Design, 3rd ed., New Jersey, John Wiley & Sons, Inc.

Diego de Moura was born in Chapecó, Santa Catarina, Brazil, in 1982. He received the degree in Electronic Systems from the Federal Institute of Santa Catarina, Brazil, in 2007, and Master's degree in Electrical Engineering from the Federal University of Santa Catarina, Brazil, in 2011. He is currently a doctoral student in Electrical Engineering of the Federal University of Santa Catarina. His current research interests are electromagnetic fields, electromagnetic compatibility, and electromagnetic modeling of electronic systems.

Adroaldo Raizer was born in Lages, Santa Catarina, Brazil, on August 11, 1963. He received the B.E. (1985) and M.E. (1987) degree in Electrical Engineering from Federal University of Santa Catarina, Brazil, and the Doctor's degree (1991) from Institut National Polytechnique de Grenoble, France. Raizer is currently a Full Professor of the Electrical Engineering Department at Federal University of Santa Catarina, Brazil. His current research interests are electromagnetic fields, electromagnetic compatibility, and numerical methods.

Uncertainty Analysis in EMC Simulation Based on Improved Method of Moments

Jinjun Bai, Gang Zhang, Lixin Wang, and Tianhao Wang

School of Electrical Engineering and Automation
Harbin Institute of Technology, Harbin, 150001, China
13B906024@hit.edu.cn, zhang_hit@hit.edu.cn, wlx@hit.edu.cn, hao3916@163.com

Abstract ─ Recently, many uncertainty analysis methods have been taken into consideration in electromagnetic compatibility (EMC) simulation. As a traditional method, the Method of Moments (MoM) owns many advantages compared with other methods, especially in calculating the high dimension problems. However, its main disadvantage is the poor accuracy. In this paper, the Richardson extrapolation has been used to improve the MoM in order to promote the accuracy. By using feature selective validation (FSV), the effectiveness of the improvement can be obviously shown compared with the standard results calculated by the Monte Carlo Method (MC).

Index Terms ─ EMC simulation, feature selective validation, Method of Moments, Richardson extrapolation, uncertainty analysis.

I. INTRODUCTION

Nowadays, the electromagnetic compatibility (EMC) community is facing a growing demand for taking uncertainty into consideration in EMC simulation. The MC [1-3] is a widely used uncertainty analysis method. Random input parameters are sampled according to their distributions, and a very large number of simulations are required to achieve accurate information. Therefore, low computational efficiency makes the MC uncompetitive, though the MC owns high accuracy. In theoretical research, the results calculated by the MC can be regarded as the standard answers in order to verify other uncertainty analysis methods.

Recently, another effective method, called the Stochastic Galerkin Method (SGM), has been taken into consideration in EMC uncertainty analysis by Canavero [4,5]. Many typical EMC problems with uncertainty parameters have been solved successfully by the SGM. The Stochastic Collocation Method (SCM) is another uncertainty analysis method which has also been applied in EMC [6,7]. These two methods are both rooted in the generalized polynomial chaos expansion theory, and they can reach a high accuracy with high computational efficiency. However, if the dimension of random variables is high enough, the realization of the SCM and the SGM will be impossible. It is well-known that such problem is also named 'curse of dimensionality'.

The MoM [5,8] is another traditional uncertainty analysis method, and it would not be affected by 'curse of dimensionality'. In addition, easy to realize and high computational efficiency are another two advantages of the MoM. However, the main disadvantage of the MoM is the low accuracy. In the paper, a novel method is presented in order to improve the accuracy of the MoM by using the Richardson extrapolation [9,10]. At last, a published example of one dimension wave propagation with uncertainty medium parameters is calculated by the MoM, the MC and the improved MoM. By using FSV, the improvement in accuracy of the novel method can be seen clearly.

The structure of the paper is as follows. In Section II, the uncertainty analysis in EMC simulation is introduced; Section III employs a brief description of the MoM; the improved MoM by using the Richardson extrapolation can be seen in Section IV; algorithm validation is shown in Section V; Section VI provides a summary of this paper.

II. THE UNCERTAINTY ANALYSIS IN EMC SIMULATION

As for the traditional EMC simulation, all the input parameters are supposed certain. However, in actual situation, some input parameters are uncertain as the uncertainty in measurement or limited knowledge. Therefore, such parameters should be modeled by the random variables. There is no doubt that the uncertainty analysis is to calculate the output parameters under the influence of uncertain input parameters.

Maxwell's equations for a wave propagating in a linear isotropic homogeneous material along the z-axis in 1D are shown as (1) and (2):

$$-\frac{\partial E_x(z,t)}{\partial z} = \mu \frac{\partial H_y(z,t)}{\partial t}, \tag{1}$$

$$-\frac{\partial H_y(z,t)}{\partial z} = \varepsilon \frac{\partial E_x(z,t)}{\partial t} + \sigma E_x(z,t), \tag{2}$$

Submitted On: February 2, 2015
Accepted On: December 6, 2015

where $E_x(z,t)$ represents the electric field oriented in the *x* direction, at a position *z* and time *t*. Similarly, $H_y(z,t)$ stands for the magnetic field oriented in the *y* direction at a position *z* and time *t*. The symbols μ, ε and σ represent the permeability, permittivity and conductivity of the medium in which the electromagnetic fields propagate.

Suppose that the medium parameters μ and ε are uncertain as the limited knowledge. It is obviously that a random event θ should be introduced in the Maxwell's equations. Therefore, the Maxwell's equations are transformed into stochastic differential equations, shown in (3) and (4). Furthermore, the output parameters E_x and H_y which we care about are also affected by the random event θ:

$$-\frac{\partial E_x(z,t,\theta)}{\partial z}=\mu(\theta)\frac{\partial H_y(z,t,\theta)}{\partial t}, \tag{3}$$

$$-\frac{\partial H_y(z,t,\theta)}{\partial z}=\varepsilon(\theta)\frac{\partial E_x(z,t,\theta)}{\partial t}+\sigma E_x(z,t,\theta). \tag{4}$$

Finite random variables can be used to model the random event θ shown as (5). According to the Karhunen-Loeve theory [11], the random variables can be obtained which are independent with each other. The independence is the basis of the subsequent processing:

$$\xi(\theta)=\{\xi_1(\theta),\ \xi_2(\theta),\ \cdots,\ \xi_n(\theta)\}. \tag{5}$$

As for the MC, the independent random variables are sampled according to their distributions, and a mass of certain Maxwell's equations will be obtained. By solving every certain Maxwell's equations, the statistical property of the solutions will be the answer of the uncertainty analysis.

Furthermore, in the results of the uncertainty analysis, there is no denying that the expectation and the variance are two main standards.

III. THE METHOD OF MOMENTS

The MoM is a traditional uncertainty analysis method with high computational efficiency. And it relies on first order truncated Taylor series expansions to obtain the estimates of the expectation and variance. The introduction of MoM is shown at first.

Suppose that *y* is the output parameter which we are interested in, and ξ_1 is the random variable that is modeled by the uncertain input parameters. The Taylor series form in the point $\xi_1=\overline{\xi_1}$ of one random variable is shown as (6):

$$\begin{aligned} y(\xi_1)&=y(\overline{\xi_1})+\left.\frac{dy}{d\xi_1}\right|_{\xi_1=\overline{\xi_1}}(\xi_1-\overline{\xi_1})\\ &+\left.\frac{d^2y}{d\xi_1^2}\right|_{\xi_1=\overline{\xi_1}}\frac{(\xi_1-\overline{\xi_1})^2}{2}+..., \end{aligned} \tag{6}$$

where $\overline{\xi_1}$ means the mean value of ξ_1. By using (6), the expectation of y and y^2 will be estimated, shown as (7) and (8):

$$E(y)=y(\overline{\xi_1})+\left.\frac{1}{2}\frac{d^2y}{d\xi_1^2}\right|_{\xi_1=\overline{\xi_1}}\sigma_{\xi_1}^2+..., \tag{7}$$

$$\begin{aligned} E(y^2)&=y^2(\overline{\xi_1})+\left.\frac{1}{2}\frac{d^2(y^2)}{d\xi_1^2}\right|_{\xi_1=\overline{\xi_1}}\sigma_{\xi_1}^2\\ &=y^2(\overline{\xi_1})+\left.\left[(\frac{dy}{d\xi_1})^2+\frac{dy}{d\xi_1}\frac{d^2y}{d\xi_1^2}\right]\right|_{\xi_1=\overline{\xi_1}}\sigma_{\xi_1}^2, \end{aligned} \tag{8}$$

where $\sigma_{\xi_1}^2$ is the variance value of the random variable ξ_1, and $E(y)$ is the expectation of the output parameter *y*.

Ignoring the higher order terms, the expectation and the variance of *y* can be obtained easily, shown as (9) and (10):

$$E(y)\approx y(\overline{\xi_1}), \tag{9}$$

$$\sigma(y)^2=E(y^2)-E(y)^2\approx(\frac{dy}{d\xi_1})^2\sigma_{\xi_1}^2. \tag{10}$$

Now, the MoM is generalized into multi-dimensional random variables. As for the random space shown as (5), two random variables $\xi(\theta)=\{\xi_1(\theta),\ \xi_2(\theta)\}$ are supposed. The results of the expectation and the variance in output parameters are shown in (11) and (12):

$$E(y(\xi))=y(\overline{\xi_1},\overline{\xi_2}), \tag{11}$$

$$\sigma(y(\xi))=\sqrt{(\frac{dy}{d\xi_1})^2\sigma_{\xi_1}^2+(\frac{dy}{d\xi_2})^2\sigma_{\xi_2}^2}, \tag{12}$$

where $y(\overline{\xi_1},\overline{\xi_2})$ stands for making certain simulation with the input parameters $\overline{\xi_1}$ and $\overline{\xi_2}$ by the use of certain EMC solver. The sensitivity from the input parameter to the output parameter is shown as (13):

$$\frac{dy(\xi)}{d\xi_1}=\frac{y(\overline{\xi_1}+\delta_1,\overline{\xi_2})-y(\overline{\xi_1},\overline{\xi_2})}{\delta_1}, \tag{13}$$

where δ_1 is a small perturbation chosen according to the variance of the input parameters [5].

From (11) and (12), it is clearly seen that only certain simulations in specific points are needed during the MoM. Thus, no changing in original solver makes the MoM easy to realize. Furthermore, just *N+1* times of the certain simulations will be enough in an uncertainty analysis problem with *N*-dimensional random variables, so the MoM is in a high computational efficiency. In another word, the MoM cannot be affected by 'curse of dimensionality'.

However, ignoring the higher order terms in the Taylor series will bring some errors; thus, next section presents an improved method which aims to decrease

such errors.

IV. THE IMPROVED METHOD OF MOMENTS

As (12) and (13) shown, the derivative needs to be estimated in calculating the variance. The bad estimation of the derivative may lead to the poor accuracy of the MoM.

The Richardson extrapolation is a method of numerical calculation which can improve the accuracy of calculating the derivative [7,8]. Furthermore, it can improve the accuracy in the variance calculating in the MoM.

According to (13), the error of the derivative calculating is in (14) and (15):

$$y(\xi_1+\delta_1)=y(\xi_1)+\delta_1\times y^{'}(\xi_1)+\frac{\delta_1^2}{2}\times y^{''}(\xi_1) +o(\delta_1^{\,2}), \tag{14}$$

$$y^{'}(x)=\frac{y(\xi_1+\delta_1)-y(\xi_1)}{\delta_1}-\frac{\delta_1}{2}\times y^{''}(\xi_1)+o(\delta_1), \tag{15}$$

where $o(\delta_1)$ stands for the infinitesimal of higher order of δ_1. Thus, the error of the estimation in (13) is $\frac{\delta_1}{2}\times y^{''}(\xi_1)-o(\delta_1)=o(1)$.

Suppose $N(\delta_1)=\frac{\mathrm{y}(\xi_1+\delta_1)-y(\xi_1)}{\delta_1}$, and (16) can be obtained by using (15):

$$y^{'}(\xi_1)=N(\delta_1)-\frac{\delta_1}{2}\times y^{''}(\xi_1)+o(\delta_1). \tag{16}$$

According to (16), (17) can be got easily by replacing δ_1 with $\frac{\delta_1}{2}$:

$$y^{'}(\xi_1)=N(\frac{\delta_1}{2})-\frac{1}{2}\times\frac{\delta_1}{2}\times y^{''}(\xi_1)+o(\delta_1). \tag{17}$$

Simple calculating process is done with (16) and (17), and the final result is shown in (19):

$$2\times y^{'}(\xi_1)=2\times N(\frac{\delta_1}{2})-\frac{\delta_1}{2}\times y^{''}(\xi_1)+o(\delta_1), \tag{18}$$

$$y^{'}(\xi_1)=2\times N(\frac{\delta_1}{2})-N(\delta_1)+o(\delta_1). \tag{19}$$

Obviously, the result in (15) is the calculating process in the MoM, the error is $o(1)$. On the other hand, the result derivative calculating in (19) is $2\times N(\frac{\delta_1}{2})-N(\delta_1)$, and the error is $o(\delta_1)$.

In terms of (19), (13) can be rewritten as it is shown in (20):

$$\frac{dy(\xi)}{d\xi_1}=2\times\frac{y(\overline{\xi_1}+\frac{\delta_1}{2},\overline{\xi_2})-y(\overline{\xi_1},\overline{\xi_2})}{\frac{\delta_1}{2}} -\frac{y(\overline{\xi_1}+\delta_1,\overline{\xi_2})-y(\overline{\xi_1},\overline{\xi_2})}{\delta_1}. \tag{20}$$

By combining (11) and (12), the uncertainty analysis results of the improved MoM can be obtained.

In this section, the Richardson extrapolation has been introduced into the MoM in estimating the variance. Furthermore, the improvement from $o(1)$ to $o(\delta_1)$, is clearly seen in mathematics. As for computational efficiency, in *N*-dimensional random variables, *2N+1* times of the certain simulations are needed. The computational efficiency in the improved MoM is slightly lower than the MoM, but it is also much higher than other methods. Furthermore, the proposed method retains all the advantages of the MoM.

V. ALGORITHM VALIDATION

In this section, a simple example in EMC uncertainty analysis is shown in order to observe the improvement. The example is published in literature [7].

One dimension wave propagation example with uncertainty medium parameters is shown as Fig. 1. The space step is $1.5\times10^{-2}m$ and the time step is $5.0\times10^{-11}s$. The number of discrete points in the electric field intensity is 151, and it is 150 in the magnetic field intensity. The sine excitation source is in the first discrete point with the amplitude $2.7\times10^{-3}V/m$ and the frequency $1.0\times10^{9}Hz$.

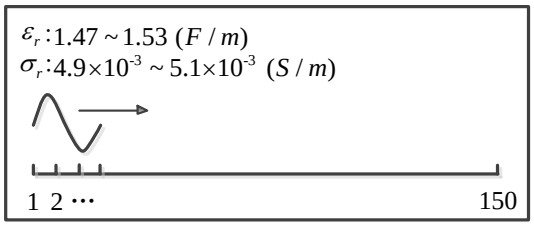

Fig. 1. The model of the example.

Suppose that the dielectric coefficient ε_r and the conductivity σ_r are uncertain parameters, and they are both in uniform distribution. The dielectric coefficient is $1.47\sim1.53(F/m)$, and the conductivity is $4.9\times10^{-3}\sim5.1\times10^{-3}(S/m)$.

The random variables ξ_1 and ξ_2 can be used to model such uncertain input parameters, as (21) and (22)

shown:

$$\varepsilon_r = \varepsilon_r^* \times (1 + 0.02 \times \xi_2), \quad (21)$$

$$\sigma_r = \sigma_r^* \times (1 + 0.02 \times \xi_1), \quad (22)$$

where, the mean values of the input parameters are $\varepsilon_r^* = 1.5\ (F/m)$ and $\sigma_r^* = 5 \times 10^{-3}\ (S/m)$. The distributions of the random variables are both uniform distribution in [-1, 1].

The small perturbations δ_1 and δ_2 are chosen as (23) and (24) shown:

$$\delta_1 = \varepsilon_r^* \times 0.02 = 0.03\ (F/m), \quad (23)$$

$$\delta_2 = \sigma_r^* \times 0.02 = 0.1 \times 10^{-3}\ (S/m). \quad (24)$$

Three uncertainty analysis methods, the MC, the MoM and the improved MoM are used in calculating this example. The certain simulation solver is the finite difference time domain (FDTD). The number of iteration times in time is 200.

Figure 2 shows the results in expectation, and it is calculated according to (11). The expectation of the magnetic field intensity and the electric field intensity in every discrete point is given, which is calculated by three different uncertainty analysis methods.

Table 1 is the evaluation result of the simulation results in Fig. 2 by using FSV. FSV can provide the credibility evaluation result in EMC simulation results. Both qualitative and quantitative description can be given. Total-GDM, a value to give a quantitative description in FSV, manifests the validity of simulation result. More details can be found in [12,13].

Taking the results calculated by the MC as the standard data, the value in Table 1 is the total-GDM value between the MC results and another method's results. According to the criterion in FSV [12,13], the calculated results in the MoM or the improved MoM are both 'Excellent'.

Figure 3 shows the results in variance in every discrete point, and Table 2 is the calculating results by using FSV. In Table 2, the result in the MoM is 'Very Good' and the improved MoM is 'Excellent'.

In other words, the improved MoM is as accurate as the MC, and much more accurate than the MoM. Thus, the improvement of the improved MoM is obvious.

At last, the computational efficiency of three methods is compared in Table 3. The MoM and the improved MoM are in the same level, but the computational efficiency of the MC is much lower than them. The simulation times in MC are 4000, and the results would be proved convergence by using the judgment method mentioned in literature [5].

In conclusion, a simple example of EMC uncertainty analysis is given in the section, and it is proved that the improvement of the proposed method is obvious by the use of the FSV. And only a little additional calculating is needed in the improvement.

In a word, the improved MoM can reach a high accuracy with high computational efficiency.

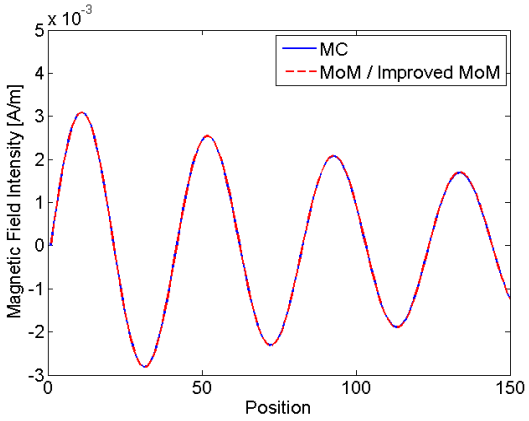

(a) Magnetic field intensity

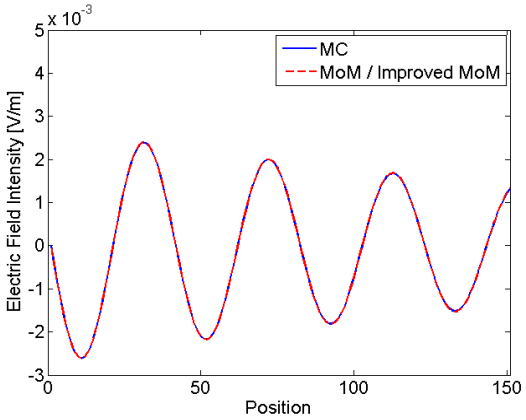

(b) Electric field intensity

Fig. 2. The results in expectation.

Table 1: The total-GDM value of the results in expectation

Expectation	MoM/Improved MoM
Electric field intensity	0.0062
Magnetic field intensity	0.0054

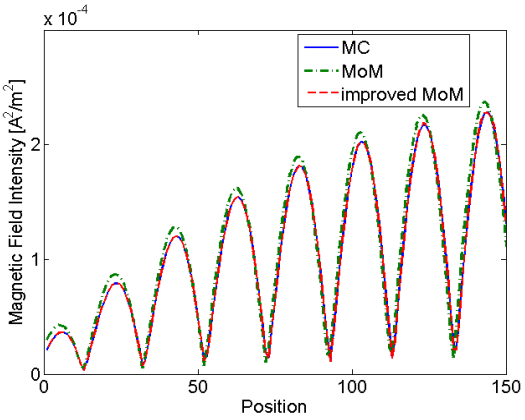

(a) Magnetic field intensity

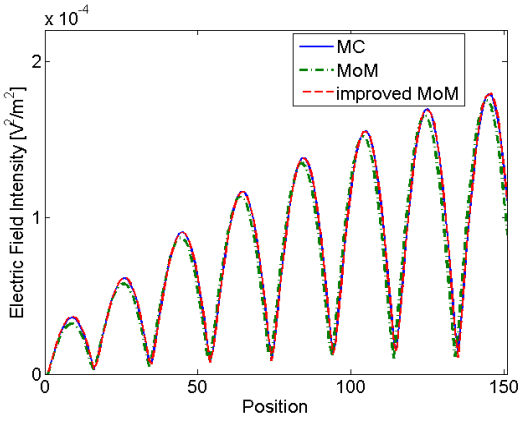

(b) Electric field intensity

Fig. 3. The results in variance.

Table 2: The total-GDM value of the results in variance

Variance	MoM	Improved MoM
Electric field intensity	0.1686	0.0192
Magnetic field intensity	0.1561	0.0109

Table 3: The comparison of computational efficiency

	MC	MoM	Improved MoM
Simulation time	86.5s	0.06s	0.1s
Times	4000	3	5

VI. CONCLUSION

In this paper, a novel method based on Richardson extrapolation is presented to make uncertainty analysis in EMC simulation, aiming at improving the accuracy of the MoM. By using a published example, the improvement of the proposed method is obviously shown. In conclusion, it is proved that the proposed method not only improves the accuracy greatly, but also remains all the advantages in the MoM.

ACKNOWLEDGMENT

This work was supported by the National Natural Science Foundational of China under Grant 51507041.

REFERENCES

[1] M. Wu, et al., "Estimation of the statistical variation of crosstalk in wiring harnesses," *IEEE International Symposium on Electromagnetic Compatibility*, pp. 1-7, 2008.

[2] G. Spadacini and S. A. Pignari, "Numerical assessment of radiated susceptibility of twisted-wire pairs with random nonuniform twisting," *IEEE Transactions on Electromagnetic Compatibility*, vol. 55, no. 5, pp. 956-964, 2013.

[3] D. Srivastava, et al., "Computation of protection zone of a lightning rod using method of moments and Monte Carlo integration technique," *Journal of Electromagnetic Analysis and Applications*, vol. 3, no. 4, pp. 118-121, 2011.

[4] P. Manfredi and F. G. Canavero, "Polynomial chaos representation of transmission-line response to random plane waves," *2012 International Symposium on Electromagnetic Compatibility*, pp. 1-6, 2012.

[5] R. S. Edwards, A. C. Marvin, and S. J. Porter, "Uncertainty analyses in the finite-difference time-domain method," *IEEE Transactions on Electromagnetic Compatibility*, vol. 52, no. 1, pp. 155-163, 2010.

[6] Y. Bagci, et al., "A fast Stroud-based collocation method for statistically characterizing EMI/EMC phenomena on complex platforms," *IEEE Transactions on Electromagnetic Compatibility*, vol. 51, no. 2, pp. 301-311, 2009.

[7] B. Jinjun, Z. Gang, et al., "Uncertainty analysis in EMC simulation based on Stochastic collocation method," *2015 IEEE International Symposium on Electromagnetic Compatibility*, pp. 930-934, 2015.

[8] R. W. Walters and L. Huyse, *Uncertainty Analysis for Fluid Mechanics with Applications*, no. ICASE-2002-1, NASA/CR-2002-211449, REC Warangal, 2002.

[9] S. A. Richards, "Completed Richardson extrapolation in space and time," *Communications in Numerical Methods in Engineering*, vol. 13, no. 7, pp. 573-582, 1997.

[10] P. J. Roache, Patrick and P. M. Knupp, "Completed Richardson extrapolation," *Communications in Numerical Methods in Engineering*, vol. 9, no. 5, pp. 365-374, 1993.

[11] M. Loeve, *Probability Theory*, Springer-Verlag Berlin and Heidelberg GmbH & Co.K, 1978.

[12] IEEE Standard for Validation of Computational Electromagnetics Computer Modeling and Simulations, IEEE STD 15971-2008, pp. 1-41, 2008.

[13] IEEE Recommended Practice for Validation of Computational Electromagnetics Computer Modeling and Simulations, IEEE STD 15972-2010, pp. 1-124, 2011.

Jinjun Bai received the B.Eng. degree in Electrical Engineering and Automation from the Harbin Institute of Technology, Harbin, China, in 2013.

He is currently working toward the Ph.D. degree in Electrical Engineering at the Harbin Institute of Technology, Harbin, China. His research interests

include uncertainty analysis methods in EMC simulation and the credibility evaluation of uncertainty analysis results in EMC simulation.

Gang Zhang received the B.Sc. in Electrical Engineering from China University of Petroleum, Dongying, China, in 2007, and the M.Sc. and Ph.D. degrees in Electrical Engineering from Harbin Institute of Technology (HIT), Harbin, China, in 2009 and 2014, respectively.

He is now with the Faults Online Monitoring and Diagnosis Laboratory at Harbin Institute of Technology. His research interests include analysis of electromagnetic compatibility, electromagnetic simulation, and the validation of CEM.

Lixin Wang received the B.S. degree in Electrical Engineering from Nankai University, Tianjin, China, in 1988, and the M.S. and D.Sc. degrees in Electrical Engineering from Harbin Institute of Technology (HIT), Harbin, China, in 1991 and 1999, respectively.

He is currently a Professor of Power Electronic and Electric Drives at the HIT. He conducts research with Faults Online Monitoring and Diagnosis Laboratory, HIT, on a wide variety of topics including electromagnetic compatibility at the electronic system level, aircraft electromechanical fault diagnosis expert system and prediction and health management (PHM) of Li-ion battery.

Tianhao Wang received the B.Eng. degree in Electrical Engineering and Automation from the Harbin Institute of Technology (HIT), Harbin, China, in 2014.

She is currently working toward the M.Sc. degree in HIT and involving in the research of uncertainty analysis method of random cables.

An Algorithm for Calculating Transient Magnetic Field and Induced Voltage Inside Wind Turbine Tower Under Lightning Stroke

Zhang Xiaoqing and Zhang Yongzheng

School of Electrical Engineering
Beijing Jiaotong University, Beijing, 100044, China
zxqiong@hotmail.com, zhangyz2@126.com

Abstract ─ This paper proposes an efficient algorithm for predicting the transient magnetic field and induced voltage inside wind turbine tower under lightning stroke. The continuous tower body is simplified as a discrete multiconductor system consisting of longitudinal and transverse branches. On the basis of the lightning current responses in the multiconductor system, the analytic formulas of the transient magnetic field are derived from the vector potential. These formulas can take account of the impact of the wavefront steepness of lightning current on the transient magnetic field. A discretization scheme is further presented to calculate the magnetic flux passing through a conductor loop. The induced voltage can be determined by finding the time rate of change of the magnetic flux. The results obtained from the proposed algorithm are also compared with those from the software Ansoft and circuit method.

Index Terms ─ Induced voltage, lightning, magnetic field, transient analysis, wind turbine tower.

I. INTRODUCTION

With a rapid growth in the utilization of wind energy for electric power supply, wind turbines (WTs) have recently increased constantly in size and rated capacity. WTs are particularly susceptible to lightning stroke owing to their tall structure and exposed position. When a lightning strikes directly to a WT, a large lightning current flows through the body of the WT and generates the transient magnetic field inside its tower. There are a considerable number of conductor loops formed by power lines, signal cables and metal conduits in the bottom space of the tower. The transient magnetic field passes through these conductor loops and induces high voltages in them. It is well known that electronic equipment is very sensitive to the electromagnetic interference and has rather low insulation strength. Component failure and equipment damage may be caused by the transient magnetic field and induced voltage. From the point of view of lightning protection design of WTs, it is necessary to predict the transient magnetic field and induced voltage inside the tower under lightning stroke. However, previous research mainly focused on the circuit analysis of the lightning transients of WTs. A few models were presented for predicting the lightning surge overvoltage and transient potential rise in WT systems [1-3]. There is almost no published literature on calculation of the transient magnetic field and induced voltage inside the tower. Although a set of empirical formulas have been given for estimation of the induced voltage amplitude [4-5], these formulas lack a high precision and fail to give the complete induced voltage waveform due to a deficiency in the exact analysis of the transient magnetic field. For an improvement on calculation of the transient magnetic field and induced voltage inside the tower, an efficient algorithm is proposed in this paper. In the proposed algorithm, the differential formulas of the transient magnetic field are first derived from the vector potential. A suitable discretization scheme is implemented to determine the magnetic flux passing through the conductor loop. Then, the induced voltage can be obtained by calculating the time rate of change of the magnetic flux. A numerical example has been given for examining the validity of the proposed algorithm, which shows that the proposed algorithm has the capability of quantitatively predicting the transient magnetic field and induced voltage inside the tower.

II. DISCRETIZATION DESCRIPTION OF WT TOWER

An actual WT tower is a tubular circular truncated cone, as shown in Fig. 1 (a). During a lightning stroke, the lightning current usually injects into the tower body from its top. For the purpose of electromagnetic transient analysis, the continuous conducting shell of the tower body may be divided into a discrete multiconductor system formed by longitudinal and transverse branches, as illustrated in Fig. 1 (b) [2-3, 6]. In the multiconductor system, each segmental arc of the transverse braches is replaced by its respective chord for simplification of the transient calculation. All the branches are taken as the

Submitted On: June 20, 2015
Accepted On: December 5, 2015

cylindrical conductors and the radii are estimated from their respective average cross-sections. Then, the multiconductor system is converted into an equivalent circuit consisting of resistances, inductances and capacitances. A current source representing the injected lightning current is applied to the top nodes of the equivalent circuit, whose parameters are taken from the technical specification of lightning protection [7]. The current distribution on all the branches can be determined by numerically solving the node voltage equations of the equivalent circuit. The detailed calculating procedure has been given in [2-3, 8-9] and will not been described here. On the basis of the current distribution, the transient magnetic field can be further calculated inside the tower.

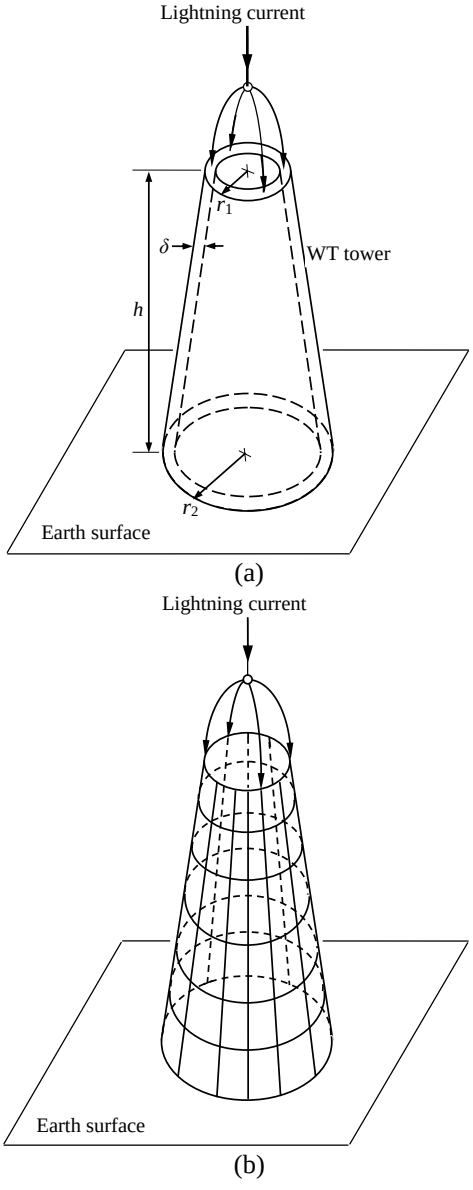

Fig. 1. (a) Tower body and (b) multiconductor system.

III. TRANSIENT MAGNETIC FIELD EQUATIONS

The transient electromagnetic fields in free space may be described by the time-dependent Maxwell equations. Considering the need of analyzing the magnetic induction effect, the solution of Maxwell equations is discussed only for magnetic field. The solution of magnetic field is based on the vector potential $\boldsymbol{A}$:

$$\boldsymbol{B} = \nabla \times \boldsymbol{A}. \tag{1}$$

The general expression of the vector potential $\boldsymbol{A}$ is [10]:

$$\boldsymbol{A}(\boldsymbol{r},t) = \frac{\mu_0}{4\pi}\int_{\Omega} \frac{\boldsymbol{J}(\boldsymbol{r}', t-\frac{R}{c})}{R} d\Omega, \tag{2}$$

where μ_0 is the permeability ($4\pi\times10^{-7}$H/m), c is the speed of light, ε_0 is the permittivity [($10^{-9}/36\pi$) F/m] and $\boldsymbol{J}$ is the current density. The geometric factors associated with (2) are illustrated in Fig. 2. For a longitudinal branch in the multiconductor system, as shown in Fig. 3, consider a differential current-carrying segment d$\boldsymbol{l}$. In cylindrical coordinates, the differential current element $\boldsymbol{J}(\boldsymbol{r}', t–R/c)\mathrm{d}\Omega$ becomes $i(r', \alpha, z', t–R/c)\mathrm{d}\boldsymbol{l}$ and the resulting differential vector potential is found by [11-13]:

$$\mathrm{d}\boldsymbol{A} = \frac{\mu_0}{4\pi}\frac{1}{R} i(r', \alpha, z', t - R/c)\mathrm{d}\boldsymbol{l}. \tag{3}$$

Substituting $\mathrm{d}\boldsymbol{l} = \mathrm{d}l\cos\gamma\mathbf{r} + \mathrm{d}l\sin\gamma\mathbf{k}$ into (3) yields:

$$\begin{aligned} \mathrm{d}\boldsymbol{A}_\theta &= 0 \\ \mathrm{d}\boldsymbol{A}_r &= \frac{\mu_0 \mathrm{d}l\cos\gamma}{4\pi}\frac{1}{R} i(r', \alpha, z', t - R/c)\mathbf{r} \\ \mathrm{d}\boldsymbol{A}_z &= \frac{\mu_0 \mathrm{d}l\sin\gamma}{4\pi}\frac{1}{R} i(r', \alpha, z', t - R/c)\mathbf{k}. \end{aligned} \tag{4}$$

In terms of (1) and (4), the differential magnetic flux density due to d$\boldsymbol{l}$ can be derived from the differential vector potential d$\boldsymbol{A}$:

$$\begin{aligned} \mathrm{d}\boldsymbol{B} = \nabla\times(\mathrm{d}\boldsymbol{A}) = \frac{1}{r}\frac{\partial(\mathrm{d}A_z)}{\partial\theta}\mathbf{r} - \Big[\frac{\partial(\mathrm{d}A_z)}{\partial r} \\ - \frac{\partial(\mathrm{d}A_r)}{\partial z}\Big]\boldsymbol{\theta} - \frac{1}{r}\frac{\partial(\mathrm{d}A_r)}{\partial\theta}\mathbf{k}. \end{aligned} \tag{5}$$

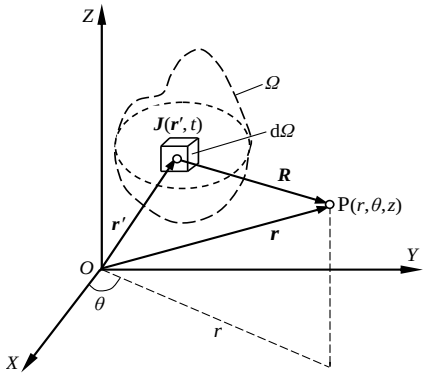

Fig. 2. Geometry for general expression of vector potential.

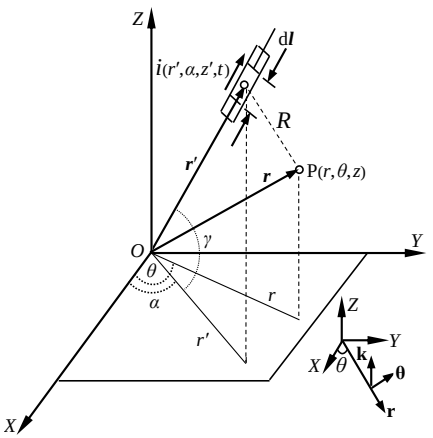

Fig. 3. A longitudinal branch.

In Fig. 3, R may be expressed by:

$$R=\sqrt{r^2+r'^2-2rr'\cos(\theta-\alpha)+(z-z')^2}. \tag{6}$$

Letting $\xi=t-R/c$ and $\Phi=\theta-\alpha$, the derivatives of $i(r',\alpha,z',t-R/c)$ with respect to r,θ,z and t are written by:

$$\begin{aligned}
\frac{\partial}{\partial r}\left[i(r',\alpha,z',t-R/c)\right]&=-\frac{r-r'\cos\Phi}{cR}\cdot\frac{\partial i(r',\alpha,z',\xi)}{\partial\xi}\\
\frac{\partial}{\partial\theta}\left[i(r',\alpha,z',t-R/c)\right]&=-\frac{rr'\sin\Phi}{cR}\cdot\frac{\partial i(r',\alpha,z',\xi)}{\partial\xi}\\
\frac{\partial}{\partial z}\left[i(r',\alpha,z',t-R/c)\right]&=-\frac{(z-z')}{cR}\cdot\frac{\partial i(r',\alpha,z',\xi)}{\partial\xi}\\
\frac{\partial}{\partial t}\left[i(r',\alpha,z',t-R/c)\right]&=\frac{\partial i(r',\alpha,z',\xi)}{\partial\xi}.
\end{aligned} \tag{7}$$

This follows that:

$$\begin{aligned}
\frac{\partial}{\partial r}\left[i(r',\alpha,z',t-R/c)\right]&=-\frac{r-r'\cos\Phi}{cR}\cdot\frac{\partial i(r',\alpha,z',t-R/c)}{\partial t}\\
\frac{\partial}{\partial\theta}\left[i(r',\alpha,z',t-R/c)\right]&=-\frac{rr'\sin\Phi}{cR}\cdot\frac{\partial i(r',\alpha,z',t-R/c)}{\partial t}\\
\frac{\partial}{\partial z}\left[i(r',\alpha,z',t-R/c)\right]&=-\frac{z-z'}{cR}\cdot\frac{\partial i(r',\alpha,z',t-R/c)}{\partial t}.
\end{aligned} \tag{8}$$

The following derivatives can be given from (6):

$$\begin{aligned}
\frac{\partial}{\partial r}\left(\frac{1}{R}\right)&=-\frac{r-r'\cos\Phi}{R^3}\\
\frac{\partial}{\partial\theta}\left(\frac{1}{R}\right)&=-\frac{rr'\sin\Phi}{R^3}\\
\frac{\partial}{\partial z}\left(\frac{1}{R}\right)&=-\frac{z-z'}{R^3}.
\end{aligned} \tag{9}$$

Substituting (4), (8) and (9) into (5) leads to the differential magnetic flux density:

$$\begin{aligned}
d\boldsymbol{B}_l=&-\frac{\mu_0 dl\sin\gamma}{4\pi}\left[\frac{r'\sin\Phi}{R^3}i(r',\alpha,z',t-R/c)\right.\\
&\left.+\frac{r'\sin\Phi}{cR^2}\frac{\partial i(r',\alpha,z',t-R/c)}{\partial t}\right]\mathbf{r}\\
&+\frac{\mu_0 dl\sin\gamma}{4\pi}\left[\frac{r-r'\cos\Phi}{R^3}i(r',\alpha,z',t-R/c)\right.\\
&+\frac{z-z'}{cR^2}\frac{\partial i(r',\alpha,z',t-R/c)}{\partial t}\\
&-\frac{\cot\gamma(z-z')}{R^3}i(r',\alpha,z',t-R/c)\\
&\left.-\frac{\cot\gamma(z-z')}{cR^2}\frac{\partial i(r',\alpha,z',t-R/c)}{\partial t}\right]\boldsymbol{\theta}\\
&+\frac{\mu_0 dl\cos\gamma}{4\pi}\left[\frac{r'\sin\Phi}{R^3}i(r',\alpha,z',t-R/c)\right.\\
&\left.+\frac{r'\sin\Phi}{cR^2}\frac{\partial i(r',\alpha,z',t-R/c)}{\partial t}\right]\mathbf{k}.
\end{aligned} \tag{10}$$

In a similar manner, the transient magnetic field equation can be derived for a transverse branch in the multiconductor system. As shown in Fig. 4, the differential magnetic flux density is given by:

$$\begin{aligned}
d\boldsymbol{B}_t=&\frac{\mu_0 dl\sin\varphi}{4\pi}\left[\frac{z-z'}{R^3}i(r',\alpha,z',t-R/c)\right.\\
&\left.+\frac{z-z'}{cR^2}\frac{\partial i(r',\alpha,z',t-R/c)}{\partial t}\right]\mathbf{r}\\
&-\frac{\mu_0 dl\cos\varphi}{4\pi}\left[\frac{z-z'}{R^3}i(r',\alpha,z',t-R/c)\right.\\
&\left.+\frac{z-z'}{cR^2}\frac{\partial i(r',\alpha,z',t-R/c)}{\partial t}\right]\boldsymbol{\theta}\\
&+\frac{\mu_0 dl\sin\varphi}{4\pi}\left[\frac{R^2-r^2+rr'\cos\Phi}{R^3r}\right.\\
&\cdot i(r',\alpha,z',t-R/c)-\frac{r-r'\cos\Phi}{cR^2}\\
&\cdot\frac{\partial i(r',\alpha,z',t-R/c)}{\partial t}\\
&+\frac{\cot\varphi\, r'\sin\Phi}{R^3}i(r',\alpha,z',t-R/c)\\
&\left.+\frac{\cot\varphi\, r'\sin\Phi}{cR^2}\frac{\partial i(r',\alpha,z',t-R/c)}{\partial t}\right]\mathbf{k}.
\end{aligned} \tag{11}$$

On the right-hand sides of (10) and (11), the terms including the current are the induction field and are the radiation field [14]. The radiation field can reflect the impact of the wavefront steepness of lightning current on the transient magnetic field. In addition, the presence of the ground is taken into account by the image method [10,13]. The image branches are installed below the earth surface. From the point of view of engineering application, the real and the image branches are considered to be symmetrical about the earth surface [10,15]. Each branch, whether it is the real or the image, needs to be subdivided into a sufficient number of segments [16]. The length of each segment is so short that the current distribution on it is approximately uniform. Then, (10) or (11) is used to calculate its magnetic field component. The magnetic flux density at an arbitrary spatial point inside the tower can be found by vectorially summing the magnetic field components contributed from the short segments on all the real and the image branches.

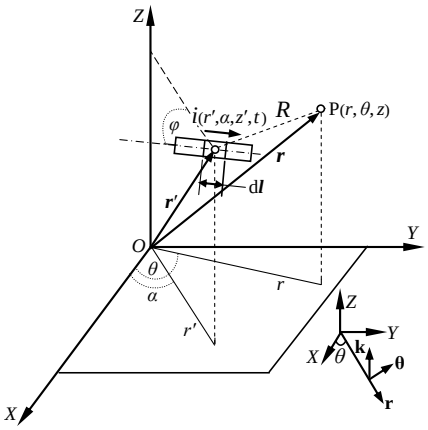

Fig. 4. A transverse branch.

IV. CALCULATION OF INDUCED VOLTAGE

A spatial conductor loop is shown in Fig. 5. The magnetic flux passing through the loop can be expressed by the surface integral of the magnetic flux density:

$$\Psi(t) = \int_S \boldsymbol{B} \cdot \mathrm{d}\boldsymbol{S}. \tag{12}$$

From Faraday's law of electromagnetic induction, the induced voltage in the loop is calculated by the time rate of change of the magnetic flux:

those including the first derivative of the current

$$u(t) = \frac{d\Psi(t)}{dt}. \tag{13}$$

Since the magnetic field distribution on the surface of the loop is usually non-uniform, the surface needs to be subdivided into a series of subareas. On each subarea, the magnetic flux density is considered to be uniform. With such a discrete approximation to (13), the magnetic flux is calculated by:

$$\Psi(j\Delta t) \approx \sum_{k=1}^{N} B_k(j\Delta t)\Delta S_k \cos\theta_k \quad (j = 1, 2\cdots, J_{\mathrm{m}}), \tag{14}$$

where Δt is the time step, N is the total number of the subareas and J_{m} is the maximum number of the time steps. In terms of (13) and (14), the induced voltage can be determined by:

$$u(j\Delta t) = \frac{\Psi(j\Delta t) - \Psi((j-1)\Delta t)}{\Delta t} \quad (j = 1, 2\cdots, J_{\mathrm{m}}). \tag{15}$$

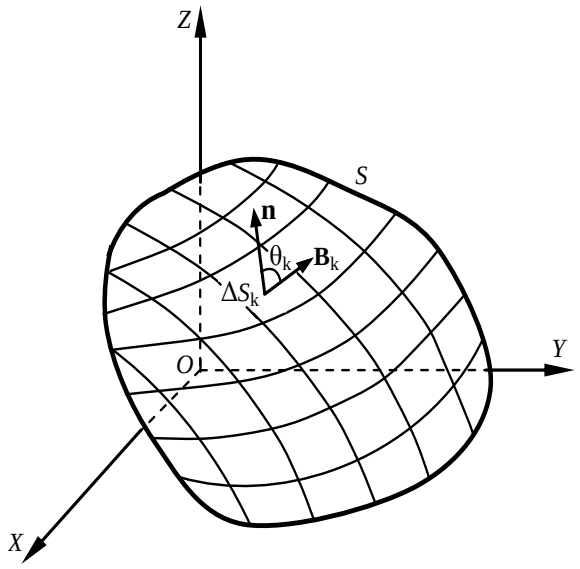

Fig. 5. Subdivision of the loop surface.

V. NUMERICAL EXAMPLE

A. Magnetic field

A Chinese-built WT with rated power of 2MW is considered here. The dimensions of its tower are r_1=1.32 m, r_2 = 2.1 m, h = 81.5 m and δ = 0.024 m, as shown in Fig. 6 (a). The parameters of the injected lightning current are 10/350 μs and 100 kA [7]. The amplitude distributions of the magnetic flux density are calculated for two cross-sections locating at z = 80 m and z = 40 m, as shown in Figs. 6 (b)-(c). Due to the spatial distribution symmetry, only a quarter of each distribution surface is depicted here. For the spatial points on the plumb line bounded by (1.3 m, π/4, 40 m) and (1.3 m, π/4, 80 m), the magnetic flux density amplitudes are also given in Fig. 6 (d), which are calculated by the proposed algorithm and software Maxwell 3D of Ansoft [6,17], respectively. The Ansoft calculation is based on the finite-element method (FEM). It can be seen from Figs. 6 (b)-(c) that, the magnetic flux density becomes higher near the tower wall and reaches a maximum under the point where the lightning current is injected. By contrast, the magnetic field is rather weak in the central zone.

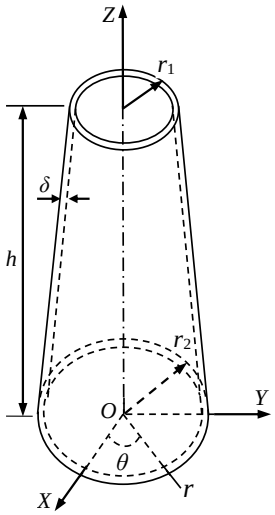

(a)

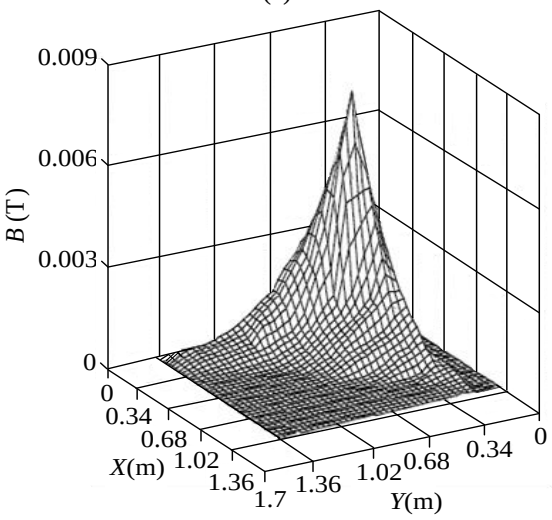

(b)

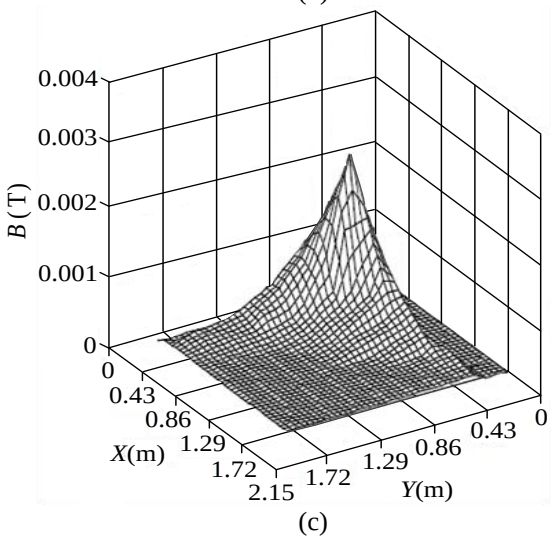

(c)

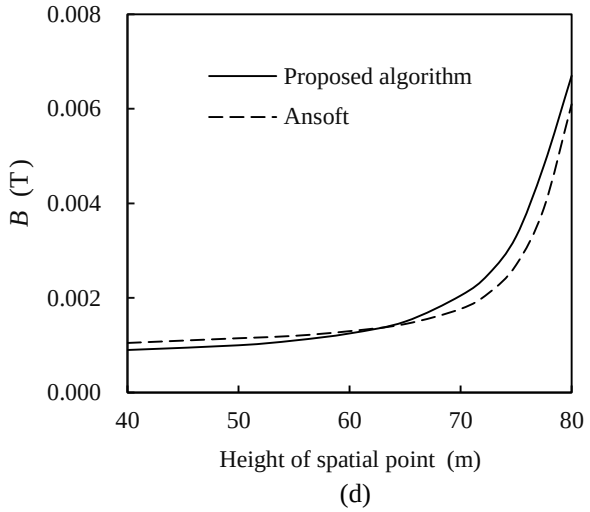

(d)

Fig. 6. (a) Dimension of the tower; (b) amplitude distribution of magnetic flux density at z = 80 m; (c) amplitude distribution of magnetic flux density at $z = 40$ m; (d) magnetic flux density amplitudes on the plumb line.

B. Induced voltage

The dimensions of the tower and lightning current parameters are the same as above. A square conductor loop with 0.3 m × 0.3 m is located on the plane YOZ, as illustrated in Fig. 7 (a). The geometric center of the loop is positioned on a line with two endpoints A and B. The coordinates of A and B are (1.0 m, π/2, 10 m) and (1.0 m, π/2, 0.16 m). Figures 7 (b) and (c) show the induced voltage waveforms at geometric centers A and B, respectively. Figure 7 (d) gives the induced voltage amplitudes at the distinct geometric centers along the line AB, where the corresponding results calculated by the circuit method are given simultaneously for comparison. In the circuit method, each side of the loop is represented by a π-type circuit consisting of resistance, inductance and capacitance. The induction effect is simulated by the mutual inductances and coupling capacitances between the sides of the loop and branches of the multiconductor system of the tower [18]. The corresponding simulation procedure has been stated in [18-19]. Figure 7 signifies that the induced voltage levels are high and can cause serious damage to the electronic equipment involved in these loops during a lightning stroke.

In Fig. 6 (d) and Fig. 7 (d), comparison of the results obtained from the proposed algorithm with those from the software Ansoft and circuit method shows that a better agreement appears between them. To a large extent, this confirms the validity of the proposed algorithm.

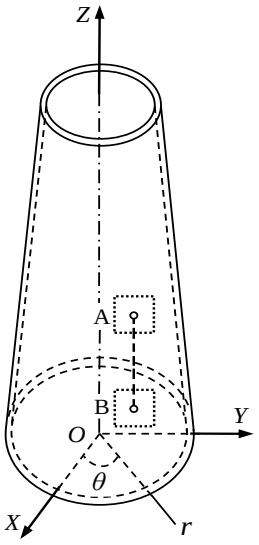

(a)

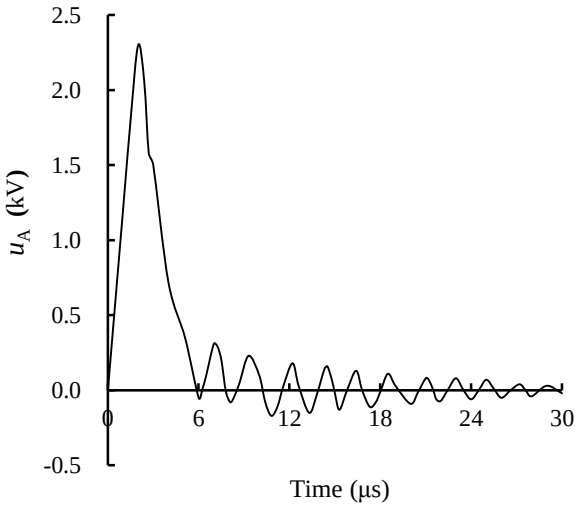

(b)

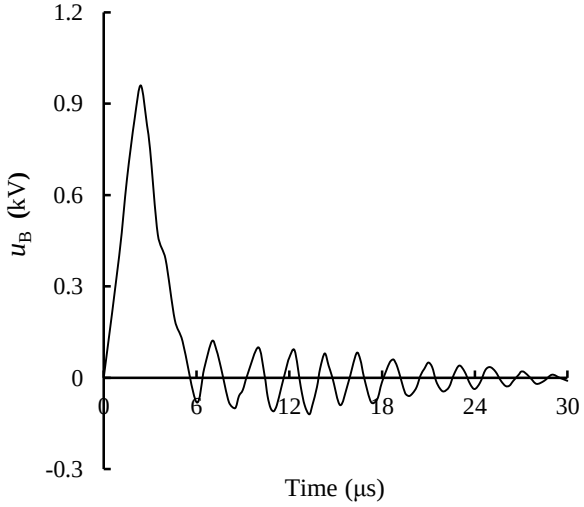

(c)

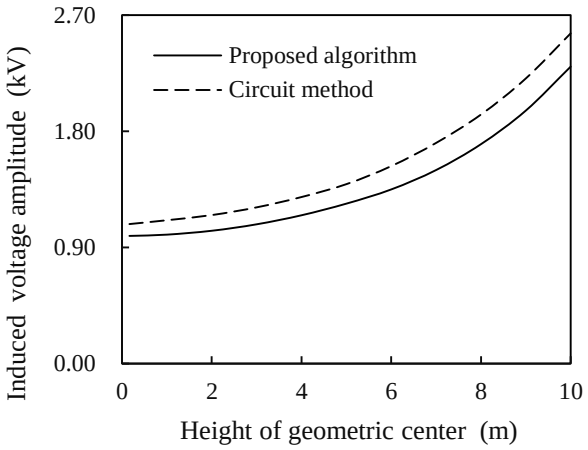

(d)

Fig. 7. (a) Conductor loop inside the tower; (b) induced voltage waveform in geometric center A; (c) induced voltage waveform in geometric center B; (d) amplitude distribution of induced voltage on line AB.

VI. CONCLUSION

An efficient algorithm has been proposed for predicting the transient magnetic field and induced voltage inside the WT tower under lightning stroke. The proposed algorithm simplifies the large-sized continuous tower body into a discrete multiconductor system. Based on the vector potential, analytic formulas have been presented for calculating the transient magnetic field generated by longitudinal and transverse current-carrying branches in the multiconductor system. The magnetic flux passing through a conductor loop is determined by evaluating the surface integral of the transient magnetic field over the surface of the conductor loop in a discretization manner. The induced voltage in the conductor loop can be obtained by finding the time rate of change of the magnetic flux. A numerical example has been given for an actual WT tower and the validity of the proposed algorithm has been checked by comparing the results obtained from the proposed algorithm with those from the software Ansoft and circuit method. The proposed algorithm is useful in quantitative prediction of the transient magnetic field and induced voltage inside the large-sized WT tower and can provide a basis for lightning protection design of multi-megawatt WTs.

ACKNOWLEDGMENT

This work is partly supported by National Natural Science Foundation of China under Award no. 51477007.

REFERENCES

[1] D. Romero, J. Montanyà, and A. Candela,

"Behavior of the wind-turbines under lightning strikes including nonlinear grounding system," *International Conference on Renewable Energy and Power Quality*, Barcelona, Spain, pp. 1-6, 1-2 Apr. 1-2, 2004.

[2] X. Q. Zhang, Y. Z. Zhang, and C. H. Liu, "A complete model of wind turbines for lightning transient analysis," *Journal of Renewable and Sustainable Energy*, vol. 6, 013113, 2014.

[3] X. Q. Zhang, "Lightning transient simulation of wind turbine towers," *International Review of Electrical Engineering*, vol. 7, no. 1, pp. 3505-3511, 2012.

[4] IEC 62305-4: 2006, IDT, *Protection against Lightning—Part 4: Electrical and Electronic Systems within Structures*, IEC Geneva, Switzerland, 2006.

[5] P. Hasse, *Overvoltage Protection of Low Voltage Systems*, The Institution of Engineering and Technology, London, UK, 2008.

[6] C. Buccella and A. Orlandi, "An efficient technique for the evaluation of lightning-induced voltage in a cylindrical vessel containing charged oil," *IEEE Trans. Industry Applications*, vol. 39, no. 2, pp. 368-373, 2003.

[7] National Standard, GB 50057-2010, *Design Code for Protection of Structures Against Lightning*, Chinese Plan Press, Beijing, China, 2010.

[8] L. Sluis, *Transients in Power Systems*, John Wiley & Sons Ltd., 2002

[9] X. Q. Zhang, "Calculation of lightning transient responses on wind turbine towers," *Mathematical Problems in Engineering*, vol. 2013, Article ID 757656, pp. 1-9, 2013

[10] C. Z. Feng, *Electromagnetic Field Theory*, Higher Education Press, Beijing, China, 2002.

[11] G. Guarnieri, S. Selleri, G. Pelosi, C. Dedeban, and C. Pichot, "Innovative basis and weight functions for wire junctions in time domain moment method," *IEE Proceedings Microwaves, Antennas and Propagation*, vol. 153, no. 1, pp. 61-66, 2006.

[12] Z. X. Zhou and J. S. Tyo, "An adaptive time-domain integral equation method for transient analysis of wire scatterer," *IEEE Trans. Antennas and Wireless Propagation Letters*, vol. 49, no. 8, pp. 1123-1129, 2001.

[13] B. S. Gru and H. R. Hiziroğlu, *Electromagnetic Field Theory Fundamentals*, Cambridge University Press, Cambridge, UK, 2004.

[14] F. Rachidi, W. Janischewskyj, A. M. Hussein, C. A. Nucci, S. Guerrieri, B. Kordi, and J. S. Chang, "Current and electromagnetic field associated with lightning-return strokes to tall towers," *IEEE Trans. Electromagnetic Compatibility*, vol. 43, no. 3, pp. 356-367, 2001.

[15] D. Pavanello, F. Rachidi, M. Rubinstein, J. L. Bermudez, and C. A. Nucci, "On the calculation of electromagnetic fields radiated by lightning to tall structures," 27th *International Conference on Lightning Protection*, Avignon, France, pp. 1-8, Sep. 13-16, 2004.

[16] A. R. Bretones, R. G. Martin, and A. Salinas, "Dotig1, a time-domain numerical code for the study of the interaction of electromagnetic pulses with thin-wire structures," *Compel-The International Journal for Computation and Mathematics in Electrical and Electronic Engineering*, vol. 8, no. 1, pp. 39-61, 1989.

[17] Ansoft User's Guide–Maxwell 3D, 2006

[18] S. Cristina and A. Orlandi, "Calculation of the induced effects due to a lightning stroke," *IEE Proceedings-B*, vol. 139, no. 4, pp. 374-380, 1992.

[19] U. Y. Iosseli, A. S. Kothanov, and M. G. Stlyrski, *Calculation of Capacitances*, Electric Power Press, Moscow, Russia, 1987.

Zhang Xiaoqing received the M.Sc. and Ph.D. degrees from Tsinghua University, Beijing, China, in 1985 and 1990, respectively, both in High Voltage Engineering. Since 1993, he has been in the School of Electrical Engineering, Beijing Jiaotong University, where he is currently a Senior Research Fellow. His research interests include electromagnetic transient simulation, lightning protection and high voltage insulation.

Comparison of Evolutionary Algorithms for Optimal Design of Broadband Multilayer Microwave Absorber for Normal and Oblique Incidence

Subhanwit Roy, Ananya Mahanti, Souptik Dutta Roy, and G. K. Mahanti

Department of Electronics and Communication Engineering
National Institute of Technology, Durgapur, West Bengal, 713209, India
subhanwit.roy@gmail.com, ananyamahanti@gmail.com, duttaroy.souptik@gmail.com, gautammahanti@yahoo.com

Abstract ─ Microwave absorbers have emerged as an indispensable industrial apparatus in today's world, owing to their multitude of uses, both civil as well as military. This paper focuses on the use of three evolutionary algorithms, namely, particle swarm optimization, bat algorithm and cuckoo search algorithm for the purpose of obtaining optimal designs of seven layer microwave absorbers over a wide frequency range, and both cases of normal and oblique incidence. The resultant optimal designs are compared in terms of maximum reflection coefficient and total thickness with those presented in existing literature.

Index Terms ─ Bat algorithm, Chew's recursive formula, cuckoo search algorithm, multilayer microwave absorber, particle swarm optimization, polarization.

I. INTRODUCTION

Right from its conception in the early 20th century, and its subsequent application in Sir J. C. Bose's oscillators [1], electromagnetic absorbers have found their use in a variety of applications, from suppressing radar echoes to reduction of background radiation in cellular telephone applications. Traditionally, three forms of microwave absorbers are available in literature, the multilayer absorber [2], the FSS (frequency selective surface screen)-coated absorber [3] and the textured absorber [4], of which, the multilayer absorber is the more common one [5] and will be taken up in this study.

The problem of creating the perfect magnetic insulator revolves around its capability of suppressing magnetic radiation from a wide spectrum of frequencies, over an extensive range of incident angles, and meanwhile keeping the absorber thin enough to be physically realizable. Over the years, primitive optimization algorithms like the simplex method or the simulated annealing method have been used, but they are notorious for getting trapped in local minima, yielding sub-optimal results [6]. Recently, several nature-inspired metaheuristic algorithms have been used for optimization purposes, most notably the genetic algorithm [5], the particle swarm optimization [6] and the differential evolution [7] and being some of them.

This paper proposes the use of three evolutionary algorithms, viz. particle swarm optimization (PSO) [8], bat algorithm (BAT) [9] and cuckoo search algorithm (CSA) [10] to design optimal wideband seven-layer microwave absorbers for both normal incidence as well as a particular case of oblique incidence (angle of incidence 50°). The results obtained by the three algorithms are contrasted with one another and these are further compared with those demonstrated in literature [7]. Performance of the three different evolutionary algorithms, namely PSO, BAT and CSA is compared in terms of maximum reflection coefficient and statistical parameters like mean, standard deviation, best and worst value of fitness function.

II. PROBLEM FORMULATION

The physical model of a generalized planar stratified microwave absorber with N layers on a substrate of a perfect electric conductor (PEC) has been shown in Fig. 1. The overall reflection coefficient between air and the microwave absorber can be calculated by recursively using Chew's algorithm [2]:

$$R_{i,i+1} = \frac{\rho_{i,i+1} + R_{i+1,i+2} exp(-2jk_{i+1}d_{i+1})}{1 + \rho_{i,i+1}R_{i+1,i+2}\, exp(-2jk_{i+1}d_{i+1})}, \quad (1)$$

where,

For TM (parallel) polarization:

$$\rho_{i,i+1} = \frac{\varepsilon_{i+1}k_i - \varepsilon_i k_{i+1}}{\varepsilon_{i+1}k_i + \varepsilon_i k_{i+1}}, \quad i < N. \quad (2)$$

For TE (perpendicular) polarization:

$$\rho_{i,i+1} = \frac{\mu_{i+1}k_i - \mu_i k_{i+1}}{\mu_{i+1}k_i + \mu_i k_{i+1}}, \quad i < N. \quad (3)$$

In the above equations, ε_i and μ_i, respectively represent the frequency dependent complex permittivity and permeability of the i^{th} layer, and k_i denotes the wave number of the i^{th} layer, given by Snell's law as follows:

$$k_i = \omega\sqrt{\mu_i\varepsilon_i - \mu_0\varepsilon_0 sin^2\theta}. \quad (4)$$

In Equation (4), ω symbolizes the frequency of the incident wave, whereas ε_0 and μ_0 denote the permittivity and permeability of free space respectively.

Mathematically, i = 0 represents air, $i = N + 1$ represents PEC for an ideal reflection backing, and $R_{0,1}$

Submitted On: January 8, 2015
Accepted On: November 8, 2015

denotes the reflection coefficient at the first interface; i.e., the overall reflection coefficient of the multilayer microwave absorber. The reflection coefficient of the last interface, i.e., $R_{N,N+1}$, is set to +1 and -1 for TM and TE polarizations respectively; a fact blatantly ignored by many papers in existing literature [7].

The primary objective of this paper is to obtain a set of layers of various thicknesses from a predefined database of sixteen different materials with varied electrical properties, which would minimize the overall maximum reflection coefficient (in decibels) of the microwave absorber over a wide band of frequencies, for a particular angle of incidence and polarization. Hence, the following objective function is used for optimization:

$$minimum\ F = 20log_{10}\left(\max\left(\left|R_{0,1}\right|\right)\right). \quad (5)$$

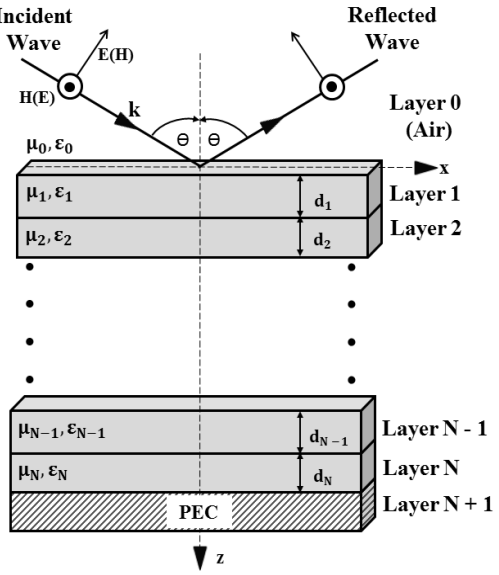

Fig. 1. Physical model of multilayer microwave absorber.

III. APPLICATION OF EVOLUTIONARY ALGORITHMS FOR OPTIMAL MULTILAYER ABSORBER DESIGN

In this paper, two different seven layer microwave absorber design problems have been considered, one for oblique incidence at an angle of incidence 50° with the normal at the point of incidence (Model 1) for TE polarization, and another for normal incidence (Model 2). By the theory of transmission lines, both TM and TE polarizations yield the same value of reflection coefficient for normal incidence [7]. As discussed in Section I, the following three evolutionary algorithms have been used for the above optimization problem.

A. Particle swarm optimization (PSO)

Introduced in 1995, particle swarm optimization emulates the swarm intelligence of bees for finding food sources in order to solve optimization problems of interest. Details about the algorithm can be found in literature [8].

For this study, an initial population of 30 particles with 14 dimensions has been considered. The two acceleration constants are linear decreased and increased respectively between 2.5 and 1.5 and vice versa. The inertia weight is linearly damped from 0.9 to 0.2 over 80% of maximum iterations and then sustained at a value of 0.2. Maximum particle velocity remains unchanged over all iterations.

B. Bat algorithm (BAT)

Bat algorithm is another evolutionary optimization algorithm motivated by the echolocation of bats. Article [9] provides an insight into this algorithm and its applications.

This research has used an initial population of 100 microbats with 14 dimensions. Loudness and pulse rate parameters are both fixed to 0.5.

C. Cuckoo search algorithm (CSA)

Cuckoo search is yet another nature-inspired optimization algorithm based on the cuckoo breeding behavior. Its uses in engineering optimization can be found in paper [10].

For this work, an initial population of 25 nests with 14 dimensions has been used. The discovery rate of alien eggs parameter is set to 0.25.

The predefined database of sixteen different fictitious materials with frequency dependent electrical permeabilities and permittivities used for this research is presented in Table 1. The database consists of four classes of materials, viz. lossless dielectric materials, lossy magnetic materials, lossy dielectric materials and relaxation-type magnetic materials. The material properties, in spite of being fictitious, are exemplary of a wide class of materials typically used in literature for microwave absorber design [7].

With reference to Table 1, the reader may consult paper [7] for the relevant equations for calculating the complex frequency dependent permittivity and permeability of each of the sixteen materials.

IV. RESULTS AND DISCUSSIONS

In this section, the optimal results for the problems under consideration are presented and discussed. For all three optimization algorithms a total number of 20 trials have been considered, with each trial consisting of 1000 iterations and a wideband frequency range of 0.1-20 GHz is swept at a step of 0.5 GHz. For each of the seven layers, the minimum and maximum thicknesses are set to 0.1 mm and 2.0 mm respectively. All calculations are executed on a personal computer with Intel® Core™ i5-3210M processor (CPU 2.50 GHz) and 8.0 GB RAM.

Table 2 compares the performance of the three algorithms for optimizing the two designs under inspection in terms of best fitness value (gbestval), worst fitness value,

standard deviation of fitness values, mean best fitness value and computational time. For all three evolutionary algorithms, Figs. 2 (a)-(b) illustrate the reflection coefficient versus frequency graphs for Models 1 and 2 respectively; whereas, the variation of the mean of best fitness value (gbestval) with iterations for both models are shown in Figs. 3 (a)-(b). The details of the optimal designs obtained for Model 1 by the three evolutionary algorithms under consideration are manifested in Table 3. Similarly, Table 4 presents the details of the optimal designs for Model 2. Tables 3 and 4 further compare these models with those obtained by differential evolution (DE), present in literature [7].

The results suggest that cuckoo search algorithm performs the best among the three discussed algorithms for obtaining a seven layer microwave absorber for both conditions of normal as well as oblique (angle of incidence 50°) incidence as far as obtaining the most optimal designs are concerned. Particle swarm optimization is also successful in obtaining a good design. The graphs indicate that bat algorithm performs well for lower values in the frequency range for oblique incidence but not so much for other cases. For both instants of normal and oblique incidence, CSA and PSO outperform DE [7] in terms of overall reflection coefficient as well as total thickness of the seven layer coating. It can also be discerned from the graphs, that CSA also has a high convergence rate along with the ability to obtain the best fitness values for both instances of normal as well as oblique incidence.

As far as computational time is concerned, it is observed that PSO is computationally the fastest and it also yields satisfactory results. CSA in spite of giving the most optimum designs, takes up the maximum run time.

Table 1: Predefined database of materials [7]

Lossless Dielectric Materials						
Material No.	μ′	μ′′	ε′	ε′′		
1	1	0	10	-		
2			50	-		
Lossy Magnetic Materials						
Material No.	μ′(1 GHz)	μ′′(1 GHz)	ε′	ε′′	a	b
3	5	10	15	0	0.974	0.961
4	3	15			1.000	0.957
5	7	12			1.000	1.000
Lossy Dielectric Materials						
Material No.	μ′	μ′′	ε′(1 GHz)	ε′′(1 GHz)	a	b
6	1	0	5	8	0.861	0.569
7			8	10	0.778	0.682
8			10	6	0.778	0.861
Relaxation-Type Magnetic Materials						
Material No.	μ_m	f_m	ε′	ε′′		
9	35	0.8	15	0		
10	35	0.5				
11	30	1.0				
12	18	0.5				
13	20	1.5				
14	30	2.5				
15	30	2.0				
16	25	3.5				

Table 2: Comparison of PSO, BAT and CSA for optimal multilayer microwave absorber design based on 20 trials

Statistical Parameters	PSO		BAT		CSA		Winner	
	Model 1	Model 2	Model 1	Model 2	Model 1	Model 2	Model 1	Model 2
Best fitness value	-10.50	-18.02	-10.07	-17.13	-10.57	-18.09	CSA	CSA
Worst fitness value	-3.96	-5.63	-4.12	-6.05	-2.87	-5.62	BAT	BAT
Standard deviation of fitness values	0.30	0.72	0.65	1.32	0.22	0.75	CSA	PSO
Mean best fitness value	-10.03	-16.35	-8.59	-13.43	-10.27	-16.91	CSA	CSA
Computational time (s)	978	980	1264	1307	1551	1523	PSO	PSO

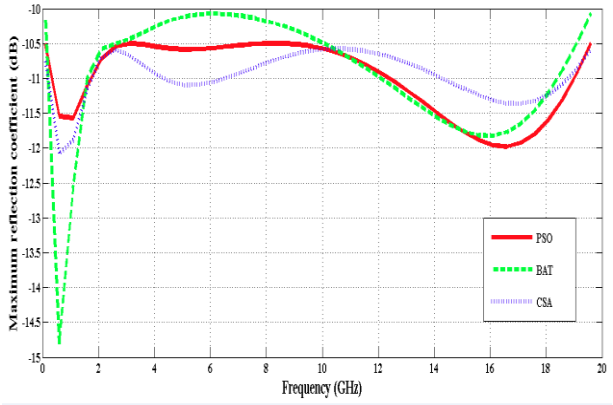

(a)

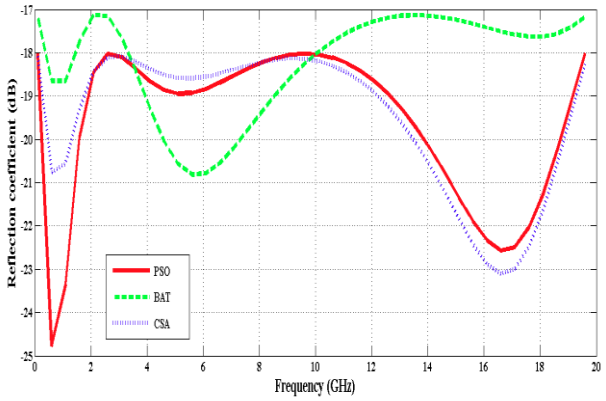

(b)

Fig. 2. (a) Reflection coefficient versus frequency for angle of incidence 50° and TE polarization (Model 1), and (b) reflection coefficient versus frequency for normal incidence and TE/TM polarization (Model 2).

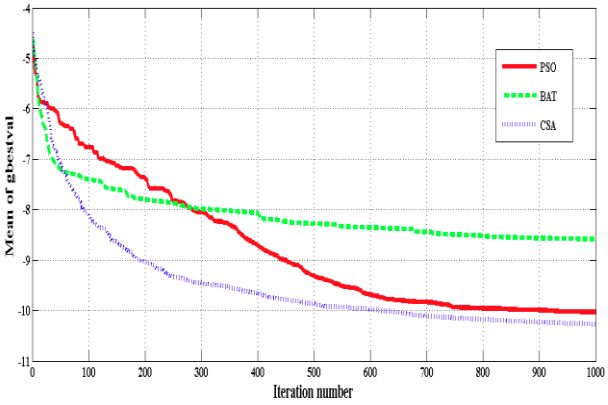

(a)

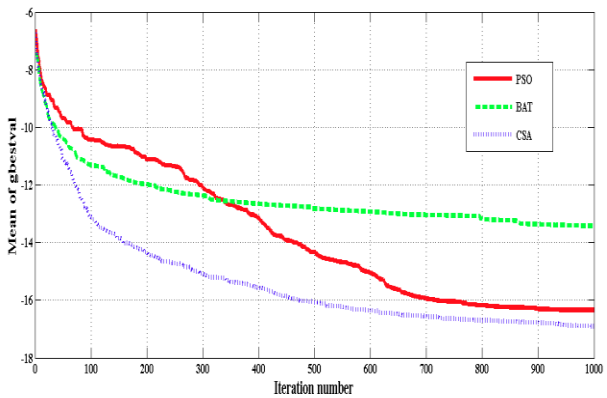

(b)

Fig. 3. (a) Mean of best fitness value (gbestval) over iterations for Model 1, and (b) mean of best fitness value (gbestval) over iterations for Model 2.

Table 3: Parameters for optimal microwave absorber design for angle of incidence 50º and TE polarization (Model 1)

	PSO		BAT		CSA		Data From [7]	
Layer	Material	Thickness	Material	Thickness	Material	Thickness	Material	Thickness
1	14	0.2544	16	0.2650	16	0.2557	16	0.2282
2	6	0.9796	6	1.9571	6	1.8731	6	1.8034
3	6	1.1676	14	1.5644	14	0.6916	14	0.5566
4	14	0.5550	9	0.4596	5	1.5107	6	0.8822
5	5	1.2927	4	1.9848	5	06469	5	1.3564
6	5	1.2657	5	0.9024	4	1.0798	5	1.9424
7	4	0.6463	7	0.6874	6	0.4594	1	0.0105
	Maximum reflection coefficient (dB) = -10.4986		Maximum reflection coefficient (dB) = -10.4727		Maximum reflection coefficient (dB) = -10.5748		Maximum reflection coefficient (dB) = -10.4	
	Total thickness (mm) = 6.1613		Total thickness (mm) = 7.8207		Total thickness (mm) = 6.5171		Total thickness (mm) = 6.8	

Table 4: Parameters for optimal microwave absorber design for normal incidence and TE/TM polarization (Model 2)

	PSO		BAT		CSA		Data From [7]	
Layer	Material	Thickness	Material	Thickness	Material	Thickness	Material	Thickness
1	16	0.2141	14	0.2108	16	0.2107	16	0.2064
2	6	1.0928	6	1.8910	6	1.1066	6	1.8762
3	6	0.8140	16	0.4632	6	0.7916	14	0.5391
4	14	0.5987	7	0.5737	14	0.5482	6	0.9499
5	5	0.9552	5	1.8523	5	1.3785	5	1.9596
6	5	1.0983	14	0.1007	6	0.5570	4	0.7817
7	4	1.2593	4	1.2121	4	1.7450	5	0.4864
	Maximum reflection coefficient (dB) = -18.0167		Maximum reflection coefficient (dB) = -17.1326		Maximum reflection Coefficient (dB) = -18.0879		Maximum reflection coefficient (dB) = -17.9	
	Total thickness (mm) = 6.0324		Total thickness (mm) = 6.3038		Total thickness (mm) = 6.3376		Total thickness (mm) = 6.8	

V. CONCLUSIONS

This paper has focused on the comparison of particle swarm optimization, bat algorithm and cuckoo search algorithm for the purpose of designing optimal wideband multilayer microwave absorbers for both normal and oblique incidences. The optimization engines have been used to minimize the overall reflection coefficient of the multilayer coating. The results obtained reflect that the design obtained by CSA and PSO are ultrathin and have a superior frequency response compared to the designs presented in literature [7]; whereas BAT produces comparable outputs too. It is seen that CSA outperforms all other algorithms in terms of obtaining the best fitness value, and thus the most optimal absorber design. With respect to computational time, PSO turns out to be the most efficient algorithm of the three, followed by BAT and CSA.

REFERENCES

[1] J. C. Bose Collected Physical Papers, Longmans, Green and Co., 1927.

[2] W. C. Chew, *Waves and Fields in Inhomogeneous Media*, IEEE Press, New York, 1995.

[3] A. Tennant and B. Chambers, "A single-layer tunable microwave absorber using an active FSS," *IEEE Microwave and Wireless Components Lett.*, pp. 46-47, 2004.

[4] S. Cui, D. S. Weile, and J. L. Volakis, "Novel planar electromagnetic absorber designs using genetic algorithms," *IEEE Transactions on Antennas and Propagation*, vol. 54, no. 6, pp. 1811-1817, 2006.

[5] L. Jiang, et al., "Pareto optimal design of multilayer microwave absorbers for wide-angle incidence using genetic algorithms," *IET Microw. Antennas Propag.*, vol. 3, iss. 4, pp. 572-579, 2009.

[6] H. Liu, L. Zhang, Y. Gao, Y. Shen, and D. Shi, "Electromagnetic wave absorber optimal design based on improved particle swarm optimization," *EMC 2009, IEICE*, pp. 797-800, 2009.

[7] N. I. Dib, M. Asi, and A. Sabbah, "On the optimal design of multilayer microwave absorbers," *Progress In Electromagnetics Research C*, vol. 13, pp. 171-185, 2010.

[8] R. V. Kulkarni and G. K. Venayagamoorthy, "Particle swarm optimization in wireless-sensor networks: a brief survey," *Systems, Man, and Cybernetics, Part C: Applications and Reviews, IEEE Transactions on*, vol. 41, no. 2, pp. 262-267, 2011

[9] X-S. Yang and X. He, "Bat algorithm: literature review and applications," *International Journal of Bio-Inspired Computation*, vol. 5, no. 3, pp. 141-149, 2013.

[10] X-S. Yang and S. Deb, "Engineering optimisation by cuckoo search," *International Journal of Mathematical Modelling and Numerical Optimisation*, vol. 1, no. 4, pp. 330-343, 2010.

Subhanwit Roy was born in Calcutta, India in 1993. He graduated with his B. Tech. in Electronics and Communication Engineering at National Institute of Technology, Durgapur, India in 2015. His research interests include microwave engineering, machine intelligence, evolutionary computing, digital signal processing, data science and analytics.

Ananya Mahanti was born in the year of 1994 in India. She is in her final year of B.Tech. degree course in Electronics and Communication Engineering in National Institute of Technology, Durgapur, India. Her research interests include antenna, microwave, electromagnetics, signal processing and optimization.

Souptik Dutta Roy was born in Calcutta, India in 1993. He graduated with his B.Tech. in Electronics and Communication Engineering at National Institute of Technology, Durgapur, India in 2015. His fields of interest include digital signal and image processing, microwave engineering and machine learning.

G. K. Mahanti was born in the year of 1967 in West Bengal, India. He obtained his B.E. in Electronics & Communication Eng. from NIT, Durgapur, India, M.E. in Electronics System and Communication from NIT, Rourkela, India and Ph.D. (Eng.) from IIT, Kharagpur, India. He has more than 20 years of teaching and research experience. Presently he is working as a Professor, Department of Electronics and Communication Engineering, National Institute of Technology, Durgapur, India. He is a Senior Member of IEEE, USA. He was former Head of the Dept. of Electronics and Communication Eng. of NIT, Durgapur.

He has produced 7 Ph.D. students so far. He has published approximately 80 papers in journals and in national and international conferences. He was the Reviewer of many international journals like Electronics Letters, IEEE Antennas and Wireless Propagation Letters, Progress in Electromagnetics Research, International Journal of Adaptive Control & Signal Processing and many conferences. He was also the Program Committee Member of many national and international conferences. His research area is array antenna synthesis, evolutionary algorithms, microwave engineering & electromagnetics.

A Study on Different Topologies of the Tubular Linear Permanent Magnet Motor Designed for Linear Reciprocating Compressor Applications

Izzeldin I. Abdalla, Taib B. Ibrahim, and Nursyarizal M. Nor

Department of Electrical and Electronic Engineering
Universiti Teknologi PETRONAS, Bandar Seri Iskandar, Perak Darul Ridzuan 32610, Malaysia
izzeldin_abdalla@yahoo.com, taibib@petronas.com.my, nursyarizal_mnor@petronas.com.my

Abstract ─ This paper presents a study on three different topologies of tubular linear permanent magnet motors (TLPMMs), with different permanent magnet (PM) structures. These motors provide direct conversion for electrical energy into a linear mechanical force, and they are directly coupled to the load. The proposed motors are equipped with quasi-Halbach magnetized moving-magnet armatures and their stator cores have been made from a soft magnetic composite (SMC) material, Somaloy 700. Based on the nonlinear time-stepping two-dimensional finite-element analysis (2-D FEA) an extensive magnetic field analysis of the proposed designs has been established. The simulation results indicate the effectiveness of the designs to drive a linear reciprocating compressor in a household refrigerator. Moreover, the simulation results have shown that, the superiority of the two designs with T-shaped and trapezoidal-shaped PMs structures over the TLPMM with conventional rectangular-shaped PMs. In addition to that, the usage of quasi-Halbach for the PMs array arrangement has a significant effect on the motor performance.

Index Terms ─ Finite-element analysis, magnetic field distribution, quasi-Halbach, soft magnetic composite material, tubular linear permanent magnet motor.

I. INTRODUCTION

Linear electromagnetic motors, which can provide a thrust force directly to a payload without any mechanical conversion means, are dedicated to widespread applications, ranging from transportation and industrial automation to healthcare and linear reciprocating compressors. Of the various linear electromagnetic motor topologies, the tubular linear permanent magnet motors (TLPMMs) with a moving-magnet are particularly attractive as compared with their flat counterparts. Because TLPMMs possess a high efficiency and high thrust force capability [1,2].

At present, the energy technologies have significant effects in a social grade of living and economic construction at all scales. This will put further pressure on energy supplies and necessitate energy conservation measures. Meanwhile, the impact of carbon and carbon dioxide (CO_2) emissions based on the Kyoto protocol has increased the major concern of the researchers [3,4].

The refrigerators represent a considerable and growing electrical load [5]. Undoubtedly, among refrigeration devices, the household refrigerator is the most important appliance in our lives today. In the fact that, the household refrigerator uses chlorofluoro-carbons (CFCs) in its installation foam, it contributes to the global warming and ozone layer depletion. It also has a significant impact on the emission of carbon and CO_2. Moreover, while the electrical energy consumption of the individual household refrigerator is small, large numbers of household refrigerators have an appreciable potential on energy consumption. In addition to that, the mechanical friction of the crank-driven piston uses the concept of rotary-to-linear movement in the compressor of the conventional refrigerator. This friction lowers the performance of the refrigerator, and also, the side force between the piston and cylinder lowers the smoothness of the operation system. All these problems are due to the inefficient reciprocating compressor system [6-9].

The conventional rotary reciprocating compressor comprises a single-phase rotary induction motor integrated with a crank as well as a reciprocating piston. The overall efficiency of the compressor is relatively low; this is due to the low efficiency of the induction motor and the mechanical friction of the crank-driven piston movement [10-12].

To enhance the performance of the conventional compressor, it must eliminate the rotary-to-linear motion mechanical conversion means. This can reduce the volume and complexity of the compressor as well as allow the compressor to operate without lubrication. This results in reducing the cost and the power loss as well as enabling a soft operation system [13].

The design of a linear motor has a significant role on the performance of the linear reciprocating compressor. This paper aims to study the performance and magnetic field distribution of a TLPMM under three different topologies, with different permanent magnet (PM) structures. These designs are proposed to drive a linear

Submitted On: October 16, 2014
Accepted On: October 22, 2015

reciprocating compressor in a household refrigerator. Such designs possess the advantages of high force capability, high efficiency, and low manufacturing cost. Moreover, the cogging force due to the stator slotting is very low. The motors were designed to produce an output power of 185 W at a speed of 2.2 m/s. The PMs have been mounted on a mild steel tube in order to produce a higher air gap field.

II. LINEAR MOTOR DESIGN

The main criteria of the appropriate design for a linear motor are based on the simple structure and reasonable cost as well as force capability. It can be noted that the performance of the TLPMM can be well improved by different PM array structures or PM array arrangements [14]. The three designs with various PM structures are rectangular-shaped PMs (Rec_PMs), T-shaped PMs (TS_PMs) and trapezoidal-shaped PMs (Trap_PMs), which are shown in Fig. 1 (a), (b) and (c), respectively. The three designs are equipped with a quasi-Halbach magnetized moving-magnet armature as indicated in Fig. 1, which is comprised of three radially magnetized magnets and two axially magnetized magnets, as presented in [15]. The air gap has been selected to be as small as mechanically possible, because a large air gap leads to an increasing in the PM volume and a reduction in the motor thrust force. However, a very small air gap results in a mechanical fault, and causes some manufacturing difficulties.

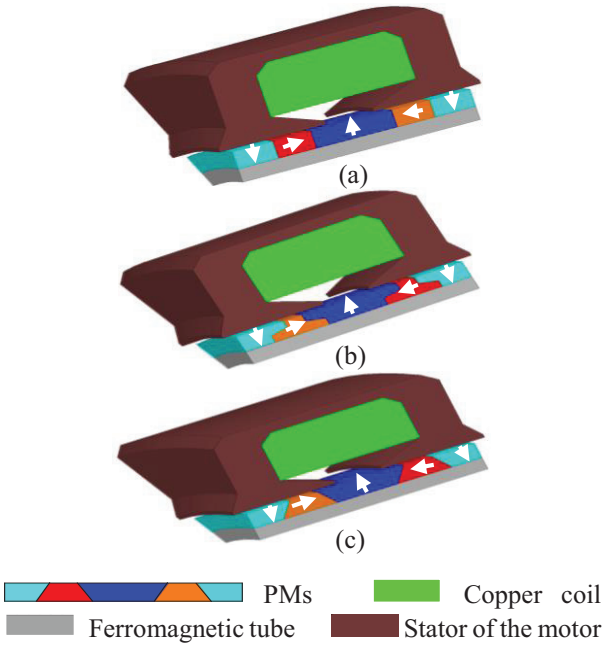

Fig. 1. 3D-FE models of the three proposed TLPMMs with: (a) Rec_PMs, (b) TS_PMs, and (c) Trap_PMs.

The common feature of the three proposed designs is that no field winding is required; only the PMs will generate the excitation field for the motor. Moreover, the stator cores of the three proposed motors are made of soft magnetic composite (SMC) material, Somaloy 700, whereas the PMs are made of rare-earth materials, such as neodymium-iron-boron (NdFeB).

III. LINEAR MOTOR MODEL

The TLPMM can be modeled as follows, the electromagnetic force, $f_e(t)$, of the TLPMM is produced by the interaction between the stator current, i_a and the PMs field. The force can be quantified by [16]:

$$f_e(t) = K_T(x(t))i_a, \tag{1}$$

where the force coefficient, K_T, is slightly position dependent due to the finite armature length. The voltage equation, v_1, associated with the equivalent circuit of the TLPMM in Fig. 2 is as follows:

$$v_1 = R_a i_a + L_s \frac{di_a}{dt} + e_1, \tag{2}$$

where e_1 is the value of induced electromotive force. The L_s and R_a are the winding inductance and resistance of the motor, respectively [16].

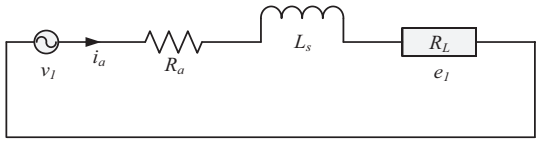

Fig. 2. Equivalent circuit of a single-phase TLPMM.

Faraday's low stated that the magnitude of e_1 is proportional to the rate of change of flux linkage (ψ), which in turn depends on the number of winding turns N_c as:

$$\psi = N_c.\phi\,. \tag{3}$$

Thus

$$e_1 = \frac{d\psi}{dt} = N_c.\frac{d\phi}{dt}\,. \tag{4}$$

When the mover is moving along the z-direction, the magnetic field in the stator is static; hence, the distribution of the air gap magnetic field varies with the position of the mover. So, the flux coupled with the winding is varied with time. The induced electromotive force can be rewritten as in (5):

$$e_1 = \frac{d\psi}{dt} = \frac{d\psi}{dz} \times \frac{dz}{dt} = v \times \frac{d\psi}{dz}, \tag{1}$$

where $v = dz/dt$ is the mover velocity along the z-direction. Thus, the back-EMF is given by the product of v, and the rate of change in the flux-linkage, ψ, with respect to the position. The inductance of a winding, L, is given by the ratio between the flux linked with the winding and the current into the winding as expressed in (6) [17]. The magnetization curve of the NdFeB magnet can be expressed as in (7) [18]:

$$L = \psi / i_a, \tag{6}$$

$$B_m = \mu_r H_m + B_r \,, \tag{7}$$

where B_m is the magnetic flux density in axial direction, H_m is the magnetizing force, B_r the magnet remanence, and μ_r is the relative permeability of the magnet.

The following three Maxwell's equations used by the FEA and relevant to magnetic field analysis of the proposed motors. Thus, (11) resulted from (8) and (9):

$$\nabla \times H = -\sigma(E) \,, \tag{8}$$

$$\nabla \times E = -\frac{\partial B}{\partial t} \,, \tag{9}$$

$$\nabla . B = 0 \,, \tag{10}$$

$$\nabla \times \frac{1}{\sigma} \nabla \times H + \frac{\partial B}{\partial t} = 0 \,. \tag{11}$$

The governing field equations of the proposed motors in the cylindrical coordinate system, in terms of the vector magnetic potential (A_θ), are given by (12) for the airspace region and (13) for magnet region:

$$\frac{\partial}{\partial z}\left(\frac{1}{r}\frac{\partial}{\partial z}\left(rA_{I\theta}\right)\right) + \frac{\partial}{\partial r}\left(\frac{1}{r}\frac{\partial}{\partial r}\left(rA_{I\theta}\right)\right) = 0 \,, \tag{12}$$

$$\frac{\partial}{\partial z}\left(\frac{1}{r}\frac{\partial}{\partial z}\left(rA_{(II\theta)}\right)\right) + \frac{\partial}{\partial r}\left(\frac{1}{r}\frac{\partial}{\partial r}\left(rA_{(II\theta)}\right)\right) = -\mu_0 \nabla \times M \,. \tag{13}$$

IV. MAGNETIC FIELD ANALYSIS

The two-dimensional finite-element analysis (2-D FEA), under Ansys Maxwell 16, commercial version has been used to design and analyze the performance of the three proposed TLPMMs. Hence, the transient solver of this software has been used to examine the electromagnetic characteristics of the three proposed designs. Hence, all the results are established in a cylindrical coordinate system. The 2-D FEA presents a significant advantage of being less time consuming as compared with the 3-D FEA. The main parameters of the design are tabulated as in Table 1. The same parameters have been used to build the 2-D axisymmetrical FE models of the three proposed designs.

Table 1: Design parameters

The Parameter	Symbol	Value
Outer radius of the stator core	R_e	50.0 mm
Yoke thickness	h_{ys}	3.3 mm
Outer radius of the magnet	R_m	20.0 mm
Magnet height	h_m	5.0 mm
Air gap length	g	0.8 mm
Tooth width	T_w	9.4 mm
Slot opening width	b_0	10.0 mm
Tooth tip height	h_t	1.0 mm
Magnet remanence	B_r	1.14 T
Length of the radial PM	T_{mr}	15.5 mm
Length of the axial magnet	T_{mz}	9.5 mm
Ferromagnetic height	h_{ym}	3.9 mm
Tooth pitch width	T_w	40 mm
Pole pitch	T_p	25 mm

Figure 3 illustrates the linear B-H curve of the NdFeB, PMs and the nonlinear B-H curve of the SMC material, Somaloy 700, which have been used in the 2-D FEA solution. Basically, the characteristics of the PMs are described by the following quantities: coercive force, H_c; relative permeability, μ_r; remanence, B_r; as well as chemical characteristics and the second quarter of the hysteresis loop [19]. In the FEA calculations, the material linearity of the NdFeB PMs has been included, such as H_C = -864 kA/m, μ_r = 1.05 and B_r = 1.14 Tesla.

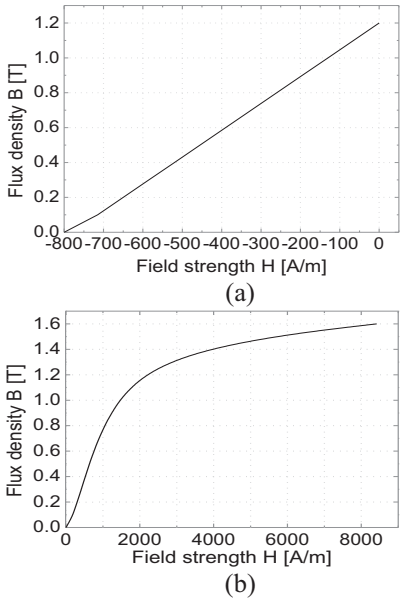

Fig. 3. B-H curves used in FEA: (a) NdFeB, (b) SMC material, Somaloy 700.

Figure 4 (a) to (c) shows the 2-D FEA predicted open-circuit magnetic flux distributions of the three proposed TLPMM designs, with quasi-Halbach magnetized armatures at the maximum armature displacement (z_d = 11 mm) and zero armature current. As can be seen, at the maximum stroke position, most of the flux from the PMs flows through the teeth and back iron, and the flux-linkage with the coil is at the maximum value. The flux is dominant in the radial direction. The resulting flux density in the tooth region varies with time as the armature reciprocates. The flux passing through the yoke is the same as in the teeth. However, the resulting flux density components in the yoke region is essentially in the axial direction.

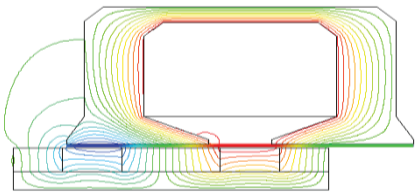

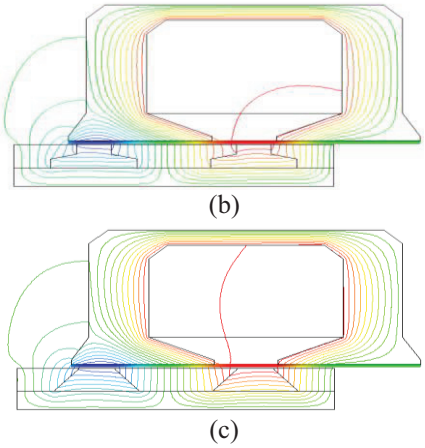

Fig. 4. Magnetic flux distribution in the three TLPMMs at z_d = 11 mm: (a) flux-lines of Rec_PMs, (b) flux-lines of TS_PMs, and (c) flux-lines of Trap_PMs.

To compare the performances of the three designs, the simulation results of the open-circuit magnetic field were established at the air gap of the motors.

Figure 5 shows the comparison among the magnetic flux distribution at the air gap of the three designs. All results have been shown at z_d = 0 mm. From Fig. 5, we can note that the maximum magnetic flux values were 0.18 mwb/m, 0.16 mwb/m and 0.17 mwb/m for the Rec_PMs, TS_PMs and Trap_PMs, respectively. The TLPMM with Trap_PM showed a higher average value for the air gap magnetic flux, which is conducive to a larger actuating force as compared with the conventional TLPMM design with Rec_PMs. Apparently, the waveform of the magnetic flux was very close to sinusoidal; subsequently, the induced voltage can be quantified by the waveform of the magnetic flux, and was most probably sinusoidal.

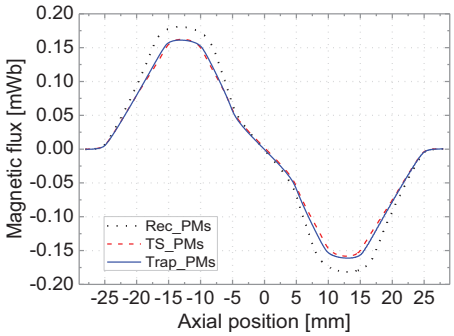

Fig. 5. Comparison between the magnetic flux distributions at the air gap of the three proposed designs.

Figure 6 compares the FEA calculation of the radial magnetic flux density, B_r, in the air gap of the three TLPMM designs as a function of the axial position without an excitation current. At the initial position of the translator, it was found that the higher average value of the air gap flux density was obtained for the proposed design with Trap_PMs. The second maximum average was found for the proposed design with TS_PMs.

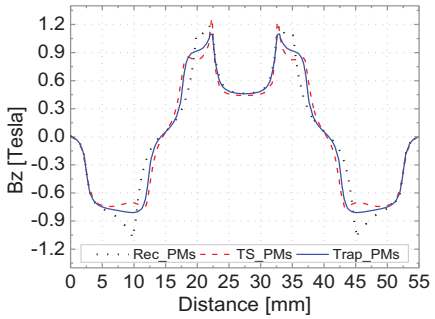

Fig. 6. Comparison of the air gap magnetic flux density components of the three designs.

The no-load magnetic field distribution was calculated using the FEA in order to find out the magnetic flux-linkage of the three designs. The displacement was generated from the forth and back movements of the motor.

The maximum flux-linkage was obtained for the TLPMM with Trap_PMs, while the TLPMM with Rec_PMs showed the lower flux-linkage in the group as represented in Fig. 7. The average value of the flux-linkage with the windings were found to be as in Table 2.

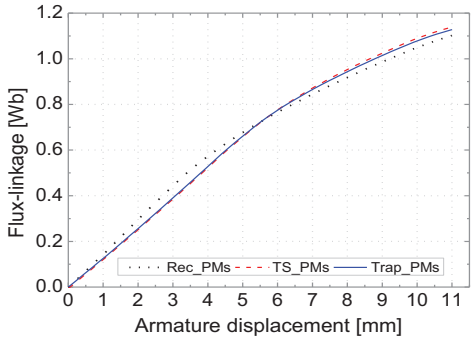

Fig. 7. Comparison of the flux-linkage of the three proposed designs.

Table 2: Average flux-linkages of the three designs

TLPMM	Rec_PMs	TS_PMs	Trap_PMs
Flux-linkage	0.6595 Wb	0.6568 Wb	0.6553 Wb

Figure 8 compares the back-EMF waveforms of the three designs. The armature translated at a mover velocity of 2.2 m/s; whereas, at the zero speed of the motor, the induced voltage was very small or zero. The average values of the back-EMFs for three proposed designs were calculated by 2-D FEA as in Table 3. Obviously, the flux-linkages and back-EMFs of the T-shaped PMs

and trapezoidal-shaped PMs were superior to the rectangular-shaped PMs design.

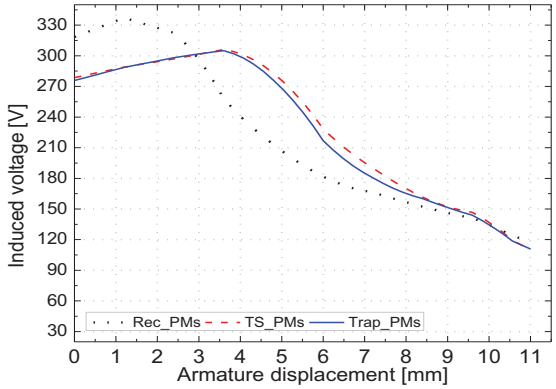

Fig. 8. Comparison of the back-EMFs of the three TLPMMs.

Table 3: Average back-EMFs of the three designs

TLPMM	Rec_PMs	TS_PMs	Trap_PMs
Back-EMF	215.0048 V	223.8931 V	220.3778 V

By passing the current $i_a = 0.5$ A into the stator coil, the reciprocating thrust force yielded as a result of the interaction between the PM field and the current of the coil, also the thrust force depended on the displacement of the PM armature. Figure 9 compares the FE simulation results of the thrust forces of the three proposed TLPMMs. The average thrust forces were quantified as 72.798 N, 83.253 N and 85.185 N for the Rec_PMs, TS _PMs and Trap _PMs, respectively.

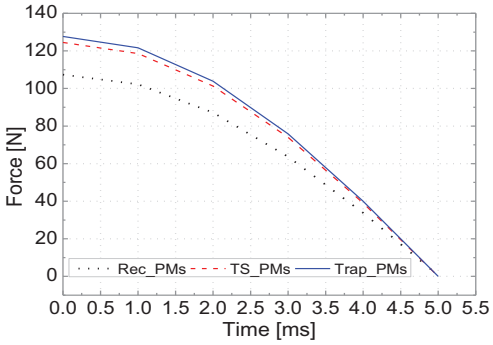

Fig. 9. Comparison of the thrust force of the three TLPMMs.

Winding inductance represents one of the key parameters for the motor performance. Figure 10 compares the calculated winding inductances of the three designs at different displacements of the mover using 2D-FEA. The average values were found to be 716.9721 mH, 751.8687 mH and 753.8792 mH for the TLPMM with Rec_PMs, TS_PMs and Trap_PMs, respectively.

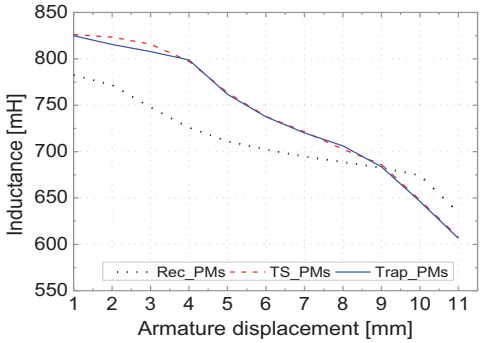

Fig. 10. Comparison of the winding inductances of the three designs.

V. CONCLUSION

In this paper, three designs of tubular linear permanent magnet motors (TLPMMs) were proposed and a 3D-FE model was developed for each one. These motors are proposed to drive a vapor linear reciprocating compressor in a household refrigerator. The three designs have different PM structures; they are the rectangular-shaped PMs (Rec_PMs), trapezoidal-shaped PMs (Trap_PMs) and T-shaped PMs (TS_PMs). These designs have been equipped with a quasi-Halbach magnetized moving-magnet armature and slotted stator with a single coil. The stator cores of all designs have been made of a soft magnetic composite (SMC) material, Somaloy 700; whereas, the PMs were made of NdFeB. Based on the nonlinear 2D-FEA, the results of the proposed designs have been established and compared which ensures an efficient operation of the proposed TLPMMs. The simulation results reveal that the proposed TLPMM with the T-shaped PMs and trapezoidal-shaped PMs are superior to the design with conventional rectangular-shaped PMs, in terms of flux-linkage, back-EMF, force capability, inductance and air gap magnetic field distributions. Subsequently, the simulation results have demonstrated the validity of the designs in driving the linear vapor reciprocating compressor. The prototype of the trapezoidal-shaped PM TLPMM has been fabricated and its testing will be presented in the coming publications.

ACKNOWLEDGMENT

The authors would like to thank University Teknologi PETRONAS (UTP), Malaysia and the Ministry of Education, Malaysia, for the financial support.

REFERENCES

[1] J. Wang and D. Howe, “Tubular modular permanent-magnet machines equipped with quasi-Halbach magnetized magnets-part I: magnetic field

distribution, EMF, and thrust force," *IEEE Trans. on Magnetics*, vol. 41, pp. 2470-2478, 2005.
[2] I. I. Abdalla, T. Ibrahim, and N. Nor, "Linear permanent magnet motor for reciprocating compressor applications," *IEEE 7th Int. Power Engineering and Optimization Conference, PEOCO*, pp. 29-34, 2013.
[3] B. J. Ruiz-Mendoza and C. Sheinbaum-Pardo, "Electricity sector reforms in four Latin-American countries and their impact on carbon dioxide emissions and renewable energy," *Energy Policy*, vol. 38, pp. 6755-6766, 2010.
[4] H. Dai, T. Masui, Y. Matsuoka, and S. Fujimori, "The impacts of China's household consumption expenditure patterns on energy demand and carbon emissions towards 2050," *Energy Policy*, 2012.
[5] J. Wang, D. Howe, and Z. Lin, "Comparative studies on linear motor topologies for reciprocating vapor compressors," *IEEE Int. Conf.* in *Electric Machines & Drives, IEMDC*, pp. 364-369, 2007.
[6] P. Binneberg, E. Kraus, and H. Quack, "Reduction in power consumption of household refrigerators by using variable speed compressors," *Int. Refrigeration and Air Conditioning Conf*., 2002.
[7] M. L. Stoop and A. J. Lambert, "Processing of discarded refrigerators in the Netherlands," *Technovation*, vol. 18, pp. 101-110, 1998.
[8] J. M. Calm and D. A. Didion, "Trade-offs in refrigerant selections: past, present, and future," *International Journal of Refrigeration*, vol. 21, pp. 308-321, 1998.
[9] S. Hou, H. Li, and H. Zhang, "An open air–vapor compression refrigeration system for air-conditioning and desalination on ship," *Desalination*, vol. 222, pp. 646-655, 2008.
[10] J. Wang, D. Howe, and Z. Lin, "Design optimization of short-stroke single-phase tubular permanent-magnet motor for refrigeration applications," *IEEE Trans. on Industrial Electronics*, vol. 57, pp. 327-334, 2010.
[11] J. Wang, D. Howe, and Z. Lin, "Analysis of a short-stroke, single-phase, quasi-Halbach magnetised tubular permanent magnet motor for linear compressor applications," *IET Electric Power Applications*, vol. 2, pp. 193-200, 2008.
[12] J. Wang, T. Ibrahim, and D. Howe, "Prediction and measurement of iron loss in a short-stroke, single-phase, tubular permanent magnet machine," *IEEE Trans. on Magnetics*, vol. 46, pp. 1315-1318, 2010.
[13] Z. Lin, J. Wang, and D. Howe, "A resonant frequency tracking technique for linear vapor compressors," *IEEE Int. Conf. in Electric Machines & Drives, IEMDC*, pp. 370-375, 2007.
[14] Y.-M. Chen, S.-Y. Fan, and W.-S. Lu, "Performance analysis of linear permanent-magnet motors with finite-element analysis," *IEEE Trans. on Magnetics*, vol. 44, pp. 377-385, 2008.
[15] I. I. Abdalla, T. Ibrahim, and N. Mohd Nor, "Analysis of a tubular linear permanent magnet motor for reciprocating compressor applications," *Applied Mechanics and Materials*, vol. 448, pp. 2114-2119, 2014.
[16] T. Ibrahim, "Short-stroke, single-phase tubular permanent magnet motors for refrigeration applications," *The University of Sheffield*, 2009.
[17] J. F. Gieras, Z. J. Piech, and B. Tomczuk, *Linear Synchronous Motors: Transportation and Automation Systems*, CRC Press, 2011.
[18] J. R. Brauer, *Magnetic Actuators and Sensors*, John Wiley & Sons, 2006.
[19] J. Pyrhönen, T. Jokinen, and V. Hrabovcová, *Design of Rotating Electrical Machines*, Wiley Online Library, 2009.

Izzeldin Idris Abdalla was born in Kordofan Province, Sudan, in 1982. He received his B.Sc. (Hons.) degree and M.Sc. in Electrical and Electronic Engineering, specializing in Power and Energy from Juba University, Sudan in the year 2005 and Universiti Teknologi PETRONAS, Malaysia in 2011, respectively. He was in the faculty of Engineering, Department of Electrical and Electronic Engineering, Juba University from 2005 to 2008. He joined Department of Electrical and Electronic Engineering, Universiti Teknologi PETRONAS, Malaysia in January 2012 as a Ph.D. student. His areas of interests are in power electronics, power systems and power quality. His current research interests are in analysis and design of electrical machines.

Taib Ibrahim was born in Kedah, Malaysia in 1972. He received the B.Eng. (Hons) in Electrical and Electronics Engineering, M.Sc. in Electrical Power Engineering and Ph.D. in Electrical Machine Design from Coventry University, U.K. in 1996, University of Strathclyde, UK in 2000 and University of Sheffield, UK in 2009, respectively. His employment experience includes Airod (M) SdnBhd and Universiti Teknologi PETRONAS (UTP). Currently, he is Leader for Power and Energy Cluster and Member for Mission Oriented Research (Energy) in UTP. His research interests range from

motion control to electromagnetic devices and their associated drives.

Nursyarizal Mohd Nor obtained his Ph.D. in Electrical Engineering from Universiti Teknologi PETRONAS (UTP), Malaysia in year 2009. In year 2001 he obtained his M.Sc. in Electrical Power Engineering from The University of Manchester Institute of Science and Technology (UMIST), UK. His areas of specialization are 'Analysis and optimization of large scale power systems' and 'State estimation'. He has several publications at his credit. His research interests are in Power Economics Operation and Control, Power Quality and Power System Analysis.

Measurement of Complex Permittivity of Polystyrene Composite at 11.64 GHz Using Cavity Perturbation Technique

Sarita Sharma [1] and Dalveer Kaur [2]

[1] Department of Electronics & Communication Engineering
Chandigarh College of Engineering & Technology, Chandigarh, 160019, India
s_saritasharma@yahoo.com

[2] Department of Electronics & Communication Engineering
I K Gujral Punjab Technical University, Jalandhar, 144601, India
dn_dogra@rediffmail.com

Abstract — Complex permittivity of polystyrene composites of different percentage of carbon black fillers are measured over the wide frequency range 8-12 GHz using X-band rectangular cavity resonator. The measurement technique uses the cavity perturbation technique. Validity of present measurement technique has been checked by measuring the dielectric properties of well-known dielectric materials (Teflon and Rexolite). Polystyrene composites are very useful for lightweight shielding and absorbing materials. It would be of great interest for the community to find its dielectric properties over wider frequency range. Due to lack of experimental data on dielectric parameters of carbon black composite in literature, the experimental study has been conducted to measure the dielectric properties of polystyrene composite over wide frequency range of X-band (8-12 GHz). In addition, the estimation of measurement error associated with this technique is also discussed.

Index Terms — Cavity perturbation, cavity resonator, complex permittivity, dielectric constant, dielectric loss, dielectric material

I. INTRODUCTION

Complex permittivity cannot be measured directly; it is usually calculated via other measurable parameters such as transmission/reflection coefficients (s-parameters), propagation constant, etc. Measurement of these parameters requires very precise and accurate experimental approach associated with specific formulas. Accurate information for the dielectric properties is required to study the possible hazard of EM field [1]. The dielectric properties of materials are determined by its molecular structure, if the molecular structure changes its dielectric properties changes. Any single technique for complex permittivity measurement is not suitable over a wide frequency range and complex permittivity. Numerous techniques for determination of dielectric properties of dielectric material have been developed [2-3]. Among various frequency domain methods for the measurements of complex permittivity, cavity perturbation technique is one of the most widely used because of its relative simplicity for precise microwave measurements of conductivity, dielectric, and magnetic properties of materials. In this technique, one measures the adiabatic change of the characteristics of a resonator upon the introduction of a foreign body (sample). This technique requires the accurate determination of quality factor and resonant frequency of microwave cavity resonator. Different cavity perturbation techniques have different limitations, i.e., the insertion of sample in the cavity [4]; size and shape of sample; type of cavity resonators etc.; hence further progress in this field is required.

Normally, the samples required for measurements in a rectangular cavity are equal to the height of the cavity. When the samples are smaller than the height of the cavity, accurate measurements are often difficult [5]. The objective of cavity perturbation technique is to measure accurately and precisely the quality factor Q and resonance frequency f_o of unloaded and loaded microwave cavity resonator using transmission or reflection coefficient (s-parameters) as a function of frequency [6-8].

A rectangular cavity resonator has been designed here with very small hole at the centre of broader side of the X-band waveguide resonator in order to insert a sample material under test for the measurement of complex permittivity [9]. Since cavity is operated in TE_{10n} mode, it has a number of resonant frequencies. The resonance frequency and quality factor of empty cavity and sample loaded cavity are measured at different resonances to perform experiment. Five samples of polystyrene composite with different percentage of carbon black are prepared by mixing polystyrene and carbon black together at room temperature. We use the similar process here to prepare the samples as given in

Submitted On: November 18, 2014
Accepted On: December 6, 2015

the cited reference [10], the only difference is that we use a glass capillary of 4 mm inner diameter to cast the mixture for uniform cylindrical shaped samples of 4 mm diameter. Measurements are performed at room temperature. The effect of casting process, pressure and temperature profile of sample preparation is not studied here.

The measurement setup uses cavity resonator and VNA. The real and imaginary parts of the complex permittivity have been calculated from the shift in the resonance frequency and change in the Q-factor. In order to verify the validity of the measurement technique, real and imaginary parts of the complex permittivity of certain standard dielectric material (Teflon and Rexolite) are measured at X-band and the measured vales are compared with the values available in literature [11]. The complex permittivity of different compositions of carbon black has been measured at X-band. The experimental results obtained at 9.77 GHz with the present method have been compared with the existing values in literature [10]. However, the dielectric data of carbon black composite over the entire frequency range of 8-12 GHz are not available for comparison.

II. THEORETICAL BACKGROUND

It was Bethe and Schwinger [12] who proposed cavity perturbation technique for the first time. Thereafter, many researchers have reported theoretical and experimental analysis of cavity perturbation techniques [6-17]. The measurements of complex permittivity ($\boldsymbol{\varepsilon^*}$) and permeability ($\boldsymbol{\mu^*}$) are performed by inserting a small, appropriately shaped sample into a cavity and determining the properties of the sample from resultant change in the resonant frequency and loaded quality factor.

The basic idea of the cavity perturbation is the change in the overall geometric configuration of the electromagnetic fields upon the insertion of a small sample must be small. Based on this assumption, a detailed derivation of the perturbation equation for the frequency shift upon the insertion of a sample into a cavity was given by Harrington [14].

When a small sample is inserted in a cavity having electric field E_0 and magnetic field H_0 in the unperturbed state, the fields in the interior of the sample are E and H. For loss less sample, the variation of resonance frequency is given by [12,13] as:

$$\frac{f_s - f_0}{f_s} = -\frac{\int(\Delta\varepsilon E.E_0^* + \Delta\mu H.H_0^*)d\tau}{\int(\varepsilon E.E_0^* + \mu H.H_0^*)d\tau}, \quad (1)$$

where ε and μ are the permittivity and permeability of the medium in the unperturbed cavity respectively. $d\tau$ is the elementary volume, $\Delta\varepsilon$ and $\Delta\mu$ are the changes in the above equations due to the introduction of the sample in the cavity. Without affecting the generality of Maxwell's equations, the complex frequency shift due to lossy sample in the cavity is given by Waldron [15] as:

$$\frac{-df^*}{f^*} = \frac{(\varepsilon_r - 1)\varepsilon_0 \int_{v_S} E.E_0^* dv + (\mu_r - 1)\mu_0 \int_{v_S} H.H_0^* dv}{\int_{v_C} (D_0.E_0^* + B_0.H_0^*)dv}, \quad (2)$$

where df^* is the complex frequency shift as the permittivity of materials is a complex quantity, so the resonance frequency is also complex. B_0, H_0, D_0 and E_0 are the fields in the unperturbed cavity and E and H is the field in the interior of the sample [16].

In terms of energy, the numerator of Equation (2) represents the energy stored in the sample and the denominator represents the total energy stored in the cavity. The total energy $\boldsymbol{W = W_e + W_m = 2\ W_e = 2W_m}$, where $\boldsymbol{W_e}$ and $\boldsymbol{W_m}$ are the electrical and magnetic energies, respectively. Two assumptions are applied in equation (2). The fields in the empty part of the cavity are negligibly changed with the insertion of the sample. The fields in the sample are uniform over its volume. Both of these assumptions can be considered valid if the sample is sufficiently small relative to the resonant wavelength. The negative sign in Equation (2) indicates that by introducing the sample the resonance frequency is lowered. When a dielectric sample is inserted into the cavity resonator at the position of maximum electric field, only the first term in the numerator is significant, since a small change in ε' at a point of zero electric field or a small change in μ at a point of zero magnetic field does not change the resonance frequency. Therefore, Equation (2) can be reduced to:

$$\frac{-df^*}{f} = \frac{(\varepsilon_r - 1)\int_{v_S} E.E_{0\max}^* dv}{2\int_{vC} |E|^2 dv}. \quad (3)$$

III. MEASUREMENT OF COMPLEX PERMITTIVITY

The cylindrical sample is taken with uniform cross sectional area '**s**' and length is greater than narrow dimension '*b*' of the cavity, so that it will occupy the entire narrow dimension of the cavity. Due to the change in the overall capacitance and conductance of the cavity on the introduction of the sample, the resonance frequency decreases from f_0 to f_s and the quality factor from Q_0 to Q_s.

The procedure for the determination of complex permittivity is described as follows.

1. The resonance frequency (f_0) and unloaded quality factor (Q_0) of the cavity resonator are measured with the empty cavity at the position of maximum electric field.
2. The sample is inserted in the cavity at the position maximum electric field without dismantling the

cavity resonator. The shifted resonance frequency f_s and loaded Q-factor Q_s are measured.

3. Knowing the volume of the cavity and the sample, the shift in resonance frequency and Q-factor, the dielectric constant and dielectric loss of the sample can be computed.

The complex resonant frequency shift is related to measurable quantities by [4], [5]:

$$\frac{df^*}{f} = \frac{f_s^2 - f_0^2}{f_s^2} + \frac{j}{2}\left(\frac{1}{Q_s} - \frac{1}{Q_0}\right). \tag{4}$$

On equating real and imaginary parts of Equation (3) and (4), we have:
For real part,

$$\frac{-(f_S - f_0)}{f_S} = \frac{(\varepsilon_r^{/} - 1)\int_{V_S} E.E_{0\max}^{*}\, dv}{2\int_{V_C} |E_0|^2\, dv}. \tag{5}$$

We may assume that E = E_0 and the value of E_0 in the TE_{10p} mode is $E_0 = E_{0max} \sin(p\pi z/l) \sin(p\pi z/l)$, where a is the broader dimension of the cavity and l is the length of the cavity. Integrating and rearranging the Equation (5), we obtain:

$$\frac{f_0^2 - f_s^2}{f_s^2} = \frac{4V_s\varepsilon^{/}}{V_c}, \qquad \varepsilon^{/} = \frac{V_c(f_0^2 - f_s^2)}{4V_s f_s^2}, \tag{6}$$

where V_c is volume of the cavity = $a \times b \times l$ (dimensions of the cavity) and V_s is the volume of the sample = $\pi r^2 h$ (r is the radius and h is the length of the sample):
For imaginary part,

$$1/2\left(\frac{1}{Q_s} - \frac{1}{Q_0}\right) = \frac{\varepsilon_r^{//}\int_{v_S} E.E_{0\max}^{*}\, dv}{2\int_{v_S} |E|^2 dv}. \tag{7}$$

Integrating and rearranging the Equation (7), we obtain:

$$\left(\frac{1}{Q_s} - \frac{1}{Q_0}\right)\frac{f_0^2}{f_s^2} = \frac{4V_S\varepsilon^{//}}{V_C}, \qquad \varepsilon^{//} = \left(\frac{1}{Q_s} - \frac{1}{Q_0}\right)\frac{V_C f_0^2}{4V_S f_s^2}, \tag{8}$$

where Q_s is the quality factor of cavity loaded with sample and Q_0 is the quality factor without sample. The measured values of Q (Q_0 & Q_s) of the cavity are calculated by the equation given below:

$$Q = \frac{f_{resonant}}{\Delta f_{3dB}} = \frac{f}{f_R(3dB) - f_L(3dB)}. \tag{9}$$

Equation (5) and (7) are the expression for complex permittivity using cavity perturbation technique [9].

IV. EXPERIMENTAL SET UP

A transmission type rectangular cavity resonator is designed and fabricated using standard WR-90 waveguide at X-band with inner dimension of 23 x 10 mm. Depending upon the modes to be propagate, the length has been chosen. The fundamental mode is TE type with *10n* where *n* is the number of half wavelength along the propagation direction. Two thin conducting sheets are used to close the two ends of the waveguide to form a cavity resonator. The inductive coupling is provided with two symmetric holes of diameter 4 mm on these end sheets. The design specifications are given below:

- Frequency Range: 8 GHz - 12 GHz (X-band);
- Cut of wavelength: 46 mm;
- Modes Propagates: 5 (TE_{105}, TE_{106}, TE_{107}, TE_{108}, TE_{109});
- Inner dimension of cavity: 22.9 x 10 x 140 mm^3;
- Outer dimension of cavity: 25 x 12 x 140 mm^3;
- Material used: Brass;
- Coupling hole: 4 mm.

In order to insert a sample material in the resonator cavity without disassembling it, a narrow hole is constructed at the centre of the broader side of the cavity. The narrow opened hole has negligible effect on changing the geometrical configuration of electromagnetic field inside the cavity. The width of the sample hole is equal to the diameter of the cylindrical sample. This rectangular waveguide cavity resonator is connected to two ports of the Network Analyzer for S-parameters measurement. A conventional thru-reflect-line (TRL) calibration technique is applied for calibration. The cavity resonator has multiple resonant frequencies in particular frequency band, TRL calibration was reused in each resonant frequency range and the measurement was separately performed in each resonant frequency range.

V. ERROR ANALYSIS

No measurement of a physical quantity can be entirely accurate. There is an inherent error margin associated with the results. Error in measurement is the difference between the measured value and the unknown, true, value of the measured quantity [18]:

$$\sigma^2_{error} = \sigma^2_{Measurement} - \sigma^2_{True}.$$

The precision of measurement can best be improved through the correction of the causes of variation in the measurement process. However, it is frequently desirable to estimate the confidence interval for the mean of measurements which includes the measurement error variation. The confidence interval for the mean of these measurements is reduced by obtaining multiple readings. To estimate the total measurement error, uncertainty analysis is conducted on the present measurements. The calculation of uncertainty requires a detailed budget

which breaks down the variance of measurement error into consistent components, each of which can be separately estimated. The detailed model becomes like: $\sigma^2_M = \sigma^2_{instrument} + \sigma^2_{fixture} + \sigma^2_{enivironment} + \sigma^2_{calibration} + \sigma^2_{sample} + \sigma^2_{analysis}$.

Uncertainty due to repeatability, i.e., series of observations/readings at different interval of time, variations in cables, connectors, relevant accessories, AC mains, change of operators, variations in environment conditions, i.e., temp, humidity etc. have been calculated by taking standard deviation of the mean of the readings of five observations of each parameters. Uncertainty due to standard deviation (Usd) is calculated as follows:

$$U_{sd} = \sqrt{(1/5(5-1)) \times \{(X_1 - X_M)^2 + (X_2 - X_M)^2 + (X_3 - X_M)^2 + (X_4 - X_M)^2 + (X_5 - X_M)^2\}}, \quad (10)$$

where X_1, X_2, X_3, X_4, X_5 are readings at different interval of time and X_M is mean value. The degree of freedom = (No. of observations) – 1, i.e., 5-1=4.

Uncertainty arises from flaw in the measurement which repeats each time a measurement is made. It is mainly due to errors in the calibration of the measuring instruments. It depends upon calibrator's accuracy, its resolution, calibration certificate, and its temperature drift specifications etc. Uncertainty due to calibrator's accuracy (U_{a1}), calibrator's resolution (U_{a2}), calibrator's calibration certificate (U_{a3}), and due to temp drift in calibrator's specifications (U_{a4}) at 95%, confidence is calculated. Combined uncertainty (Uc) will be:

$$Uc = \sqrt{(U_{sd})^2 + (U_{a1})^2 + (U_{a2})^2 + (U_{a3})^2 + (U_{a4})^2}. \quad (11)$$

Overall measurement uncertainty ±U = kUc; where k = 1.96 for 95% confidence level. At 95% confidence interval, the error is ± 1.5 ppm.

VI. RESULTS AND DISCUSSION

The dielectric constant and dielectric loss of Teflon and Rexolite are measured at X-band. Table 1 shows a comparison of complex permittivity of Rexolite obtained with the present method and other method in literature [11]. The experimental results for Rexolite are in good agreement with those obtained using other method in literature.

The values for Teflon have been presented earlier in reference [9]. The cavity was connected to a network analyzer and could be excited to operate in five modes. Accordingly, five resonant peaks corresponding to frequencies around 8.46, 9.15, 9.96, 10.7 and 11.64 GHz appeared on the screen of the analyzer. The S-parameter (transmission co-efficient) measurement for Rexolite in X-band is shown in Fig. 1. Figure 1 shows the expected shifts in resonance frequency and quality factor. 3 dB down point on the resonance curves are noted down to calculate quality factor (Q_0) of empty cavity and sample loaded cavity (Q_s). Using Equations (6) & (8), dielectric constant and dielectric loss of sample materials have been calculated.

Complex permittivity of different samples of polystyrene composite are measured at X-band (8-12 GHz). Comparison of the dielectric constant and dielectric loss for different composition of carbon black at resonance frequency of 9.96 GHz obtained with the present experiment and available in literature [10] is presented in Fig. 2.

Table 1: Comparison of dielectric constant & dielectric loss of Rexolite

	Measured			Literature		
f_0 (GHz)	f_S (GHz)	ε′	ε″	f_S (GHz)	ε′	ε″
8.46	8.245	2.34	0.0021	8.78	2.35	0.0012
9.15	8.93	2.209	0.0013	-	2.36	0.00128
9.96	9.705	2.35	0.0012	9.927	2.33	0.0002
11.64	11.34	2.37	0.0002	11.08	2.33	0.0002

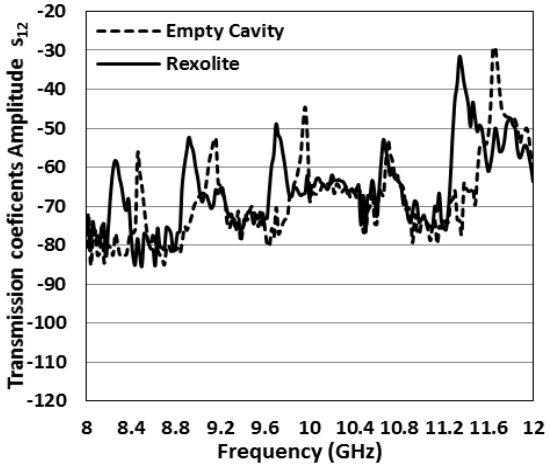

Fig. 1. Transmission coefficient measurement for Rexolite in X-band.

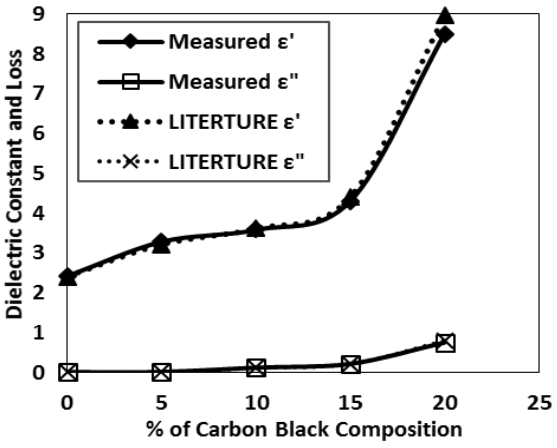

Fig. 2. Comparison of ε' & ε" at different % of carbon black composition.

The shift in resonance frequency & Q-factor depend on the dielectric properties of the material; the dielectric constant and dielectric loss of each composites of carbon black are measured on that specific frequency. In present measurement, the shift in resonance frequency for various carbon compositions varies from 9.70 GHz to 9.57 GHz. The experimental values of dielectric constant and dielectric loss for different polystyrene composite at 9.77 GHz are in good agreement with those obtained in literature. Finally, the dielectric properties of polystyrene composites are measured at X-band using this two port transmission type cavity resonator. Tables 2 (a) & 2 (b) shows experimental values of dielectric constant and dielectric loss for different composites of carbon black.

The dielectric parameters of five different samples; sample 1 (100% PS + 0% CB), sample 2 (95% PS + 5% CB), sample 3 (90% PS + 10% CB), sample 4, (85% PS + 15% CB) and sample 5 (80% PS + 20% CB) of polystyrene composite at wider frequency range of 8-12 GHz are also represented in Figs. 3 (a) & (b).

Table 2 (a): Dielectric constant **(ε′)** of polystyrene composite at various resonance frequencies (f_0) in X-band (8-12 GHz)

f_0 (GHz)	0% CB	5% CB	10% CB	15% CB	20% CB
8.46	2.29	3.249	3.856	7.95	7.95
9.15	2.313	3.265	4.076	8.234	8.234
9.96	2.415	3.28	4.3	8.5	8.5
11.64	2.59	3.3	5.1	9.08	9.08

Table 2 (b): Dielectric loss **(ε")** of polystyrene composite at various resonance frequencies (f_0) in X-band (8-12 GHz)

f_0 GHz)	0% CB	5% CB	10% CB	15% CB	20% CB
8.46	0.007	0.0084	0.115	0.198	0.699
9.15	0.0076	0.0087	0.118	0.204	0.712
9.96	0.0080	0.0098	0.1200	0.215	0.750
11.64	0.011	0.0127	0.1295	0.24	0.795

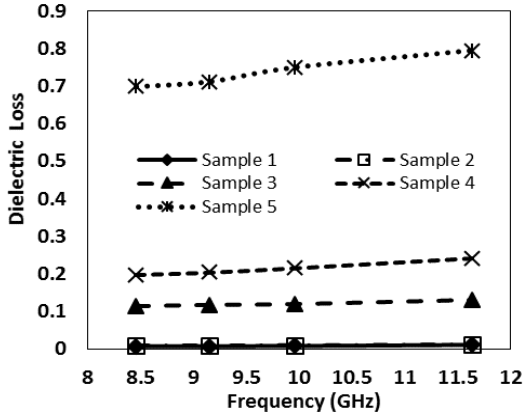

(a)

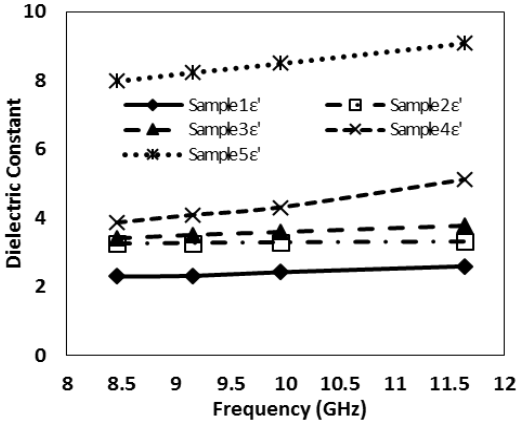

(b)

Fig. 3. (a) Variation of measured dielectric constant as a function of frequency, and (b) variation of measured dielectric loss as a function of frequency.

VII. CONCLUSION

In this paper, cavity perturbation technique for measuring the complex permittivity of polystyrene composite at X-band is described. We have presented measured results compared with those existing in literature to show good agreement. It has been observed from Tables 2 (a) & 2 (b) that, the values of dielectric constant and dielectric loss are increasing with the increase of carbon black concentration in polystyrene. For polystyrene composites, the dielectric data over entire frequency range are not available, so the dielectric behavior of polystyrene composites presented here is of great interest for the community. Measurement error has been estimated and found that at 95% confidence interval, the error is ± 1.5 ppm. The dielectric properties of the material can be measured with existing cavity resonator with an accuracy of 1.5 ppm.

ACKNOWLEDGMENT

We acknowledge Microwave Laboratory at Bharat Electronics for measurement purposes in this work. The authors are sincerely thankful to reviewers for their critical comments and suggestion to improve the quality of the paper.

REFERENCES

[1] A. Lonappan, G. Bindu, V. Thomas, and K. T. Mathew, "Analysis of human semen using microwaves," *Progress In Electromagnetics Research, PIER 57*, pp. 277-284, 2006.

[2] H. E. Bussey, "Measurement of RF properties of materials – a survey," *Proc. IEEE*, vol. 55, no. 6, pp. 1046-1053, 1967.

[3] A. Kraszewski, "Microwave aquametry – a review," *J. Microwave Power & Electromag. Energy*, vol. 15, no. 4, pp. 209-220, 1980.

[4] M. Ikeda, T. Fukunaga, and T. Miura, "Influence of sample insertion hole on resonant cavity perturbation measuring method," *Microwave Symposium Digest, 2003 IEEE MTT-S International*, vol. 2, pp. 1423-1426, 2003.

[5] A. Verma and D. C. Dube, "Measurement of dielectric parameters of small samples at X-band frequencies by cavity perturbation technique," *Instrumentation and Measurement, IEEE Transactions*, vol. 54, issue 5, pp. 2120-2123, Oct. 2005.

[6] J. Baker-Jarvis, E. J. Vanzura, and W. A. Kissick, "Improved technique for determining complex permittivity with transmission/reflection method," *IEEE Trans. Microwave Theory Tech*., vol. 38, no. 8, pp. 1096-1103, 1990.

[7] P. J. Petersan and S. M. Anlagea, "Measurement of resonant frequency and quality factor of microwave resonators: comparison of methods," *Journal of Applied Physics*, vol. 84, no. 6, pp. 3392-3402, Sep. 15, 1998.

[8] M. D. Janezic and J. A. Jargon, "Complex permittivity determination from propagation constant measurements," *IEEE Microwave and Guided Wave Letters*, vol. 9, no. 2, pp. 76-78, 1999.

[9] S. Sharma, et al., "Measurement of dielectric constant and loss factor of the dielectric material at microwave frequencies," *Journal of Electromagnetic Waves & Applications*, MIT USA, PIERS 69, pp. 47-54, 2007.

[10] R. A. Abdulnabi, "The cavity perturbation method for the measurement of the dielectric properties of (polystyrene/carbon black) composite." *Journal of Basrah Researches (Sciences)*, vol. 37, no. 1, pp. 1-7, Feb. 15, 2011.

[11] M. Hajian, et al., "Measurement of complex permittivity with waveguide resonator using perturbation technique," *Microwave and Technology Letters*, vol. 21, no. 4, May 20, 1999.

[12] H. A Bethe and J. Schwinger, *NRDC Report D1-117*, Cornell University, Mar. 1943.

[13] V. R. K. Murthy and R. Raman, "A method for the evaluation of microwave dielectric and magnetic parameters using rectangular cavity perturbation technique," *Solid State Communication*, vol. 70, no. 8, pp. 847-850, 1989.

[14] R. F. Harrington, *Time-Harmonic Electromagnetic Fields*, McGraw-Hill, New York, 1961.

[15] R. A. Waldron, "Perturbation theory of resonant cavities," *Proc. IEE*, vol. 170C, pp. 272-274, 1960.

[16] R. Coccioli, G. Pelosi, and S. Selleri, "Characterization of dielectric materials with the finite element method," *IEEE Trans. Microwave Theory Tech*., vol. 47, pp. 1106-1111, July 1999.

[17] L. Erdogan and C. Akley, "Dielectric properties of oil sands at 2.45 GHz with $TE_{1,0,11}$ mode determined by a rectangular cavity resonator," *Journal of Microwave Power and Electromagnetic Energy*, vol. 45, no. 1, pp. 15-23, 2011.

[18] E. L. Grant and R. S. Leavenworth, *Statistical Quality Control*, 6th edition, McGraw-Hill, New York, 1988.

Sarita Sharma received first class B.Tech and M.Tech degrees in Electronics and Communication Engineering from PTU, Jalandhar (Punbaj), India. She worked as Faculty in the Department of Electronics Technology, Guru Nanak Dev University, Amritsar, India. Thereafter, she joined as Asst. Professor in the Department of ECE at Chandigarh College of Engineering and Technology, Chandigarh, India. She is presently working with CCET as Sr. Asst. Professor. Her research interests are in the area of microwave passive devices, RF communication systems, and microwave measurements

Dalveer Kaur received the first class M.Tech. degree in Micro-electronics in 2003 and the Ph.D. degree in Electronics & Microwave Engineering in 2010 from Guru Nanak Dev University, Amritsar, India. Since 2010, she is working as Asst. Professor in the Department of Electronics & Communication Engineering, Punjab Technical University, Jalandhar, India. Her research interests are in the area of microwave communication, microwave devices, and microwave measurements.